

**Numerical and Experimental Study of the Influence of
Frost Formation and Defrosting on the Performance of
Industrial Evaporator Coils**

by

Nawaf Faisal Aljuwayhel

A dissertation submitted in partial fulfillment of the
requirements for the degree of

Doctor of Philosophy
(Mechanical Engineering)

at the

UNIVERSITY OF WISCONSIN-MADISON
2006

Acknowledgements

First and foremost, I want to express my deepest gratitude to my advisors, Professor G. Nellis, Professor D. Reindl, and Professor S. Klein, for their constant guidance, patience, continuous encouragement and support throughout my graduate studies. It was an honor to work under their supervision and I am indeed very privileged to have been one of their students.

Also I would like to extend my sincere thanks to the rest of the Solar Energy Lab faculty members including, Professor W. Beckman, Professor J. Mitchell, Professor T. Shedd and Professor J. Pfothenhauer for their technical support and for providing a great research atmosphere.

Many thanks must be given to the dedicated staff of the Industrial Refrigeration Consortium (IRC), especially for T. Jekel and D. Dettmers, who were so kind to dedicate some of their valuable time to discuss some of the problems related to this research.

A very special thanks must be extended to Wells' Dairy (Blue bunny) for allowing me to use their facilities to conduct the experimental part of this research and for providing most of the experiment instrumentation.

I would particularly wish to thank KUWAIT UNIVERSITY and especially the mechanical engineering department for the financial support and for providing me such great opportunity to conduct my Masters and Doctorial studies at the UNIVERSITY OF WISCONSIN-MADISON.

All my life, my parents have stressed the importance of hard work and the value of a good education. They have always provided guidance whenever I needed it, and the support and love received from them and my brothers and sisters have been the

foundation of all my successes. I hope I have made them all as proud of me as I am of them.

Finally, no words could express the love and appreciation I have for my wife. She has been my constant source of support and understanding, without which I could not have survived. Although I could never give back to her what she given to me, I promise to do my best. It is with this that I dedicate this work to her and to my sons Faisal and Khalid.

NUMERICAL AND EXPERIMENTAL STUDY OF THE INFLUENCE OF FROST
FORMATION AND DEFROSTING ON THE PERFORMANCE OF INDUSTRIAL
EVAPORATOR COILS

Nawaf Faisal Aljuwayhel

Under the supervision of Associate Professor G. F. Nellis, Professor S. A. Klein and
Professor D. T. Reindl

at the University of Wisconsin-Madison

The main objective of an evaporator in any refrigeration system is to extract thermal energy from a conditioned space by recirculating air through a refrigerated coil. However, when an air-cooled evaporator operates at a temperature below the freezing point of water with a coincident entering air dew point temperature that is above the evaporator coil surface temperature, frost will form on the evaporator surface. The presence of frost reduces the performance of an evaporator and the penalty is proportional to the amount of frost that has accumulated. For this reason, the accumulated frost must be periodically removed by the use of a defrost process.

A variety of methods are used to remove frost, however, the most widely-used defrost technique in industry is hot gas defrosting (HGD). The HGD technique depends on temporarily converting the evaporator to a condenser by passing hot gas through the coil; the hot gas is usually obtained directly from the compressor discharge. The HGD technique is a simple and effective method to remove frost rapidly, and the additional hardware required for the HGD process is relatively inexpensive to install. However, during the HGD process, a fraction of the energy supplied to the coil is ultimately transferred to the refrigerated in various forms and becomes a parasitic load (latent and

sensible) on the refrigerated space. This additional energy added to the space must be extracted by other evaporators within the freezer space (or, if only one evaporator is in the space then the product temperature must rise). Hence, both the frosting and the defrosting processes penalize the efficiency of the cooling system.

In this research, the performance of a large scale industrial evaporator operating under frosting conditions is experimentally monitored during both cooling mode (which occurs under frosting conditions) and defrost mode. Theoretical models of the evaporator coil during the cooling and the defrosting modes have been developed and validated using the experimental data. The degradation of the performance of the evaporator during the cooling mode and the parasitic heat load associated with the defrost mode are presented. The two models are used to optimize the net cooling by minimizing all the penalties associated with running the refrigeration system. Guidelines relative to the most energy efficient operation of industrial refrigeration systems are presented.

Table of contents

Acknowledgements	I
Abstract	III
List of figures	IX
List of tables	XIX
Chapter 1 Introduction	1
1.1 Research motivation.....	1
1.2 Research Objectives	10
1.3 Outline of the thesis	12
1.4 References	15
Chapter 2 Literature Review.....	16
2.1 Definitions and terminology.....	16
2.2 Literature review	21
2.2.1 Mechanisms of frost formation	21
2.2.2 Review of Existing Frost Experimental Data and Models:.....	22
2.2.2.1 Experimental Studies	23
2.2.2.2 Numerical Studies.....	27
2.2.3 Review of Existing Defrost Experimental Data and Models:	36
2.3 Nomenclature	42
2.4 References	44
Chapter 3 Frost Model.....	48
3.1 Formulation of the frost model:.....	48
3.2 Heat transfer equations:.....	51
3.2.1 Air-side heat transfer and pressure drop:.....	59
3.2.2 Refrigerant heat transfer and pressure drop:	62
3.3 Summary.....	66
3.4 Nomenclature	67
3.5 References	70

Chapter 4	Frost Experiment	72
4.1	Experiment facility:	72
4.2	Design of Experiment:.....	76
4.3	Instrumentation and data Acquisition:.....	78
4.3.1	Flow and temperature Measurements.....	78
4.3.2	Relative Humidity Measurements	82
4.3.3	Data Acquisition System.....	84
4.4	Experiment uncertainty:	85
4.4.1	Uncertainty Analysis	86
4.5	Experiment results:	87
4.6	Summary.....	96
4.7	Nomenclature	97
4.8	References	97
Chapter 5	Frost Model Validation.....	98
5.1	Comparison between the frost experimental data and the model predictions	98
5.2	Effects of Lewis Number on the frost model prediction.....	103
5.3	Summary.....	106
5.4	References	107
Chapter 6	Defrost Model.....	108
6.1	Model development :	109
6.2	Heat and Mass Transfer Equations	114
6.2.1	Energy balance on the evaporator coil tubes:.....	114
6.2.2	Energy balance on the evaporator coil fins:	121
6.2.3	Energy balance on the evaporator coil tube-frost:.....	123
6.2.4	Energy balance on the evaporator fin-frost:.....	127
6.2.5	Energy balance on the penthouse walls and enclosed air :.....	129
6.3	Sensitivity Analysis	133
6.4	Summary.....	136
6.5	Nomenclature	138

6.6	References	139
Chapter 7	Defrost Experiment	140
7.1	Experiment Facility	140
7.2	Design of Experiment	141
7.2.1	Instrumentation.....	144
7.3	Experimental Results	147
7.3.1	Visual Study of the Frost Melting Sequence	148
7.3.2	Water Condensate Flow Rate	151
7.3.3	Penthouse-Air Temperature.....	153
7.4	Summary.....	159
Chapter 8	Defrost Model Validation.....	161
8.1	Validation of the HGD model of the penthouse evaporator	161
8.2	Heat load calculation.....	168
8.3	Summary.....	180
8.4	References	182
Chapter 9	Net Cooling Optimization.....	183
9.1	Penalties considered in the analysis:	183
9.1.1	Penalties due to Frost Accumulation.....	184
9.1.2	Penalties due the frost removal.....	186
9.2	Overall System Efficiency and the Cost of Frost	191
9.3	Infiltration load	192
9.4	Optimization results.....	195
9.5	Effects of moisture infiltration to the overall system efficiency.....	217
9.6	Summary.....	223
Chapter 10	Counter-flow versus Parallel-flow Circuiting Evaporators	226
10.1	Counter-flow versus parallel-flow circuiting during cooling mode operation.....	226
10.1.1	Formulation of the frost model.....	227

10.2 Counter-flow versus parallel-flow circuiting performance over an entire refrigeration cycle.....	237
10.3 Summary.....	240
10.4 Nomenclature	242
10.5 References	242
Chapter 11 Conclusion.....	243
11.1 Conclusions	243
11.1.1 Frost numerical model and frost experiment	244
11.1.2 Defrost numerical model and defrost experiment	245
11.1.3 Net cooling optimization.....	247
Appendix A	250
Appendix B	254
Appendix C	256
Appendix D	261

List of Figures

Figure 1.1	Heavy frost formation on a low temperature blast freezer coil (left) and the light billowy structure of the frost (right)	3
Figure 1.2	Close-up of low temperature evaporator coil before frost formation (left) and after 1 day of frost formation (right)	3
Figure 1.3	Schematic of a direct expansion evaporator	4
Figure 1.4	Schematic of a natural recirculation evaporator	5
Figure 1.5	Schematic of liquid overfeed evaporator	5
Figure 1.6	Floor mounted evaporator coil	6
Figure 1.7	Ceiling-hung evaporator coil	6
Figure 1.8	Penthouse evaporator coil	7
Figure 1.9	Schematic of flow in the Hot Gas Defrost (HGD) mode	9
Figure 2.1	Schematic of a heat exchanger showing (a) the minimum flow area shaded with downward diagonal lines, (b) coil face area, (c) Fin pitch and fin thickness, (d) The equivalent area appropriate for a plate fin in a staggered tube arrangement, as suggested by Schmidt (1949)	17
Figure 2.2	Parallel plates geometry used in the Reynolds number defined in Eq. (2.14)	
Figure 3.1	Schematic showing evaporator coil with multiple rows of finned tubes with multiple refrigerant circuits and the direction of the air and the refrigerant flow.	49
Figure 3.2	Schematic diagram showing one evaporator coil circuit and the direction of the air and the refrigerant flow.	49
Figure 3.3	Schematic diagram showing the first and the second evaporator coil sections as well as the direction of the air and refrigerant flow.	50
Figure 3.4	Schematic of the energy flows in frosted section of cooling coil	52

Figure 4.1	Penthouse enclosure; Schematic showing the outside dimensions of the penthouse (top). Photograph showing the penthouse that encloses the evaporator coil (bottom).	74
Figure 4.2	Penthouse plan view showing the internal dimensions of the penthouse enclosure.	75
Figure 4.3	Schematic of the experiment coil and the flow path of the air.	75
Figure 4.4	Schematic of the penthouse-plenum setup	76
Figure 4.5	Schematic showing locations for measurements taken during the experiments.	77
Figure 4.6	Schematic showing the exact location of each velocity mass flow meter and Thermistor (top) mounting detail (bottom).	80
Figure 4.7	Schematic showing the horizontal gap between the coil fins.	81
Figure 4.8	Schematic showing the exact location of the relative humidity sensors ($RH_{in,1}$ and $RH_{in,2}$)	82
Figure 4.9	Schematic showing the exact location of the relative humidity sensors ($RH_{o,1}$ and $RH_{o,2}$) (top) and the mounting (bottom)	83
Figure 4.10	Time-dependent spatially-averaged air velocity on the downstream side of the evaporator (with time 0 being an ice-free coil) throughout all of the experimental tests.	88
Figure 4.11	Time-dependent measured air velocity of each velocity sensor and the calculated average air velocity down stream side of the evaporator; (a) Run #1, (b) Run #3.	89
Figure 4.12	Time-dependent spatially-averaged inlet and outlet air temperatures throughout the experiment	90
Figure 4.13	Time-dependent temperature difference between the inlet and outlet air flows.	91
Figure 4.14	Time-dependent relative humidity of the inlet air.	91
Figure 4.15	Time-dependent humidity ratio of the inlet and outlet air.	92
Figure 4.16	Time-dependent mass flow rate of the frost accumulation.	94
Figure 4.17	Time-dependent mass accumulation of frost.	94

Figure 4.18	Time-dependent evaporator cooling capacity as frost accumulates.	95
Figure 5.1	Comparison between the average face velocity of the evaporator coil measured in the experiment and the face velocity predicted by the counter-flow frost model over time.	99
Figure 5.2	Comparison of the time-dependent spatially-averaged inlet and outlet air temperatures measured during the experiment and the inlet and outlet air temperature predicted by the frost model	100
Figure 5.3	Comparison of the inlet and outlet air temperature difference measured during the experiment and the temperature difference predicted by the counter-flow frost model over time.	101
Figure 5.4	Comparison of the evaporator cooling capacity measured during the experiment and the evaporator cooling capacity predicted by the counter-flow frost model over time.	102
Figure 5.5	Comparison of the total mass of frost predicted by the counter-flow frost model and the total mass of frost obtained using the experimental data over time.	102
Figure 5.6	Frost accumulation rate and the total mass for accumulated frost over time for three different Lewis numbers	104
Figure 5.7	Cooling coil capacity prediction of the frost model for three different Lewis numbers.	104
Figure 5.8	Percentage of the blockage of the air path caused by frost accumulation at different rows of the evaporator coil over time for (a) Lewis number of 1.0 and (b) Lewis number of 0.85.	105
Figure 6.1	Schematic of the evaporator coil with multiple rows of finned tubes with multiple refrigerant circuits and the direction of the hot-gas flow.	110
Figure 6.2	Schematic of one evaporator coil circuit and the direction of the hot-gas flow.	111
Figure 6.3	Schematic of the first, the second and the last evaporator coil sections as well as the direction of the hot-gas flow.	111

Figure 6.4	Schematic of the frosted tube and the equivalent circular fins	111
Figure 6.5	Schematic of the computational domain	112
Figure 6.6	Schematic of the four lumped capacities that together represent the computational domain.	114
Figure 6.7	Schematic showing the sensible heat transfer rates to and from the evaporator coil tubes during the hot-gas process; a) pre-heating and melting stages, b) dry heating stage, c) bleeding stage.	115
Figure 6.8	Conduction heat transfer from the evaporator coil metal and frost surfaces to the air.	120
Figure 6.9	Convection heat transfer from the evaporator coil metal and frost surfaces to the air	120
Figure 6.10	Schematic showing the sensible heat transfer rates to and from the evaporator coil fins during the hot-gas process; a) pre-heating and melting stages, b) dry heating and bleeding stages.	122
Figure 6.11	Schematic showing the sensible heat and the latent heat transfer rates to and from the tube-frost during the hot-gas process; a) pre-heating stage, b) melting stage	124
Figure 6.12	The variation in the frost temperature as a function of the frost enthalpy.	124
Figure 6.13	Schematic diagram showing the sensible heat and the latent heat transfer rates to and from the fin-frost during the hot-gas process; a) pre-heating stage, b) melting stage.	128
Figure 6.14	Schematic showing the sensible heat and the latent heat transfer rates to and from the penthouse-air during the four stages of the hot-gas process.	131
Figure 7.1	Schematic of flow in the Hot Gas Defrost (HGD) mode.	143
Figure 7.2	Elevation view downstream of the evaporator coil showing the location of each air velocity transducer and thermistor	145

Figure 7.3	Schematic showing the exact location of thermistors used to measure the interface temperature between the penthouse-air and the freezer-air.	145
Figure 7.4	Schematic showing the exact location of thermistors used to measure the air temperature between the evaporator coil fins; (a) side-view, (b) front-view.	146
Figure 7.5	Gross evaporator capacity as a function of time for the 5 HGDCs measured during the pump-out period.	148
Figure 7.6	Time-lapse photos of the evaporator coil during HGDC #1	151
Figure 7.7	Photograph of the penthouse drain during HGDC #1.	152
Figure 7.8	Mass and volumetric flow rates of the drained water of HGDC #1.	152
Figure 7.9	Measured air temperature at the evaporator core as a function of time during an HGDC at six different elevations (see Figure 7.4).	154
Figure 7.10	Spatially-averaged air temperature at the evaporator core and at down-stream side the evaporator coil.	155
Figure 7.11	Air temperature measured at the down-stream side of the evaporator core at five different elevations as a function of time during an HGDC.	156
Figure 7.12	Spatially-averaged air temperature at the down-stream side of the evaporator coil during HGDCs #2-5.	157
Figure 7.13	Spatially-averaged air temperature at up-stream side of the evaporator coil during HGDC #2-4.	158
Figure 8.1	Comparison between the average penthouse air temperature predicted by the HGD model and the spatially-averaged air temperature measured at the evaporator core and at down-stream side the evaporator coil during HGDC #1.	164
Figure 8.2	Comparison of the average water condensate mass flow rate predicted by the HGD model and the measured during the HGDC#1 as a function of time.	165

Figure 8.3	Comparison between the average penthouse air temperature predicted by the HGD model and the spatially-averaged air temperature measured at the down-stream side the evaporator coil during HGDC #2-5 versus time.	166
Figure 8.4	Average water condensate mass flow rate predicted by the HGD model prior to 24 and 48 hours of cooling mode versus time.	167
Figure 8.5	The predicted average temperature of the penthouse walls, penthouse air and the hot gas as well as the total mass of the remaining frost for a defrost process that follow 48 hours of cooling operation.	168
Figure 8.6	Total melting heat load and the total mass of frost for both the penthouse and the ceiling-hung evaporator coils throughout the HGDC prior to 48 hours of cooling versus time	171
Figure 8.7	Total parasitic heat load and the total mass of frost for both the penthouse and the ceiling-hung evaporator coils throughout the HGDC that occurs after 48 hours of cooling operation.	172
Figure 8.8	Total mass of the evaporated and sublimated frost during the HGDC of the penthouse and the ceiling-hung evaporator coils versus time.	173
Figure 8.9	Total hot gas defrost load and the total mass of frost during a HGDC that occurs after 48 hours of cooling operation; both the penthouse and the ceiling-hung evaporator are shown.	174
Figure 8.10	Hot gas defrost efficiency and the total mass of frost during a HGDC prior to 48 hours of cooling of both the penthouse and the ceiling-hung evaporator coils versus time.	176
Figure 9.1	Actual and the ideal evaporator cooling capacity versus time during the cooling operation mode.	185
Figure 9.2	Total energy loss during the cooling mode due to frost accumulation versus time during the cooling operation mode.	186

- Figure 9.3** Actual and the ideal evaporator cooling capacity as a function of time during the pump-out stage. Also shown are the measured data for gross cooling capacity during pump-out as a function of time for 5 different defrost cycles. 188
- Figure 9.4** Ideal cooling capacity during the hot gas and the bleed stages as a function of time. 189
- Figure 9.5** Quantitative representation of the total parasitic heat load during the hot gas stage versus time. 190
- Figure 9.6** Penalties as a function of cooling operation intervals between defrost cycles for two days of continuous penthouse evaporator operation using a hot gas stage dwell period that is equal to ; a) the exact time required to melt the frost, b) 150% of the exact time required to met the frost, and a constant dwell period of d) 30 minutes, c), and d) 40 minutes. 198
- Figure 9.7** Frost penalties as a function of cooling operation intervals between defrost cycles for two days of continuous operation of a ceiling-hung evaporator using hot gas stage dwell periods that are equal to ; a) the exact time required to melt the frost, b) 150% of the exact time required to met the frost, and a constant dwell period of d) 30 minutes, c), and d) 40 minutes. 201
- Figure 9.8** Percentage of the overall penalty that is due to the hot gas defrost parasitic heat load as a function of the cooling operation interval for different dwell periods of hot gas stage for the penthouse evaporator coil. 202
- Figure 9.9** Percentage of the overall penalty that is due to the hot gas defrost parasitic heat load as a function of the cooling operation interval for different dwell periods of hot gas stage for the ceiling-hung evaporator coil. 203

Figure 9.10	Percentage increase in the overall penalty associated with frost accumulation and removal for the ceiling-hung as compared to the penthouse evaporator as a function cooling operation interval for different dwell periods of the hot gas stage.	204
Figure 9.11	Overall system efficiency as a function of cooling operation interval for a penthouse evaporator coil with various hot gas stage dwell periods.	206
Figure 9.12	Overall system efficiency as a function of cooling operation interval for a ceiling-hung evaporator coil with various hot gas stage dwell periods.	206
Figure 9.13	Annual electrical penalty as a function of cooling operation interval for a penthouse evaporator coil with various hot gas stage dwell periods.	208
Figure 9.14	Annual electrical penalty as a function of cooling operation interval for a ceiling-hung evaporator coil with various hot gas stage dwell periods.	208
Figure 9.15	Annual cost of frost as a function of cooling operation interval for a penthouse evaporator coil with various hot gas stage dwell periods.	209
Figure 9.16	Annual cost of frost as a function of cooling operation interval for a ceiling-hung evaporator coil with various hot gas stage dwell periods.	210
Figure 9.17	Excessive frost accumulation on the inlet refrigerant header and the frame of the evaporator coil.	212
Figure 9.18	Excessive frost accumulation on the bottom of the evaporator coil	212
Figure 9.19	Cooling capacity prediction of the frost model for three different inlet air relative humidity versus time of cooling.	218
Figure 9.20	Density of frost at a constant inlet air temperature to the evaporator coil with three different inlet air relative humidity versus total mass of accumulated frost.	218

Figure 9.21	Overall system efficiency of penthouse evaporator coil with a constant inlet air temperature and three different inlet air relative humidity as a function of cooling operation interval	219
Figure 9.22	Overall system efficiency of penthouse evaporator coil with a constant inlet air temperature and three different inlet air relative humidities as a function of the total mass of the accumulated frost and the Defrost number.	222
Figure 10.1	Schematic diagram showing evaporator coil with multiple rows of finned tubes with multiple refrigerant circuits and the direction of the air and the refrigerant flow for both the counter-flow and parallel-flow arrangements	228
Figure 10.2	Schematic of the first and the second evaporator coil sections as well as the direction of the air and refrigerant flow for counter-(left) and, parallel-(right) flow arrangement.	229
Figure 10.3	Comparison between the evaporator cooling capacity predicted by the counter-flow frost model and the parallel-flow frost model versus time.	229
Figure 10.4	Predicted air and refrigerant temperature and UA across the evaporator coil for (a) parallel-flow and (b) counter-flow configuration.	231
Figure 10.5	Cooling capacity across the evaporator for the counter-flow and parallel-flow configuration.	232
Figure 10.6	Comparison between the air velocity predicted by the counter-flow frost model and the parallel-flow frost model over time	233
Figure 10.7	Comparison between the total mass of the accumulated frost predicted by the counter-flow and the parallel-flow frost model over time.	234
Figure 10.8	Comparison of the frost accumulation rate at each row predicted by the counter-flow frost model and the parallel-flow frost model.	235

- Figure 10.9** Percentage of the blockage of the air path caused by frost accumulation at different rows of the evaporator coil over time for (a) counter-flow and (b) parallel-flow circuiting. 236
- Figure 10.10** Actual and the ideal evaporator cooling capacity of the counter-flow and the parallel-flow circuiting evaporators versus time during the cooling operation mode. 238
- Figure 10.11** overall system efficiency of counter-flow and parallel-flow circuiting evaporator coils versus cooling operation intervals between defrost 240

List of Tables

Table 2-1	Error comparison between the frost model predictions and the experimental results from Oskarsson et al. (1990)	34
Table 3-1	Parameter J_b defined in Eq.(3.45), Paliwoda (1992)	64
Table 3-2	Coefficient of resistance, x_b defined in Eq.(3.44), Paliwoda (1992)	64
Table 4-1	Geometry and operating conditions of the coil used in the experiment	73
Table 4-2	Average coil face parameters.	86
Table 4-3	Summary of the estimated uncertainties of the measured variables.	87
Table 4-4	Summary of the estimated uncertainties of the calculated results.	87
Table 4-5	Initial and final cooling rates for five experiment runs along with the percentage loss of the cooling rate.	95
Table 6-1	The value of the experimentally fitted parameters for the base case	133
Table 6-2	Results of the Hot Gas Defrost base case	134
Table 6-3	Defrost model sensitivity analysis	136
Table 7-1	Time duration for each of the four main stages for each HGDC and the time duration of the cooling mode operation prior to each HGDC.	147
Table 7-2	Summary of the effects of the various hot gas defrost process on the refrigeration system.	159
Table 8-1	Geometry and operating conditions of the coil used to develop the hot gas defrost model.	162
Table 8-2	Time duration for each of the four main stages for each HGDC and the time duration of the cooling mode operation prior to each HGDC	164
Table 8-3	HGDP time setting used for the heat load calculation	169
Table 8-4	Energy distribution of a HGDS prior to 48 hours of cooling of penthouse evaporator coil.	179
Table 8-5	Energy distribution of a HGDS prior to 24 hours of cooling of penthouse evaporator coil.	179

Table 8-6	Energy distribution of a HGDS prior to 48 hours of cooling of ceiling-hung evaporator coil.	179
Table 8-7	Energy distribution of a HGDS prior to 24 hours of cooling of ceiling-hung evaporator coil	180
Table 8-8	The exact time required for a complete frost removal from a penthouse and a ceiling hung evaporators for a different cooling time length between defrost cycles.	196
Table 9-1	The exact time required for a complete frost removal from a penthouse and a ceiling hung evaporators for a different cooling time length between defrost cycles.	
Table 9-2	Frost penalties and the annual cost of frost for a penthouse evaporator coil with a cooling operation interval of 12 hours and various hot gas stage dwell times.	213
Table 9-3	Frost penalties and the annual cost of frost for a penthouse evaporator coil with a cooling operation interval of 24 hours and various hot gas stage dwell times.	213
Table 9-4	Frost penalties and the annual cost of frost for a penthouse evaporator coil with a cooling operation interval of 36 hours and various hot gas stage dwell times.	214
Table 9-5	Frost penalties and the annual cost of frost for a penthouse evaporator coil with a cooling operation interval of 48 hours and various hot gas stage dwell times.	214
Table 9-6	Frost penalties and the annual cost of frost for a ceiling-hung evaporator with a cooling operation interval of 12 hours and various hot gas stage dwell times.	215
Table 9-7	Frost penalties and the annual cost of frost for a ceiling-hung evaporator with a cooling operation interval of 24 hours and various hot gas stage dwell times.	215
Table 9-8	Frost penalties and the annual cost of frost for a ceiling-hung evaporator with a cooling operation interval of 36 hours and various hot gas stage dwell times.	216

Table 9-9	Frost penalties and the annual cost of frost for a ceiling-hung evaporator with a cooling operation interval of 48 hours and various hot gas stage dwell times.	216
Table 10-1	Summary of total system efficiency for the counter-flow and parallel-flow circuiting designs for a 12 hour defrost interval and a hot gas stage duration that is 150% of the ideally terminated value.	237

Chapter 1 Introduction

1.1 Research motivation

Refrigeration is an enabling technology for everything from air conditioning for occupant comfort to cooling or freezing as required in industrial and food processing. Vapor compression is the most widely applied technology for providing useful refrigeration. In vapor compression refrigeration systems, a minimum of four basic components are required: a compressor, condenser, expansion device, and an evaporator. The focus of this research is on air-cooling evaporators in vapor compression refrigeration systems.

The main objective of an evaporator in any refrigeration system is to extract thermal energy from the space that must be cooled and transfer it to the refrigerant. If an air-cooling evaporator operates at a temperature below the freezing temperature of water with a coincident entering air dew point temperature above the evaporator coil surface temperature, then frost will form on the evaporator surface. The presence of frost penalizes the cooling capacity of the evaporator. In this situation, the evaporator provides both sensible cooling and dehumidification. Dehumidification involves the extraction of moisture from the air stream; the extracted moisture will be deposited on the coil surfaces in the form of frost.

The physical structure of the frost layer forming on an evaporator will depend on a number of factors including the coil operating temperature, entering air dew point temperature and relative humidity, and the velocity of the air passing through the coil.

Often, the frost layer consists of a porous structure composed of individual ice crystals and air pockets. Figure 1.1 shows one example of a very light frost structure that can form on an evaporator coil. In this situation, the evaporator operates at a low temperature, -40°C , in order to quickly freeze an unpackaged hot food product. This combination of low temperature and high moisture load leads to a very fluffy, light frost structure. Over time, the increasing amount of accumulated frost will substantially reduce the rate of air flow through the coil; however, the structure of the frost remains very light and fluffy and therefore a mechanical disturbance (e.g., a high velocity blast of air) can easily dislodge the frost from the coil surface. Figure 1.2 shows another example of frost forming on an evaporator coil; in this case, the frost structure is much denser and more tightly attached to the evaporator coil surface. The situation in Figure 1.2 corresponds to the evaporator coil operating at a somewhat higher temperature of -30°C in order to maintain storage of finished packaged ice cream products. This combination of higher temperature and moderate moisture load leads to a much denser frost structure.

The significance of the frost formation is twofold. First, the presence of frost reduces the ability of an evaporator fan to move air across the coil; as a result, the refrigeration capacity of the evaporator is significantly reduced. Second, the thermal conductivity of the air pockets formed within the frost structure is extremely low; this effect also leads to a reduction in the evaporator performance. For these reasons, the frost that accumulates on the outside surfaces of the coil during operation must periodically be removed using some type of defrost process



Figure 1.1 Heavy frost formation on a low temperature blast freezer coil (left) and the light billowy structure of the frost (right)

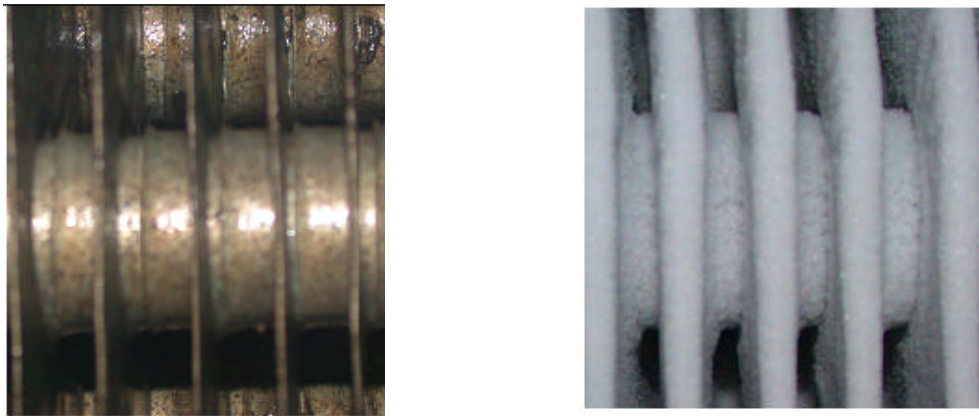


Figure 1.2 Close-up of low temperature evaporator coil before frost formation (left) and after 1 day of frost formation (right).

Evaporators can be classified according to the method used to feed the evaporator with refrigerant:

- 1: direct expansion evaporators (Figure 1.3),
- 2: natural recirculation (gravity flooding) evaporators (Figure 1.4), and
- 3: liquid overfeed (forced feed) evaporator (Figure 1.5).

The fundamental difference between these designs is related to the entering and leaving vapor quality of the refrigerant and the corresponding refrigerant mass flow rate for a given rate of heat transfer. In the natural recirculated and the liquid overfed systems, the evaporator is supplied with more refrigerant than can be converted to vapor by the

refrigeration load whereas the direct expansion system utilizes an expansion valve that controls the evaporator pressure in order to ensure that all of the refrigerant is converted to vapor before it leaves the evaporator and enters the suction line. In the natural recirculation system, the mass flow rate of the refrigerant is controlled by gravity and the elevation of the mean liquid level in the separator whereas the refrigerant mass flow rate is controlled by a pump in the liquid overfeed system; the pump forces the refrigerant to pass through the evaporator coils to overfeed the system so that refrigerant exits the evaporator with a low vapor quality.

Each of these evaporator types has associated advantages and disadvantages that depend on the refrigerant used, the suction temperature, the evaporator heat flux, the size of the equipment, and the system cost. The most popular evaporators for industrial refrigeration systems are natural recirculation and the liquid overfeed systems.

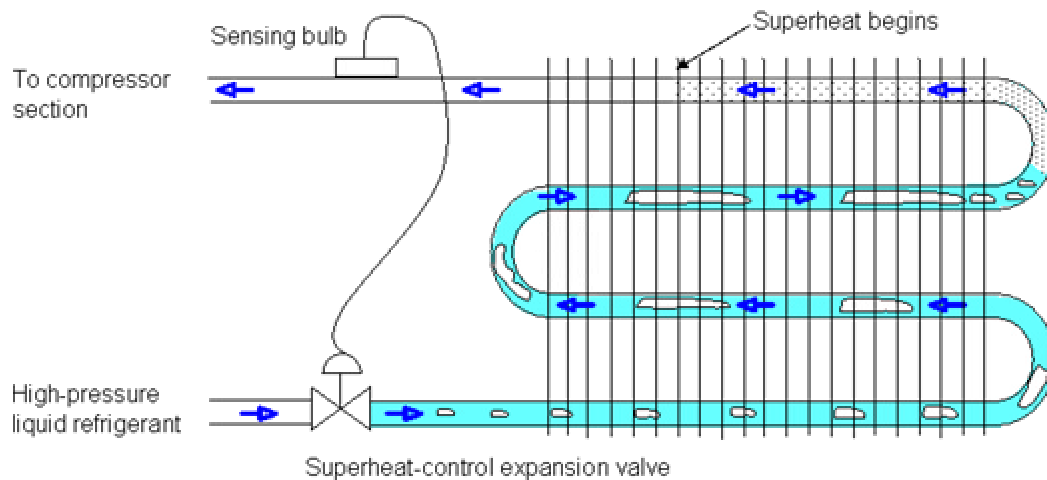


Figure 1.3 Schematic of a direct expansion evaporator

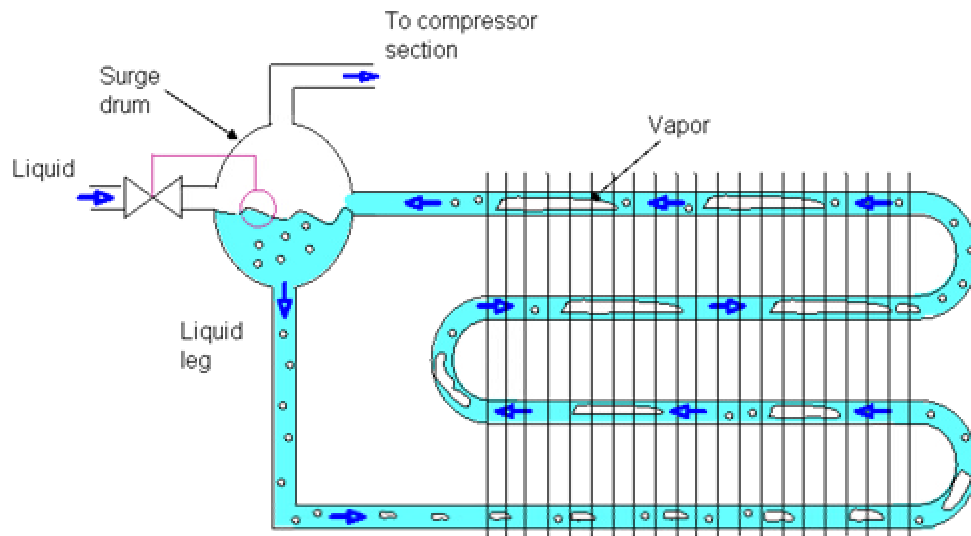


Figure 1.4 Schematic of a natural recirculation evaporator

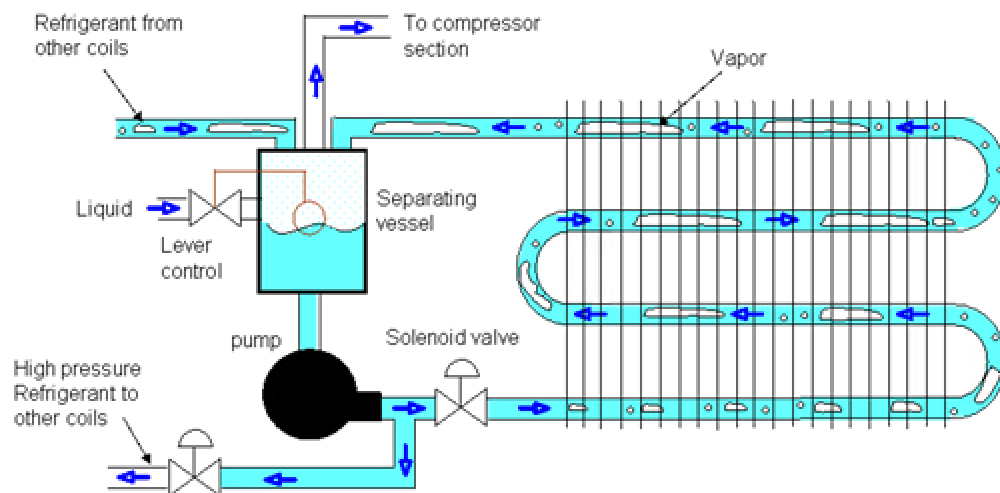


Figure 1.5 Schematic of a liquid overfeed evaporator

Also evaporator coils can be classified according to their installation:

- 1: floor mounted evaporator (Figure 1.6),
- 2: ceiling-hung evaporator (Figure 1.7), and
- 3: penthouse evaporator (Figure 1.8).



Figure 1.6 Floor mounted evaporator coil



Figure 1.7 Ceiling-hung evaporator coil



Figure 1.8 Penthouse evaporator coil

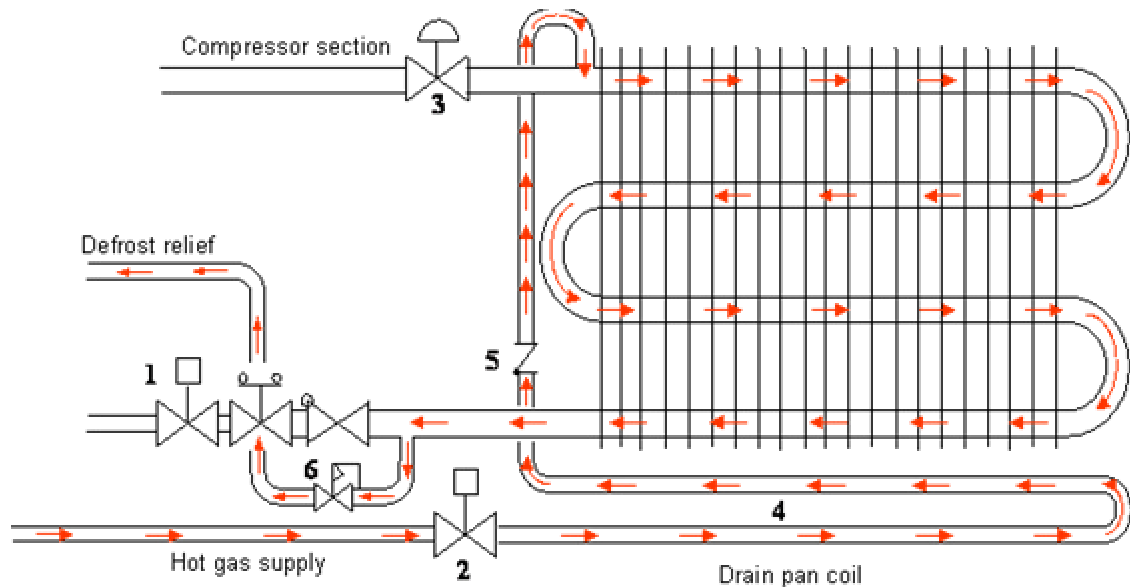
Each of these evaporator installation types has associated advantages and disadvantages. For example the floor mounted evaporators are easy to maintain, however since they are mounted on the freezer floor their presence will reduce the available freezer space. Ceiling-hung evaporators provide better air circulation and do not reduce the available freezer space, however in most cases they are hard to reach and to maintain. Finally penthouse evaporators provide good air circulation and are easy to maintain, however their initial cost is high.

Regardless of the type of the evaporator being considered, if the air passing through the coil reaches a temperature that is below the freezing temperature of water (as is necessary in any freezer application) and if the air contains moisture (which is unavoidable due to infiltration, doorways and other forms of external exposure) then frost will form on the evaporator coils. As this frost builds up, the cooling capacity of the evaporator is

degraded and therefore it is necessary to periodically remove the frost (defrost the coil) in order to maintain the required thermal performance of the evaporator.

A variety of methods are used to remove frost; the most widely-used defrost technique in industry is hot gas defrosting (HGD). The HGD method depends on reversing the flow of refrigerant within the evaporator so that during the hot gas defrost process the evaporator operates as a condenser; refrigerant in the form of hot vapor (typically obtained directly from the compressor discharge) is condensed as it transfers heat to the melting frost. The hot gas cycle is initiated by closing the liquid line solenoid valve, opening the hot gas solenoid valve and closing the suction stop valve (Figure 1.9). The hot gas enters the evaporator through the drain pan, heating the drain pan and then flows into the suction line through pan check valve (PCV). The PCV keeps liquid refrigerant from draining into the drain pan coil during normal operation of the refrigeration cycle. The hot gas then flows through the evaporator tubes where it melts frost on the coil and finally leaves the evaporator through a defrost relief regulator. The HGD method depends upon heating the evaporator coils using a superheated vapor in order to melt the frost and therefore during the HGD process, a parasitic heat load is introduced to the conditioned space. The additional heat added to the space must be extracted by other evaporators within the freezer space (or, if only one evaporator is in the space then the product temperature must rise). Also, a large part of the energy transferred from the hot gas is used to heat the evaporator pan and coil to a temperature above the melting temperature of the frost. This metal has a large thermal capacity and it must be cooled back to the evaporator's normal operating temperature at the conclusion of the defrost

cycle. This stored energy also represents an extra cooling load on the system. Stoecker, et al. (1983) reported that 24% to 27% of the total heat input during a single defrost cycle is used to heat up the evaporator coil sufficiently to melt the frost.



- | | |
|--|----------------------------|
| 1 Liquid line solenoid valve (closed) | 4 Drain pan heater |
| 2 Hot gas line solenoid valve (open) | 5 Pan check valve (PCV) |
| 3 Compressor suction stop valve (closed) | 6 Defrost relief regulator |

Figure 1.9 Schematic of flow in the Hot Gas Defrost (HGD) mode

Frost does not build up uniformly across the evaporator surface which leads to large non-uniformities in the frost thickness at the onset of the HGD process. As a result, frost will be cleared from some parts of the evaporator faster than others and the defrost heat that is added to the clear surface will be convected to the freezer space as the HGD process is continued for a sufficient time so that all of the frost is removed from the more built-up regions. The convected heat as well as the sublimated frost (i.e., the frost that is directly transformed into vapor) and the frost that is melted and subsequently evaporates all represent an additional heat load that must be subsequently removed from the freezer

space. According to Cole (1989), more than 80% of the energy required to defrost an evaporator coil in a freezer is ultimately transferred back into the refrigeration system as added load. Neiderer (1976) reported that only 15% to 25% of the total heat input during a defrost cycle is removed from the refrigerated space with the melt and the remaining energy (75% to 85%) is returned to the refrigeration system as a parasitic load. Coley (1983) states that during each defrost cycle, at least 15% of the ice sublimates into the room where it must be removed again.

The frosting and the defrosting processes both penalize the efficiency of the cooling system. The operator must therefore select the interval between defrosts and the duration of the defrost cycle such that their cumulative impact on the cooling system (i.e., the reduction of the time averaged integrated coefficient of performance or time averaged system efficiency) is minimized. Defrosting too frequently will lead to a large parasitic heat input to the freezer during the defrost processes whereas waiting too long between defrosts will lead to a large degradation of the time averaged capacity of the evaporator as compared to its rated capacity.

1.2 Research Objectives

The primary goal of this research is to investigate the effects of frost formation and defrost processes with the aim of optimizing the overall operation of a refrigeration system. The research project includes both theoretical and experimental investigations of the frost and defrost processes. The results of these investigations are used to provide practical guidance relative to the selection of defrost parameters and also aid in the design

of efficient refrigeration equipment. In order to reach the primary goal of this research, the following general objectives were pursued.

Development of a theoretical model of an evaporator coil during cooling mode

operation: In order to understand frost build up on the evaporator coil external surfaces during the cooling mode operation, the first goal of this research is to develop a computational model that predicts the frost formation rate and the heat extraction rate of the evaporator coil during the cooling mode operation. This model is needed in order to:

1. obtain the frost thermal properties and the frost thickness at the end of the cooling mode which are required inputs for the defrost computational model, and
2. quantify the reduction of the evaporator coil's heat transfer capacity that is related to the accumulation of frost on the coil surfaces (i.e., quantify the penalty of not defrosting).

Development of a theoretical model of an evaporator coil during defrost mode

operation: The second goal of this research is to develop a computational model that simulates the evaporator coil during the defrost mode. This model is needed in order to:

1. quantify the parasitic (sensible and latent) load during the defrost process based on the frost properties and the amount of frost on the coil (inputs obtained from the frost model),
2. estimate the time required to complete defrost cycle, and
3. conduct parametric studies that provide an understanding of the effects of changing the time required to conduct the defrost cycle.

Design and conduct field experiments on an evaporator coil during cooling and

defrost mode operations: The third objective of this research is to perform field experiments on a full-scale and installed industrial evaporator coil; this objective is needed due to the lack of experimental data that is available in the literature for large scale evaporators operating under both frosting or defrosting modes. These experimental data are required to validate both of the theoretical models mentioned above. Also, visualization of the frost melting process during the defrost cycle is required to help to develop an appropriate defrost model.

Integrate the models and apply them to optimize the entire refrigeration cycle

The final and most important objective of the research is to integrate the frost and defrost models in order to optimize the overall process and to provide guidelines that are based on solid, engineering models rather than rules-of-thumbs. These design guidelines will enable operators to choose the appropriate intervals between defrost cycles and the duration of the defrost cycle that minimize the impact on the cooling system coefficient of performance.

1.3 Outline of the thesis

In the following chapter a brief description of some of the terminology and the definitions that are used throughout this document to describe the various part of the heat exchanger is presented, followed by a literature review of mechanisms of frost formation,

frosting experiment data, theoretical models of frost buildup, and finally defrost experiment data and defrost theoretical models.

Chapter 3 describes the numerical model of frost model operation of a large-scale, ammonia-feed evaporator coil used in an industrial refrigeration system and operating under low temperature air and refrigerant conditions that has been developed for this research. This chapter starts by describing all of the assumptions used to construct the model, followed by a description of the heat and mass transfer equations that are used in the numerical model as well as the correlations required to calculate the pressure drop and the heat and mass transfer coefficients. Chapter 4 describes the experimental study that has been conducted in order to quantify the influence of frost formation on the performance of an industrial evaporator coil. The chapter starts by presenting the experiment facility and provides the details of the experiment including information about each of the instruments and the data acquisition system. Finally, the experiment uncertainty analysis and the experiment results are presented and discussed. Chapter 5 presents a comparison between the frost experiment data and the frost numerical model predictions.

Chapter 6 describes the numerical model that has been developed to simulate the Hot Gas Defrost Process (HGDP) of an industrial evaporator coil. This chapter starts by describing all of the assumptions used to construct the model, followed by a description of the heat and mass transfer equations that are used in the numerical model and a sensitivity analysis for some of the model parameters that are particularly difficult to estimate and have been adjusted to fit the experimental results. Chapter 7 describes the HGDP experiment. This chapter starts by presenting the experiment facility and provides

the details of the experiment, followed by the experiment results and discussion. In Chapter 8, a comparison between the HGDP numerical model predictions and the experiment data is presented.

In Chapter 9, the entire refrigeration cycle (cooling mode and defrost mode) on an industrial evaporator coil is optimized in by considering all the penalties associated with frost accumulation and frost removal. In this chapter, the overall system efficiency and the cost of frost are calculated for different cooling operation intervals between defrost cycles as well as different dwell periods during the defrost cycles. The frost theoretical model described in Chapter 3 is used a gain in Chapter 10 to evaluate the impact of using parallel-flow as opposed to counter-flow circuiting tubes arrangement of an industrial evaporator coil operating under frost condition. The two different designs are evaluated in terms of the frost distribution across the evaporator coil, the associated temporal reduction in cooling capacity during operation and the overall system efficiency. Finally, Chapter 11 presents the conclusions from this research and recommendations for future work.

1.4 References

Cole, R.A., 1989, *“Refrigeration loads in a freezer due to hot gas defrost and their associated cost.”* ASHRAE Transactions, Vol. 95, Part 2

Coley, M.B., 1983, *“The cost of frost.”* ASHRAE Journal, Vol. 82, No. 9.

Niederer, D.H., 1976, *“Frosting and defrosting effects on coil heat transfer.”* ASHRAE Transactions, Vol. 82, Part 1

Stoecker, W.F., 1957, *“How frost formation on coils effects refrigeration systems.”* Refrigerating Engineering, vol. 65, No. 2.

Stoecker, W.F., 1960, *“Frost Formation on Refrigeration Coils.”* ASHRAE Transactions, Vol. 66.

Stoecker, W.F.; J.J. Lux; and R.J. Kooy. 1983. *“Energy Considerations in Hot-Gas Defrosting of Industrial Refrigeration Coils.”* Final report. ASHRAE RP-193.

Chapter 2 Literature Review

There is a variety of terminology and nomenclature that has been used in the literature to describe the various part of the heat exchanger. Therefore, this chapter will begin with a presentation of the specific terminology and definitions that are used throughout this document in order to describe the various parts of the heat exchanger. This is followed by a literature review that focuses on the mechanism of frost formation, frost experiment data, models of frost formation, and finally defrost experiment data and models.

2.1 Definitions and terminology

- Bare tube outside surface area: A_b is the outside tube surface area that is in contact with the air and is equal to the total tube surface area less the tube surface area that is covered by the fins:

$$A_b = \pi D_o (T_l - N_{fin} F_{thk}) \quad (2.1)$$

where D_o is the outer diameter of the tube, T_l is the tube length, N_{fin} is the total number of rectangular plate fins of the evaporator coil and F_{thk} is the fin thickness.

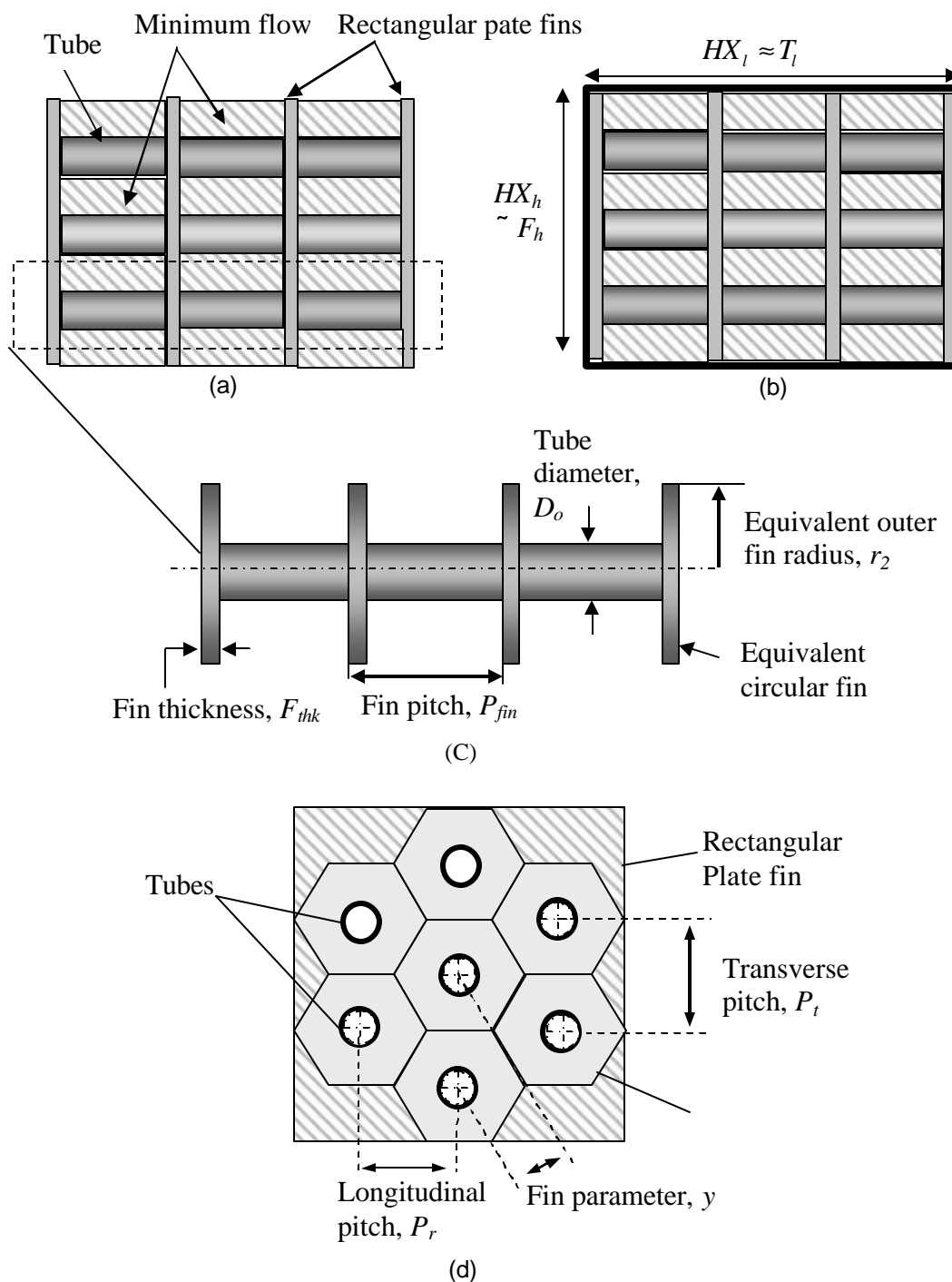


Figure 2.1 Schematic of a heat exchanger showing (a) the minimum flow area shaded with downward diagonal lines, (b) coil face area, (c) Fin pitch and fin thickness, (d) The equivalent area appropriate for a plate fin in a staggered tube arrangement, as suggested by Schmidt (1949).

- Fin surface area: A_{fin} is the total surface area of the equivalent circular fins per tube (assuming that the evaporator coil rectangular plate fins are divided into a smaller circular fins served by each tube) :

$$A_{fin} = 2p N_{fin} (r_2^2 - r_1^2) \quad (2.2)$$

where r_1 is the equivalent fin inner radius and equal to half of the tube outer diameter, D_o , and r_2 is the outer fin equivalent radius. The outer fin equivalent radius is defined in Eq.(2.3) Schmidt (1949).

$$r_2 = 0.635 P_t \sqrt{\frac{2y}{P_t} - 0.3} \quad (2.3)$$

$$2y = \sqrt{P_r^2 + \frac{P_t^2}{4}} \quad (2.4)$$

where y is the fin parameter, and P_r and P_t are the longitudinal and transverse tube pitches, respectively, which are illustrated in Figure 2.1.

- Total heat transfer area: A_{tot} is the total surface area of the metal that is in contact with the air per tube and is equal to the sum of the bare tube outside surface area A_b and fin surface area A_{fin} :

$$A_{tot} = A_b + A_{fin} \quad (2.5)$$

- Effective heat transfer area: A_e is the sum of the bare tube surface area and the fin surface area reduced by the fin efficiency (i.e., the effective fin surface area):

$$A_e = A_b + \mathbf{h}_f A_{fin} \quad (2.6)$$

where \mathbf{h}_f is the equivalent circular fins efficiency described by Eq. ((2.7), Incropera and DeWitt (1996))

$$\mathbf{h}_f = \frac{2r_1}{m(r_2^2 - r_1^2)} \left[\frac{K_1(mr_1)I_1(mr_2) - K_1(mr_2)I_1(mr_1)}{I_0(mr_1)K_1(mr_2) + K_0(mr_1)I_1(mr_2)} \right] \quad (2.7)$$

$$m = \sqrt{\frac{2h_{air}}{k_{fin}F_{thk}}} \quad (2.8)$$

where K_n and I_n are modified Bessel function of first and second kind, respectively, m is the fin constant, h_{air} is the air side heat transfer coefficient, and k_{fin} is the fin thermal conductivity.

- Fin effectiveness: \mathbf{h}_f is the effective heat transfer area divided by the total heat transfer area:

$$\mathbf{h}_f = \frac{A_e}{A_{tot}} \quad (2.9)$$

- Coil face surface area: $HX_{fc,area}$, illustrated by the bold box in Figure 2.1: is the surface area of the heat exchanger side that is perpendicular to the air flow, it can be approximated using the following equation:

$$HX_{fc,area} = HX_h HX_l \approx F_h T_l \quad (2.10)$$

where HX_h is the evaporator coil height which is approximately equal to the height of the plate fin, F_h , and HX_l is the evaporator coil length which is approximately equal to length of the tube at one section, T_l .

- Fin face area: F_{fcarea} is the projected area of the rectangular plate fin that is perpendicular to the air flow and is equal to the product of the fin thickness and the rectangular plate fin height:

$$F_{fcarea} = N_{fin} F_h F_{thk} \quad (2.11)$$

- Tube face area: T_{fcarea} is the projected area of the tubes that is perpendicular to the air flow and it is equal to the total number of the vertical tubes $N_{t,v}$ multiplied by the tube diameter and bare tube length:

$$T_{fcarea} = N_{t,v} \cdot D_o \cdot (T_l - N_{fin} F_{thk}) \quad (2.12)$$

- Minimum flow area: A_{min} is the air minimum free flow area, illustrated by the cross-hatched area in Figure 2.1; the minimum flow area is equal to the coil face area minus the fin face area and the tube face area:

$$A_{min} = HX_{fc,area} - [F_{fcarea} + T_{fcarea}] \quad (2.13)$$

2.2 Literature review

2.2.1 Mechanisms of frost formation

The process of frost formation on the surfaces of an evaporator coil is a result of two mechanisms. The first mechanism is the buildup of small ice particles that exist in the free air stream and accumulate by impaction or interception when they contact the evaporator coil surfaces (Malhammar 1988, Mango et al. 2005). The air stream in this case is supersaturated; i.e., a metastable state that is initiated when a moist warm air is suddenly cooled, causing the moisture in the air to transform into tiny ice crystals. These ice crystals normally appear as a dense “fog” and they have an affinity for cold surfaces. Because the frost associated with the accumulation of these ice particles has a low density, it can build up very rapidly. The blockage of air flow through the coil can be mitigated or managed by mechanical or pneumatic (air knife) removal. This type of frost formation process is observed in regions of very large moisture content, for example evaporator coils that are located near doors or in blast freezers that are freezing unpackaged products.

The second mechanism for frost growth is the diffusion of water vapor onto cold surfaces due to the difference in the water vapor concentration of the air stream and the surface of the frost layer (Sanders, 1974). The water mass that is transferred to the frost surface creates two distinct effects in the frost layer. A portion of the water vapor is deposited onto the frost layer; thereby, contributing to further frost growth while the remainder of the water vapor diffuses into the frost layer where it changes phase and densifies the frost. This type of frost layer forms relatively slowly with a very high

density. Because of its dense structure, it is typically not possible to mechanically or pneumatically control or remove this type of frost; therefore, it must be periodically removed using a defrost process. The high density frost formation process is observed in regions of relatively low air temperature with low moisture content, for example evaporator coils that are placed in a refrigerated warehouse used for the long-term storage of food products.

In this document, only the second mechanism for frost formation will be discussed and studied, this is most common for evaporators placed in regions of moderate water content.

2.2.2 Review of Existing Frost Experimental Data and Models:

The frost formation problem has received varying degrees of attention over the last 70 years. A large number of experimental and theoretical investigations have been reported relative to frost properties, the mechanisms of frost growth, and the heat transfer involved in frost growth. A summary of some of the frost growth investigations performed for surfaces with simple geometries is provided in (appendix A). For heat exchangers with more complex geometry, such as a finned-tube heat exchanger, the literature that is available is more limited in part due to the large number of variables that affect frost growth, the complex surface geometry of the heat exchanger coils, and the thermodynamic properties of the frost. Most of the studies available on frosting of a finned-tube heat exchanger geometry have been experimental and there have been few attempts to develop models that are capable of simulating the physics of the frosting process.

2.2.2.1 *Experimental Studies*

Stoecker (1957), Hosoda et al. (1967), and Gatchilov et al. (1979) have studied the frosting process for a finned-tube heat exchanger and report that the heat transfer rate increases during the initial stage of frosting and decreases with time thereafter as frost continues to build. The initial increase in the heat transfer was attributed to the increase in the air velocity and frost surface roughness, both of which lead to an increase of the air-side heat transfer coefficient, as well as an increase in the heat transfer area as nuclei of the frost crystals acts like small fins. However, the enhancement in the heat transfer rate occurs only for a very short period of time relative to the total operating time between defrosts. As the frost continues to build, the thermal resistance of the frost increases and the heat transfer drops steadily even when a fixed air velocity test condition is achieved in the laboratory; in practice, the increasing flow resistance of the frosted coil will result in a decreasing air flow rate which also contributes to a reduced heat transfer rate.

Rite et al. (1991) performed an experiment related to the behavior of a domestic refrigerator during frosting and quantified the effect of relative humidity, inlet air velocity, inlet air temperature, and inlet refrigerant temperature. The air flow rate was maintained at a constant value throughout each test. During these tests it was reported that the heat transfer rate increased continuously with the build up of frost during the 10 hour test periods. This increase is related to: 1) a decrease in the contact resistance between fins and the tube as the gap filled with frost, 2) an increase in the air-side convective heat transfer coefficient due to a greater surface roughness, and 3) an increase in the surface area of the tube and fins as the frost built up. A parametric study on the

effect of changing the relative humidity and inlet air temperature showed that: 1) an increasing air relative humidity results in a thicker frost layer and thus a higher pressure drop, 2) an increasing inlet air temperature (while maintaining a constant relative humidity) results in an increase of the frost thickness. Unfortunately, the experiment was carried out using a constant air velocity test condition across the coil as the frost builds up which is not representative of the conditions that are present in actual refrigeration applications.

Lee et al (1996) experimentally studied the effect of fin spacing, fin arrangement, tube arrangement, air temperature, air humidity, and air velocity on both the frost growth and thermal performance of a finned-tube heat exchanger operating under frosting condition. The time associated with each test was four hours and it was found that the heat transfer rate decreased during the initial stage of the frost built up (for approximately 1 hour) and then increased to a maximum before finally decreasing again for the remainder of the test. The time required to reach the point of maximum heat transfer was found to depend, primarily, on the fin spacing; larger fin spacing was associated with a longer operating time required to obtain the maximum heat transfer. It was also found that the change in the heat transfer rate was larger for the small fin spacing runs; increasing the fin spacing from 5.0 to 10.0 mm increases the operating time to full blockage by 100% but also decreases the average cooling capacity by 50% due to the reduction of the heat transfer area. A staggered, finned-tube heat exchanger provided 17% higher heat transfer rate than an in-line finned-tube heat exchanger. Increasing the relative humidity of the inlet air leads to a thicker frost layer with a reduced frost density and a larger thermal resistance. Increasing the air velocity leads to a reduction in thermal resistance, an

increase in the frost thickness (frost growth rate), and an increase in the frost density. Increasing the inlet air temperature results in a reduction of the frost thickness, an increase in the frost density, and a decrease of thermal resistance. It should be noted that when the effect of inlet air temperature was examined, the relative humidity was not held constant; rather, the relative humidity of the higher inlet air temperature tests was less than the relative humidity of the lower inlet air temperature. As a result, the results of this parametric study were likely confounded.

Yan et al. (2003) investigated the effect of frost formation by conducting experiments on flat finned-tube heat exchangers with a single tube and multiple tube rows using various fin pitches. The experiment was performed in a humidity-controlled room and the effect of relative humidity, inlet air velocity, inlet air temperature, and inlet refrigerant temperature were examined. The flow rate of air was maintained constant throughout each test by adjusting the speed of the centrifugal fan that energized the wind tunnel and the test period was two hours. The tests showed that, in almost every case, the heat transfer rate remained constant during the initial stage of the frost built up (for about 30 min) and then decreased continually until the end of the test period. It was also shown that the frost formation is greater for a lower air flow rate (which is opposite to what Lee et al. (1996) and Rite et al. (1991) reported). It was reported that the pressure drop increases rapidly as the relative humidity is increased. Another interesting observation was that, for a constant relative humidity of 70%, an increase of the inlet air temperature from 2.5°C to 5.0°C leads to an increase in the frost thickness and thus an increase in the pressure drop; however, a further increase of the inlet air temperature from 5.0°C to 7.5°C

leads to a slight reduction in the frost layer thickness. The effect of frost on the performance of the heat exchanger decreases significantly as the fin pitch increases.

The experimental studies described above reported significantly different trends relative to the impact of fin spacing, fin arrangement, tube arrangement, air temperature, air humidity, and air velocity on the frost growth and the thermal performance of a finned-tube heat exchanger. These different results are likely due to the strong dependence of the frost thermal properties to the precise experimental conditions.

The specific experimental discrepancy related to the effect of the air velocity was investigated subsequently by O'Neal (1985) both experimentally and numerically. O'Neal compared the experimental results obtained from different researchers and conducted additional experiments on frost formation for parallel plates and reported that there is a critical Reynolds number (or velocity), above which the frost growth shows little dependence on Reynolds number. Below this critical value, the frost growth is dependent on the Reynolds number. The critical Reynolds Re_p , suggested by O'Neal is approximately 15,900.

$$Re_p = \frac{U_{air} (2H) \rho_{air}}{\mu_{air}} \quad (2.14)$$

where H is available height between the two parallel plates, shown in Figure 6.

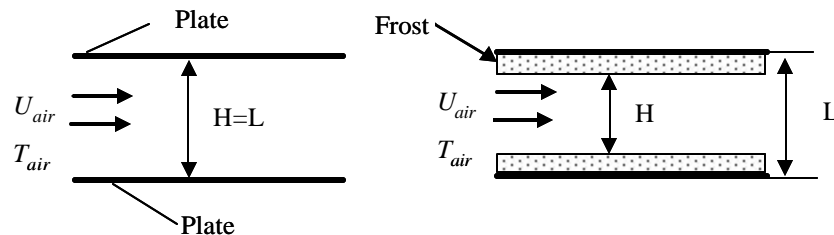


Figure 2.2 Parallel plates geometry used in the Reynolds number defined in Eq. (2.14)

Despite some inconsistencies in the results, almost all of the experimental studies reached the same conclusion regarding the effect of inlet air relative humidity and fin spacing on the performance of a finned tube heat exchanger under frosting condition. These results can be summarized as follows:

- 1- High inlet air relative humidity leads to faster frost formation and thus a greater pressure drop across the coil.
- 2- The effect of frost build up on the performance of the heat exchanger decreases significantly as the fin pitch increases.

2.2.2.2 *Numerical Studies*

The number of models that have been developed to simulate the impact of frost formation on the performance of finned-tube heat exchangers is relatively limited compared to the number of experimental studies. However, despite the complexity of the problem, there have been some encouraging results reported for relatively simple models.

Most researchers who develop computational models for evaporators operating under frost conditions use the same principles that are used for computational models of evaporators operating under wet conditions (i.e., the temperature of the coil surface is less than the air dew point temperature); in both cases, there is a combined mass and heat transfer (i.e., both a sensible and latent heat transfer). The same correlations for refrigerant side heat transfer coefficient and pressure drop are used; since there are no correlations available in the literature to calculate the air side heat transfer coefficient and pressure drop for an evaporator operating under frost condition, previous researchers

have used correlations that were developed for evaporators working under wet or, occasionally, dry conditions with some modification to account for the area reduction due to frost build up. However since the frosting process is transient and since the frost thickness is expected to vary significantly in the air flow direction, all researchers have divided the heat exchanger into sub-sections and modeled each row of the heat exchanger as a separate heat exchanger. All researchers have developed their models assuming that the process is quasi-steady; that is, the process was divided into time steps and within each time step, the process is assumed to be at steady-state. The frost properties (e.g., the frost layer thickness, thermal conductivity and density) at the end of each time step are used as inputs for the next time step. The refrigerant heat transfer coefficient, pressure drop, and the air properties at the exit of each sub-section are provided as inputs to the following sub-section for the same time interval. However, it is not clear how previous researchers have dealt with the air side heat transfer coefficient and pressure drop since the available correlations are for average heat transfer coefficient and pressure drop across the entire evaporator coil and not for individual rows. All have researchers used the Lewis correlation, Eq.(2.15), to predict the mass transfer coefficient h_m based on the calculated air heat transfer coefficient h_{air} .

$$h_m = \frac{h_{air}}{Le c_{p_{dry,a}}} \quad (2.15)$$

where Le is the Lewis number and $c_{p_{dry,a}}$ is the specific heat for dry air. According to Threlkeld (1970), the Lewis number for water vapor in air lies in the range of 0.90 to 0.92; however, other investigators have used slightly different values of the Lewis number in their calculations. For example, Domanski (1982), McQuiston (1975), and

Malhammar (1986) use a Lewis number of 1.0 while Oskarsson (1990) suggests a Lewis number of 0.95 and Al-mutawa et al. (1997) use a Lewis number of 0.845.

The most significant difference between the previously described computational models of frost formation lies in the correlations that are used to calculate the rate of frost formation. It has been shown that while a large portion of the extracted moisture adds to the frost thickness, there is a fraction of the moisture that will diffuse into the existing frost layer and increase its density. Therefore, this section will not focus on comparing the different correlations used to calculate the air and the refrigerant sides heat transfer coefficients and the pressure drop; rather, this section will concentrate on reviewing the available models used to calculate the frost formation rate and investigate how these various models compare to experimental data as well as the applicability of the available frost formation rate models to the type of the evaporator coil and the working conditions that are considered in the current research.

One of the most widely used models for calculating the portion of the water vapor mass that is transferred from the bulk air stream and diffuses into the frost layer (\dot{m}_p) and increases the frost density was suggested by O'Neal (1983):

$$\dot{m}_r = A_{tot} \cdot D_s \left[\frac{1 - (\mathbf{r}_{frost} / \mathbf{r}_{ice})}{1 + (\mathbf{r}_{frost} / \mathbf{r}_{ice})^{0.5}} \right] \frac{d\mathbf{r}_v}{dy} \quad (2.16)$$

where D_s is water vapor diffusion coefficient, \mathbf{r}_{frost} is the frost density, and \mathbf{r}_{ice} is pure ice density. The final variable in Eq. (2.16) is the gradient of the water vapor density through the frost layer. An approximate method to calculate the water vapor density gradient is provided in the next chapter. Based on the previous description of the

mechanism of frost formation, the following equations that represent a mass balance can be written:

$$\dot{m}_{frost} = \dot{m}_p + \dot{m}_d \quad (2.17)$$

$$\dot{m}_d = A_{tot} \cdot \mathbf{r}_{frost} \left(\frac{d\mathbf{d}_{frost}}{dt} \right) \quad (2.18)$$

$$\dot{m}_r = A_{tot} \cdot \mathbf{d}_{frost} \left(\frac{d\mathbf{r}_{frost}}{dt} \right) \quad (2.19)$$

where \dot{m}_{frost} is the rate of the total mass water vapor transferred to the cold surface at time t , \dot{m}_d is the portion of the water vapor that increases the frost layer thickness, \dot{m}_r is the portion of the water vapor mass which is transferred from the bulk air stream and diffuses in to the frost layer, \mathbf{d}_{frost} is the frost layer thickness, and t denotes time. By calculating the total water vapor transfer and integrating Eqs. (2.17) to (2.19), the frost layer thickness and density at any instant time can be obtained. A system of mass and energy balances is required to obtain \dot{m}_{frost} .

The second model that can be used to predict the frost growth was proposed by Malhammar (1986). Malhammar noted that the accuracy of any model that used to predict the frost growth depends on the accuracy of the frost density prediction. The parameters that Malhammar suggest most strongly affect the frost density include: time, coil temperature, air velocity, and air humidity. Therefore, Malhammar developed a system of equations to calculate frost density:

$$\mathbf{r}_{frost} = \left[\left(\frac{N_{frost}}{R_v} \right) \left(\frac{\dot{q}_{tot}}{\dot{q}_{lat}} \right) \left(\frac{dp_v}{dT_c} \right) \right] \quad (2.20)$$

where \dot{q}_{tot} and \dot{q}_{lat} are the total heat transfer rate and the latent heat transfer rate averaged over the time interval dt , respectively. R_v is the ideal gas constant for water vapor and N_{frost} is defined as the frost number and is calculated using the following equation:

$$N_{frost} = V_m \left(1.05 + \sqrt{0.693 + K_1 N_{time}} \right) \quad (2.21)$$

where N_{time} is defined as the time number and calculated using the following equation:

$$N_{time} = t \left[\left(\frac{\dot{q}_{lat}}{\dot{q}_{tot}} \right) \left(\frac{R_v T_c}{D_s} \right) \right] \quad (2.22)$$

where T_c is the absolute coil temperature (an average of the tubing and the fin temperatures), R_v is the ideal gas constant and D_s is the water vapor diffusion coefficient. The last variable in Eq.(2.20) is the rate of change of saturated water vapor pressure with temperature and is given by Eq.(2.23), which represents the saturation curve for water:

$$\frac{dp_v}{dT_c} = \left(4.325 \times 10^{10} \right) \exp\left(\frac{-5619}{T_c} \right) \quad (2.23)$$

The heat resistance number, V_m , and the empirical quantity, K_1 , in Eq.(2.21), are obtained from the following equations:

$$\text{for } 0 \leq Re_o \leq 2600 \quad V_m = 204, \quad K_1 = 2.58 \times 10^{-14} + (1.91 \times 10^{-16}) Re_o \quad (2.24)$$

$$\text{for } 2600 \leq Re_o \leq 5200 \quad V_m = 113 + (3.5 \times 10^{-5}) Re_o, \quad K_1 = 5.23 \times 10^{-13} \quad (2.25)$$

$$\text{for } 5200 \leq Re_o \leq 22000 \quad V_m = 295, \quad K_1 = (3.06 \times 10^{-20}) N_{ice}^{1.93} \quad (2.26)$$

where Re_o is the Reynolds number, defined as:

$$Re_o = 2 \left(\frac{G_{max} P_{fin}}{\mathbf{m}_{air}} \right) \quad (2.27)$$

where G_{\max} is the mass flux of the air based on the minimum flow area and P_{fin} is the fin pitch. N_{ice} , shown in Eq.(2.26), is defined as the ice frost number and is calculated according to:

$$N_{ice} = N_{frost} \frac{\mathbf{r}_{ice}}{\mathbf{r}_{frost}} \quad (2.28)$$

According to Malhammer, the proposed model agrees with his test points to within $\pm 20\%$. By solving Eqs. (2.20) to (2.28), the frost density at any particular time can be obtained and the increase of the frost thickness over a specific time interval can be then calculated according to:

$$\mathbf{d}_{frost} = \frac{\dot{m}_{frost} \Delta t}{A_{tot} \mathbf{r}_{frost}} \quad (2.29)$$

where \dot{m}_{frost} is the total mass flow rate of the transferred water vapor to the cold surface at some interval time Δt .

Oskarsson et al. (1990), Kondepudi et al. (1993), Seker et al. (2004a) and Yao et al. (2004) have all developed numerical frosting models. The key assumptions used to develop these models are, essentially, the same and are summarized in (Appendix B, Table B.1). The geometric details of the heat exchanger coil used in the numerical models as well as the ambient and operating conditions are summarized in (appendix B, Tables B2 to B4). The models developed by Kondepudi et al. (1991), Seker et al. (2004a) and Yao et al. (2004) all use the correlation developed by O'Neal (1983), Eq.(2.16), in order to calculate the mass of water vapor diffused through the porous frost layer. Also, the three models use the same correlation, suggested by Sanders (1974), in order to calculate the frost thermal conductivity (k_f), Eq.(2.30):

$$k_f = (1.202 \times 10^{-3}) r_{frost}^{0.963} \quad (2.30)$$

where k_f is the frost thermal conductivity in [W/m-K] and r_{frost} is the frost density in [kg/m³]. Equation (2.30) is a curve fit to measured density and thermal conductivity data for frost forming on a flat plate, the range of operating conditions include: wall temperature, T_w , from -8 to 12 F (-22 to 11°C), air temperature, T_{air} , from 14 to 32 F (-10 to 0°C) and air velocity, U_{air} , from 13 to 30 fps (4 to 9 m/s).

The predictions from the three models show that an increase in the relative humidity or the entering air temperature causes an increase in the frost accumulation rate and, as a consequence, a decrease in the air mass flow rate with an increase in the air-side pressure drop. However, the model developed by Yao et al. (2004) showed that an increase in the inlet air velocity leads to a decrease in the frost formation rate which contradicts the results of Kondepudi et al. (1991) and Seker et al. (2004). A detailed row by row prediction of frost accumulation rate provided by Yao et al. (2004a) showed that the frost accumulation rate is much higher for the first rows than the last rows.

The predictions of the model developed by Kondepudi et al. (1993) were found to be within 15-20% of the measured data for the companion experiment. The numerical model predictions provided by Seker et al. (2004a) showed significant under-prediction of the pressure drop and over-prediction of the conductance, relative to the experimental measurements performed by Seker et al. (2004b). The predicted mass of frost accumulated from the model provided by Yao et al. (2004) are found to agree with the experimental results with a maximum error of 8.6% after one hour.

Oskarsson et al. (1990) developed evaporator models for operation with dry, wet, and frosted finned surfaces. In their frost model, the Malhammar (1986) model, Eq.(2.20),

was used to predict the frost formation rate along with Eq.(2.31), attributed to Malhammar (1986), in order to calculate the frost thermal conductivity.

$$k_f = \frac{0.202 \mathbf{r}_{frost} (1 - \mathbf{r}_{frost} / 1860)}{V_m - 0.189 \mathbf{r}_{frost}} \quad (2.31)$$

where k_f is the frost thermal conductivity in [W/m-K], \mathbf{r}_{frost} if the frost density in [kg/m³], V_m is the heat resistance number defined in Eqs. (2.24) through (2.26) and Re_o is the Reynolds number defined in Eq.(2.27).

Table 2-1 summarizes the comparison between the predictions of the numerical model and the experimental results. Notice that the model under-predicts the frost formation rate and over-predicts the heat transfer rate. The maximum error between the model and the experimental results is approximately 30%. Note that Oskarsson et al. (1990) did not incorporate the change in the minimum free flow area that occurs due to frost formation when calculating the air-side heat transfer coefficient. Also, the dry fin efficiency equations were used without accounting for the insulating effect related to the frost. However, the frost thickness was accounted for in the calculation of the air pressure drop and a fan curve was used to predict the air mass flow rate as a function of time.

Table 2-1 Error comparison between the frost model predictions and the experimental results from Oskarsson et al. (1990)

% error between model and experiment							
Time (hr)	1	3	5	7	9	11	13
\dot{q}	+3	+1.4	+2.1	+14.8	+24.6	+30.4	+30.9
\dot{m}_{air}	+7.2	-8.8	+4.9	+9.2	+13.4	+9.1	-4.4
m_{frost}	-25.2	-18.4	-34.3	-29.4	-20.6	-16.5	-12.4
\dot{m}_{refr}	+3.0	+2.4	+1.8	+14.9	+24.6	+30.9	+31.0
	\dot{q} :heat transfer rate			m_{frost} : mass of frost accumulation			
	\dot{m}_{refr} : refrigerant mass flow rate				\dot{m}_{air} : air mass flow rate		

In a recent study, Na et al. (2004) develop a theoretically based numerical model of frost deposition and growth. Unlike the other models described here, which assumed that the water vapor is saturated at the interface between the air stream and the frost layer, Na et al. assume that a supersaturated condition exists at the frost surface. The degree of super saturation is predicted using Eq.(2.32):

$$\begin{aligned}
 S_{ss} &= 0.808 \left(p_{v,\infty} / p_{vs,\infty} \right) \left(p_{vs,frost} / p_{vs,\infty} \right)^{-0.657} - 1 \\
 T_{frost} + 14^\circ C &< T_{air} < T_{frost} + 20^\circ C \\
 -40^\circ C &< T_{frost} < 0^\circ C
 \end{aligned} \tag{2.32}$$

where S_{ss} is the degree of super saturation, which is dimensionless and defined as:

$$S_{ss} \equiv \left[(p_v - p_{vs}) / p_{vs} \right] \tag{2.33}$$

where $p_{vs,frost}$ is the frost surface saturated vapor pressure and $p_{v,\infty}$ and $p_{vs,\infty}$ are the inlet air vapor pressure and saturated vapor pressure, respectively. T_{frost} and T_{air} are the temperatures of the frost surface and the inlet air, respectively.

Na et al. (2004) claim that the saturated surface assumption over-predicts the mass transfer rate from the air stream to the frost surface which results in higher frost growth rate than is measured during experiments. The Na et al. model was validated against experimental results to within an absolute error of 15%. However, Eq. (2.32) is valid only over a very narrow region; the temperature difference between the inlet air and the frost surface must be at least 15°C, which is substantially larger than is typically encountered for most industrial evaporator coils.

The above review shows that either the model proposed by O'Neal (1983) or Malhammar (1986) for the calculation of the portion of the transferred water vapor mass from the bulk air stream that diffuses into the frost layer (\dot{m}_r) will yield an acceptable prediction when they are incorporated in a numerical model and used to study the influence of frost formation on the performance of evaporator working under frost conditions. Therefore, both models will be used in the development of the frost model for the current research; a recommendation regarding which model is more accurate can be provided based on the experimental measurements and will be provided later in the research

2.2.3 Review of Existing Defrost Experimental Data and Models:

A hot gas defrost process is complex and involves spatial and time variation of the refrigerant, metal, and air temperatures. The total heat input during a hot gas process is hard to quantify or measure because the hot gas that leaves the evaporator coil is in a two phase state with a quality that depends significantly on the amount of frost and condensed water that is adhered to the coil at any instant time. Also, an energy balance on the air side is complex because the energy that is extracted from the hot gas is utilized in many different forms (e.g., heating the evaporator coil metal surfaces, melting the frost, re-evaporating condensed water, and direct transfer to the environment by natural convection). Due to these complexities, there have been very few experiments or numerical models that have been developed to study defrost process. One key problem with modeling the hot gas defrost process is that it is at least somewhat stochastic; during the hot gas defrost, the frost on the evaporator coil will not melt uniformly through the

coil. The frost over some portion of the coil remains attached to the evaporator coil surfaces until it is completely melted and sublimated while the frost at other locations is partially melted and then detaches from the coil surface, falling to a lower coil or to the hot drain pan.

Perhaps because of this complexity, there have been few attempts to study the hot defrost process. Among the investigators who have examined the defrosting of freezer coils are Kerschbaumer (1971), Niederer (1976), Stocker et al. (1983), Coley (1983), Cole (1989), Krakow et al. (1992,1993) Al-mutawa et al. (1997) and more recently Hoffenbecker et al (2004). Niederer (1976) attempted to determine the amount of thermal energy required for defrost by measuring the amount of hot gas that condenses during the hot gas defrost cycle and the power input during an electric defrost cycle. It was found that only 15 to 25% of the total energy has been utilized by the process was actually used to melt the frost; the remaining 75 to 85% of the energy went to the surrounding environment and the coil/cabinet surfaces. Kerschbaumer (1971) defined the defrost efficiency (h_d) to be the ratio of the total energy required to melt the accumulated frost only to the total amount of defrost energy input.

Stoecker et al. (1983) conducted field and laboratory studies of hot gas defrost. Their study mainly focused on the possibility of using a reduced hot gas pressure (as compared to the hot gas pressure that is commonly used in the industrial refrigeration) in order to perform a satisfactory defrosts. The study showed that a lower defrost inlet pressure can provide a satisfactory defrost process provided that the hot gas pressure is at least 15 psi (100 kPa) above the setting of the outlet pressure regulator. Also, they suggested that the

thermal losses associated with the defrost process will be less with the lower inlet pressure; however, they failed to assess the impact of the increased time that is required to complete a defrost cycle; the use of a lower hot gas pressure translates to a longer duration process and therefore, the total energy lost to the ambient may be larger even if the rate of heat transfer is lower.

Coley (1983) suggested that during a defrost cycle for a freezer, at least 15% of the frost sublimates (i.e., is directly transformed into vapor) into the surrounding refrigerated air space; this represents an additional load on the system. Cole (1989) showed that Coley's (1983) assertions were valid with data presented by Stocker et al. (1983). He presented data obtained from a manufacturer which provides a breakdown of the various heat loads encountered during a typical defrost of an ammonia evaporator coil and included a graphical analysis of the estimated cost associated with coil defrost. Cole (1989) suggested that the largest part of the energy required to defrost an evaporator in a freezer goes back into the system as added load, typically more than 80%, resulting in a defrosting efficiency of less than 20%. Coley (1983) also suggested that approximately 24 to 28% (depending on material used for the evaporator coil) of the heat input is required to warm the evaporator coil sufficiently to melt the frost. Al-mutawa et al. (1997) studied the defrost loads associated with a laboratory evaporator coil and showed that their results agreed with the rule-of-thumb that the combined contribution of the fan and defrost heat loads exceed 15% of the net refrigeration load.

Krakow et al. (1992, 1993) developed a numerical model to simulate the hot gas defrost process by idealizing as four separate stages that depend on the outside surface condition: preheating, melting, vaporizing, and dry heating. The coil was divided into elements and each element of the coil was assumed to pass through three or four stages. The model predicts that the major portion of the energy goes towards melting frost and vaporizing water. The energy used to vaporize the remaining surface water (after all frost is being melted) is found to be approximately 64% of the energy used to melt the frost; this is because the enthalpy required to vaporize a unit mass of water is approximately seven times greater than the enthalpy required to melt a unit mass of frost. Furthermore, the energy convected to the ambient air was found to be a negligible proportion of the total energy associated with the hot gas defrost process which is in contradiction to the experimental results discussed above.

Al-mutawa et al. (1998) developed an analytical model for hot gas defrosting of a cylindrical coil cooler (i.e., an evaporator coil with no fins). In their model, a moving boundary technique is used and the defrost process was divided into two stages, pre-melting and melting stages. The pre-melting stages was defined as the time before the frost layer touching the wall of the cooler reaches the triple-point temperature of water; that is, the time required to detach the frost from the cylinder wall. A constant heat flux from the hot gas is assumed and a forced convection heat transfer based on an air velocity of 5.5 ft/s is used. A Lewis number of 0.845 is used to calculate the convective mass transfer coefficient and the air stream that passes throughout the computational domain is assumed to have a constant temperature that is equal to the freezer temperature and a

constant relative humidity of 50%. All of the heat transfer mechanisms (conduction, convection, sublimation and evaporation) are assumed to take place in the gap between the tube and the inner frost surface whereas the gap is assumed to increase with time as the frost gets melted.

The model shows that the energy that is used to melt the frost is approximately 8% of the total defrost heat input and the energy associated with evaporation and sublimation are 25.6 and 29%, respectively, of the total defrost energy input. The model also showed that the time required to complete a defrost cycle decreases with increasing defrost heat flux.

Hoffenbecker et al (2004) developed a numerical model to simulate hot gas defrost process on industrial evaporator coils. In the numerical model, the fin surrounding each tube is approximated as a disc. Also the model assumes that the frost is uniformly distributed throughout the evaporator coil so that only one unit cell (i.e., one face of the circular fin with the associated frost and tube length) must be considered. Adiabatic boundary conditions are applied at the two corresponding lines of symmetry. The fin base is assumed to be at a constant temperature and only the frost that is attached to the fin is considered in the computational domain; the tubes are assumed to be frostless which results in an air gap between the outer radius of the frostless tube and the inner radius of the frost volume. The computational domain was discretized in radius and axial position. The model assumes that all of the water that results from the melting of the frost nodes remains attached to the coil and does not drain into the evaporator pan; however, to avoid a computational discontinuity the thermal conductivity of the water nodes is set to equal

to the thermal conductivity and specific heat of the air whereas the density is left equal to the water density. This was done in order to provide a heat transfer path through these water nodes since the air that is in contact with the frost in the computational domain was modeled as a large heat sink with a constant temperature and relative humidity equal to the freezer temperature and relative humidity throughout the defrost cycle. The convection and the evaporation heat transfers are assumed to only occur at the face of annular frost nodes that are located at the side of the computational domain that is always in contact with the freezer air. Note that the model does not consider sublimation heat transfer. Nevertheless, the model predictions were validated against experiment data provided by (Stoecker et al. (1983)) and show good agreement.

Detailed predictions for a defrost case study showed that the energy consumed to melt the frost is about 55% of the total input defrost heat, whereas 22% of the total energy is used to warm the evaporator material and 24% of the total energy is directly released to the freezer either by convection or evaporation. Also, results from a parametric analysis accomplished with the model show that an optimal hot gas temperature exists and is a function of both the accumulated mass and density of frost on the evaporator. The model predicted the defrost efficiency decreases with decreasing hot gas temperature. This result contradicts those of Stoecker et al. (1983) who suggested that the thermal losses associated with the defrost process will be reduced when using a reduced hot gas temperature due to the lower temperature difference between the evaporator coil surface and the freezer temperature. However the model developed by Hoffenbecker et al (2004) showed that the defrost dwell time required to achieve a full melt of the accumulated frost will ultimately reduce the defrost efficiency.

2.3 Nomenclature

Symbol	Description	Dimensions
A_b	= Bare tube outside surface area	$[m^2]$
A_{min}	= Minimum free flow area	$[m^2]$
A_{tot}	= Total heat transfer area	$[m^2]$
A_e	= Effective heat transfer area	$[m^2]$
A_{fin}	= Fin surface area	$[m^2]$
cp_a	= Specific heat for air	$[J\ kg^{-1}\ K^{-1}]$
D_o	= Tube outside diameter	$[m]$
D_s	= Water vapor diffusion coefficient	$[m^2\ s^{-1}]$
F_h	= Fin height	$[m]$
F_{thk}	= Fin thickness	$[m]$
F_{fcarea}	= Fin face area	$[m^2]$
G_{max}	= Mass flux of the air based on the minimum flow area	$[Kg\ m^{-2}\ s^{-1}]$
H	= Distance between two frosted parallel plates	$[m]$
h_{air}	= Convective air side heat transfer coefficient	$[W\ m^{-2}\ K^{-1}]$
h_m	= Mass transfer coefficient	$[Kg\ m^{-2}\ s^{-1}]$
HX_{fcarea}	= Evaporator coil face surface area	$[m^2]$
HX_l	= Length of the evaporator coil	$[m]$
HX_h	= Height of the evaporator coil	$[m]$
k_{fin}	= Fin thermal conductivity	$[W\ m^{-1}\ K^{-1}]$
k_f	= Frost thermal conductivity	$[W\ m^{-1}\ K^{-1}]$
k_{tube}	= Tube thermal conductivity	$[W\ m^{-1}\ K^{-1}]$
L	= Distance between two parallel plates	$[m]$
Le	= Lewis number	-
\dot{m}_{frost}	= Rate of the water vapor transfers to the evaporator coil surfaces	$[Kg\ s^{-1}]$
\dot{m}_d	= Rate of the water vapor increases the frost layer thickness	$[Kg\ s^{-1}]$
\dot{m}_r	= Rate of the water vapor diffuses into the frost layer	$[Kg\ s^{-1}]$
N_t	= Total number of tubes	-
N_{fin}	= Total number of fins	-
$N_{t,v}$	= Number of tubes at each row	-
N_{frost}	= Frost number	-

N_{ice}	=	Ice frost number	-
N_{time}	=	Time number	-
$p_{v,\infty}$	=	Inlet air flow vapor pressure	[kPa]
$p_{vs,\infty}$	=	Inlet air flow saturated vapor pressure	[kPa]
$p_{vs,frost}$	=	Frost surface saturated vapor pressure	[kPa]
P_{fin}	=	Fin pitch	[m]
P_t	=	Transverse tube pitch	[m]
P_r	=	Longitudinal tube pitch	[m]
\dot{q}_{tot}	=	Total heat transfer rate	[kW]
\dot{q}_{lat}	=	Latent heat transfer rate	[kW]
\dot{q}_{sen}	=	Sensible heat transfer rate	[kW]
r_1	=	Tube outside radius	[m]
r_2	=	Fin equivalent radius	[m]
Re_o	=	Reynolds number based on (2 x fin pitch) and the air mass flux	-
Re_p	=	Reynolds number based on the distance between two frosted parallel plates	-
R_v	=	Ideal gas constant	[J kg ⁻¹ K ⁻¹]
S_{ss}	=	Degree of super saturation	-
T_c	=	Average temperature of the Evaporator coil surface	[K]
T_{air}	=	Air temperature	[K]
T_{refr}	=	Refrigerant temperature	[K]
T_{frost}	=	Frost surface temperature	[K]
T_l	=	Tube length at one row	[m]
T_{fcarea}	=	Tube face area	[m ²]
ΔT_{lm}	=	Log temperature difference	-
U_{air}	=	Air face velocity	[m s ⁻¹]
V_m	=	Heat resistance number	-
\mathbf{m}_{air}	=	Air viscosity	[kg m ⁻¹ s ⁻¹]
\mathbf{d}_{frost}	=	Frost thickness	[m]
\mathbf{r}_{frost}	=	Density of the frost	[Kg m ⁻³]
\mathbf{r}_{ice}	=	Density of pure ice	[Kg m ⁻³]
\mathbf{r}_{air}	=	Density of the air	[Kg m ⁻³]
\mathbf{h}_t	=	Fin effectiveness	-
\mathbf{h}_f	=	Fin efficiency	-

2.4 References

Al-Mutawa, N.K., 1997, Experimental investigations of frosting and defrosting of evaporator coils at freezer temperatures, PhD thesis, Department of Mechanical Engineering, University of Florida

Cole, R.A., 1989, *Refrigeration loads in a freezer due to hot gas defrost and their associated cost.* ASHRAE Transactions, Vol. 95, Part 2

Coles, W., and R. Ruggei., 1954, *Experimental investigation of sublimation of ice at subsonic and supersonic speeds and its relation to heat transfer.* National Advisory Committee for Aeronautics, TN 3104.

Coley, M.B., 1983, *The cost of frost.* ASHRAE Journal, Vol. 82, No. 9.

Domanski, P. 1982, Computer modeling and prediction of an air source heat pump with a capillary tube, Ph.D. dissertation, The Catholic University of America.

Gatchilov, T.S. and V.S. Ivanova., 1979, *Characteristics of the frost formed on the surface of the finned air coolers.* XV International Congress of Refrigeration, Venice, Paper # B2-71.

Hoffenbecker, N., 2004, Investigation of alternative defrost strategies. MS thesis, Department of Mechanical Engineering, University of Wisconsin- Madison.

Hosoda, T. and H. Uzuhashi., 1967, *Effects of frost on the heat transfer coefficient.* Hitachi Review, Vol. 16, No. 6.

Incropera, F. and D. DeWitt, 1990, Introduction to Heat Transfer, John Wiley & Sons, 2nd edition.

Kerschbaumer, H.G., 1971, *Analysis of the Influence of Frost Formation on Evaporators and of the Defrost Cycles on Performance and Power Consumption of Refrigeration Systems.* XIII International Congress of Refrigeration, Washington, D.C., Paper # 3.11

Kondepudi, S.N., 1988, The Effects of Frost Growth on Finned Tube Heat Exchangers Under Laminar Flow. Ph.D. Dissertation, Department of Mechanical Engineering, Texas A & M University, December.

Kondepudi, S.N. and D.L. O'Neal., 1987, *The Effects of Frost Growth on Extended Surface Heat Exchanger Performance: A Review*. ASHRAE Transactions, Vol. 93, Part 2

Kondepudi, S.N. and D.L. O'Neal., 1988, "*Performance of Triangular Spine Fins Under Frosting Conditions.*" Heat Recovery Systems & CHP, Vol. 8, No. 1.

Kondepudi, S.N. and D.L. O'Neal., 1989a, "*Effect of Frost Growth on the Performance of Louvered Finned Tube Heat Exchangers.*" International Journal of Refrigeration. Vol. 12, No. 3.

Kondepudi, S.N. and D.L. O'Neal., 1989b, "*The Effects of Frost Formation on the Thermal Performance of Finned Tube Heat Exchangers.*" AIAA Paper # 89-1741, AIAA 24th Thermophysics Conference, Buffalo, New York, June.

Kondepudi, S.N. and D.L. O'Neal., 1989c, "*The Performance of Finned Tube Heat Exchangers Under Frosting Conditions.*" Collected Papers in Heat Transfer 1989, ASME Winter Annual Meeting, San Francisco, California, HTD-Vol. 123, December.

Kondepudi, S.N. and D.L. O'Neal., 1990, "*The Effects of Different Fin Configurations on the Performance of Finned-Tube Heat Exchangers Under Frosting Conditions.*" ASHRAE Transactions, Vol. 96, Part 2.

Kondepudi, S.N. and D.L. O'Neal., 1991a, "*Frosting Performance of Tube Heat Exchangers with Wavy and Corrugated Fins.*" Experimental Thermal and Fluid Science, Vol. 4, No. 5.

Kondepudi, S.N. and D.L. O'Neal, 1991b, "*Modeling Tube-Fin Heat Exchangers Under Frosting Conditions.*" XVIII International Congress of Refrigeration, Montreal, Canada, Paper # 242, August.

Kondepudi, S. and D. O'Neal., 1993, "*Performance of Finned-Tube Heat Exchangers Under Frosting Conditions: I. Simulation Model, and II. Comparison of Experimental Data with Model.*" International Journal of Refrigeration, Vol. 16, No.3.

Krakow, K.I., and S. Lin., 1992, "*A model of hot gas defrosting of evaporators. Part 1 and 2.*" ASHRAE Transactions, Vol. 98, Part 1.

Krakow, K.I., and S. Lin., 1993, "*An idealized model of reversed cycle hot gas defrosting. Part 1 and 2. .*" ASHRAE Transactions, Vol. 99, Part 2.

Lee, T.H., K.S. Lee and W.S. Kim., 1996, "*The effects of frost formation in a flat plate finned tube heat exchanger.*" International Refrigeration Conference at Purdue.

Malhammar, A., 1988, "*Monitoring frost growth in evaporators is a complex process.*" The Australian institute of refrigeration, air conditioning and heating, Vol,2

Malhammar, A., 1986, "*Frostpaslag via flansade ytor.*" Doktorsav handling, Kungliga Tekniska Hogskolan, Stockholm, Sweden.

McQuiston, F.C., 1981, "*Finned tube heat exchangers: state of the art for the air side,*" ASHRAE Transactions, Vol, 87, Part 1.

McQuiston, F.C., 1978, "*Heat, mass and momentum transfer data for five plate-fin-tube heat transfer surfaces,*" ASHRAE Transactions, Vol, 84, Part 1.

McQuiston, F.C. 1975, "*Fin efficiency with combined heat and mass transfer,*" ASHRAE transaction., Vol. 81, Part 1

Mango, P. and Sherif, S., 2005, "Psychrometric Charts and Property Formulations of Supersaturated Air", *HVAC&R Research*, Vol. 11, No. 1.

Na, B. and Webb, R., 2004, "*New model for frost growth rate.*" International Journal of Heat and Mass Transfer, Vol. 47

Niederer, D.H., 1976, "*Frosting and defrosting effects on coil heat transfer.*" ASHRAE Transactions, Vol. 82, Part 1

O'Neal, D.L., 1983, The effects of frost formation on the performance of a parallel plate heat exchanger, PhD thesis, Department of Mechanical Engineering, Purdue University.

O'Neal, D.L., and D.R. Tree., 1985, "*A Review of frost formation in simple geometries.*" ASHRAE Transactions, Vol. 91.

Oskarsson, S.P., K.I. Krakow, and S. Lin., 1990, "*Evaporator models for operation with dry, wet, and frosted finned surfaces Part I and II*", ASHRAE transaction., Vol. 96.

Rite, R.W., and R.R. Crawford., 1991, "*The effect of frost accumulation on the performance of domestic refrigerator-freezer finned tube evaporator coil.*" ASHRAE Transactions, Vol. 97, Part 2.

Sanders, C.T., 1974, Frost formation: the influence of frost formation and defrosting on the performance of air coolers, PhD. Thesis, Technische Hogeschool, Delft, The Netherlands.

Schmidt, T.E., 1949, "*Heat transfer calculation for extended surfaces.*" Refrigerating Engineering, vol. 57.

Seker, D., H. Karatas, and N. Egrican., 2004a "*Frost formation on fin-and-tube heat exchangers. Part I- Modeling of frost formation on fin-and-tube heat exchanger.*" International Journal of Refrigeration, Vol. 24

Seker, D., H. Karatas, and N. Egrican., 2004b "*Frost formation on fin-and-tube heat exchangers. Part II- Experimental investigation of frost formation on fin-and-tube heat exchanger.*" International Journal of Refrigeration, Vol. 27

Stoecker, W.F., 1957, "*How frost formation on coils effects refrigeration systems.*" Refrigerating Engineering, vol. 65, No. 2.

Stoecker, W.F., 1960, "*Frost Formation on Refrigeration Coils.*" ASHRAE Transactions, Vol. 66.

Stoecker, W.F.; J.J. Lux; and R.J. Kooy. 1983. "*Energy Considerations in Hot-Gas Defrosting of Industrial Refrigeration Coils.*" Final report. ASHRAE RP-193.

Threlkeld, J.L., 1970, Thermal environmental engineering, 2nd ed. Englewood Cliffs, NJ: Prentice Hall Book Co.

Yan, W.M., H.Y. Li, Y.J. Wu, J.Y. Lin, and W.R. Chang, 2003, "*Performance of finned tube heat exchangers operating under frosting conditions.*" International Journal of Heat and Mass Transfer, Vol. 46 (6)

Yao, Y., Y. Jiang, S. Deng, and Z. Ma., 2004, "*A study on the performance of the airside heat exchanger under frosting in an air source heat pump water heater/chiller unit.*" International Journal of Heat and Mass Transfer, Vol. 47

Chapter 3 Frost Model

This chapter describes a theoretical model of a large-scale, ammonia-fed evaporator coil used in an industrial refrigeration system and operating under low temperature air and refrigerant conditions which are typically encountered in refrigerated storage spaces. The model is used to simulate the performance of a counter-flow circuited evaporator coil design under frosting conditions. Note that all of the correlation and equations used to develop the model are presented in this chapter; however alternative correlations are available and a comparison between the predictions obtained using some of the correlations (programmed in the model) and most of the other correlations that are available in the literature versus experimental data can be found in Appendix C.

3.1 Formulation of the frost model:

A liquid overfed evaporator coil consisting of multiple rows of finned tube with multiple refrigerant circuits (Figure 3.1) is considered. The air distribution and the inlet refrigeration properties for each circuit in any row are assumed to be the same; therefore the model is formulated for a single refrigerant circuit (Figure 3.2) that is assumed to be representative of the remaining (n) circuits in the coil.

The evaporator coil air-side heat transfer surfaces are rectangular plate fins that are modeled as equivalent circular fins each attached to a tube (Figure 2.1) according to Schmidt 1949.

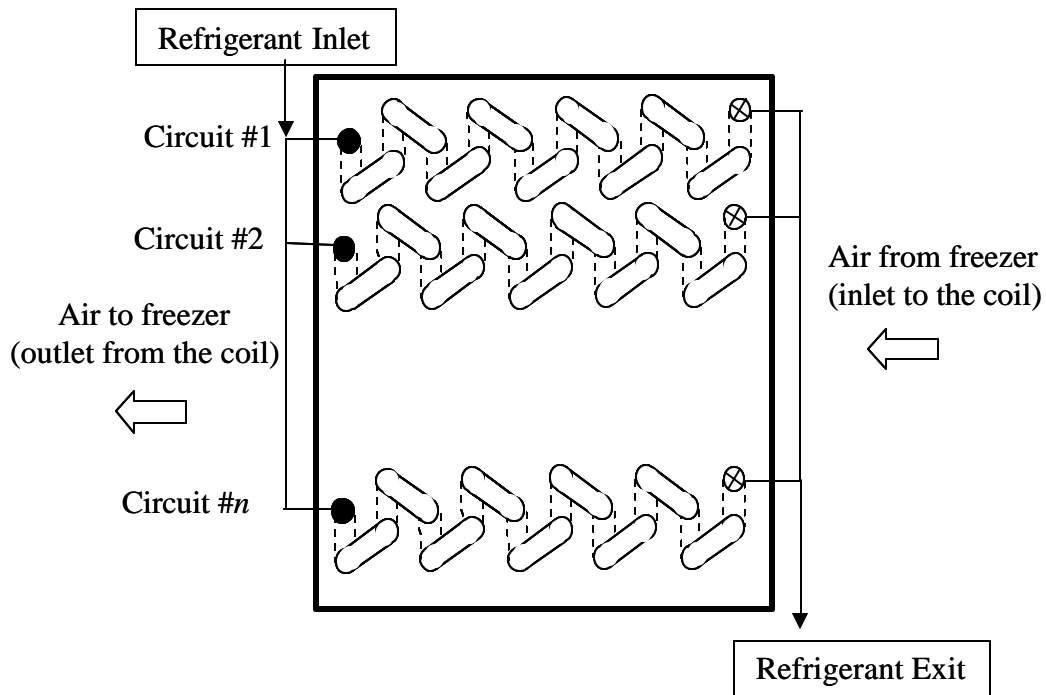


Figure 3.1 Schematic showing evaporator coil with multiple rows of finned tubes with multiple refrigerant circuits and the direction of the air and the refrigerant flow.

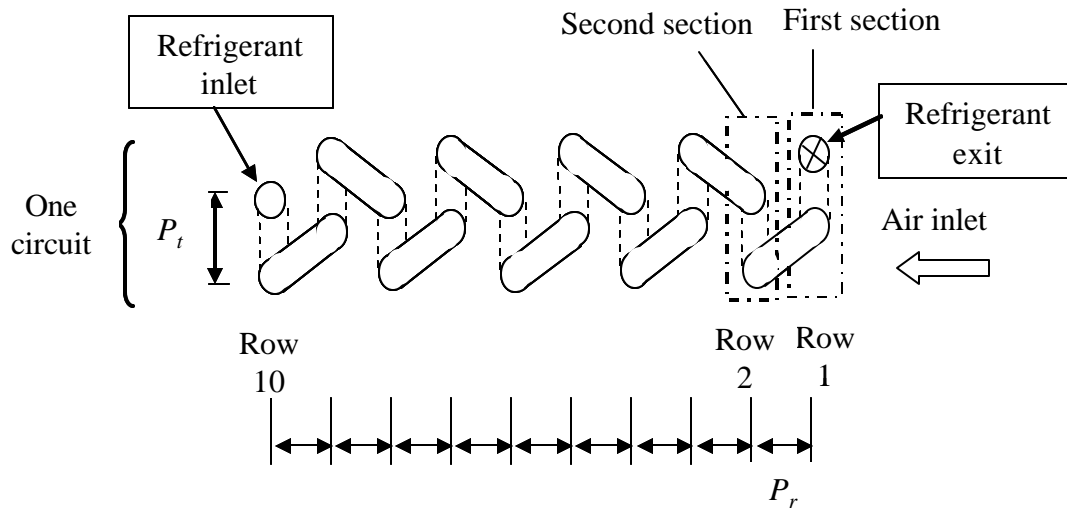


Figure 3.2 Schematic diagram showing one evaporator coil circuit and the direction of the air and the refrigerant flow.

An individual evaporator circuit is divided into a number of sections that is equal to the total number of the coil rows in the flow direction (10 for the geometry shown in Figure 3.2). The thermal properties of the freezer air are the inlet conditions associated with the first section. The outlet air and refrigerant properties for each section become the inlet properties for the next section (Figure 3.3).

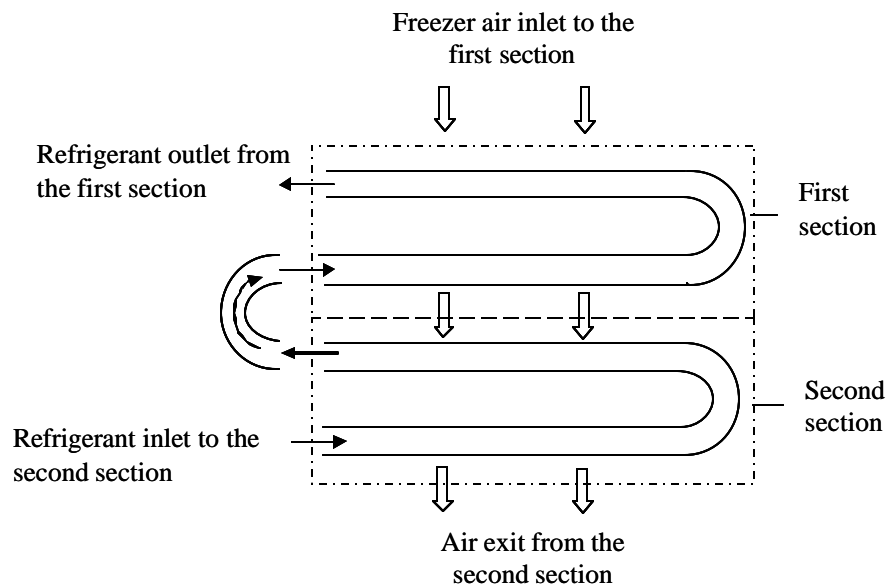


Figure 3.3 Schematic diagram showing the first and the second evaporator coil sections as well as the direction of the air and refrigerant flow.

Although the frosting process is a transient one, the model is quasi-steady; that is, the process is divided into time steps and within each time step, the process is assumed to be at steady-state. The frost properties (e.g., frost layer thickness, thermal conductivity and density) at the end of each time step are used as inputs for the next time step.

3.2 Heat transfer equations:

The frosting process model must include both mass transfer and heat transfer between the air and the coil surface. In addition, the model must account for the local gradients in air temperature, humidity, and enthalpy through the air boundary layer near the surface.

Figure 3.4 shows a control volume for a section of frosted tube. Sensible and latent heat transfer occurs through the pores in the frost layer to the tube wall at the beginning of the frost formation process; this energy is expected to be significant only during the initial stages of the frost formation. However, as the frost continues to form, all of the possible direct air paths to the tube through the frost layer will be filled as the frost density increases. Sensible heat is transferred from the air to the frost surface; this energy transfer is driven by the temperature difference between the air and the frost surface. Water vapor is also transferred from the air stream to the frost surface by virtue of a water vapor pressure difference between the air (high vapor pressure) and the frost surface (lower vapor pressure). Some fraction of the moisture transferred to the frost surface is deposited onto the frost surface, causing the frost layer to thicken. The remainder of the moisture diffuses into the frost layer increasing its density. The heat of sublimation caused by the phase change of the moisture is transferred through the frost layer by conduction together with the sensible heat transfer from the air.

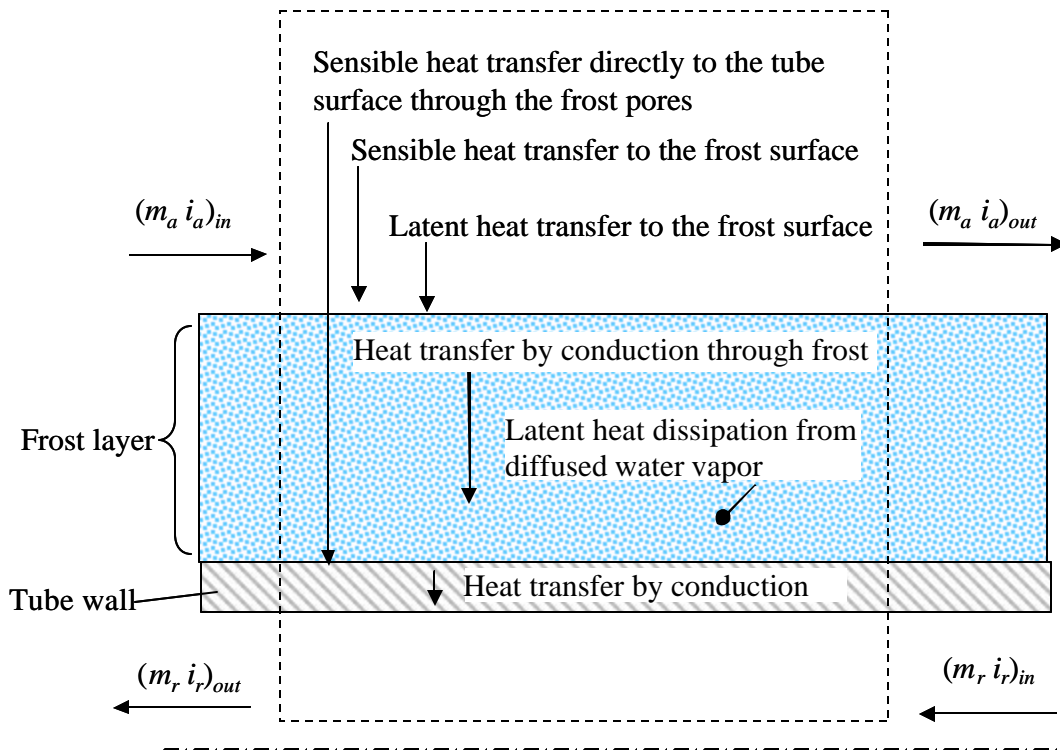


Figure 3.4 Schematic of the energy flows in frosted section of cooling coil

The overall energy balance that relates the enthalpy change of the moist air stream to the enthalpy rise of the two-phase refrigerant is:

$$\dot{q}_{tot} = \dot{m}_a (i_{ain} - i_{aout}) = \dot{m}_r (i_{rout} - i_{rin}) \quad (3.1)$$

where \dot{m}_a and \dot{m}_r are the air and refrigerant mass flow rates, respectively, and i_{ain} , i_{aout} and i_{rin} and i_{rout} are the inlet and outlet air and refrigerant enthalpies, respectively.

The air enthalpies are a function of the air temperature T_a , pressure p_a and relative humidity RH_a ; the refrigerant enthalpies are a function of the refrigerant temperature T_r , pressure p_r and quality x .

The total heat transfer (\dot{q}_{tot}) is the sum of the sensible heat transfer rate (\dot{q}_{sen}) and the latent heat transfer, (\dot{q}_{lat}). The sensible heat transfer rate can be expressed as:

$$\dot{q}_{sen} = h_a A_e (T_{a,ave} - T_{f,ave}) \quad (3.2)$$

where A_e is the effective heat transfer area, defined previously in Eq. (2.6). $T_{f,ave}$ and $T_{a,ave}$ are the average frost surface temperature and the average air dry bulb temperature within the section, respectively. The average air temperature is defined as:

$$T_{a,ave} = T_{r,ave} + \Delta T_{lm} \quad (3.3)$$

where $T_{r,ave}$ is the average refrigerant temperature and ΔT_{lm} is the log-mean temperature difference between the air and refrigerant.

Because the typical industrial refrigeration air-cooling evaporator is driven by a constant speed fan, the air mass (and volume) flow rate will decrease as frost accumulates due to the increase in the flow resistance of the coil. As a consequence, the air-side convective heat transfer coefficient (h_a in Eq.(3.2)) will also change. In the model, the mass flow rate of air through the coil is fixed by the intersection of the evaporator's fan curve and the resistance curve associated with the frosted coil. Specific correlations for the air-side pressure drop or convective heat transfer coefficient associated with a frosted coil were not found. Rather, the pressure drop equation described in Kays et al. (1964) is used with a friction factor correlation suggested by McQuiston (1981). The correlation suggested by McQuiston (1981) is used to calculate the air-side convective heat transfer coefficient. These correlations were developed for a bare coil; however, the effect of the frost built up is approximated, by using the air mass flux based on the minimum free flow

area and the local velocity considering the effect of the frost thickness as it is going to be shown in (sections 3.2.1).

The latent air-side convection heat transfer rate can be calculated using the convective mass transfer coefficient, (h_m) defined by Threlkeld (1970):

$$h_m = \frac{h_a}{Le \, cp_a} \quad (3.4)$$

where Le is the Lewis number and cp_a is the specific heat capacity of dry air. According to Threlkeld, the Lewis number for water vapor in air lies in the range of 0.90 to 0.92. Other investigators have used slightly different values of the Lewis number in their calculations; for example, Domanski [14], McQuiston [15], and Malhammar et al. [1] use a Lewis number of 1.0 while Oskarsson et al. [4] suggests a Lewis number of 0.95 and Al-mutawa et al. [16] use a Lewis number of 0.845. For the current study, Lewis number of 1.0 is used and a sensitivity analysis showing the effect of Lewis number on the model predictions is presented in chapter 5.

The latent heat transfer rate is calculated according to:

$$\dot{q}_{lat} = h_m \, i_{sg} \, A_e \left(\mathbf{w}_{airave} - \mathbf{w}_f \right) \quad (3.5)$$

where i_{sg} is heat of sublimation of water, \mathbf{w}_{airave} and \mathbf{w}_f are the average specific humidity ratio of the air and the saturation humidity ratio at the frost surface temperature, respectively. The average specific humidity of the air is calculated as suggested by Oskarsson et al. (1990):

$$\frac{\mathbf{w}_{aave} - \mathbf{w}_{ain}}{\mathbf{w}_{aout} - \mathbf{w}_{ain}} = \frac{T_{aave} - T_{ain}}{T_{aout} - T_{ain}} \quad (3.6)$$

where \mathbf{w}_{ain} and \mathbf{w}_{aout} are the specific humidities of the entering and the exiting air at each evaporator section.

Rearranging Eq. (3.5) so that it has the same form as Eq. (3.2) yields:

$$\dot{q}_{lat} = h_{lat} \cdot A_e (T_a - T_f) \quad (3.7)$$

where h_{lat} is the latent heat transfer coefficient which, from inspection of Eqs. (3.5) and (3.7), can be expressed as :

$$h_{lat} = h_m \cdot i_{sg} \cdot \left(\frac{\mathbf{w}_{aave} - \mathbf{w}_f}{T_{aave} - T_f} \right) \quad (3.8)$$

The total heat transfer rate within any section of the heat exchanger is then:

$$\dot{q}_{tot} = \dot{q}_{sen} + \dot{q}_{lat} = (h_a + h_{lat}) \cdot A_e \cdot (T_{aave} - T_f) \quad (3.9)$$

Note that all of the parameters used in Eq. (3.9) are associated locally with the particular subsection of the evaporator coil that is being considered, including the effective heat transfer area A_e .

The fin efficiency \mathbf{h}_f which is described in Eq.(2.7) Incropera and DeWitt (1996)), is defined as:

$$\mathbf{h}_f = \frac{T_a - T_{fin}}{T_a - T_b} \quad (3.10)$$

where T_{fin} and T_b are the average fin temperature and the tube temperature, respectively. The fin efficiency described in Eq. (2.7) is strictly valid only for dry conditions. A frosting coil involves also mass transfer and frost accumulation; therefore, Eq. (2.7) is modified in order to account for the presence of the frost on the fin efficiency.

There are two effects that must be considered. First, the total heat transfer coefficient, h_{airtot} , will tend to increase due to the latent air-side convective heat transfer coefficient, which is related to the latent energy transferred by the mass transfer process. The total heat transfer coefficient will therefore be the sum of the convective air side heat transfer coefficient h_a and the latent air side convective heat transfer coefficient, h_{lat} ; this effect will tend to decrease the fin efficiency. However, the accumulation of a frost layer will tend to insulate the fin conductively and this effect will tend to increase the fin efficiency. In order to account for these two effects, the fin parameter m defined in Eq. (2.7) is modified as follows:

$$m = \sqrt{\frac{2h_{eff}}{k_{fin}F_{thk}}} \quad (3.11)$$

$$h_{eff} = \left(\frac{1}{(h_a + h_{lat})} + \frac{d_f}{k_f} \right)^{-1} \quad (3.12)$$

where h_{eff} is the effective heat transfer coefficient that accounts simultaneously for both of the effects described above, k_{fin} is the fin thermal conductivity, F_{thk} is the fin thickness and d_f is the thickness of the frost layer and k_f is the frost thermal conductivity which is calculated using the correlation developed by (Lee et al. (1994), Eq. (3.13)). This

modification of the fin parameter m was also suggested and used by Kondepudi et al. (1993).

$$k_f = 0.132 + 3.13 \cdot 10^{-4} \cdot r_f + 1.6 \cdot 10^{-7} \cdot r_f^2 \quad (3.13)$$

where k_f is the frost thermal conductivity in [W/m-K] and r_f if the frost density in [kg/m³].

A thermal contact resistance between the coil tubes and the fins (R_c) is included in the total fin efficiency (h_{fc}) using Eq. (3.14):

$$\frac{1}{h_{fc} A_{fin} h_{eff}} = \frac{1}{h_f A_{fin} h_{eff}} + \frac{R_c}{A_{finc}} \quad (3.14)$$

where A_{finc} is the contact surface area between the coil tubes and fins.

Rearranging Eq.(3.14) yields:

$$h_{fc} = h_f \left[1 + h_f A_{fin} h_{eff} \left(\frac{R_c}{A_{finc}} \right) \right]^{-1} \quad (3.15)$$

The value of the thermal contact resistance used in the model is:

$$R_c = 0.0625 \times 10^{-4} \text{ (m}^2 \text{K/W)} \quad (3.16)$$

The rate of water vapor transferred from the air stream (\dot{m}_f) is equal to the rate of water vapor transferred to the heat exchanger tube and fin surfaces and is defined as:

$$\dot{m}_f = \dot{m}_a \cdot (\mathbf{w}_{ain} - \mathbf{w}_{aout}) \quad (3.17)$$

$$\dot{m}_f = h_m \cdot A_e \cdot (\mathbf{w}_{ave} - \mathbf{w}_f) = \frac{\dot{q}_{lat}}{i_{sg}} \quad (3.18)$$

The frost growth rate and the thickness of the frost layer are calculated using both methods that were available in the literature and presented in Chapter 2 (O'Neal (1983) and Malhammar (1986)).

However the correlation provided by O'Neal (1983) is found to be under-predicts the frost density as compared to the frost density predicted by the system of equations provided by Malhammar (1986) and therefore over-predicts the degradation of the evaporator cooling load overtime as compared to the experiment data shown in chapter 5.

The increase in the frost layer thickness (Δd_f) over a specific time interval of duration (Δt) is calculated according to:

$$\Delta d_f = \frac{\dot{m}_f \Delta t}{A_{tot} r_f} \quad (3.19)$$

where (A_{tot}) is the total heat transfer area. Note that Eq. (3.19) implies that the frost will form uniformly over the tube and fin surface at any location; however, the model allows for the non-uniform buildup of frost through successive rows in the coil.

The minimum free flow area of the air stream (A_{min}) is required to compute the pressure drop, air side heat transfer coefficient and air stream mass flux; the minimum free flow area is calculated as shown in Eq.(2.13) .

The equation of the minimum free flow area of the air stream (Eq.(2.13)) includes two geometrical terms the fin face area (F_{fcare} , Eq. (2.11)) and the tube face area (T_{fcare} , Eq.(2.12)) in dry operation conditions these two terms are constant, however because the model is used to simulate frost formation which will leads eventually to the reduction of theses areas, Eqs. (2.11) and (2.12) are modified in order to account for the temporal

reduction in area that is associated with the accumulation of frost on the coil tubes and fins:

$$F_{fcarea} = N_f \cdot F_h \cdot (F_{thk} + 2\mathbf{d}_{frost}) \quad (3.20)$$

$$T_{fcarea} = N_{v,t} \cdot (D_o + 2\mathbf{d}_{frost}) \cdot (T_l - F_{fcarea}) \quad (3.21)$$

The air stream mass flux is:

$$G_{amax} = \frac{\dot{m}_a}{A_{min}} \quad (3.22)$$

The total heat transfer rate can finally be expressed as:

$$\dot{q}_{tot} = \frac{(T_{aave} - T_{rave})}{\frac{1}{(h_a + h_{lat}) A_e} + \frac{\mathbf{d}_f}{k_f A_e} + \frac{R_{fa}}{A_e} + \frac{\ln(D_o/D_i)}{2\mathbf{p}Lk_{tube}} + \frac{1}{h_{tp} A_i} + \frac{R_{fr}}{A_i}} \quad (3.23)$$

where k_{tube} is the thermal conductivity of the tubes and h_{tp} is the refrigerant-side two-phase heat transfer coefficient computed using a system of equations developed by (Jung et al. (1989), section 3.1.2). R_{fa} and R_{fr} are the fouling factor on the air and the refrigerant side. The fouling factors as suggested by Rosenhow et al. (1985) are:

$$R_{fa} = 3.5 \times 10^{-4} \text{ (m}^2\text{k/W)} \quad (3.24)$$

$$R_{fr} = 3.5 \times 10^{-4} \text{ (m}^2\text{k/W)} \quad (3.25)$$

3.2.1 Air-side heat transfer and pressure drop:

The pressure drop across the evaporator coil ($\Delta P_{tot,a}$) is calculated using the equation described in Kays and London (1964), Eq.(3.26), with the friction factor (f) suggested by McQuiston (1981), Eq.(3.28).

$$\Delta p_{total,air} = \frac{G_{a,max}}{2r_{ain}} \left[\frac{f}{4} \frac{A_{tot}}{A_{min}} \frac{r_{ain}}{r_{a,m}} + (1+s^2) \left(\frac{r_{ain}}{r_{aout}} - 1 \right) \right] \quad (3.26)$$

where r_{ain} , r_{aout} , and $r_{a,m}$ are the inlet, outlet, and average air density and s is ratio of the minimum flow area to the coil face surface area of the heat exchanger (HX_{fcaea} , Eq. (2.10)):

$$s = \frac{A_{min}}{HX_{fcaea}} \quad (3.27)$$

The friction factor suggested by McQuiston (1981) is:

$$f = 4.904 \cdot 10^{-3} + 1.382(f_1 \cdot f_2)^2 \quad (3.28)$$

where

$$f_1 = \text{Re}_D^{-0.25} \left[\frac{D_o}{2R^*} \right]^{0.25} \left[\frac{(P_t - D_o) P_{fin}}{4(1 - P_{fin} F_{thk})} \right]^{-0.4} \left[\frac{P_t}{2R^*} - 1 \right]^{-0.5} \quad (3.29)$$

$$R^* = \frac{D_o}{2} \left[\frac{(P_t - D_o) N_{finm} + 1}{(A_{tot}/A_{tube})} \right]^{-1} \quad (3.30)$$

$$f_2 = [0.6 + \text{Re}_{fin}^{-0.15}] \left[\frac{P_{fin}}{P_{fin} - F_{thk}} \right]^{-3} \quad (3.31)$$

where R^* is a type of hydraulic radius, as defined by Eq.(3.30), P_t and P_{fin} are the transverse tube pitch and fin pitch, respectively. N_{finm} is the number of fins per meter.

Re_D and Re_{fin} are the Reynolds numbers as defined in Eqs.(3.32) and (3.33), respectively.

$$Re_D = \frac{G_{amax} D_o}{m_a} \quad (3.32)$$

$$Re_{fin} = \frac{G_{a,max} P_{fin}}{m_a} \quad (3.33)$$

The air-side convective heat transfer coefficient (h_a) is calculated using Eq. (3.34) together with the correlation suggested by McQuiston (1981), Eq.(3.35), to calculate the Colburn factor (j_a):

$$h_a = \frac{j_a G_{a,max} c_{p_a}}{Pr^{2/3}} \quad (3.34)$$

$$j_a = \left[0.0014 + 0.2618 j_p j_w \right] \left[\frac{1 - N_{row} (1280) Re_L^{-1.2}}{1 - (5120) Re_L^{-1.2}} \right] \quad \text{where } N_{row} > 4 \quad (3.35)$$

where N_{row} is the number of coil rows and Re_L is the Reynolds number, which is defined as:

$$Re_L = \frac{G_{amax} P_r}{m_a} \quad (3.36)$$

where P_r is longitudinal tube pitch (the distance between rows in the flow direction).

The j_w and j_p parameters in Eq. (3.35) are calculated according to:

$$j_w = \left[0.95 + 0.4 \cdot 10^{-5} \cdot Re_{fin}^{1.25} \right] \left[\frac{P_{fin}}{P_{fin} - F_{thk}} \right] \quad (3.37)$$

$$j_p = Re_D^{-0.4} \left(\frac{A_{tot}}{A_{tube}} \right)^{-0.15} \quad (3.38)$$

where Re_D and Re_{fin} are the Reynolds numbers as defined in Eqs. (3.32) and (3.33).

Although Eqs. (3.26) through (3.38) were developed for evaporator coils operating under no frost condition, the effect of the frost built up is incorporated approximately by using the appropriate air mass flux (G_{amax}) that is calculated based on the minimum air free flow area and the local velocity, which changes as the frost thickness increases. The fin thickness, F_{thk} , used in these equation is modified to, F_{thkmod} , to incorporate the change in the frost thickness as follows:

$$F_{thk,mod} = F_{thk} + 2d_f \quad (3.39)$$

3.2.2 Refrigerant heat transfer and pressure drop:

Pressure drop on the refrigerant-side has typically been ignored in frost models (for example, Kondepudi et al. (1993), Seker et al. (2004)); however, the refrigerant-side pressure-drop plays a significant role in the industrial evaporator coils because it produces a non-negligible temperature change on the refrigerant-side of the circuit significantly affects the distribution of the frost formation and therefore the behavior of the coil under frosting conditions.

The correlations developed by Muller, et al. (1986) are used to predict the frictional, two-phase refrigerant pressure gradient $(dp/dL)_{ip}$ in a straight tube:

$$\left(\frac{dp}{dL}\right)_{tp} = [A + 2(B - A)x](1 - x)^{1/C} + Bx^3$$

$$A = \left(\frac{dp}{dL}\right)_{liq} = z_{liq} \frac{G_{tp}^2}{2r_{rliq} D_{in}}$$

$$B = \left(\frac{dp}{dL}\right)_{gas} = z_{gas} \frac{G_{tp}^2}{2r_{rgas} D_{in}}$$
(3.40)

where

$$z_{liq} = \frac{64}{Re_{liq}}, z_{gas} = \frac{64}{Re_{gas}} \quad \text{for } Re_{liq}, Re_{gas} \leq 1187$$

$$z_{liq} = \frac{0.3164}{Re_{liq}^{1/4}}, z_{gas} = \frac{0.3164}{Re_{gas}^{1/4}} \quad \text{for } Re_{liq}, Re_{gas} > 1187$$
(3.41)

$$Re_{liq} = \frac{G_{tp} D_i}{m_{liq}}$$
(3.42)

$$Re_{gas} = \frac{G_{tp} D_i}{m_{gas}}$$
(3.43)

where A is the single-phase liquid pressure drop, B is the single-phase vapor pressure drop, x is the flow quality, z is the friction factor, G_{tp} is the refrigerant mass velocity and D_{in} is the inside tube diameter.

The refrigerant pressure drop due to the tube bends Δp_{tpbend} is calculated using Eq.(3.44) from Paliwoda (1992):

$$\Delta p_{tpbend} = \frac{G_{tp}^2}{2r_{rliq}} \mathbf{x}_b \mathbf{b}_b$$
(3.44)

$$\mathbf{b}_b = [\mathbf{J}_b + 3(1 - \mathbf{J}_b)x](1 - x)^{0.333} + x^{(2.276)}$$
(3.45)

$$\mathbf{a}_b = \frac{r_{bend}}{D_o} = \frac{P_t}{2D_o}$$
(3.46)

where b_b is the two phase multiplier and is defined in Eq.(3.45), J_b is the ratio of the liquid to dry saturated vapor pressure drop in tube bends and is provided in Table 3-1 as a function of refrigerant temperature and x_b is the coefficient of local resistance to single-phase flow and is provided in Table 3-2 as a function a_b , where a_b is defined in Eq.(3.46). The parameter r_{bend} is the radius of bend and P_t is the evaporator coil tube transverse pitch.

Table 3-1 Parameter J_b defined in Eq. (3.45), Paliwoda (1992)

Saturation temperature (R717)	J_b
20	0.0220
0	0.0115
-20	0.0054
-40	0.0023

Table 3-2 Coefficient of resistance, x_b defined in Eqn.(3.44), Paliwoda (1992)

a_b	x_b	a_b	x_b
1	0.28	2.0	0.160
1.25	0.21	2.5	0.140
1.5	0.19	3.0	0.130
1.75	0.175	4.0	0.12

The refrigerant-side heat transfer coefficient (h_{tp}) is computed using a correlation developed by Jung (1989), Eq.(3.47), for two-phase flow refrigerant is used:

$$h_{tp} = N_{nb} \cdot h_{SA} + F_{tp} \cdot h_{liq} \quad (3.47)$$

and

$$\begin{aligned} N_{nb} &= 4048 X_{tt}^{1.22} Bo^{1.13} && \text{for } X_{tt} < 1 \\ N_{nb} &= 2 - 0.1 X_{tt}^{-0.28} Bo^{-0.33} && \text{for } 1 < X_{tt} \leq 5 \end{aligned} \quad (3.48)$$

where N_{nb} is a factor related to nucleate boiling and X_{tt} is Martinelli parameter, defined as:

$$X_{tt} = \left(\frac{1-x}{x} \right)^{0.9} \left(\frac{\mathbf{r}_{r,gas}}{\mathbf{r}_{rliq}} \right)^{0.5} \left(\frac{\mathbf{m}_{rliq}}{\mathbf{m}_{r,gas}} \right)^{0.1} \quad (3.49)$$

Bo is boiling number and is defined as:

$$Bo = \frac{\dot{q}''}{G_p \cdot i_{fg}} \quad (3.50)$$

where \dot{q}'' is heat flux and i_{fg} is latent heat of vaporization. h_{SA} is the nucleate boiling heat transfer coefficient and is calculated using the Stephan and Abdelsalam equation, as described by Jung (1989):

$$h_{SA} = 207 \frac{k_{rliq}}{bd} \left(\frac{\dot{q}'' \cdot bd}{k_{rliq} \cdot T_{rsat}} \right)^{0.674} \left(\frac{\mathbf{r}_{r,gas}}{\mathbf{r}_{rliq}} \right)^{0.581} Pr^{0.533} \quad (3.51)$$

where bd is bubble break diameter, defined as:

$$bd = 0.0146 \mathbf{b} \left[2t / \left(g (\mathbf{r}_{rliq} - \mathbf{r}_{rgas}) \right) \right]^{0.5} \quad \text{with } \mathbf{b} = 35^\circ \quad (3.52)$$

F_{tp} is the two phase enhancement factor, defined as:

$$F_{tp} = 2.37 \left(0.29 + \frac{1}{X_{tt}} \right)^{0.85} \quad (3.53)$$

h_{liq} is the single phase liquid heat transfer coefficient:

$$h_{liq} = \frac{k_{rliq}}{D_i} 0.023 Re_{liq}^{0.8} Pr^{0.4} \quad (3.54)$$

where Re_{liq} is the liquid refrigerant Reynolds number and defined in Eq. (3.42).

3.3 Summary

The frost numerical model based on the equations derived in this chapter is implemented using the Engineering Equation Solver, or EES, software (Klein, 2006). Although the frosting process is a transient one, the model is quasi-steady; that is, the process is divided into time steps and within each time step, the process is assumed to be at steady-state.

The model takes all of the evaporator coil geometries and the inlet air and refrigerant thermal properties as the required user input and calculates all of the air, refrigerant and frost thermal and physical properties at each row of the evaporator coil. The frost properties (e.g., frost layer thickness, thermal conductivity and density) at the end of each time step are used as an input for the next time step.

3.4 Nomenclature

Symbol	Description	Dimensions
A_b	= Bare tube outside surface area	$[m^2]$
A_{tot}	= Total heat transfer area	$[m^2]$
A_e	= Effective heat transfer area	$[m^2]$
A_{fin}	= Fin surface area	$[m^2]$
A_i	= Tube cross section area	$[m^2]$
A_{min}	= Minimum free flow area	$[m^2]$
cp_a	= Specific heat for air	$[J\ kg^{-1}\ K^{-1}]$
D_i	= Tube inside diameter	$[m]$
D_o	= Tube outside diameter	$[m]$
F_{fcarea}	= Fin face area	$[m^2]$
f	= Friction factor	$[-]$
F_{thk}	= Fin thickness	$[m]$
G_{amax}	= Mass flux of the air based on the minimum flow area	$[kg\ m^{-2}\ s^{-1}]$
G_{tp}	= Refrigerant mass velocity	$[kg\ m^{-2}\ s^{-1}]$
h_a	= Convective air side heat transfer coefficient	$[W\ m^{-2}\ K^{-1}]$
h_m	= Mass transfer coefficient	$[kg\ m^{-2}\ s^{-1}]$
h_{lat}	= Latent heat transfer coefficient	$[W\ m^{-2}\ K^{-1}]$
h_{eff}	= Effective air heat transfer coefficient	$[W\ m^{-2}\ K^{-1}]$
h_{SA}	= Refrigerant nucleate boiling heat transfer coefficient	$[W\ m^{-2}\ K^{-1}]$
h_{tp}	= Two phase refrigerant heat transfer coefficient	$[W\ m^{-2}\ K^{-1}]$
HX_{fcarea}	= Evaporator coil face surface area	$[m^2]$
i	= Enthalpy	$[kJ\ kg^{-1}]$
i_{sg}	= Heat of sublimation of water	$[kJ\ kg^{-1}]$
i_{fg}	= Latent heat of vaporization	$[kJ\ kg^{-1}]$
j_a	= Colburn factor	$[-]$
k_{fin}	= Fin thermal conductivity	$[W\ m^{-1}\ K^{-1}]$
k_f	= Frost thermal conductivity	$[W\ m^{-1}\ K^{-1}]$
k_{tube}	= Tube thermal conductivity	$[W\ m^{-1}\ K^{-1}]$
Le	= Lewis number	$[-]$

\dot{m}	=	mass flow rate	[kg s ⁻¹]
$N_{t,v}$	=	Number of tubes at each row	[-]
N_{finm}	=	Number of fins per meter	[-]
N_{row}	=	Number of coil rows	[-]
P_{fin}	=	Fin pitch	[m]
Δp_{total}	=	Total pressure drop across the evaporator coil	[Pa]
Δp_{ipbend}	=	Frictional two phase refrigerant pressure drop for tube bends	[Pa]
$(dp/dL)_{ip}$	=	Frictional two phase refrigerant pressure drop for straight tubes	[Pa m ⁻¹]
P_t	=	Transverse tube pitch	[m]
P_r	=	Longitudinal tube pitch	[m]
Pr	=	Prandtl number	[-]
\dot{q}_{tot}	=	Total heat transfer rate	[kW]
\dot{q}_{lat}	=	Latent heat transfer rate	[kW]
\dot{q}_{sen}	=	Sensible heat transfer rate	[kW]
r_{bend}	=	Radius of the tube bends	[m]
Re_o	=	Reynolds number based on (2 x fin pitch) and the air mass flux	[-]
Re_L	=	Reynolds number based on the longitudinal tube pitch and the air mass flux	[-]
Re_D	=	Reynolds number based tube diameter and the air mass flux	[-]
Re_{fin}	=	Reynolds number based fin pitch and the air mass flux	[-]
Re_{liq}	=	Reynolds number based on the refrigerant mass velocity and the liquid refrigerant viscosity	[-]
Re_{gas}	=	Reynolds number based on the refrigerant mass velocity and the gas refrigerant viscosity	[-]
R_c	=	thermal contact resistance	[m ² K W ⁻¹]
R_{fa}	=	Air side fouling factor	[m ² K W ⁻¹]
R_{fr}	=	Refrigerant side fouling factor	[m ² K W ⁻¹]
r_1	=	Tube outside radius	[m]
r_2	=	Fin equivalent radius	[m]
T	=	Temperature	[K]
T_{fcare}	=	Tube face area	[m ²]
T_l	=	Tube length at one row	[m]
x	=	Refrigerant quality	[-]

Greek symbols

<i>r</i>	=	Density	[kg m ⁻³]
<i>h_f</i>	=	Fin efficiency	[-]
<i>w</i>	=	Specific humidity	[kg/kg]
<i>d_f</i>	=	Thickness of frost layer	[m]
<i>m</i>	=	viscosity	[kg m ⁻¹ s ⁻¹]

Subscripts

in	=	Inlet to the evaporator coil section
out	=	Outlet from the evaporator coil section
ave	=	Averaged
f	=	Frost
a	=	Air
r	=	Refrigerant

3.5 References

- Al-Mutawa, N.K., 1997, Experimental investigations of frosting and defrosting of evaporator coils at freezer temperatures, PhD thesis, Department of Mechanical Engineering, University of Florida
- Domanski, P. 1982, Computer modeling and prediction of an air source heat pump with a capillary tube, Ph.D. dissertation, The Catholic University of America.
- Incropera, F. and D. DeWitt, 1990, Introduction to Heat Transfer, John Wiley & Sons, 2nd edition.
- Jung, D. S., and D.A. Didion., 1989, "*Horizontal flow boiling heat transfer using refrigerant mixtures*," ER-6364, research project 8006-2.
- Klein, S. and F. Alvarado, 2006, Engineering equation solver, F-Chart Software, Middleton, WI.
- Kays, W.M., and A.L. London., 1964, Compact Heat Exchangers, McGraw-Hill Book Company, New York.
- Kondepudi, S.N. and D. O'Neal., 1993, "A Simplified Model of Pin Fin Heat Exchangers Under Frosting Conditions." ASHRAE Transactions, Vol. 99, No. 1.
- Kondepudi, S. and D. O'Neal., 1993, "*Performance of Finned-Tube Heat Exchangers Under Frosting Conditions: I. Simulation Model, and II. Comparison of Experimental Data with Model.*" International Journal of Refrigeration, Vol. 16, No.3.
- Lee, K., T. Lee, and W. Kim., 1994, "*Heat and Mass Transfer of Parallel Heat Exchanger under Frosting Conditions*", SAREK Journal, Vol. 6, No. 2.
- Malhammar, A., 1986, "*Frostpaslag via flansade ytor.*" Doktorsav handling, Kungliga Tekniska Hogskolan, Stockholm, Sweden.
- McQuiston, F.C., 1981, "*Finned tube heat exchangers: state of the art for the air side,*" ASHRAE Transactions, Vol, 87, Part 1.
- McQuiston, F.C., 1978, "*Heat, mass and momentum transfer data for five plate-fin-tube heat transfer surfaces,*" ASHRAE Transactions, Vol, 84, Part 1.
- McQuiston, F.C. 1975, "*Fin efficiency with combined heat and mass transfer,*" ASHRAE transaction., Vol. 81, Part 1

Muller, H. and K. Heck., 1986, "A simple friction pressure drop correlation for two phase flow heat transfer of ammonia." *Chemical Engineering Processing*, 20.

Nelson, B., 1990, "Design of Evaporators for Liquid Overfeed Systems", *ASHRAE Transactions*, Vol. 96, No. 1.

Oskarsson, S.P., K.I. Krakow, and S. Lin., 1990, "Evaporator models for operation with dry, wet, and frosted finned surfaces Part I and II", *ASHRAE transaction.*, Vol. 96.

Paliwoda, A., 1992, "Generalized method of pressure drop calculation across pipe components containing two-phase flow of refrigerants." *International Journal of Refrigeration*, Vol. 15, (2).

Rosenhow, W.M., J.P. Hartnett, and E.N. Ganic, 1985, Handbook of heat transfer applications, New York, McGraw Hill, 2nd edition.

Sanders, C.T., 1974, Frost formation: the influence of frost formation and defrosting on the performance of air coolers, PhD. Thesis, Technische Hogeschool, Delft, The Netherlands.

Schmidt, T.E., 1949, "Heat transfer calculation for extended surfaces." *Refrigerating Engineering*, vol. 57.

Seker, D., H. Karatas, and N. Egrican., 2004a "Frost formation on fin-and-tube heat exchangers. Part I- Modeling of frost formation on fin-and-tube heat exchanger." *International Journal of Refrigeration*, Vol. 24

Seker, D., H. Karatas, and N. Egrican., 2004b "Frost formation on fin-and-tube heat exchangers. Part II- Experimental investigation of frost formation on fin-and-tube heat exchanger." *International Journal of Refrigeration*, Vol. 27

Threlkeld, J.L., 1970, Thermal environmental engineering, 2nd ed. Englewood Cliffs, NJ: Prentice Hall Book Co.

Yao, Y., Y. Jiang, S. Deng, and Z. Ma., 2004, "A study on the performance of the airside heat exchanger under frosting in an air source heat pump water heater/chiller unit." *International Journal of Heat and Mass Transfer*, Vol. 47

Chapter 4 Frost Experiment

This chapter describes a field experiment used to investigate the effect of frost formation on the performance of a low-temperature large-scale evaporator coil used in industrial refrigeration systems. A series of experiments are conducted to determine the in-situ coil cooling capacity of the evaporator over time as frost builds on its surfaces. Field-measured quantities include inlet and outlet air temperatures, inlet and outlet air relative humidity, and air volume flow rate. These measurements provide a baseline set of experimental data that used to validate the numerical frost model described in Chapter 3.

4.1 Experiment facility:

The coil selected for this experimental investigation is a liquid overfed evaporator manufactured by the King company (Model IRF-90-0310-GG-5-037-717R) that is installed in a penthouse on the roof of the Wells Dairy warehouse in Le Mars, Iowa. The coil is used to maintain a space temperature of -20°F (-29°C) for the long-term storage of ice cream products. The geometric details of the coil used in the experiment and the nominal operating conditions are summarized in Table 4-1. Figure 4.1 shows an isometric view of the penthouse with its overall dimensions. Figure 4.2 shows a plan view of the key components in the penthouse.

Table 4-1: Geometry and operating conditions of the coil used in the experiment

Parameter	Value
Fin pitch	0.85 cm (3 fns/inch)
Face area	8.23 m ² (88.6 ft ²)
Tube diameter	19.05 mm (0.75 inch)
Tube length	5.5 m (18 ft)
Number of fans	5
Fan power @ -30°F (-34°C) air temperature	2.33 kW (3.125 hp)
Rated CFM	1699 m ³ /min (60000 cfm)
Number of tubes	260
Number of tube row	10
Tube transverse pitch,	57 mm (2.25 inch)
Tube longitudinal pitch,	44 mm (1.75 inch)
Evaporation temperature	-34.4°C (-30 F)
Coil temperature difference	5.6°C
Base rating	23.8 kW _T /K
Nominal capacity	130 kW _T
Fin material	Aluminum
Tube material	Galvanized steel
Refrigerant	Ammonia
Evaporator coil type	Controlled-pressure receiver-liquid overfeed

During the cooling mode operation, warehouse air enters the penthouse through a grate that is located in the penthouse floor perpendicular to the upstream coil face. The air is then drawn across the evaporator coil by five fans that are located in the penthouse floor perpendicular to the coil on the downstream side of the evaporator, as shown in Figure 4.3. The fans discharge the air into a plenum through five round extension ducts, each with an opening of 0.97 m (38 inches). The plenum then distributes the cold air to the

freezer environment through 10 round exit ducts. The plenum is attached to the freezer ceiling. The penthouse-plenum configuration is shown in Figure 4.4.

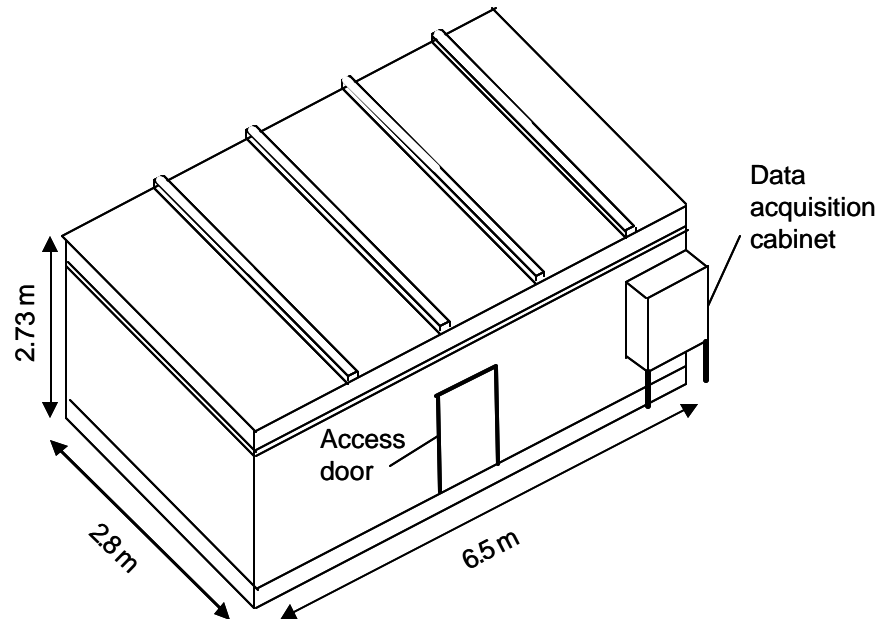


Figure 4.1 Penthouse enclosure; Schematic showing the outside dimensions of the penthouse (top). Photograph showing the penthouse that encloses the evaporator coil (bottom).

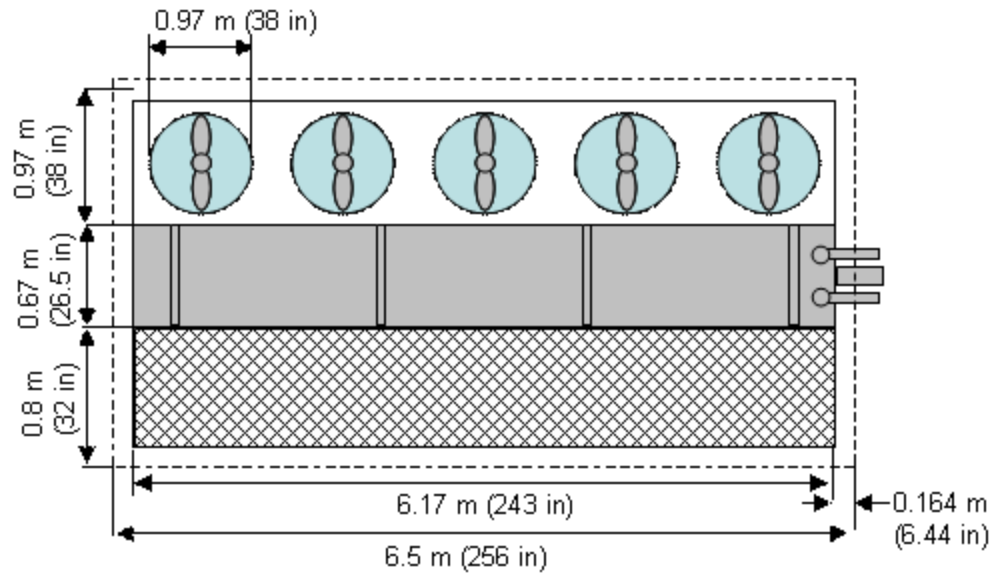


Figure 4.2 Penthouse plan view showing the internal dimensions of the penthouse enclosure.

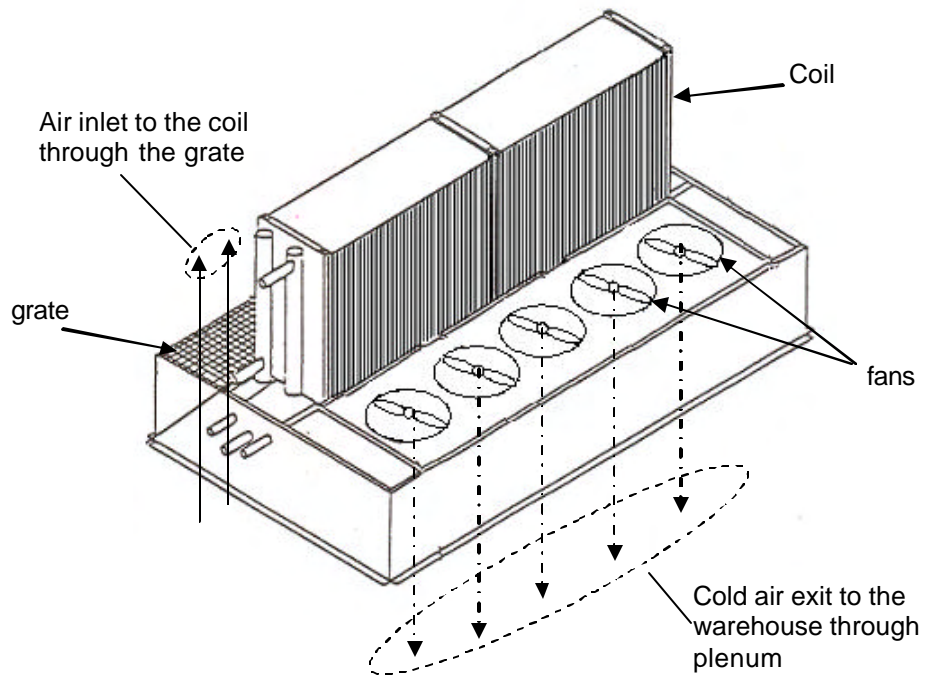


Figure 4.3: Schematic of the experiment coil and the flow path of the air.

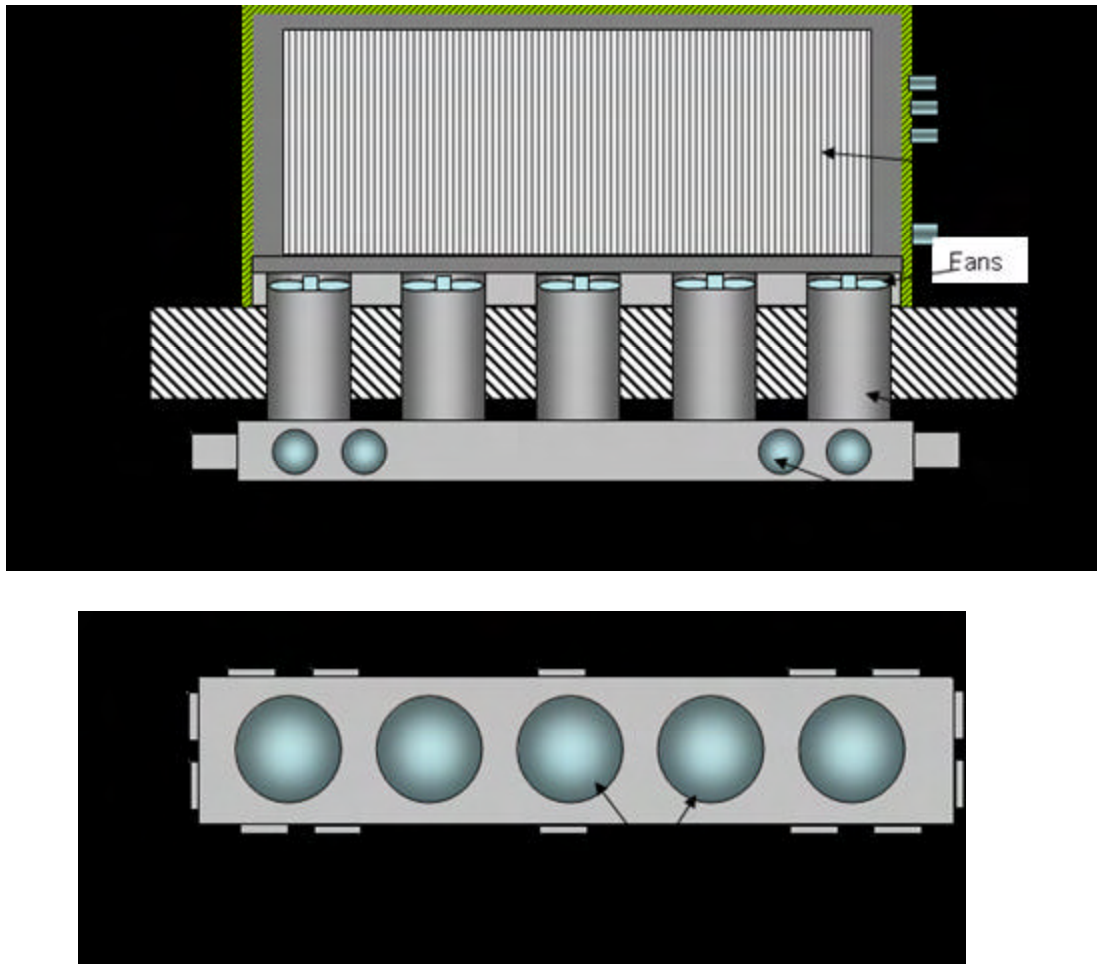


Figure 4.4: Schematic of the penthouse-plenum setup

4.2 Design of Experiment:

Since the frosting process includes both sensible and latent air-side heat transfer, the evaporator coil heat transfer rate can be determined by applying an energy balance on the air-side across the coil:

$$\dot{q}_t = \dot{m}_a (i_{i,ave} - i_{o,ave}) \quad (4.1)$$

where \dot{q}_t is the evaporator coil heat transfer rate, $i_{i,ave}$ and $i_{o,ave}$ are the bulk enthalpies of the air up-stream and down-stream of the evaporator coil, respectively. The air mass

flow rate, \dot{m}_a , can be computed according to:

$$\dot{m}_a = \rho_o V_{oave} A_f \quad (4.2)$$

where ρ_o is the down-stream evaporator coil air density, V_{oave} is the average velocity of air through the coil face, and A_f is the evaporator coil face area.

The rate of frost accumulation, \dot{m}_{fr} , can be computed using the following equations:

$$\dot{m}_{fr} = \dot{m}_a (w_{iave} - w_{oave}) \quad (4.3)$$

where w_{iave} and w_{oave} are the average up-stream and down-stream humidity ratios, respectively.

Figure 4.5 shows the location of the air property measurements required to carry out the calculations represented by Eqs. (4.1) to (4.3). Note that Figure 4.5 does not reflect the exact location or number of instruments used in the experiments; rather, it illustrates the state variables that result from averages of individual sensors.

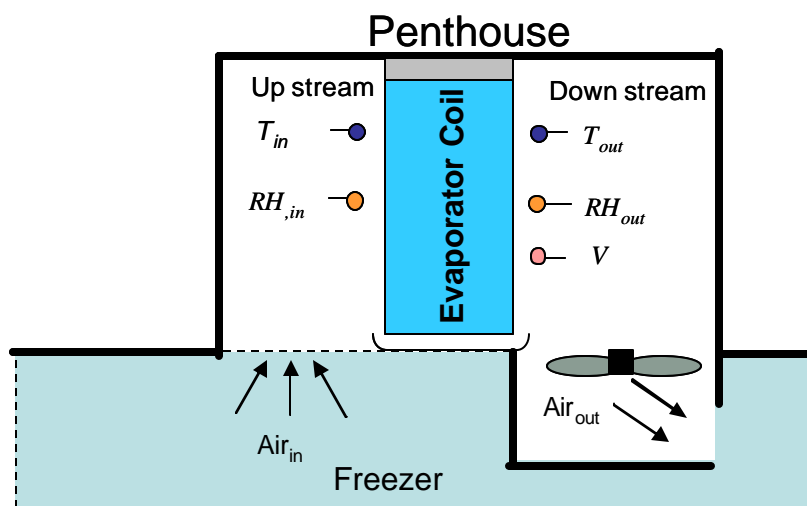


Figure 4.5: Schematic showing locations for measurements taken during the experiments.

4.3 Instrumentation and data Acquisition:

This section describes the data acquisition system and the instruments that were installed to measure the evaporator coil cooling capacity with an air-side energy balance. Measurements consist of air velocity, air inlet and exit temperatures, and air inlet and exit relative humidity. In addition, instrumentation was installed to measure the air-side pressure drop.

4.3.1 Flow and temperature Measurements

The average air velocity is determined by measuring air velocity at five separate locations along the downstream face of the evaporator coil using air velocity mass flow transducers; model FMA-903-V. These air velocity transducers have a range of 0 to 1000 ft/min (0 to 5.1 m/s) with an accuracy of $\pm 3\%$ of full scale. The air velocity mass flow transducers also measure and correct for temperature effects; the allowable temperature and pressure range for these instruments are -40 to 250 °F (-40 to 121 °C) and atmospheric pressure to 150 psig (1.0 MPa). All air velocity sensors were tested and calibrated by the manufacturer according to specifications provided by the U.S. National Institute of Standards and Technology. A schematic of the air velocity mass flow transducer is shown in (Appendix D, Figure D.1).

Each of the five air velocity mass flow transducers is connected to analog voltage inputs on a Campbell scientific data logger model CR23X. Power for the transducers is obtained from external power supplier; Model 72-2005; the transducers require 18 Vdc with a maximum current draw of 300 mA.

The five air velocity flow meters (labeled V_1 , V_2 ... V_5) are mounted using unistrut fixtures installed downstream of the evaporator. These fixtures were installed vertically and attached to the ceiling and the floor of the penthouse. The unistruts were placed 36 inch (0.9m) apart in order to divide the coil face into six equal areas and offset 12 inch (0.3 m) from the downstream face of the coil. In order to avoid the presence of any turbulence caused by the unistrut fixture which could affect the accuracy of the velocity measurement, each velocity sensor is mounted at an angle so that the horizontal distance between the tip of the air velocity sensor and the associated unistrut fixture is approximately 4 inch (0.1m) (see Figure 4.6). Since the air velocity leaving the coil is expected to vary in both the vertical and the horizontal directions, the five air velocity mass flow meters were mounted along a diagonal across the coil face (as shown in Figure 4.6).

Note that the coil fins are not continuous from the top to the bottom of the coil, there is a discontinuity exactly at the mid-point of the coil which provides an open path across the coil at the half way of the coil height; this open path is less restrictive than the air path at any other location across the evaporator (as shown in Figure 4.7); as a result, the velocity mass flow meter V_3 was mounted so that its tip is almost at the same level as the slit between the discontinued fins.

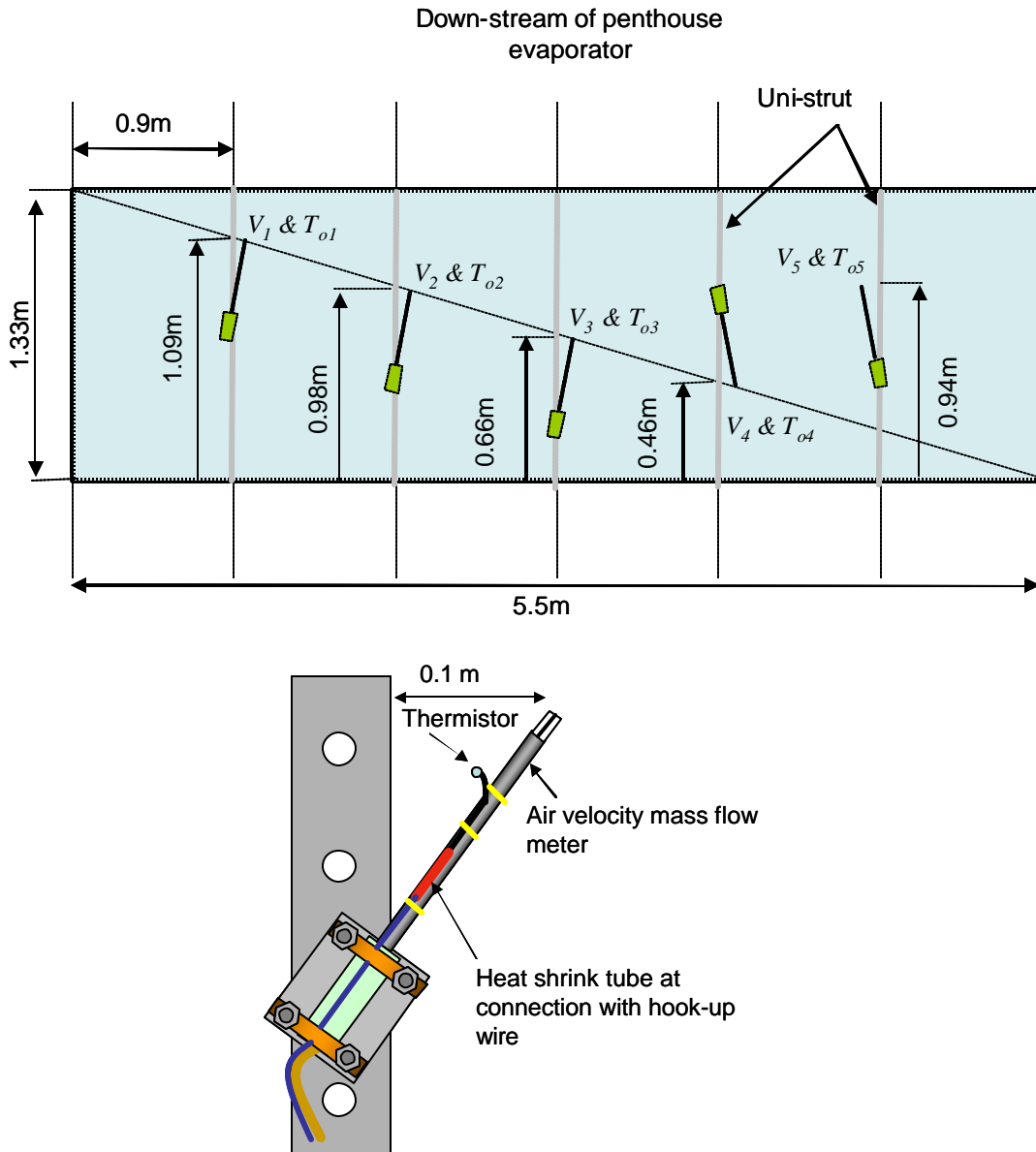


Figure 4.6: Schematic showing the exact location of each velocity mass flow meter and Thermistor (top) mounting detail (bottom).

The average inlet and outlet air temperatures are determined by using nine thermistors; model 44130. The thermistors are encased in Teflon and have an accuracy of ± 0.1 °C. The working temperature range is -80 to +120 °C (-110 to 250 °F). A schematic of a thermistor is shown in (Appendix D, Figure D.2); heat shrink tube is used to connect each

thermistor to its hook-up wire that runs to the data acquisition logger. Five thermistors ($T_{o,1}, T_{o,2}, \dots, T_{o,5}$) are used and averaged in order to provide a measure of the average outlet air temperature. The five thermistors are also spaced diagonally across down stream coil face; each thermistor is mounted adjacent to a corresponding velocity flow meter as shown in Figure 4.7. The remaining four thermistors ($T_{in,1}, T_{in,2}, \dots, T_{in,4}$) are used to obtain an average inlet air temperature. The four thermistors are attached directly to the grid that is upstream of the evaporator. The five outlet thermistors and four inlet thermistors are placed into two different groups of thermistors; each group of thermistors is connected in series to the external current source and provided with a constant $10 \mu\text{A}$ current; with a current source, model 101.

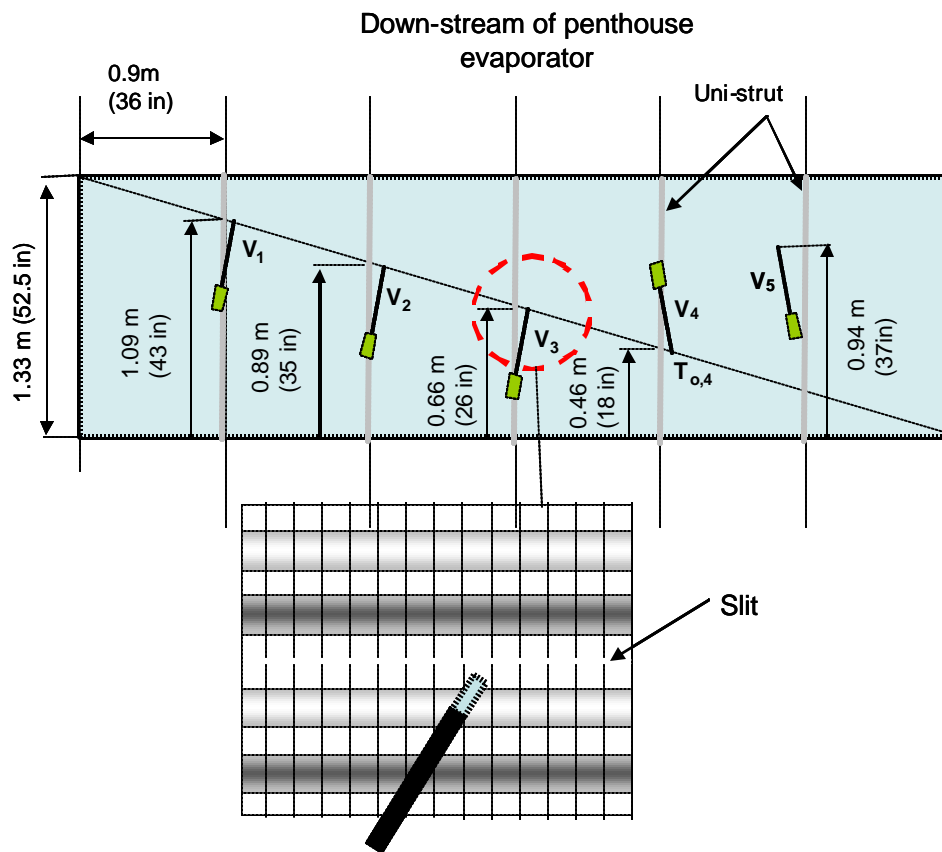


Figure 4.7: Schematic showing the horizontal gap between the coil fins.

4.3.2 Relative Humidity Measurements

The average inlet and outlet air relative humidity were both measured in this experiment using four humidity sensors, model HIH-3602-A. The relative humidity sensors are characterized by a linear relationship between output voltage and relative humidity and can tolerate a working temperature range of -40° to 85°C (-40° to 185°F) with an accuracy of $\pm 2\%$. A schematic of the relative humidity sensor is shown in (Appendix D, Figure D.3).

Two relative humidity sensors were mounted upstream and downstream of the evaporator. The humidity sensors used to measure the inlet air relative humidity ($RH_{in,1}$ and $RH_{in,2}$) are mounted above the defrost coil drain pan and 0.30 m from the upstream coil face, as shown in Figure 4.8.

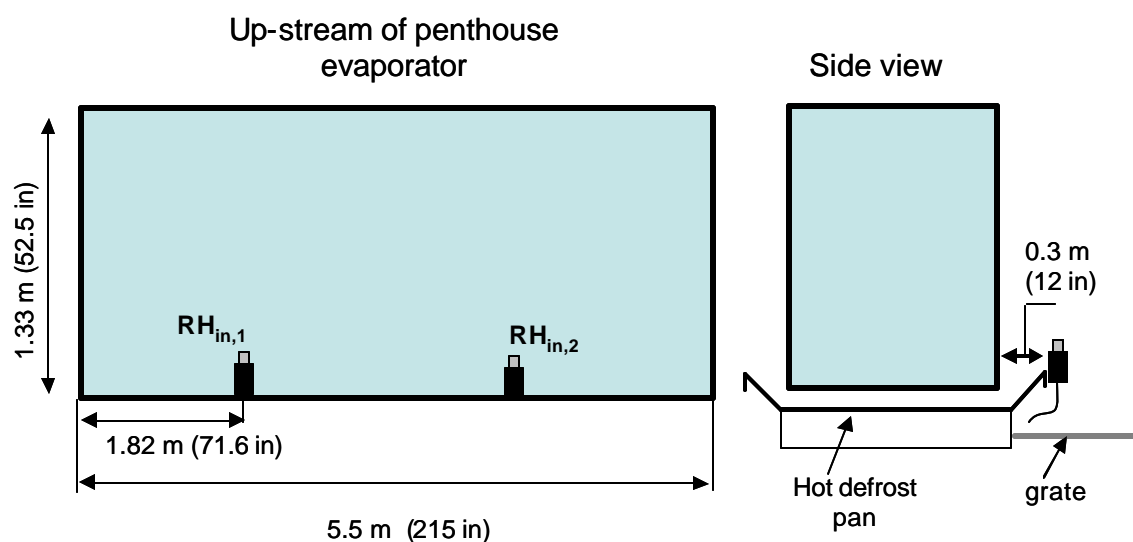


Figure 4.8 Schematic showing the exact location of the relative humidity sensors ($RH_{in,1}$ and $RH_{in,2}$)

The two relative humidity sensors used to measure the outlet air relative humidity ($RH_{o,1}$ and $RH_{o,2}$) are attached at an elevation of 0.46 and 0.89 m and offset by 0.30 m from the downstream face of the coil, as shown in Figure 4.9.

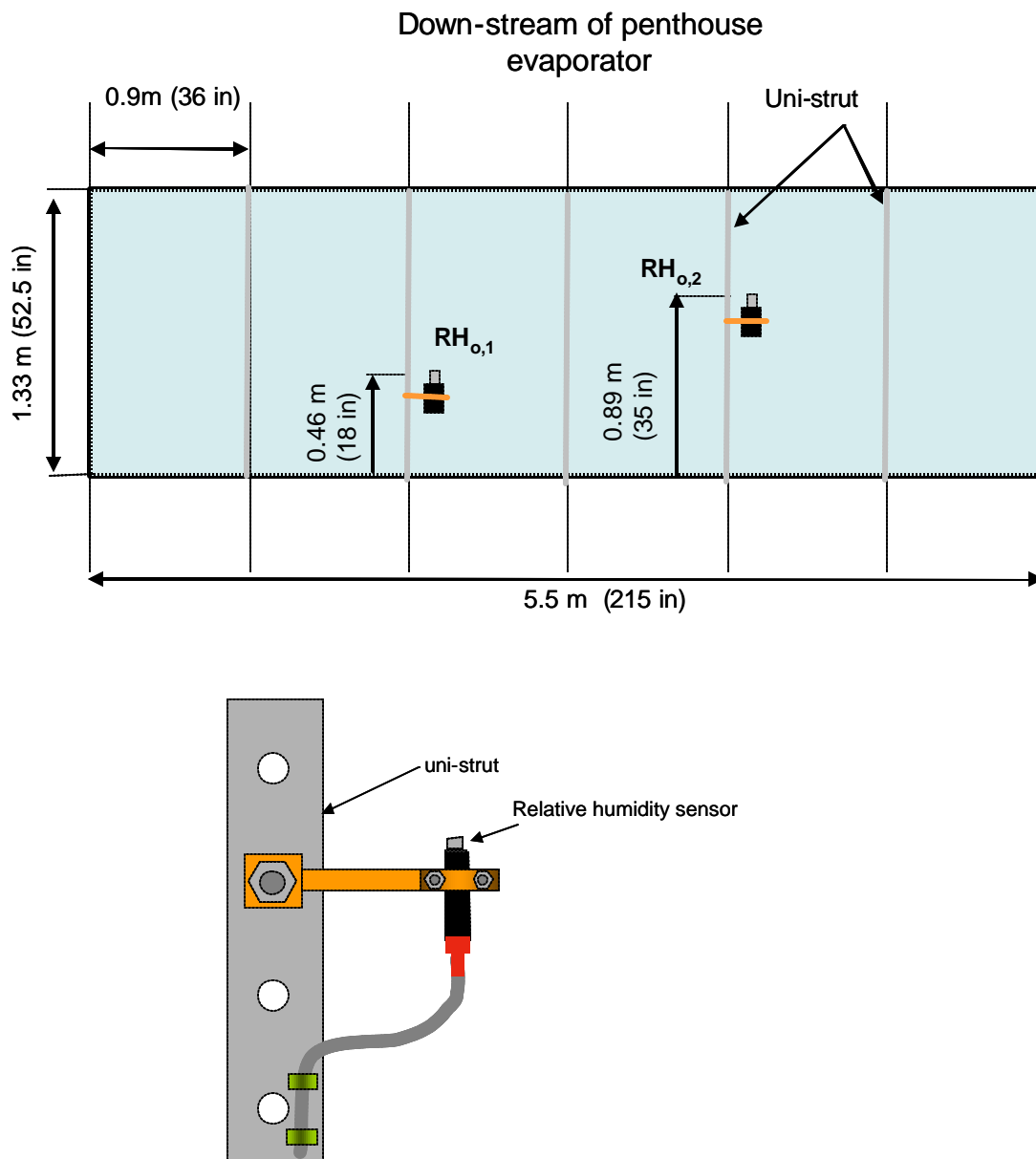


Figure 4.9 Schematic showing the exact location of the relative humidity sensors ($RH_{o,1}$ and $RH_{o,2}$) (top) and the mounting (bottom)

Each of the four relative humidity sensors has four wires; two wires are connected to one of the analog inputs on the data logger while the other pair is connected to a 5 Vdc power output in the data logger.

4.3.3 Data Acquisition System

The data acquisition system consists of a relay multiplexer, a data logger and a removable, laptop computer. The relay multiplexer, model AM16/32, is connected to the Campbell scientific CR23X micro-logger. Both the data logger and the relay multiplexer are enclosed in a water-proof enclosure, as shown in appendix D. The data logger can be connected via an RS-232 port to the serial port of the computer. The computer is used for programming the data logger and for data retrieval.

The primary data logger program was created using the development software SCWIN in order to measure the air inlet and outlet temperature, inlet and outlet air relative humidity, air velocity and air pressure. The program is then transferred to software PC208W which is used to download the program to the data logger and also to retrieve data. Both software packages were provided by Campbell Scientific. All sensor channels were given a range of ± 5000 mV and used a 60 Hz rejection filter to suppress noise from the power supply. All data were averaged over a time period of 1 minute before storing.

The data logger enclosure and all the power supplies and the differential pressure transducer were mounted within a water-proof enclosure that is attached to the outside wall of the penthouse, a photograph of the enclosure is provided in (Appendix D, Figures D.4 and D.5).

4.4 Experiment uncertainty:

The air velocity, dry bulb temperatures and relative humidity are measured using the experimental setup discussed in the previous section. Data were collected during cooling mode operation following the completion of a defrost cycle (i.e., starting with a clean coil); the test was repeated five times (the tests are referred to as runs #1, 2, 3, 4 and 5). Measured data from each transducer are collected at one minute intervals for a period of 42 hours, except during runs #2 and #5 where the data collection spanned 31 and 22 hours, respectively. The one minute observations were averaged in order to develop one hour time average information for performance analysis of the cooling mode operation.

A spatially-averaged coil face air velocity (V_{ave}), inlet and outlet air humidity ($RH_{i,ave}$ and $RH_{o,ave}$, respectively) and the average inlet temperature ($T_{i,ave}$) were obtained by calculating the mean value of the spatial one-hour interval averaged data. The bulk air temperature on the down-stream side of the evaporator ($T_{o,ave}$) was calculated using a velocity-weighted average of the outlet temperatures, as shown in Table 4-2. The spatially-averaged data for each experiment run are provided in Appendix A. The inlet and outlet air humidity ratios and enthalpies were calculated using moist air property correlations based on the average temperature and relative humidity at these locations.

Table 4-2 Average coil face parameters.

Parameter	Equation
Average air velocity	$V_{oave} = \left(\sum_{n=1}^5 V_n \right) / 5 \quad (4.4)$
Average air inlet relative humidity	$RH_{iave} = (RH_{i1} + RH_{i2}) / 2 \quad (4.5)$
Average air outlet relative humidity	$RH_{oave} = (RH_{o1} + RH_{o2}) / 2 \quad (4.6)$
Average air inlet temperature	$T_{iave} = \left(\sum_{n=1}^4 T_{i,n} \right) / 4 \quad (4.7)$
Average air outlet temperature	$T_{oave} = \left(\sum_{n=1}^5 T_{o,n} V_n \right) / \sum_{n=1}^5 V_n \quad (4.8)$

4.4.1 Uncertainty Analysis

The uncertainty associated with any of the variables measured in the experiment (referred to generically here as VR) can be related to three different factors:

1. the design uncertainty of the instrument used in the experiment , dVR_m ,
2. the location of the instrument (i.e., spatial variations across the coil), dVR_L , and
3. the assumed random fluctuation and the scatter in the instrument readings, dVR_t .

The overall uncertainty for each variable is calculated using the root sum square (RSS) technique which assumes that these sources of uncertainty are normally distributed and uncorrelated; the results are summarized in Table 4-4.

$$\left(dVR_{overall} \right)^2 = \left(dVR_x \right)^2 + \left(dVR_L \right)^2 + \left(dVR_m \right)^2 \quad (4.9)$$

The 95% confidence level uncertainties of the calculated quantities are estimated using typical propagation of error techniques represented by Eq. (4.10) and the results are summarized in Table 4-4:

$$dR = \sqrt{\sum_i \left(\frac{\partial R}{\partial VR_i} \right)^2 dVR_{overalli}^2} \quad (4.10)$$

where dR is the uncertainty of the measured result, R .

Table 4-3: Summary of the estimated uncertainties of the measured variables.

Variable	dVR_m	dVR_L	dVR_t	$dVR_{overall}$
T_{in}	$\pm 0.1^\circ\text{C}$	$\pm 0.2^\circ\text{C}$	$\pm 0.01^\circ\text{C}$	$\pm 0.22^\circ\text{C}$
T_o	$\pm 0.1^\circ\text{C}$	$\pm 0.3^\circ\text{C}$	$\pm 0.04^\circ\text{C}$	$\pm 0.3^\circ\text{C}$
V	$\pm 0.15 \text{ m/s}$	$\pm 0.3 \text{ m/s}$	$\pm 0.04 \text{ m/s}$	$\pm 0.3 \text{ m/s}$
RH_{in}	$\pm 2\%$	$\pm 0.2\%$	$\pm 0.017\%$	$\pm 2\%$
RH_o	$\pm 2\%$	$\pm 0.5\%$	$\pm 0.016\%$	$\pm 2\%$

Table 4-4: Summary of the estimated uncertainties of the calculated results.

Calculated Result, R	dR
$i_{i,ave}$	$\pm 0.12 \text{ kJ/kg}$
$i_{o,ave}$	$\pm 0.15 \text{ kJ/kg}$
$w_{i,ave}$	$\pm 5.0\text{E-}06 \text{ kg}_w/\text{kg}_a$
$w_{o,ave}$	$\pm 3.60\text{E-}06 \text{ kg}_w/\text{kg}_a$
\dot{m}_{fr}	$\pm 0.83 \text{ kg/hr}$
m_{fr}	$\pm 1.5\%$
\dot{q}_t	$\pm 8.70 \text{ kW}_T$

4.5 Experiment results:

The time variation of the average air velocity on the down-stream side of the evaporator throughout each of the four experimental runs is shown in Figure 4.10. Notice the general trend of decreasing average face velocity with time which is attributable to the increase of air flow resistance associated with frost accumulation on the coil.

Because a fixed speed fan is used to move air through the coil, the increase in air flow resistance results in a decrease in the flow rate.

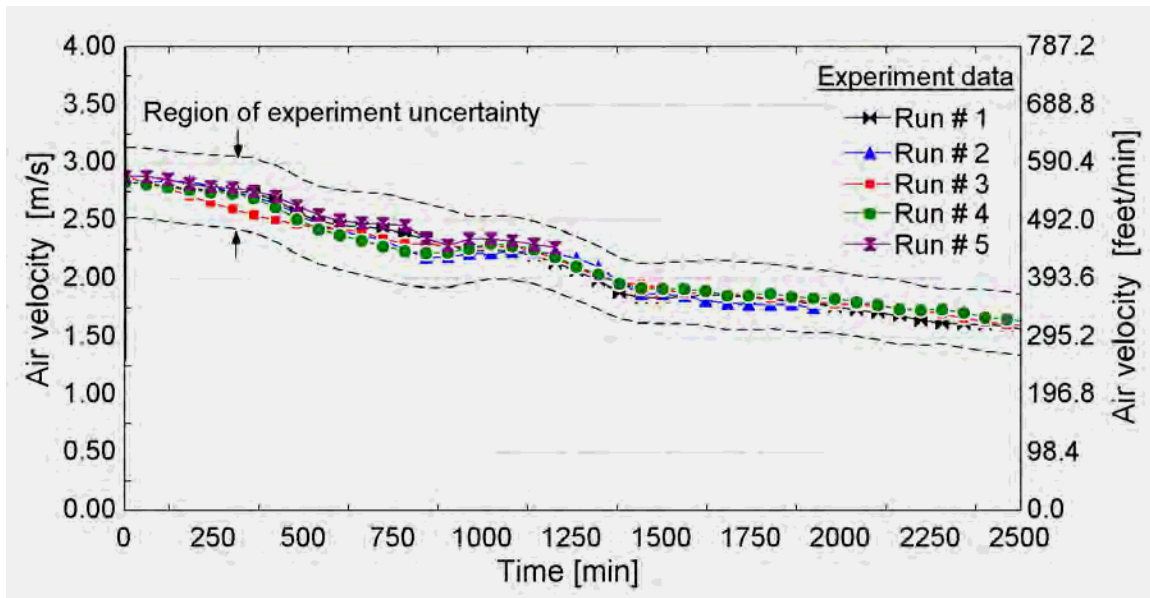
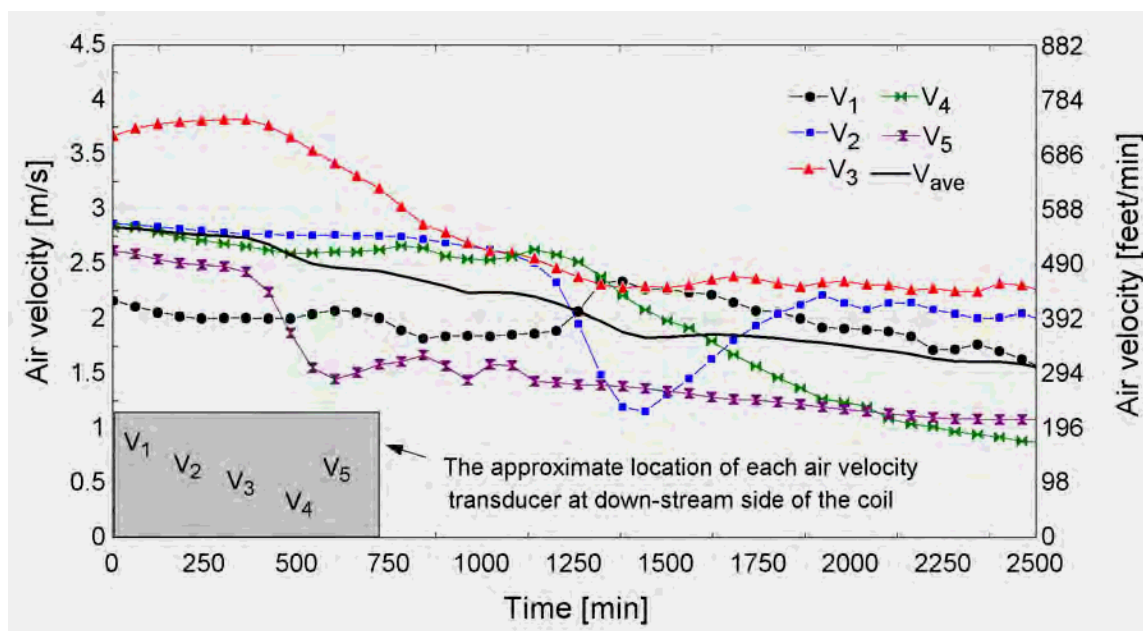


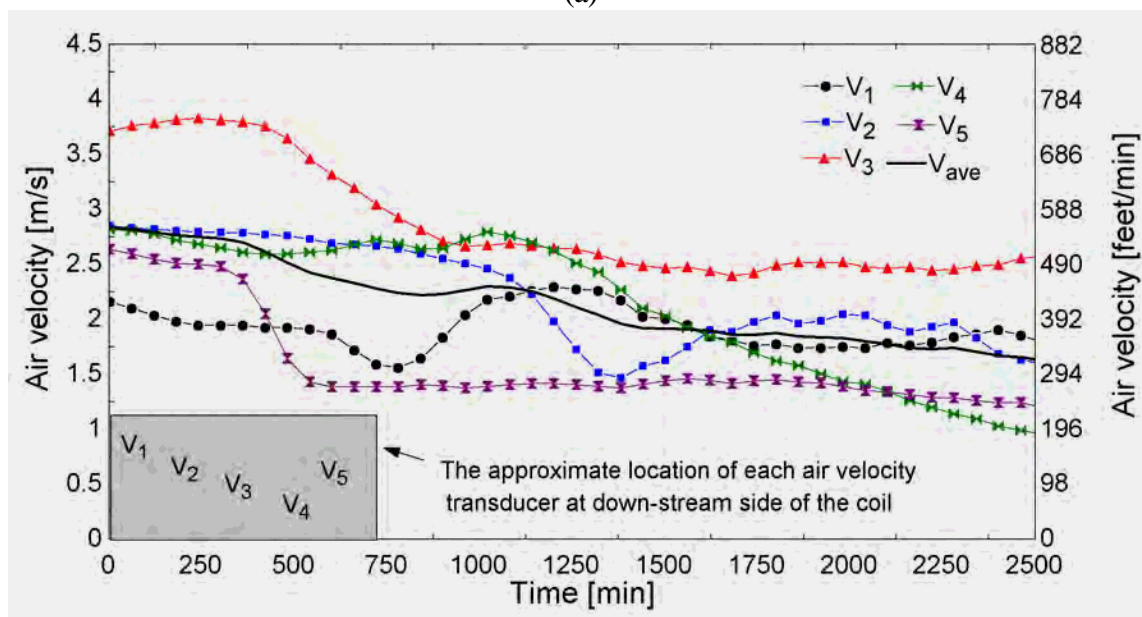
Figure 4.10 Time-dependent spatially-averaged air velocity on the downstream side of the evaporator (with time 0 being an ice-free coil) throughout all of the experimental tests.

Figure 4.11 (a) and (b) illustrate the temporal variation of air velocity at the five spatial locations along the coil face for runs #1 and #3, respectively. Also shown is the average downstream air velocity calculated using Eq.(4.4). Figure 4.11 shows that the velocity readings obtained from each of the separate velocity sensors is fairly consistent from run to run. For example, notice that the velocity reading associated with sensor V_3 (located in the center of the coil) is consistently higher than the velocity reading from the other four sensors at the beginning of each run. This difference was expected since the free air path across the evaporator at the elevation where the velocity sensor was mounted is slightly larger than the free air path anywhere else across the evaporator due to a manufactured discontinuity in the evaporator coil fins which causes lower air resistance and therefore higher velocity. Figure 4.11 also shows that the air flow rate is highly non-uniform

across down-stream the evaporator coil; this non-uniformity is mainly due to the design of the evaporator coil penthouse.



(a)



(b)

Figure 4.11 Time-dependent measured air velocity of each velocity sensor and the calculated average air velocity down stream side of the evaporator; (a) Run #1, (b) Run #3.

The time variation of the bulk air inlet and outlet dry bulb temperature for each of the five different runs is shown in Figure 4.12. The change in temperature experienced by the air as it passes through the coil is shown in Figure 4.13 for each of the five runs. Figure 4.12 and Figure 4.13 show that the temperature drop of the air as it passes through the coil continuously increases as frost builds up; this is related to the continuous decrease in the average air velocity that was shown Figure 4.10. As the average air velocity decreases, the coil effectiveness increases, which causes a reduction in the leaving temperature of the air. It should be noted that the improved effectiveness is not sufficient to make up for the overall reduction in the coil refrigeration capacity associated with the reduction of the flow rate. It will be shown subsequently that the capacity of the evaporator continuously decreases over time.

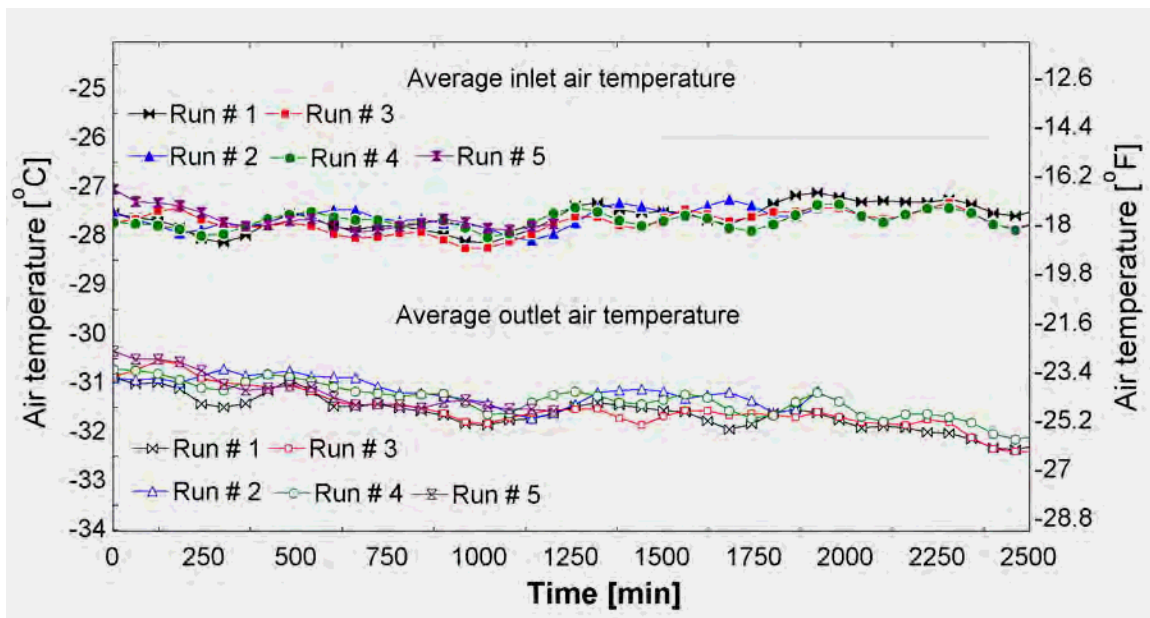


Figure 4.12 Time-dependent spatially-averaged inlet and outlet air temperatures throughout the experiment

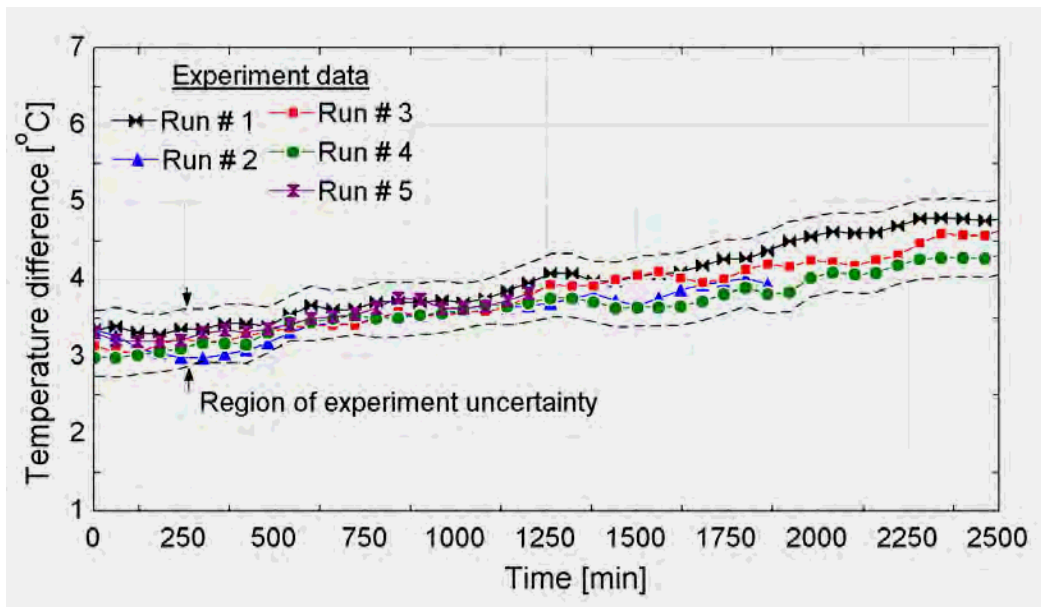


Figure 4.13 Time-dependent temperature difference between the inlet and outlet air flows.

Figure 4.14 and Figure 4.15 illustrate the time variation of the average inlet air relative humidity and the average inlet and outlet air humidity ratios, respectively, during the five runs. Figure 4.14 shows that the relative humidity is nearly constant during the duration of the experiment for the five runs.

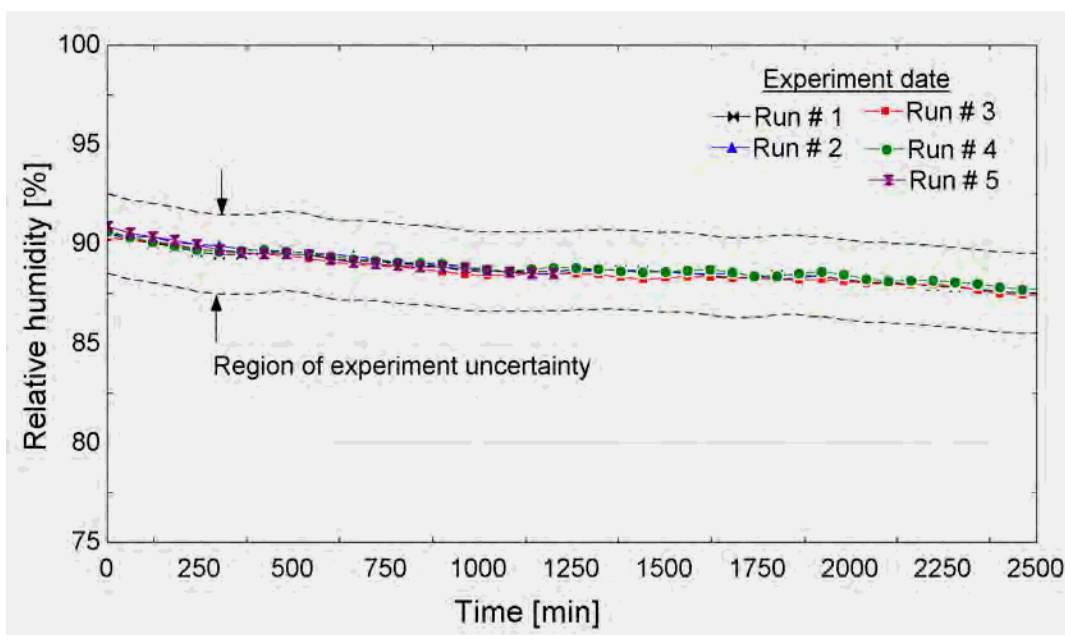


Figure 4.14 Time-dependent relative humidity of the inlet air.

Figure 4.15 shows that the humidity ratio of the exit air is always lower than that of the inlet air, as expected since moisture removed from the air builds up at the coil surface in the form of frost.

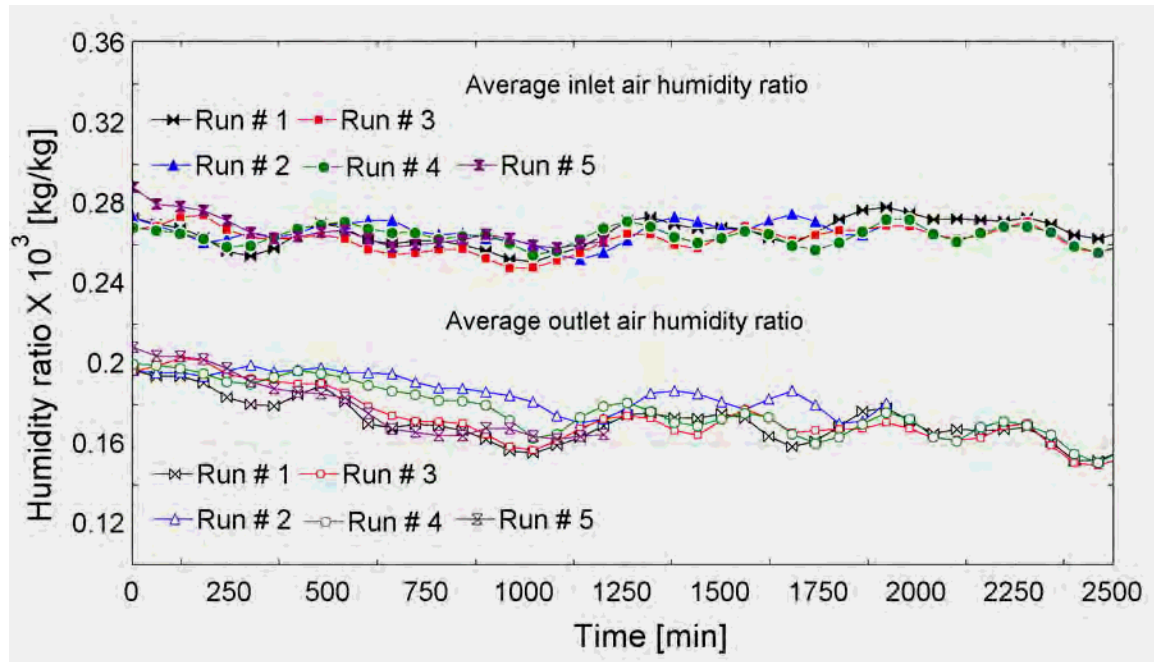


Figure 4.15 Time-dependent humidity ratio of the inlet and outlet air.

Figure 4.16 illustrates the rate of frost accumulation (\dot{m}_{fr}) as a function of time throughout the five runs. The rate of frost accumulation was calculated from a mass balance on the water carried by the air, Eq.(4.3). Figure 4.17 shows the mass of the accumulated frost as a function of time (m_{fr}) for the five runs. Figure 4.17 indicates that the mass of the accumulated frost grows essentially linearly with time; this is because the rate of frost accumulation changes only slightly during each run.

A hot gas defrost cycle was carried out at the conclusion of run # 5 and the quantity of melted frost was measured directly by collecting the condensate emanating from the coil drain. The total mass of condensate for Run #5 was 188 kg. The estimate of

accumulated frost that is obtained from integrating the frost accumulation rate over time is 200 ± 3 kg as noted in Figure 4.17. The discrepancy in these values is likely attributable to the experimental error associated with collecting and measuring the melt and the experimental error associated with calculating the total mass of the frost. The discrepancy could also be attributed to a portion of the frost being re-evaporated to the freezer space plus the portion of the melted frost that remains adhered to the coil surfaces and the drain pan at the end of the defrost cycle. Coley (1983) stated that during each defrost cycle, at least 15% of the ice sublimates back into the conditioned space to be removed again. However the current experiment shows that for a coil being defrosted in a penthouse enclosure, the total accumulated frost that transfers back to the conditioned room as a latent load is less than 6%. If it assumed that the thickness of the condensate film remaining on the coil surfaces after the defrost is about $1.0 \mu\text{m}$, then the moisture mass remaining is approximately 9 kg (19.8 lbm) which is equal to 4.5% of the total accumulated frost that remains inside the pent-house, leaving only 1.5% of the total accumulated frost that could possibly transfer back to the conditioned space as a latent load.

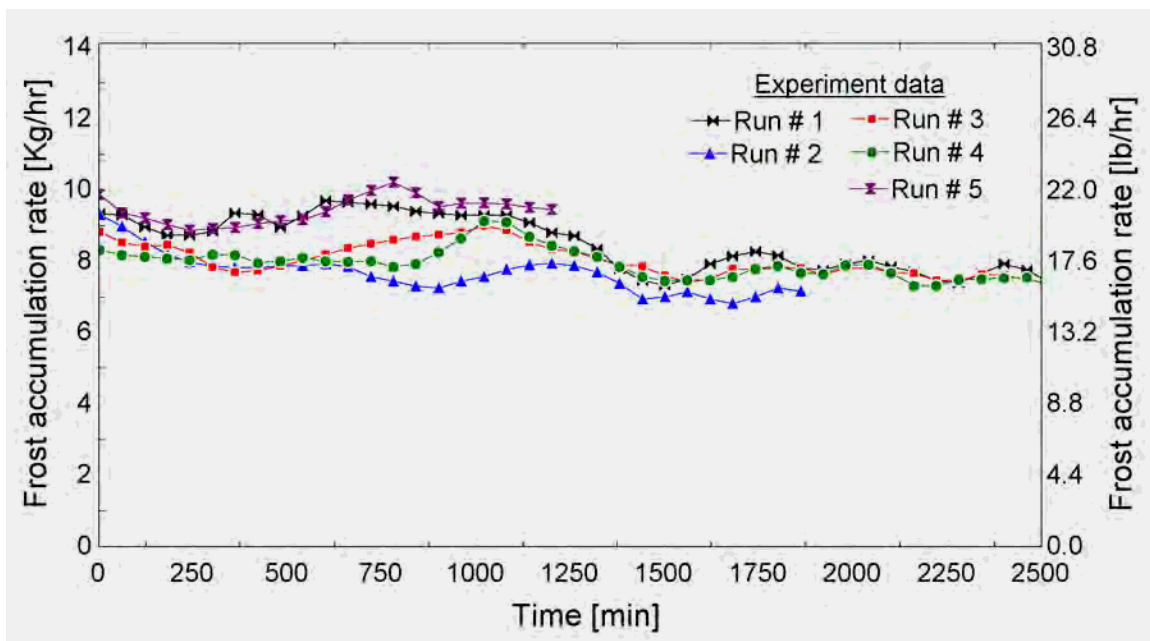


Figure 4.16 Time-dependent mass flow rate of the frost accumulation.

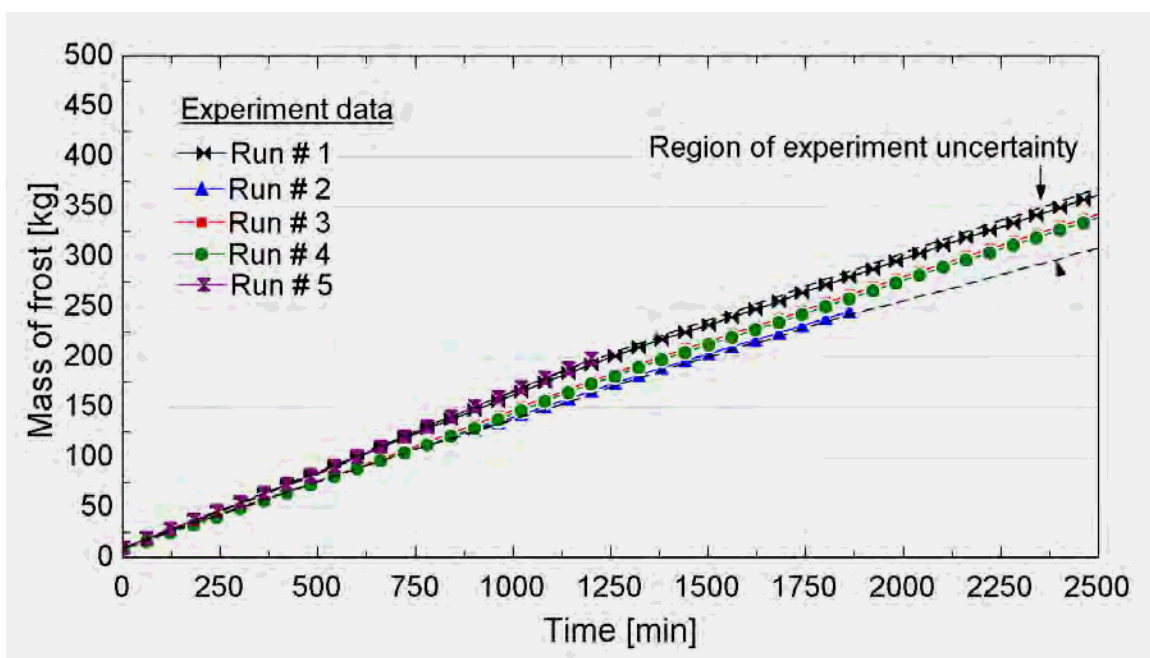


Figure 4.17 Time-dependent mass accumulation of frost.

Figure 4.18 shows the evaporator cooling capacity as a function of time for the five runs calculated using Eq.(4.1). It can be seen from Figure 4.18 that the evaporator coil cooling capacity decreases monotonically as expected, mainly due the decreases in the air mass flow rate. The initial and the final calculated rates of cooling for each run along with the loss of cooling capacity are summarized in Table 4-5.

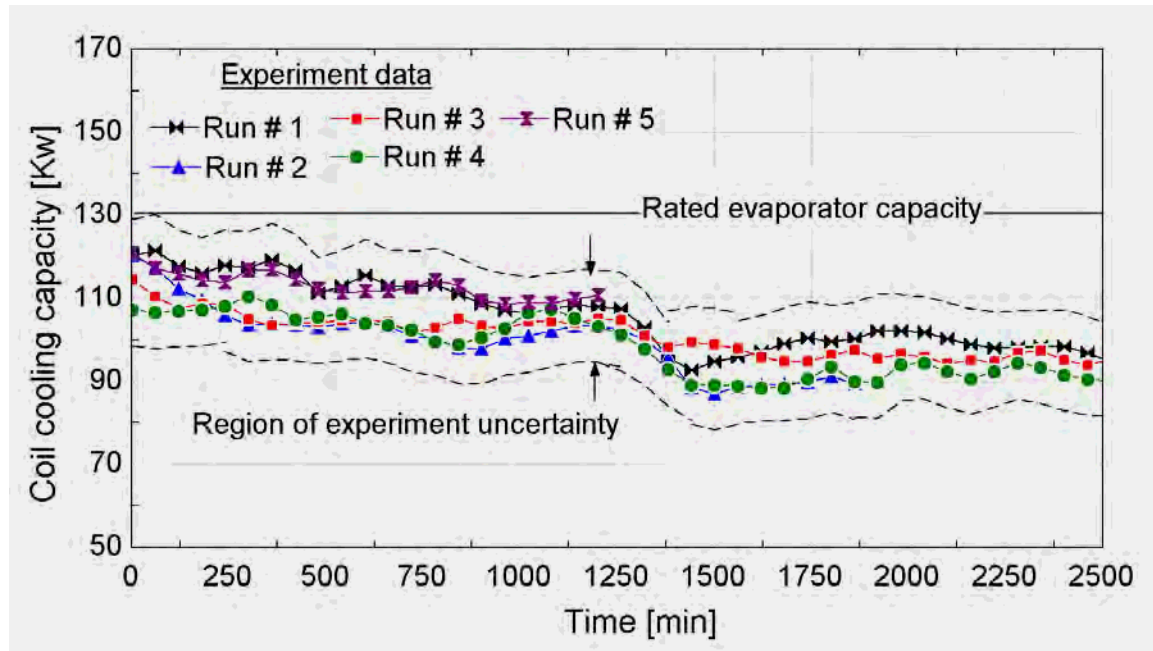


Figure 4.18 Time-dependent evaporator cooling capacity as frost accumulates.

Table 4-5 Initial and final cooling rates for five experiment runs along with the percentage loss of the cooling rate.

Run	Initial Capacity [kW _T]	Operating Interval [hours]	Final Capacity [kW _T]	Capacity Loss [kW _T]
1	121.5±8.7	42	94.3±8.7	27.2 ±8.7
2	120.4±8.7	31	89.5±8.7	30.9±8.7
3	114.5±8.7	42	93.9±8.7	20.6±8.7
4	110.4±8.7	42	90.1±8.7	20.3±8.7
5	120.8±8.7	22	110.7±8.7	10.1±8.7

4.6 Summary

An experiment has been conducted in order to measure the in-situ coil cooling capacity of a large scale industrial evaporator coil as frost builds up on its surface. The measured data from the experiment are provided in Appendix D. Based on the experimental results, the following conclusions can be made:

- The accumulation of frost on the surfaces of the evaporator coil causes an increase in the resistance to air flow and an associated drop in the air mass flow rate through the evaporator coil.
- As the mass flow rate of the air passing through the evaporator coil decreases, the temperature drop of the air passing through the coil increases and, as a result, the leaving air temperature decreases.
- The evaporator cooling capacity decreases monotonically with time, mainly due the decrease in the air mass flow rate.

4.7 Nomenclature

Symbol	Description	Dimensions
A_f	= Evaporator coil face area	$[m^2]$
i	= Enthalpy	$[kJ\ kg^{-1}]$
\dot{m}	= mass flow/accumulation rate	$[kg\ s^{-1}]$
m	= mass	$[kg]$
\dot{q}	= heat transfer rate	$[W]$
RH	= relative humidity	$[-]$
T	= temperature	$[K]$
V	= velocity	$[m\ s^{-1}]$
ρ	= density	$[kg\ m^{-3}]$
w	= humidity ration	$[-]$
<i>Subscripts</i>		
A	= air	
ave	= spatially-averaged	
fr	= frost	
i	= inlet to the evaporator coil	
o	= outlet from the evaporator coil	
t	= total	

4.8 References

Coley, M.B., 1983, "The cost of frost." ASHRAE Journal, Vol. 82, No. 9.

Chapter 5 Frost Model Validation

The equations and correlations described in Chapter 3 are combined to form a numerical model of a liquid overfeed ammonia evaporator with a counter-flow circuiting. The evaporator model is implemented using the Engineering Equation Solver software (Klein [9]). The predictions of the counter-flow frost model are compared with experimental data obtained from the field experiment on an industrial air-cooling evaporator described in Chapter 4. The details associated with the experimental evaporator coil are summarized in Table 4-1.

5.1 Comparison between the frost experimental data and the model predictions

Although the inlet air dry bulb temperature and relative humidity vary slightly throughout any experiment, constant values of $-27.65\text{ }^{\circ}\text{C}$ ($-17.7\text{ }^{\circ}\text{F}$) inlet air temperature and 90% inlet air relative humidity were used for the simulations since these values represent the average observed during the experiment. A Lewis number of 1.0 is used to calculate the mass transfer coefficient and the model presented by Malhammar (1986) (Eqs. (2.20) to(2.29)) is used to calculate the frost density.

The fan curve provided by the evaporator coil manufacturer was used to predict the variation in the air flow rate as the coil accumulates frost; thereby, imposing an air-side pressure drop. Liquid ammonia from a controlled-pressure receiver enters the evaporator with a temperature of $-34.4\text{ }^{\circ}\text{C}$ (30°F) and quality of 7%.

Figure 5.1 shows the time variation of the average air velocity at the evaporator coil face measured in the experiment (an average of measurements made at 5 spatial locations across the face taken for 5 different experimental runs) as well as the air velocity predicted by the counter-flow frost model (solid line). Both the experimental data and the frost model show that the air velocity decreases with time; this behavior is mainly due to the increase in the air flow resistance caused by the frost accumulation on the evaporator coil surfaces. Also it can be seen from Figure 5.1 that the air velocity predicted by the counter-flow frost model agrees reasonably well with the measured average air velocity.

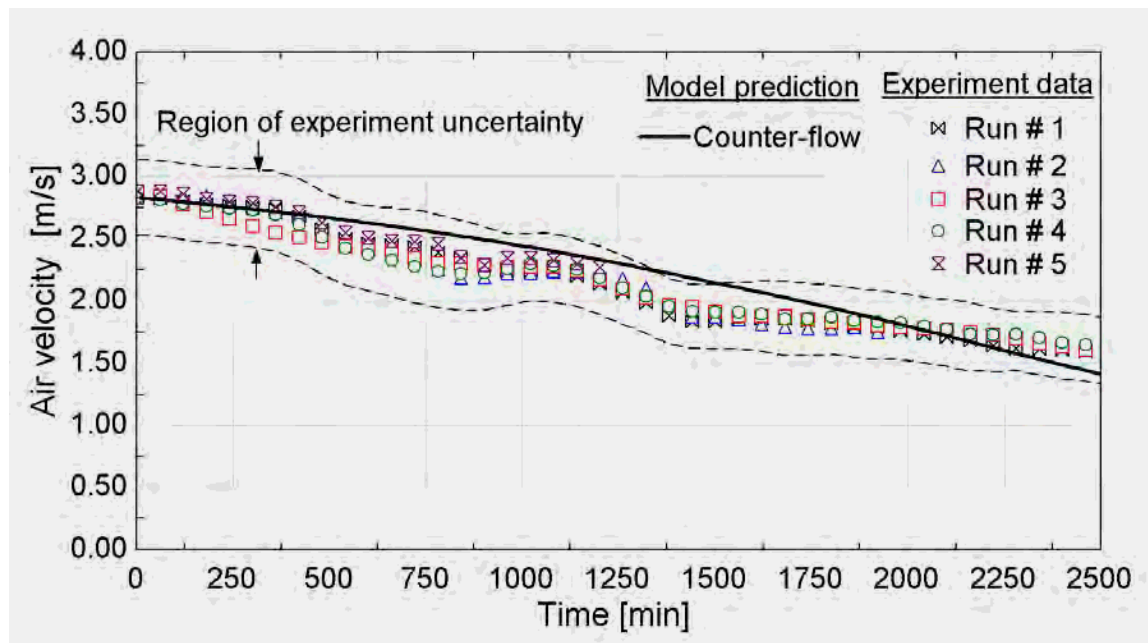


Figure 5.1 Comparison between the average face velocity of the evaporator coil measured in the experiment and the face velocity predicted by the counter-flow frost model over time.

Figure 5.2 and Figure 5.3 compares the inlet and the outlet air temperature and the inlet to outlet air temperature difference measured during the experiment with the frost model

prediction, respectively. Note that the measured temperature difference is the bulk temperature averaged over 5 spatially separated velocity and temperature measurements and that 5 separate experimental runs are shown. Figure 5.3 shows that the temperature difference predicted by the counter-flow frost model matches the data to within experimental uncertainty over the entire frost process. Both the model prediction and the experimental data show that the inlet to outlet air temperature difference increases monotonically due to the reduction in the air flow rate. As the air flow rate drops, the coil effectiveness is increased and thus the exiting air temperature more closely approaches the refrigerant-side temperature (Figure 5.2).

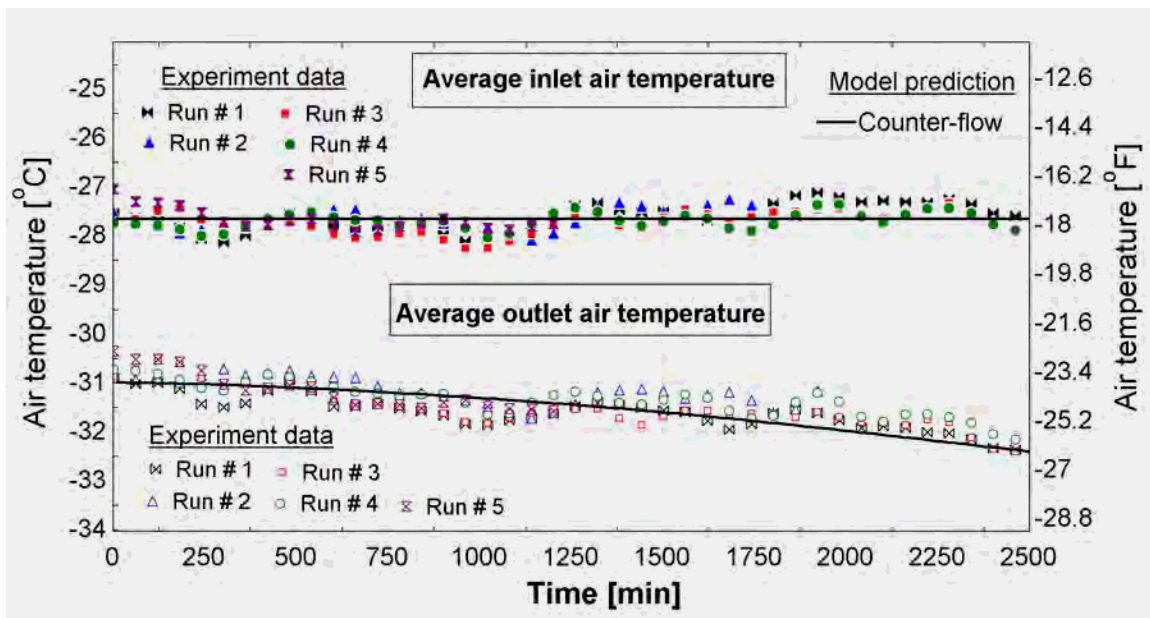


Figure 5.2 Comparison of the time-dependent spatially-averaged inlet and outlet air temperatures measured during the experiment and the inlet and outlet air temperature predicted by the frost model

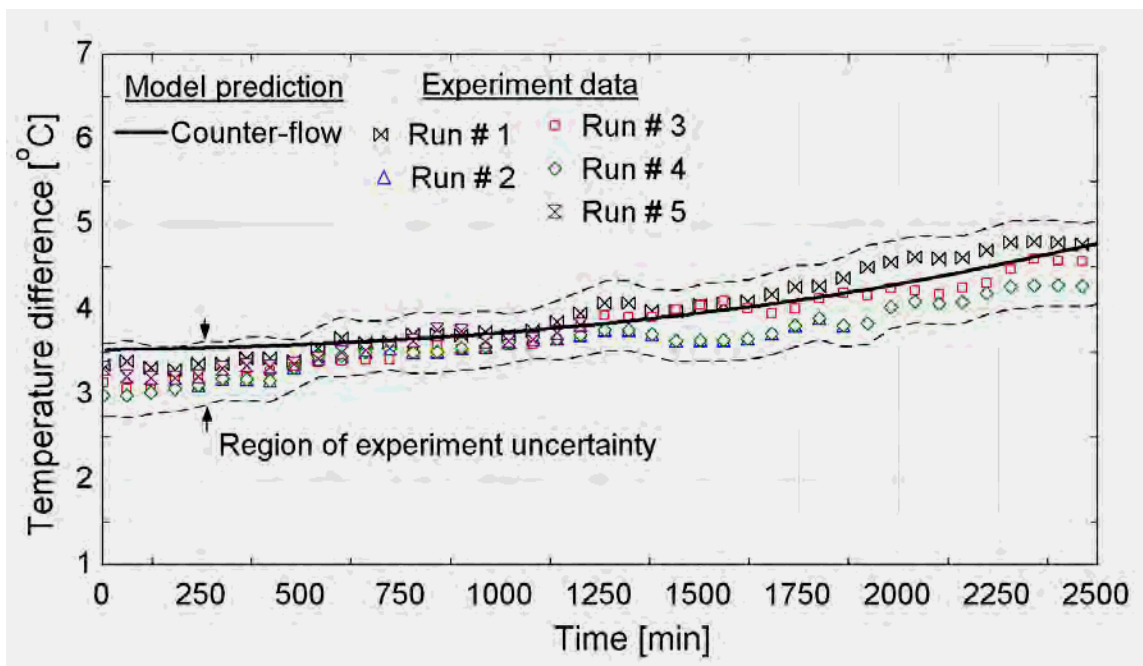


Figure 5.3 Comparison of the inlet and outlet air temperature difference measured during the experiment and the temperature difference predicted by the counter-flow frost model over time.

Figure 5.4 shows the evaporator cooling capacity obtained from an air-side energy balance using the experimental data (again, all 5 runs are shown) and predicted by the counter-flow frost model. The evaporator coil cooling capacity decreases monotonically due to the increase in the air flow resistance as well as the insulating effect of the frost. The cooling capacity predicted by the counter-flow frost model agrees well with the measured evaporator cooling capacity.

Figure 5.5 shows the total accumulated mass of frost based on a water vapor mass balance using the experimental data and predicted by the counter-flow frost model. The total mass of the accumulated frost increases nearly linearly with time and that the counter-flow model slightly under-predicts the experimental data.

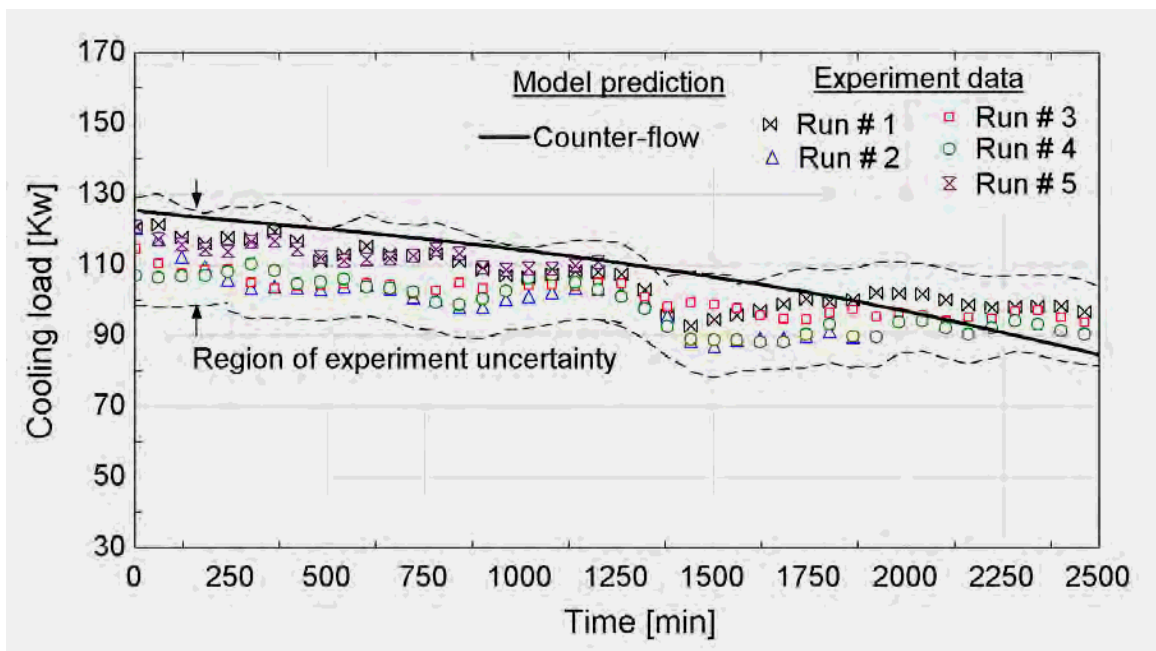


Figure 5.4 Comparison of the evaporator cooling capacity measured during the experiment and the evaporator cooling capacity predicted by the counter-flow frost model over time.

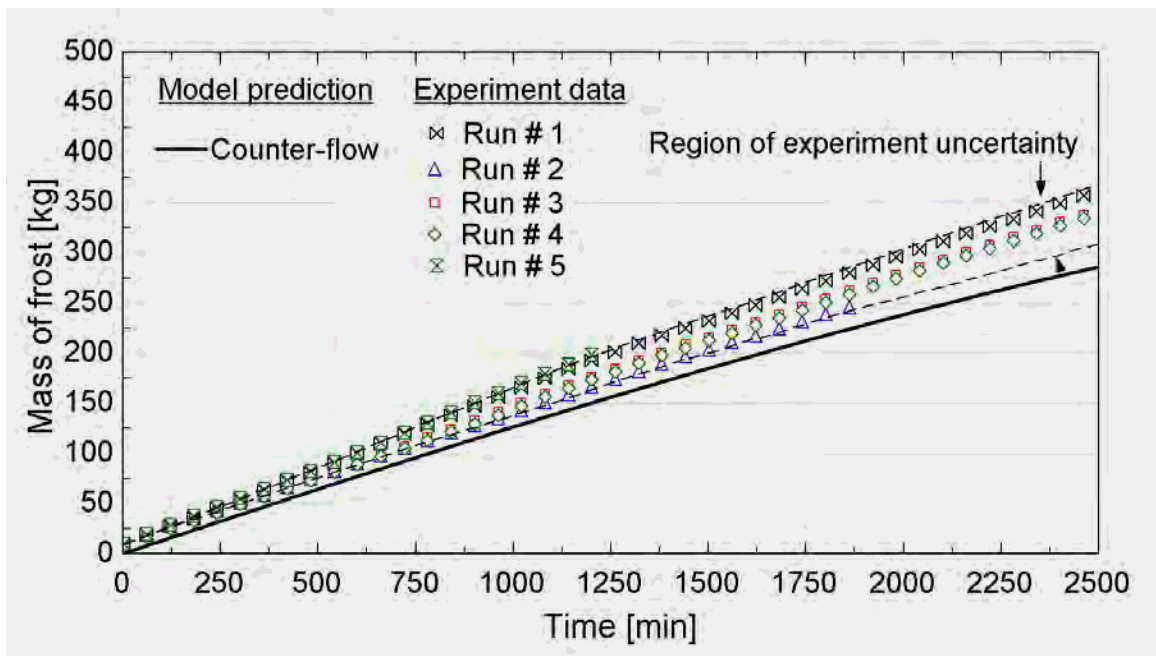


Figure 5.5 Comparison of the total mass of frost predicted by the counter-flow frost model and the total mass of frost obtained using the experimental data over time.

5.2 Effects of Lewis Number on the frost model prediction

To assess the sensitivity of the frost model to the value of the Lewis number, simulations were run using identical conditions but varying Lewis number between 0.85 and 1.0. The predicted frost accumulation rate, total mass of accumulated frost and the cooling capacity are compared in Figure 5.6 and Figure 5.7.

Figure 5.6 shows that as the Lewis number decreases, the frost accumulation rate will increase. Eventually, the high rate of frost accumulation leads to larger mass of accumulated frost and, as a consequence, a higher pressure drop and lower air velocity. Figure 5.6 shows that at some point during the simulation, the frost accumulation rate predicted using a Lewis number of 0.85 will drop faster than for a Lewis number of 1.0. These effects balance and cause the total mass of the accumulated frost at the end of the simulation for Lewis numbers between 0.85 and 1.0 to be nearly the same. However the frost distribution across the evaporator coil is not the same. The accumulated frost is more concentrated in the first few rows for the smaller value of Lewis number and therefore the air velocity drops faster for the Lewis number of 0.85 as compared to 1.0. The cooling coil capacity prediction is therefore slightly higher for the larger Lewis number, as shown in Figure 5.7.

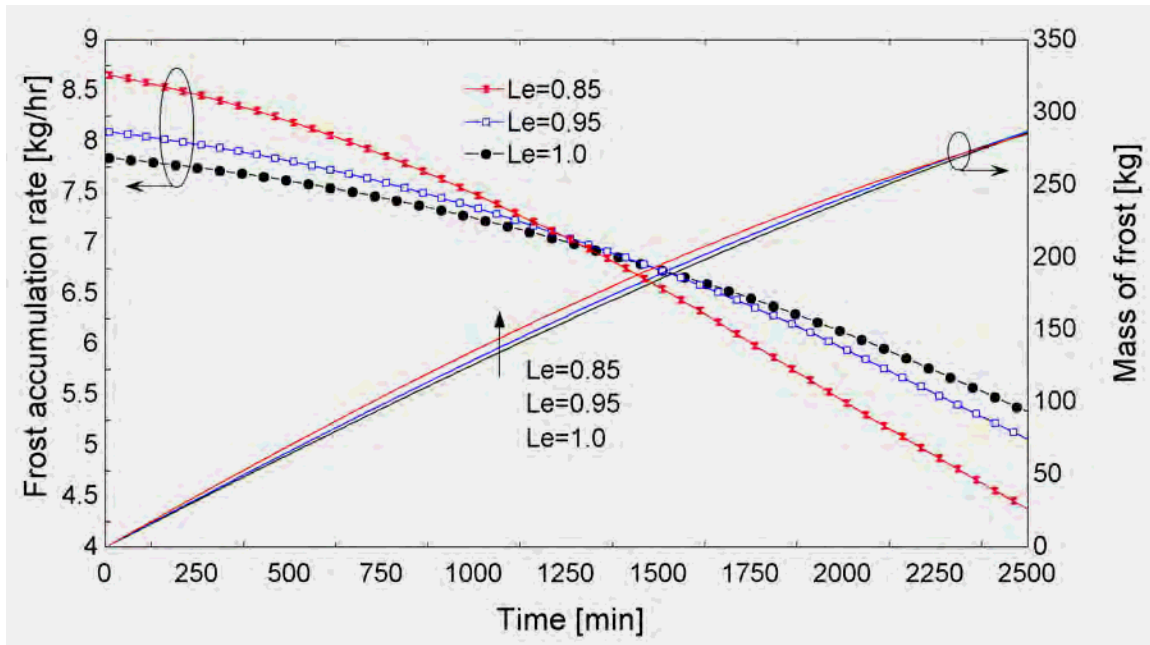


Figure 5.6 Frost accumulation rate and the total mass for accumulated frost over time for three different Lewis numbers

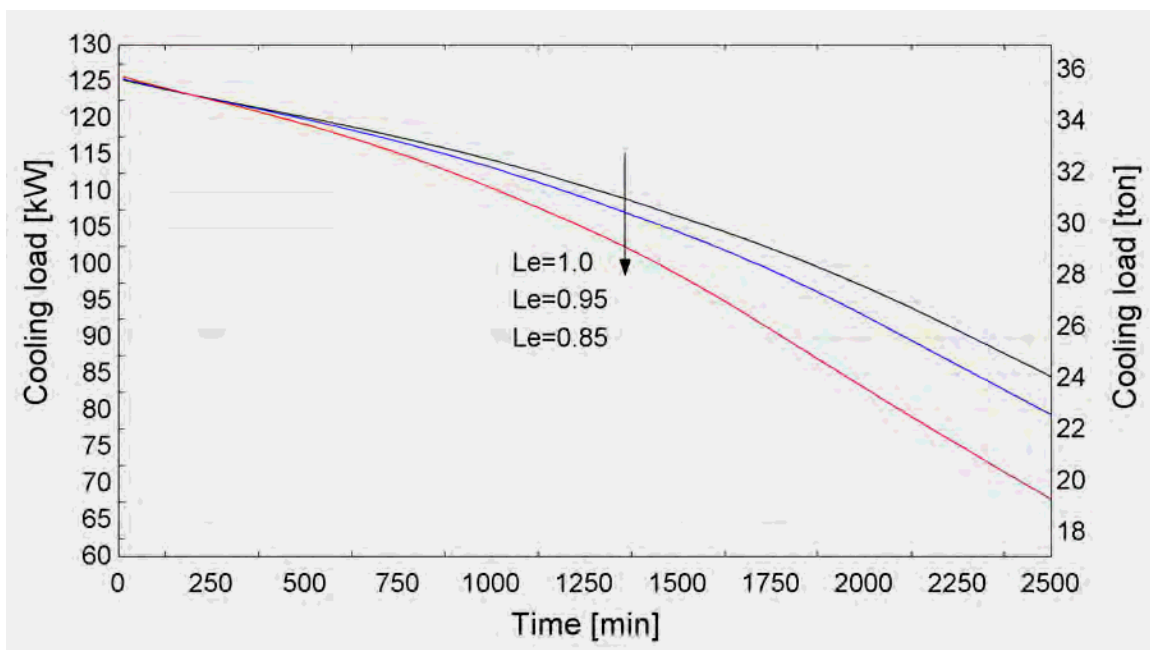
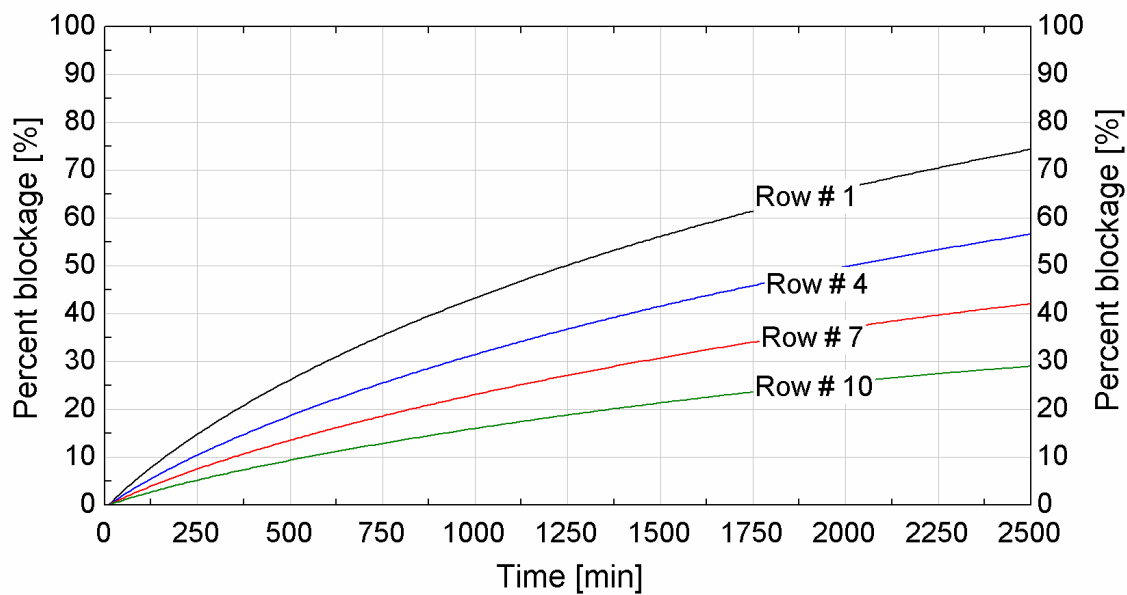
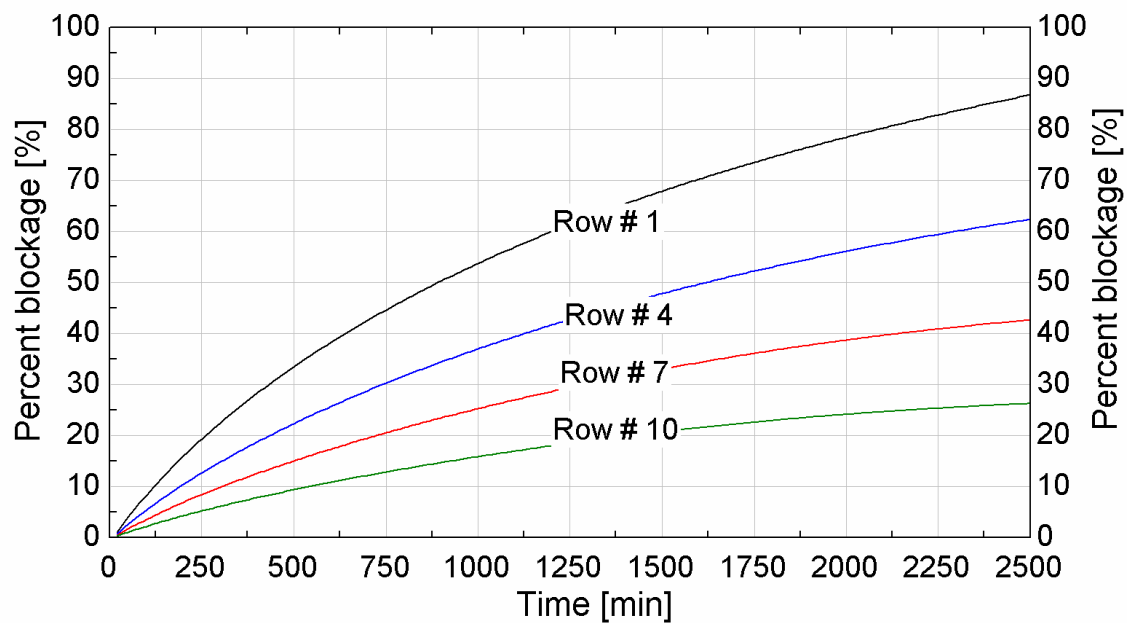


Figure 5.7 Cooling coil capacity prediction of the frost model for three different Lewis numbers.



(a)



(b)

Figure 5.8 Percentage of the blockage of the air path caused by frost accumulation at different rows of the evaporator coil over time for (a) Lewis number of 1.0 and (b) Lewis number of 0.85.

5.3 Summary

A theoretical model of a counter-flow circuiting liquid ammonia overfeed evaporator coil subjected to frost accumulation has been developed and validated. The model predictions agreed with the experimental data in terms of air flow rate, exit air temperature, evaporator cooling capacity and the total mass of accumulated frost.

Also, the model showed that the frost distribution across counter-flow circuiting evaporators is not uniform; more frost tends to accumulate in the first few rows that are exposed to the incoming air than in the last rows. This prediction is in agreement with observations by Kondepudi et al (1993) and Yao et al. (2004). This concentration of the frost build up causes the flow resistance of the evaporator to increase rapidly which results in a corresponding, large reduction in the flow rate of air and refrigeration capacity.

5.4 References

Kondepudi, S. and D. O'Neal., 1993, "*Performance of Finned-Tube Heat Exchangers Under Frosting Conditions: I. Simulation Model, and II. Comparison of Experimental Data with Model.*" International Journal of Refrigeration, Vol. 16, No.3.

Malhammar, A., 1988, "*Monitoring frost growth in evaporators is a complex process.*" The Australian institute of refrigeration, air conditioning and heating, Vol,2

Malhammar, A., 1986, "*Frostpaslag via flansade ytor.*" Doktorsav handling, Kungliga Tekniska Hogskolan, Stockholm, Sweden.

Yao, Y., Y. Jiang, S. Deng, and Z. Ma., 2004, "*A study on the performance of the airside heat exchanger under frosting in an air source heat pump water heater/chiller unit.*" International Journal of Heat and Mass Transfer, Vol. 47

Chapter 6 Defrost Model

A detailed, physical model of the Hot Gas Defrost Process (HGDP) is extremely difficult to generate due to the complex and transient nature of the process. The HGDP is at least somewhat stochastic; during the hot gas defrost, the frost on the evaporator coil does not melt uniformly through the entire evaporator coil surfaces. In fact the frost does not melt uniformly even along one tube of the evaporator coil. It has been experimentally observed that while the frost might remain attached over some portions of the coil until it is completely melted or sublimates, in other parts of the coil the frost will partially melt and then detach from the coil surface and fall either onto a lower tube or into hot drain pan.

The thermal properties of frost vary considerably during the HGDP depending on the location of the frost; however, the total mass and heat capacity of the mixture of frost and water that remains on the coil surface will continuously decrease due to the combined action of gravity, melting, and sublimation. The melting process will lead to the development of air channels at random locations, exposing the evaporator metal surfaces to the surrounding air; therefore, the total mass and heat capacity of the frost may locally increase at some locations due to the diffusive and convective transport of the water that has melted at other locations.

The free-convection heat transfer between the coil and frost surfaces and the air will vary with location, geometric orientation of the coil, frost thickness and other effects such as air currents that might result from the action of other evaporator fans or the opening of

freezer doors. The mass flow rate and state of the hot gas flowing through each circuit of a multi-circuit coil may also vary substantially.

Clearly a complete model of the HGDP is not feasible; certainly such a model would ultimately be so computationally intensive as to be useless for an optimization of the process. Fortunately, a very detailed model is also not necessary to meet the objectives of this work. The objective of the theoretical model is not a detailed simulation of the microscopic mechanisms associated with the HGDP; rather, the required outputs of the model include the time required for substantially complete frost removal and the associated rate of the parasitic heat load. These two outputs must be predicted to within an acceptable level of accuracy using a physics-based model. This chapter discusses the development of a 1st order model of the HGDP that includes most of the important physics without focusing on the micro-scale details; therefore, the model requires some calibration against experimental data in order to be predictive. Given the difficulties discussed above, this technique seems most appropriate.

6.1 Model development:

A liquid overfed evaporator coil consisting of multiple rows of frosted finned tubes with a number of refrigerant circuits is considered (Figure 6.1). The model is formulated for a single refrigerant circuit (Figure 6.2) that is assumed to be representative of the remaining circuits in the coil (i.e. uniform flow of refrigerant to each individual circuit).

An individual evaporator circuit is divided into a number of sections equal to the total number of coil rows in the flow direction (Figure 6.3). Because the circuiting of the coil includes two passes for each row, each section is modeled as a single tube with length

that is twice the length of the individual evaporator coil tubes. This results in a total number of tubes that is equal to the total number of evaporator coil rows.

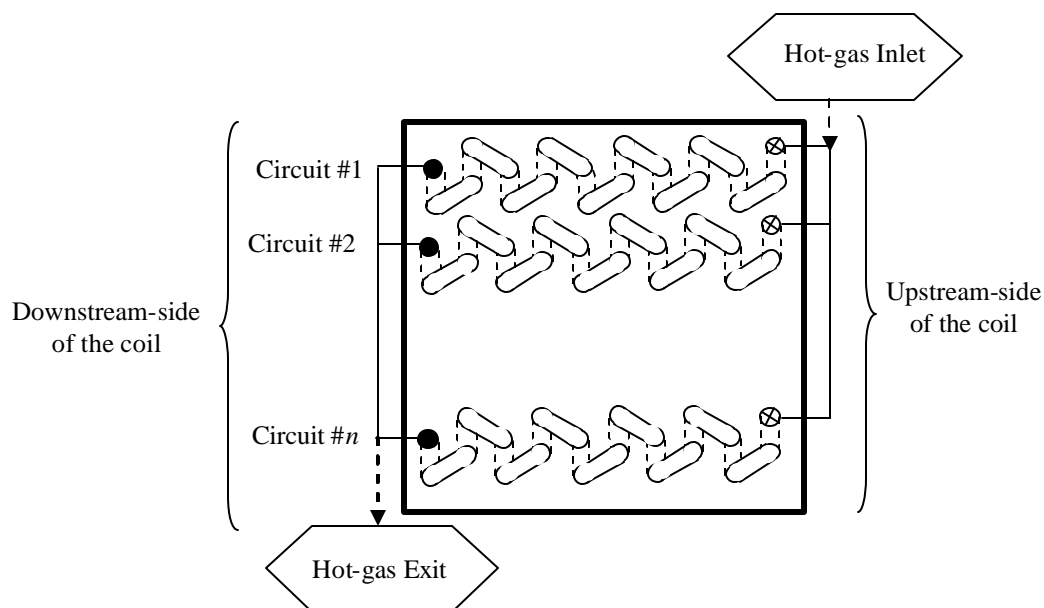


Figure 6.1 Schematic of the evaporator coil with multiple rows of finned tubes with multiple refrigerant circuits and the direction of the hot-gas flow.

The air-side heat transfer surfaces of the evaporator coil are rectangular plate fins that are modeled as equivalent circular fins, each attached to a tube (Figure 6.4, Schmidt (1949)). The frost properties (density and thermal conductivity) are assumed to be constant throughout the hot-gas defrost process. The frost density and thermal conductivity as well as the initial frost thickness for each section is obtained from the frost numerical model discussed in the previous chapter. Note that the frost thickness and thermal properties are assumed to be uniform along each tube in any section, but they do vary from one row to the next as the frost builds non-uniformly in the air-flow direction. Therefore, the computational domain, effectively, includes only one frosted fin with its associated frosted tube for each evaporator coil row (Figure 6.5); the other fins in the row

are assumed to behave identically to the modeled fin (i.e. uniform frost growth and melt across the coil face).

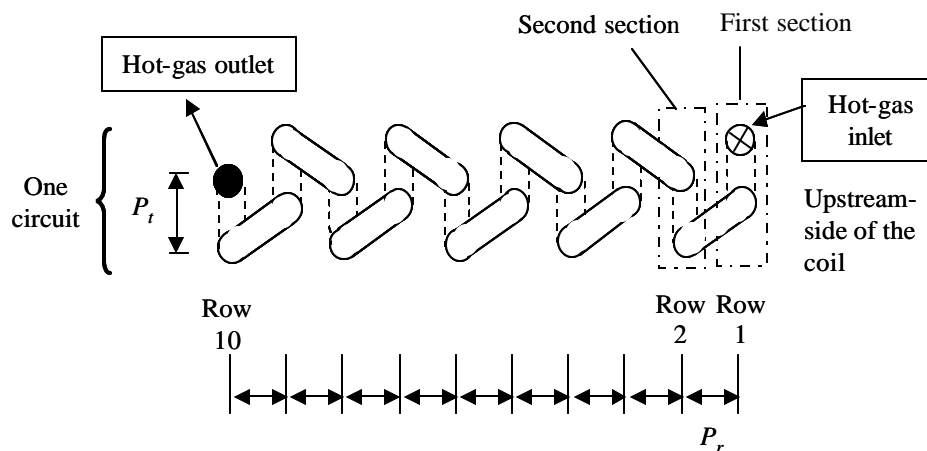


Figure 6.2 Schematic of one evaporator coil circuit and the direction of the hot-gas flow.

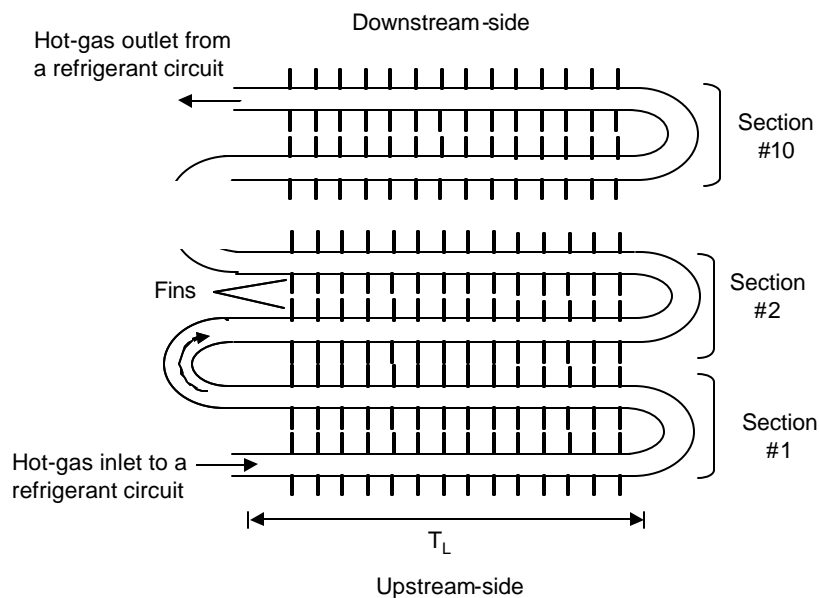


Figure 6.3 Schematic of the first, the second and the last evaporator coil sections as well as the direction of the hot-gas flow.

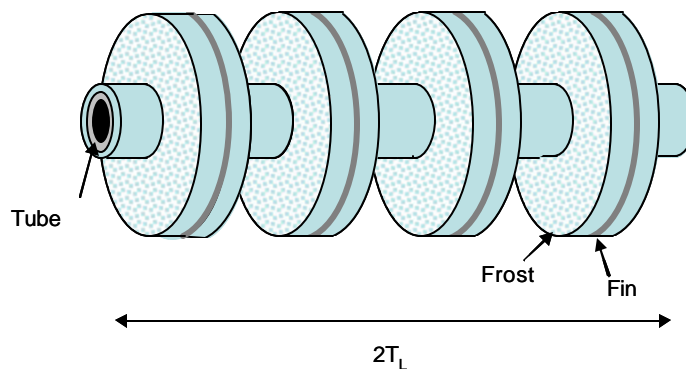


Figure 6.4 Schematic of the frosted tube and the equivalent circular fins

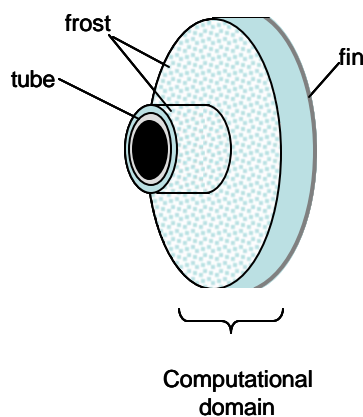


Figure 6.5 Schematic of the computational domain

The hot-gas defrost process for any given section is modeled as occurring in four separate stages as described below. It should be noted that, due to differences in the initial frost accumulation within each row (section) of the coil, different sections of the evaporator will progress through these stages at different times during the overall defrost cycle.

1. The pre-heating stage: is the process of raising the coil and accumulated frost from its initial temperature to the triple point temperature of the frost. During the pre-heating stage, the frost thickness is assumed to be constant while the frost temperature rises.

2. The melting stage: includes the actual phase change processes (melting, evaporation and sublimation). During this stage, the frost temperature is assumed to be constant (and equal to the triple point temperature) while the frost thickness is reduced as thermal energy from condensing refrigerant inside the tubes is transferred to the frost through the tube walls and fins.
3. The dry-heating stage: is the process of convectively heating the surrounding environment through the evaporator coil after all frost has melted.
4. The bleeding stage: is the final stage of the hot-gas defrost process in which the hot-gas supply to the coil is terminated and the coil pressure reduced (i.e., bled off) before the cold refrigerant is allowed to resume to its normal flow.

The computational domain is divided into four main parts (fin, tube, fin-frost and tube-frost) as shown in Figure 6.6. During the hot-gas defrost process, the frost accumulated on both the fin and tube surfaces at any section will pass through the first two defrost stages (i.e., the pre-heating and the melting stages) at different times. Also, as previously mentioned, the fin-frost or the tube-frost at any particular section will pass through the different defrost stages at different times from the frost located in other stages.

The model is designed to simulate the hot-gas defrost of a penthouse mounted evaporator coil or a ceiling hung evaporator. For the case of the penthouse evaporator coil, three additional features must be considered. These include the heat capacity of the penthouse wall material, the heat capacity of the air that is confined in the penthouse enclosure, and the infiltration rate of air between the penthouse and the adjoining freezer

space. For the ceiling hung evaporator case, the freezer air is modeled as a large (infinite) sink for both dry bulb temperature and moisture. This is accomplished by setting a constant freezer air dry bulb temperature and humidity ratio throughout the hot-gas defrost cycle regardless of the amount heat or mass is transferred to the freezer space. The term “air” that is used in this chapter refers to the freezer air in the case of the ceiling-hung evaporator whereas in the case of the penthouse evaporator it refers to the air locally confined in the penthouse unit itself. In either case, the “air” is interacting with the evaporator coils and receives both heat (convective thermal energy) and mass (moisture) given off by the fins and tubes during the defrost process.

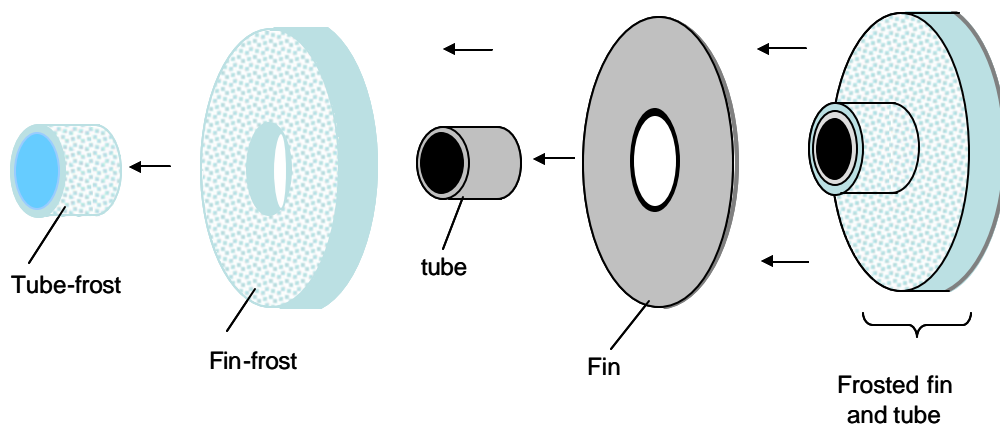


Figure 6.6 Schematic of the four lumped capacities that together represent the computational domain.

6.2 Heat and Mass Transfer Equations

6.2.1 Energy balance on the evaporator coil tubes:

Figure 6.7 shows a control volume associated with the evaporator coil tube during a hot-gas defrost process. Figure 6.7 also shows the heat transfer rates to and from the coil tube control volume during each of the four hot-gas defrost stages; the imbalance in these heat transfer rates is manifested as an energy storage in the tube (not shown).

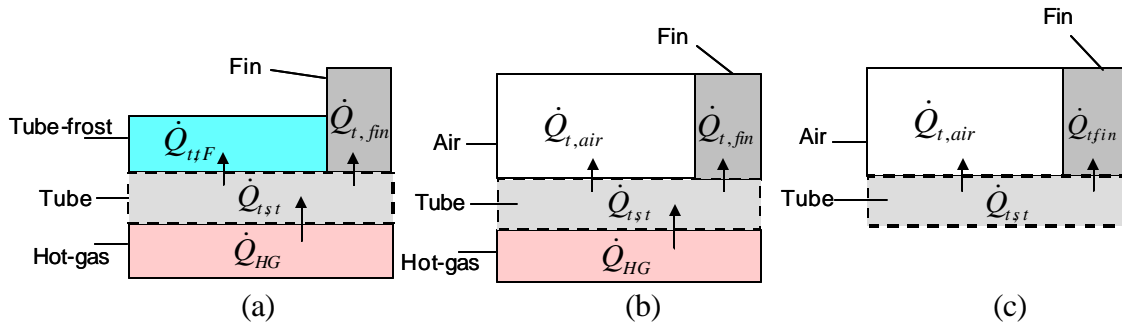


Figure 6.7 Schematic showing the sensible heat transfer rates to and from the evaporator coil tubes during the hot-gas process; a) pre-heating and melting stages, b) dry heating stage, c) bleeding stage.

During the preheating and the melting stages, some of the heat transferred from the condensing hot-gas to the tube (\dot{Q}_{HG}) will be stored in the tube and result in an increase in the tube temperature (T_t). The rest of the energy transferred from the hot-gas will be transferred from the tube to the frost accumulated on the tube surface (\dot{Q}_{tF} i.e., the portion of the frost that is covering only the part of the tube between adjacent fins) and the tube-fins (\dot{Q}_{tfin}). The energy equation for the tube balances the heat absorbed by the tube with that transferred away from the tube against heat transfer from the hot-gas during the pre-heating and the melting stages, Figure 6.7(a):

$$m_t C_t \frac{\partial T_t}{\partial t} = \dot{Q}_{HG} + \dot{Q}_{tF} + \dot{Q}_{t,fin} \quad (6.1)$$

where m_t and C_t are the total mass and specific heat capacity of the bare metal tube at any section, respectively. The variable \dot{Q}_{HG} represents the heat transfer rate from the hot-gas to the tube metal and is calculated as:

$$\dot{Q}_{HG} = \frac{A_{is} (T_{HG} - T_t)}{R_{f,HG} + (h_{HG})^{-1}} \quad (6.2)$$

where A_s is the inside surface area of the section tube, $R_{f, HG}$ is a fouling factor at the hot-gas side, and T_{HG} and h_{HG} are the temperature of the hot gas and the convective heat transfer coefficient between the hot-gas and the internal surface of the tube, respectively.

The fouling factor on the hot-gas side used in the current defrost model is the same as fouling factor used for the refrigerant side in the previously discussed frost model:

$$R_{f, HG} = 3.5 \times 10^{-4} \frac{\text{m}^2 \text{ K}}{\text{W}} \quad (6.3)$$

During a typical hot-gas defrost process the hot-gas supplied to the evaporator coil is in a slightly superheated state while the hot gas leaving the evaporator coil is in either a liquid or two-phase state with a quality that depends significantly on heat given up during the migration of refrigerant vapor through the coil. The total heat given up by the hot gas will depend on the coil temperature which is a function of the amount of frost and condensed water that is adhered to the coil at any instant time; therefore, neither the hot-gas temperature or the hot-gas convective heat transfer coefficient will be constant (either in space or time) throughout the hot gas process. However, according to Zurcher et al. (2001), the maximum two-phase heat transfer coefficient for ammonia at a low mass flux lies between 2,000 and 4,000 W/m²-K. Since the hot-gas mass flux is expected to be relatively low (due to the presence of a defrost relief regulator), the current model assumes a constant hot-gas convective heat transfer coefficient that lies in the middle of this range:

$$h_{HG} = 3000 \frac{\text{W m}^2}{\text{K}} \quad (6.4)$$

The heat transfer rate from the tube metal to the tube-frost, \dot{Q}_{tF} shown in Eq. (6.1), is calculated according to:

$$\dot{Q}_{tF} = \frac{A_{tF} (T_{tF} - T_t)}{R_{f,air} + R_{c,F} + \frac{d_{tF}}{k_F}} \quad (6.5)$$

where A_{tF} is the total internal surface area of the tube-frost at any section, $R_{f,air}$ is the fouling factor on the outer surface of the tube, T_{tF} is the temperature of tube-frost, d_{tF} is the thickness of the tube-frost, k_F is the thermal conductivity of the frost (which is assumed to be constant throughout the defrost process), and $R_{c,F}$ is a contact resistance between the frost layer and the tube.

The value of the external surface fouling factor (on the air side) that is used in the defrost model is the same as the air-side fouling factor used in the previously discussed frost model:

$$R_{f,air} = 3.5 \times 10^{-4} \frac{\text{m}^2\text{K}}{\text{W}} \quad (6.6)$$

Al-Mutawa et al. (1997) define a pre-melting stage which occurs prior to the previously described melting stage; they state that “during the pre-melting stage, the temperature of the frost layer touching the outside surface of the evaporator tubes rises to the triple point temperature as soon as the hot-gas defrost process is initiated (on the order of 10^{-3} seconds)”. This rapid temperature rise causes a very thin frost layer to melt almost instantaneously; thereby, establishing a thin layer of air and water mixture between the evaporator metal surfaces and the frost layer. The presence of this air/water interface results in an additional thermal resistance. The contact resistance ($R_{c,F}$) shown in Eq.(6.5) provides a mechanism for simulating the thermal resistance associated with the pre-melted frost:

$$R_{c,F} = 3 \times 10^{-2} \frac{\text{m}^2 \text{K}}{\text{W}} \quad (6.7)$$

Note that the value used for the contact resistance shown in Eq.(6.7) is found to provide the best fit the experimental data (described in a subsequent chapter).

The heat transfer rate between the tube metal and the attached fins, ($\dot{Q}_{t,fin}$) in Eq.(6.1), is calculated according to:

$$\dot{Q}_{t,fin} = \frac{(T_{fin} - T_t)}{\frac{R_{c,fin}}{A_{c,fin}} + \frac{\ln(\bar{r}/r_o)}{2p N_{fin} F_{thk} k_{fin}}} \quad (6.8)$$

where $A_{c,fin}$ is the total contact surface area between tube section and its associated fins, $R_{c,fin}$ is the thermal contact resistance, N_{fin} is the total number of fins at any section, F_{thk} and k_{fin} are the fin thickness and thermal conductivity, respectively, T_{fin} is the average fin temperature, r_o is the outer tube radius and \bar{r} is the mass average fin radius, defined as:

$$\bar{r} = \sqrt{\frac{r_o^2 + r_{fin}^2}{2}} \quad (6.9)$$

Once all of the frost accumulated on the tube at any section is melted, the heat transfer between the tube and the tube-frost will be eliminated and replaced with $\dot{Q}_{t,air}$, which is the heat transfer rate between the tube and the air (i.e., the dry-heating stage is initiated as shown in Figure 6.7(b)). The energy equation in the dry-heating stage balances the heat transfer from the hot-gas and the heat transfer carried away from the tube to the air:

$$m_t C_t \frac{\partial T_t}{\partial t} = \dot{Q}_{HG} + \dot{Q}_{air} + \dot{Q}_{t,fin} \quad (6.10)$$

$$\dot{Q}_{tair} = \frac{A_{os} (T_{air} - T_t)}{R_{f,air} + (h_{t,air})^{-1}} \quad (6.11)$$

where A_{os} is the total outer surface area of the tube at any section and $h_{t,air}$ is the convective heat transfer coefficient between the tube surface and the air (at temperature T_{air}).

At the beginning of the defrost cycle, the frost thickness varies from row to row because the frost builds non-uniformly in the air-flow direction. The thickness of the frost on both the tubes and fins will be greater on the entering air side of the coil when compared to the leaving air side of the coil, as show previously in Chapter 5. Therefore during the few first minutes of the defrost cycle, the viscous force on the air between the evaporator fins and tubes is much higher than the buoyancy force, especially at the first few rows since the distance between any two fins is much less than diameter of the fins (i.e. $(W/H) < 1$, Figure 6.8). As a result, the heat transfer from the evaporator coil metal and frost surfaces to the air at these few rows is likely to initially occur by conduction; this may transition to free convection when the frost on the fins begin to melt so that the distance between the fins increases. The heat transfer from the evaporator coil metal and frost surfaces to the air in the last few rows is likely to be characterized as free convection throughout the process due to the small frost thickness. Also, most of the ceiling-hung and penthouse evaporator coils are covered along the top and the sides in order to force the air to flow from the face of the coil to the opposite side during the cooling mode; therefore, the convective air currents must include at least some component that is perpendicular to gravity (see Figure 6.9). The flow cannot simply enter from the bottom and rise as it is heated through the top.

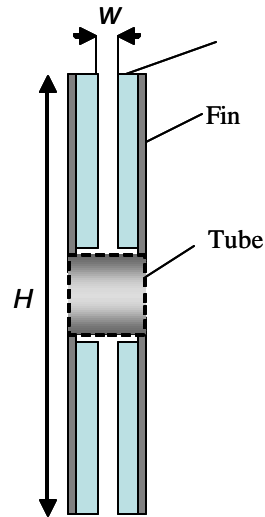


Figure 6.8 Conduction heat transfer from the evaporator coil metal and frost surfaces to the air.

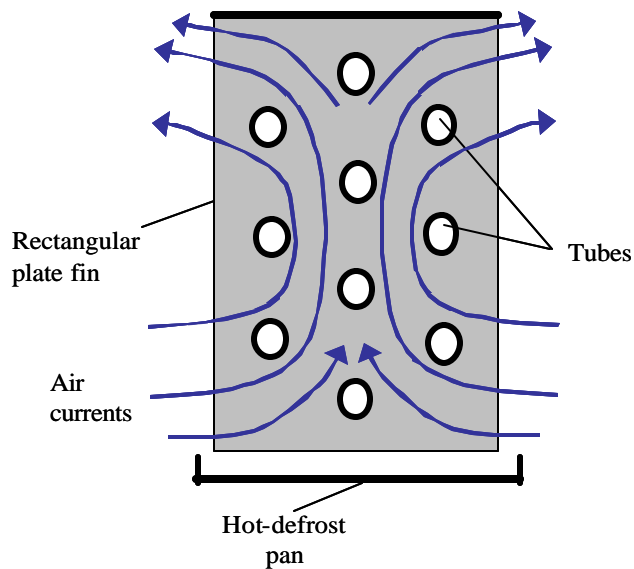


Figure 6.9 Convection heat transfer from the evaporator coil metal and frost surfaces to the air.

Unfortunately, empirical correlations for free convection within an evaporator coil under these conditions could not be found; this is likely because the normal operation of an evaporator coil is under forced flow conditions. Therefore a constant average Nusselt number (\overline{Nu}) is assumed to characterize the free convection process that occurs throughout the defrost cycle. The average Nusselt number provides one of the adjustable

parameters that is varied to achieve an adequate match between the simple HGDP model predictions and the experimental data. An average Nusselt number of 2.5 was found to provide the best fit; note that this Nusselt number is physically reasonable as it is likely that the free convection is dominated by conduction and fluid motion is not large.

The convection heat transfer coefficient is

$$h_{t,air} = \frac{\overline{Nu} k_{air}}{2r_o} \quad (6.12)$$

Once the hot-gas supply is eliminated (i.e., the bleed off stage is initiated as shown in Figure 6.7(c)), the temperature of the evaporator tubes and fins will begin to decrease due to the stoppage of supplied energy (hot gas) and coincident heat loss to the surrounding air. A control volume around the evaporator coil tube at any section during the bleeding stage yields:

$$m_t C_t \frac{\partial T_t}{\partial t} = \dot{Q}_{t,air} + \dot{Q}_{t,fin} \quad (6.13)$$

6.2.2 Energy balance on the evaporator coil fins:

Figure 6.10 shows a control volume around an evaporator coil fin during the hot-gas defrost process and indicates the heat transfer rates to and from this control volume during each of the four hot-gas defrost stages.

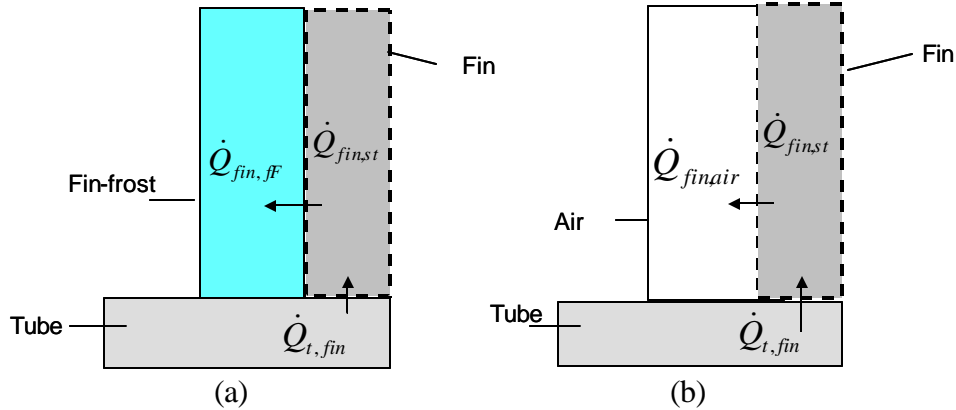


Figure 6.10 Schematic showing the sensible heat transfer rates to and from the evaporator coil fins during the hot-gas process; a) pre-heating and melting stages, b) dry heating and bleeding stages.

During the preheating and the melting stages, some of the energy transferred from the tube to the fins will be stored in the fin material and result in an increase in the fin temperature, while the remaining energy will be transferred from the fins to the frost. An energy balance on the control volume around the fins during the pre-heating and melting stages, Figure 6.10(a), provides:

$$m_{fin} C_{fin} \frac{\partial T_{fin}}{\partial t} = -\dot{Q}_{t,fin} + \dot{Q}_{fin,ff} \quad (6.14)$$

where m_{fin} is the total mass of the fin material, C_{fin} is the specific heat capacity of the fin material, $\dot{Q}_{fin,ff}$ is the sensible heat transfer rate from the tube to the fin-frost which is calculated according to:

$$\dot{Q}_{fin,ff} = \frac{A_{fin} N_{fin} (T_{ff} - T_{fin})}{R_{c,F} + \frac{d_{ff}}{k_F}} \quad (6.15)$$

where A_{fin} is the total surface area of both sides of the fin, T_{ff} is the temperature of fin-frost, and d_{ff} is the thickness of the fin-frost layer.

Once all of the frost accumulated on the fins at any section has been completely melted (i.e., the dry-heating and bleeding stages have been initiated, Figure 6.10(b)), the heat transfer between the fins to the fin-frost is eliminated and replaced with \dot{Q}_{finair} , which represents the heat transferred from the fin to the surrounding air. A control volume around the fin during the dry-heating and bleeding stages yields:

$$m_{fin} C_{fin} \frac{\partial T_{fin}}{\partial t} = -\dot{Q}_{t,fin} + \dot{Q}_{finair} \quad (6.16)$$

$$\dot{Q}_{finair} = h_{finair} A_{fin} N_{fin} (T_{air} - T_{fin}) \quad (6.17)$$

where h_{finair} is the convective heat transfer coefficient from the fin surface to the air:

$$h_{finair} = \frac{\overline{Nu} k_{air}}{2r_{fin}} \quad (6.18)$$

where \overline{Nu} is the same average Nusselt number used previously in eq. (6.12)

6.2.3 Energy balance on the evaporator coil tube-frost:

Figure 6.11 shows a control volume around the tube-frost during the hot-gas defrost process and indicates both the sensible and latent heat transfer rates to and from the control volume during the pre-melting and the melting stages of the hot-gas defrost process.

Figure 6.12 shows the frost layer temperature versus enthalpy; notice that during the pre-melting stage the frost layer temperature increases as energy is stored (i.e., as enthalpy increases) until the frost layer temperature reaches the triple point temperature at which point enthalpy will increase independently of temperature as is typical in a phase-

change process. This occurs until the phase change is completed and the frost enthalpy is increased by the enthalpy of fusion. Therefore, during the pre-heating stage the model is formulated so that all of the energy stored in the frost results only in an increase in the enthalpy and temperature of the entire frost and the frost layer thickness and volume remain constant. As a consequence, only sensible heat transfer from the frost layer to the air is considered during the pre-heating stage (no evaporation or sublimation mechanisms are considered during this state of the defrost process).

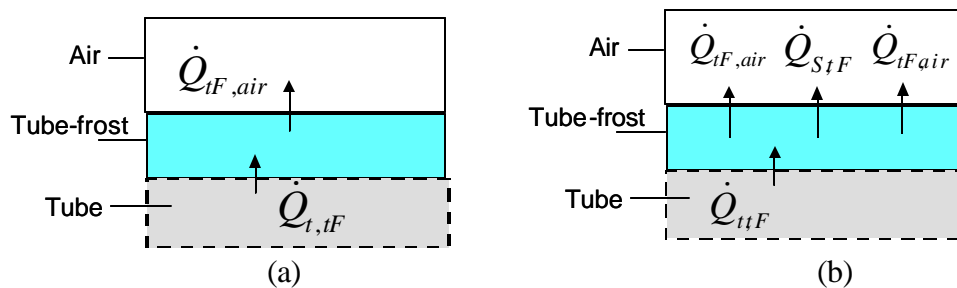


Figure 6.11 Schematic showing the sensible heat and the latent heat transfer rates to and from the tube-frost during the hot-gas process; a) pre-heating stage, b) melting stage

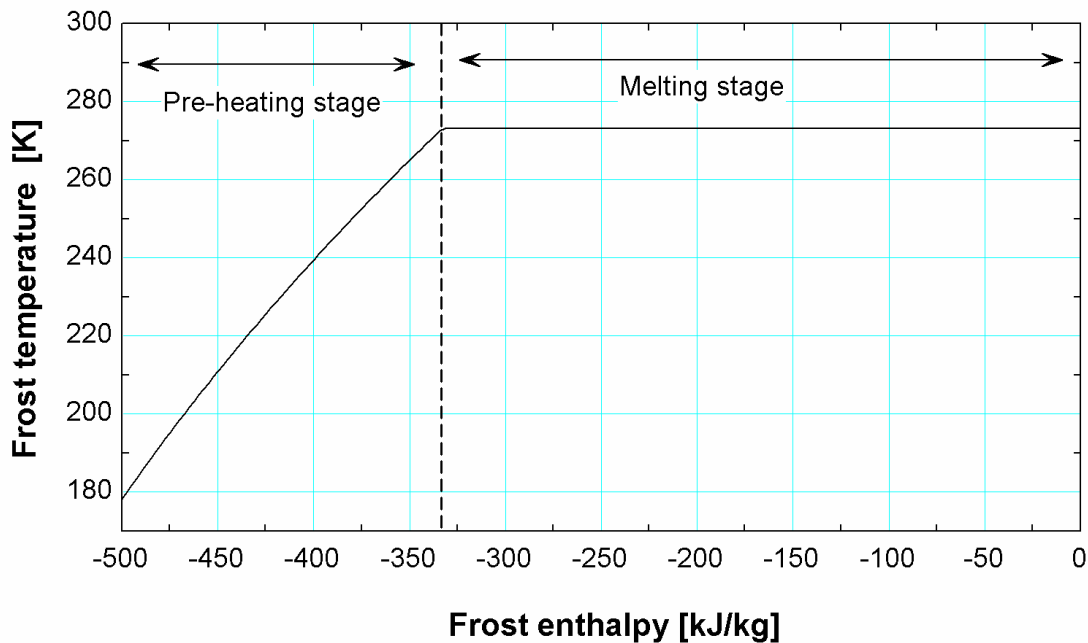


Figure 6.12 The variation in the frost temperature as a function of the frost enthalpy.

During the pre-heating stage, the energy equation balances the sensible heat transfer from the evaporator tubes and the heat transfer transferred from the tube-frost to the air:

$$V_{tF} \mathbf{r}_F \frac{di_{tF}}{\partial t} = -\dot{Q}_{tF} + \dot{Q}_{tFair} \quad (6.19)$$

where V_{tF} is the total volume of the tube-frost at any section, \mathbf{r}_F is the frost density (again, the density is assumed to be constant throughout the hot-gas defrost process and equal to the initial value of the frost density which is characteristic of the frost formation process), i_{tF} is the tube-frost enthalpy and \dot{Q}_{tFair} is the sensible heat transfer between the tube-frost layer and the air.

The sensible heat transfer between the tube-frost layer and the air (\dot{Q}_{tFair}) is calculated according to:

$$\dot{Q}_{tFair} = A_{tF} h_{tFair} (T_{air} - T_{tF}) \quad (6.20)$$

where h_{tFair} is the convective heat transfer coefficient between the tube-frost surface and the air:

$$h_{tFair} = \frac{\overline{Nu} k_{air}}{2(r_o + \mathbf{d}_{tF})} \quad (6.21)$$

Referring back to Figure 6.12, it can be seen that as soon as the frost enthalpy reaches a value of -333 kJ/kg, the phase-change process begins and the frost temperature thereafter remains constant at the triple point temperature. The frost is modeled as a lumped capacitance and therefore the enthalpy gradient in the frost is neglected; the accumulated frost will actually melt gradually rather than all at once. In the defrost model, it is assumed that during the melting stage, the specific enthalpy of the frost will

remain constant and therefore any energy storage in the frost layer will manifest itself as a reduction in the thickness of the frost layer accompanied by the removal of an equivalent amount of energy corresponding to liquid water. The frost thickness will continue to decrease until it reaches zero which signifies the end of the melting stage.

An energy balance on the control volume around the tube-frost during the melting stage (Figure 6.11(b)) leads to:

$$A_{tF} r_F i_{sf} \frac{\partial d_{tF}}{\partial t} = -\dot{Q}_{tF} + \dot{Q}_{tF,air} + \dot{Q}_{S,tF} + \dot{Q}_{E,tF} \quad (6.22)$$

where i_{sf} is the enthalpy of fusion (i.e., the enthalpy difference between liquid and ice), and $\dot{Q}_{S,tF}$ and $\dot{Q}_{E,tF}$ are the latent heat transfer rates due to sublimation and evaporation, respectively. Note that both the sublimation and the evaporation latent heats are assumed to occur simultaneously as suggested by Al-Mutawa et al. (1998).

The latent heat rates due to evaporation and sublimation of the tube-frost ($\dot{Q}_{S,tF}$ and $\dot{Q}_{E,tF}$) are calculated using Eqs.(6.23) and (6.24), respectively:

$$\dot{Q}_{S,tF} = h_{m,tF} A_{tF} i_S (\mathbf{w}_{air} - \mathbf{w}_{tF}) \quad (6.23)$$

$$\dot{Q}_{E,tF} = h_{m,tF} A_{tF} i_E (\mathbf{w}_{air} - \mathbf{w}_{tF}) \quad (6.24)$$

where i_S is the latent heat of sublimation (2834 kJ/kg), i_E is the latent heat of fusion (2501 kJ/kg), \mathbf{w}_{air} and \mathbf{w}_{tF} are the specific humidity of the air and the saturated specific humidity of the frost layer surface, respectively, and $h_{m,tF}$ is the mass transfer coefficient which is assumed to be equal for both evaporation and sublimation mechanisms. The mass transfer coefficient is calculated according to Threlkeld (1970).

$$h_{mtF} = \frac{h_{tFair}}{cp_{air}Le} \quad (6.25)$$

where (Le) is the Lewis number and (cp_{air}) is the specific heat of air. Lewis number is assumed to be 1.0 to be consistence with the previously described frost model.

6.2.4 Energy balance on the evaporator fin-frost:

Figure 6.13 shows a control volume around the fin-frost during hot-gas defrost process and indicates the sensible and latent heat transfer rates to and from the control volume during the pre-heating and the melting stages of the hot-gas defrost process. The same assumptions that were used to model the behavior of the tube-frost are again used in modeling the behavior of the fin-frost; the fin-frost is assumed to experience a temperature and enthalpy increase during the pre-heating process without any sublimation or evaporation (and therefore at a constant volume) and during the melting stage the temperature of the frost is assumed to remain and constant equal to the triple point temperature while the fin-frost layer thickness is reduced in response to the energy storage. The process continues until the thickness of the frost layer reaches zero which indicates the end of the melting stage.

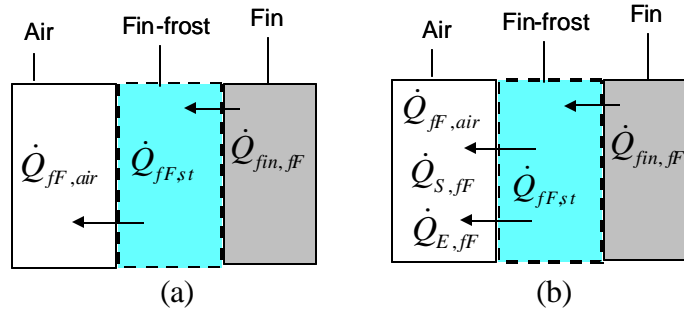


Figure 6.13 Schematic diagram showing the sensible heat and the latent heat transfer rates to and from the fin-frost during the hot-gas process; a) pre-heating stage, b) melting stage.

An energy balance on the control volume around the fin-frost during the pre-melting stage, Figure 6.13(a), gives:

$$V_{fF} \mathbf{r}_F \frac{di_{fF}}{\partial t} = -\dot{Q}_{fin,fF} + \dot{Q}_{fFair} \quad (6.26)$$

where V_{fF} is the total volume of the fin-frost at any section, i_{fF} is the enthalpy of fusion of the fin-frost, and \dot{Q}_{fFair} is the sensible heat transfer rate between the fin-frost layer and the air; calculated according to:

$$\dot{Q}_{fFair} = A_{fF} h_{fFair} N_{fin} (T_{air} - T_{fF}) \quad (6.27)$$

where h_{fFair} is the convective heat transfer coefficient between the fin-frost surface and the air:

$$h_{fFair} = \frac{\overline{Nu} k_{air}}{2r_{fin}} \quad (6.28)$$

The energy balance on the control volume around the fin-frost during the melting stage is formulated as:

$$A_{fF} \mathbf{r}_F i_{sf} \frac{\partial d_{fF}}{\partial t} = -\dot{Q}_{fin,fF} + \dot{Q}_{fFair} + \dot{Q}_{S,fF} + \dot{Q}_{E,fF} \quad (6.29)$$

The latent heat rates due to evaporation and sublimation of the fin-frost ($\dot{Q}_{S,tF}$ and $\dot{Q}_{E,tF}$) are calculated as shown in Eqs.(6.30) and, (6.31) respectively

$$\dot{Q}_{S,ff} = h_{m,ff} A_{ff} i_s (\mathbf{w}_{air} - \mathbf{w}_{ff}) \quad (6.30)$$

$$\dot{Q}_{E,ff} = h_{m,ff} A_{ff} i_E (\mathbf{w}_{air} - \mathbf{w}_{ff}) \quad (6.31)$$

where (\mathbf{w}_{ff}) is the saturated specific humidity of the fin-frost layer surface. $h_{m,ff}$ is the mass transfer coefficient from the fin-frost surface and it is assumed to be equal for both evaporation and sublimation mechanisms.

The fin-frost mass transfer coefficient is also calculated according to Threlkeld (1970) with a Lewis number equal to 1.0.

$$h_{m,ff} = \frac{h_{ffair}}{cp_{air} Le} \quad (6.32)$$

6.2.5 Energy balance on the penthouse walls and enclosed air :

In order to simulate a hot-gas defrost of an evaporator coil displaced in a penthouse enclosure, the heat capacities of the penthouse wall and the air enclosed in the penthouse must be considered in order to evaluate the latent and sensible parasitic heat loads that characterize the defrost process. An energy balance on a control volume around the penthouse wall (assuming that the walls are fully insulated externally) is the same for all four defrost stages:

$$m_p C_p \frac{\partial T_p}{\partial t} = \dot{Q}_{p,air} + \dot{Q}_{E,p} \quad (6.33)$$

where m_p , C_p and T_p are the total mass, specific heat capacity and the temperature of the penthouse metal wall, respectively, and $\dot{Q}_{p,air}$ and $\dot{Q}_{E,p}$ are the sensible and latent heat transfer rate between the enclosed air and the penthouse metal wall, respectively. The sensible and the latent heat transfer rates are calculated using Eqs. (6.34) and (6.35):

$$\dot{Q}_{p,air} = A_p h_{p,air} (T_{air} - T_p) \quad (6.34)$$

$$\dot{Q}_{E,p} = h_{m,p} A_p i_E (\mathbf{w}_{air} - \mathbf{w}_p) \quad (6.35)$$

where A_p and T_p are the total surface area and the temperature of the penthouse wall, which is assumed to be equal to the freezer-air temperature at the beginning of the simulation, \mathbf{w}_p is the saturated specific humidity at the wall temperature, and $h_{p,air}$ is the convective heat transfer coefficient with the wall:

$$h_{p,air} = \frac{k_{air} \overline{Nu}_{L,p}}{L_p} \quad (6.36)$$

where (L_p) is the height of the penthouse walls. $(\overline{Nu}_{L,p})$ is the average Nusselt number for vertical plate as suggested by Churchill et al. (1975):

$$\overline{Nu}_{L,p} = 0.68 + \frac{0.670 Ra_{L,p}^{1/4}}{\left[1 + (0.492/Pr)^{9/16}\right]^{4/9}} \quad Ra_{L,p} \leq 10^9 \quad (6.37)$$

where $(Ra_{L,p})$ is the Rayleigh number based on the penthouse wall height.

$$Ra_{L,p} = \frac{g \Pr (T_p - T_{air}) (L_p)^3}{\left[(T_{air} + T_p)/2\right] \mathbf{n}^2} \quad (6.38)$$

The mass transfer coefficient between the air and the penthouse wall in Eq. (6.35) is also calculated according to Threlkeld (1970) with a Lewis number equal to 1.0:

$$h_{m,p} = \frac{h_{p,air}}{cp_{air}Le} \quad (6.39)$$

Figure 6.14 shows a control volume around the penthouse-air and the sensible heat and latent heat transfer rates to and from the penthouse-air during hot-gas defrost process.

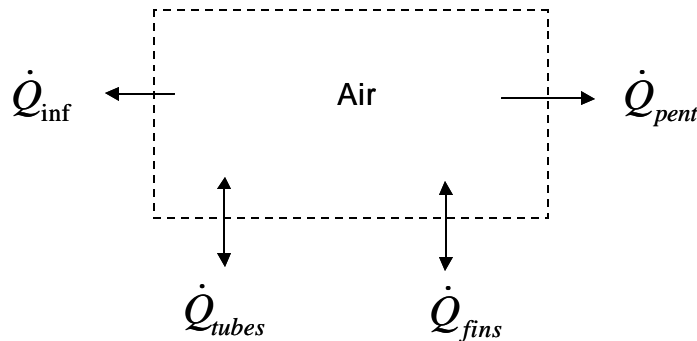


Figure 6.14 Schematic showing the sensible heat and the latent heat transfer rates to and from the penthouse-air during the four stages of the hot-gas process.

The energy equation balances the sensible and the latent heat transfer from/to the penthouse air during the hot-gas defrost process:

$$V_{air} \rho_{air} C_{air} \frac{\partial T_{air}}{\partial t} = \dot{Q}_{tubes} + \dot{Q}_{fins} + \dot{Q}_{pent} + \dot{Q}_{inf} \quad (6.40)$$

where \dot{Q}_{tubes} is the sum of all the sensible and the latent heat transfer between the penthouse-air and the evaporator coil tubes and tube-frost:

$$\dot{Q}_{tubes} = - \left[\sum_{i=1}^{N_{rows}} N_c \left(\dot{Q}_{tFair} + \dot{Q}_{StF} + \dot{Q}_{E,tF} + \dot{Q}_{i,air} \right)_i \right] \quad (6.41)$$

The term \dot{Q}_{fins} in Eq. (6.40) is the sum of all the sensible and the latent heat transfer that occurs between the penthouse-air and the evaporator coil fins and fin-frost:

$$\dot{Q}_{fins} = - \left[\sum_{i=1}^{N_{rows}} N_c \left(\dot{Q}_{fFair} + \dot{Q}_{S,FF} + \dot{Q}_{E,FF} + \dot{Q}_{finair} \right)_i \right] \quad (6.42)$$

where N_c is the number of the evaporator coil circuits.

The term \dot{Q}_{pent} is the sum of the sensible and the latent heat transfer from the penthouse-air to the penthouse-walls:

$$\dot{Q}_{pent} = - \left(\dot{Q}_{pAir} + \dot{Q}_{E,p} \right) \quad (6.43)$$

The increase in the penthouse-air temperature due to the hot-gas parasitic heat load results in a decrease in the penthouse-air density; therefore, the penthouse-air will tend to remain in the penthouse enclosure during the hot-gas defrost process, reducing air infiltration from the freezer space (i.e., the system is stable). However there are three main factors that may result in the transfer of energy associated with the hot-gas defrost parasitic heat load from the penthouse enclosure to the main freezer:

- the expansion or the increase in the penthouse-air volume due to its increased temperature,
- heat transfer by conduction between the penthouse-air and the freezer-air up-stream of the evaporator coil through the inlet air grate, and
- the pressure difference between the penthouse-air and the freezer-air induced by the air flow parallel to the inlet air grate to the penthouse caused by the other operating evaporator coils in the same freezer.

It is extremely difficult to quantify the individual contribution of each of the aforementioned factors and therefore it was decided to define the term \dot{Q}_{inf} in Eq. (6.40) as representing a total infiltration heat transfer rate:

$$\dot{Q}_{inf} = \dot{m}_{inf} \overline{Cp}_{air} \left(T_{frz} - T_{air} \right) \quad (6.44)$$

where T_{frz} is a constant freezer-air temperature, \overline{Cp}_{air} is the air specific heat calculated using average penthouse-air and freezer-air temperature, and \dot{m}_{inf} is the total infiltration mass flow rate.

An infiltration mass flow rate of 0.2 (kg/s) is found to provide the best fit the experimental data (described in a subsequent chapter).

6.3 Sensitivity Analysis

In order to evaluate to the sensitivity of the predicted results to the four experimentally fitted parameter (h_{HG} , $R_{c,F}$, \overline{Nu} and \dot{m}_{inf}), a series of calculations were performed in which each of the four parameters was varied independently and the results were compared to a base case (summarized in Table 6-1). The refrigerant temperature is assumed to be constant with time at 26.7°C (80F). The geometry and other characteristics of the fins and tubes of the evaporator coil are identical to the evaporator coil used in the experiment and discussed previously. The initial frost mass, density and thermal conductivity at each row of the evaporator coil are obtained from the prediction of the frost model described previously at the end of 48 hours simulation of cooling mode operation.

Table 6-1: The value of the experimentally fitted parameters for the base case

Parameter	value
h_{HG}	3000 [W/m ² -K]
$R_{c,F}$	3.0x10 ⁻² [m ² -K/W]
\overline{Nu}	2.5
\dot{m}_{inf}	0.2 [kg/s] (24% air changes per minute)

The time required for a complete removal of the frost, the total parasitic heat load at the end of the complete removal of the frost and the total parasitic heat load at the conclusion of the Hot Gas Defrost Cycle (HGDC) for the base case are shown in Table 6-2.

Table 6-2 Results of the Hot Gas Defrost base case

Parameter	value
Time required for a complete removal of the frost	10.79 [min]
Total parasitic heat load at the end of a complete frost removal	55.0 [MJ]
Total parasitic heat load at the end of a complete HGDC	75.11 [MJ]

The impact of the parameters listed in Table 1 on the time required for a complete removal of the frost, the total parasitic heat load at the end of the complete removal of the frost and the total parasitic heat load at the conclusion of the HGDC are summarized in Table 6-3. The total parasitic heat load is defined as the total heat transfer from the hot gas less the total heat stored in the frost:

$$Parasitic\ heat\ load = \sum_{row=1}^{row=10} N_t \left[\int_{t=0}^{t=time} \dot{Q}_{HG} dt - \left(\int_{t=0}^{t=time} \dot{Q}_{fF_{st}} dt + \int_{t=0}^{t=time} \dot{Q}_{tF_{st}} dt \right) \right]_{row} \quad (6.45)$$

where N_t is the number of tubes at each row and $\dot{Q}_{tF_{st}}$ and $\dot{Q}_{fF_{st}}$ are the rate of the energy storage in the tube-frost and the fin-frost, respectively.

Note that the length of the hot gas period is assumed to be 40 minutes regardless of the actual time that is required for complete removal of the frost; this was done in order to understand the effect of each parameter on the dry-heating period. The results for each parameter are provided in terms of the percentage change relative to the base case.

The results of the sensitivity analysis indicated that none of the parameters have a significant impact on the parasitic heat load at the end of complete frost removal. However, the contact resistance between the frost and the tube surface has a substantial effect on the required time for complete frost removal and the infiltration mass flow rate has a substantial effect on the parasitic heat load at the end of a complete hot gas defrost cycle. The results shown in Table 2 suggest that the value of the average Nusselt number and hot gas heat transfer coefficient have an extremely small effect on the results and therefore the assumptions used in the modeling are likely adequate. The value of $R_{c,F}$ does effect the time required for frost removal but not the parasitic; given that any reasonable optimization strategy will add some margin to the hot gas defrost duration, the value of $R_{c,F}$ is also not important with respect to the use of the model as an optimization tool. Finally, the infiltration mass flow rate does have some effect on the total parasitic (a 25% change in the mass flow rate results in a 5% change in the parasitic) and therefore this parameter should be chosen with some care.

Table 6-3 Defrost model sensitivity analysis

Parameter	? %	Time [min]	% Time	%P.L. Frost	%P.L. HGDC
h_{HG}	+25%	10.66	-1.2%	-0.04%	+0.07%
h_{HG}	+50%	10.57	-2.0%	-0.05%	+0.11%
\overline{Nu}	+25%	10.73	-0.5%	+0.7%	+1.57%
\overline{Nu}	+50%	10.65	-1.3%	+1.23%	+2.67%
$R_{c,F}$	-25%	9.83	-8.8%	-0.94%	+0.3%
$R_{c,F}$	+25%	11.76	+9.0%	+0.93%	+0.29%
\dot{m}_{inf}	+25%	10.82	+0.25%	+1.0%	+4.57%
\dot{m}_{inf}	-25%	10.76	-0.25%	-1.8%	-4.93%
? %	Percent change in the parameter value from the base case value.				
%Time	Percent change in the time required for a complete frost removal compared to the base case				
%P.L. Frost	Percent change in the total parasitic heat load at the end of a complete frost removal compared to the base case.				
%P.L. HGDC	Percent change in the total parasitic heat load at the end of a complete HGDC compared to the base case.				

6.4 Summary

A 1st order model of the Hot Gas Defrost Process (HGDP) based on the equations derived in this chapter is implemented using the Engineering Equation Solver (Klein, 2006) software. The proposed model includes most of the important physics without focusing on the micro-scale details; therefore, the model requires some calibration against experimental data to be predictive.

The model requires as inputs all of the evaporator coil geometric information, the hot gas temperature and the frost thermal and physical properties (e.g frost thickness, density and thermal conductivity) at each row at the initiation of the defrost process. The model subsequently calculates the time required to melt all of the frost, the hot gas parasitic heat

load, the mass flow rate of the water condensate and the ultimate disposition of the energy transferred from the hot gas. The initial thermal and physical properties of the frost are obtained from the frost theoretical model that was described previously in Chapters 3 to 5.

6.5 Nomenclature

Symbol	Description	Dimensions
A	= surface area	$[\text{m}^2]$
A_c	= Contact surface area	$[\text{m}^2]$
C	= Specific heat	$[\text{kJ kg}^{-1} \text{K}^{-1}]$
h	= Convective heat transfer coefficient	$[\text{W m}^{-2} \text{K}^{-1}]$
F_{thk}	= Fin thickness	$[\text{m}]$
h_m	= Mass transfer coefficient	$[\text{kg m}^{-2} \text{s}^{-1}]$
i	= Enthalpy	$[\text{kJ kg}^{-1}]$
k	= Thermal conductivity	$[\text{W m}^{-1} \text{K}^{-1}]$
Le	= Lewis Number	$[-]$
L_p	= Heigh of the penthouse walls	$[\text{m}]$
m	= mass	$[\text{kg}]$
N_{fin}	= Total number of fins at any section	$[-]$
\overline{Nu}	= Average Nusselt number	$[-]$
Pr	= Prandtl number	$[-]$
\dot{Q}	= Heat transfer rate	$[\text{W}]$
\dot{Q}_E	= Latent heat rate due to evaporation	$[\text{W}]$
\dot{Q}_S	= Latent heat rate due to sublimation	$[\text{W}]$
R_f	= Fouling factor	$[\text{m}^2 \text{K W}^{-2}]$
R_c	= Contact resistance	$[\text{m}^2 \text{K W}^{-2}]$
$Ra_{L,p}$	= Reynolds number based on the penthouse wall height	$[-]$
r_o	= Outer tube radius	$[\text{m}]$
r_{fin}	= Outer radius of the equivalent circular fin	$[\text{m}]$
\bar{r}	= Mass average fin radius	$[\text{m}]$
T	= Temperature	$[\text{K}]$
V	= Total volume	$[\text{m}^3]$
Greek symbols		
d	= Frost layer thickness	$[\text{m}]$
ρ	= Density	$[\text{kg m}^{-3}]$
w	= Specific humidity	$[-]$
Subscripts		
fin	= Fin	
t	= Tube	
is	= Inside	
os	= Outside	

<i>tF</i>	=	Tube-frost
<i>fF</i>	=	Fin-frost
<i>HG</i>	=	Hot-gas
<i>F</i>	=	Frost
<i>air</i>	=	Air
<i>sf</i>	=	Fusion
<i>S</i>	=	Sublimatio
<i>st</i>	=	Storage
<i>p</i>	=	Penthouse wall

6.6 References

Al-Mutawa, N.K., 1997, Experimental investigations of frosting and defrosting of evaporator coils at freezer temperatures, PhD thesis, Department of Mechanical Engineering, University of Florida

Churchill, S.W., and H.H.S. Chu, 1975, “*Correlating Equation for laminar and turbulent free convection from a vertical plate,*” International Journal of heat and Mass Transfer, Vol. 18.

Schmidt, T.E., 1949, “*Heat transfer calculation for extended surfaces.*” Refrigerating Engineering, vol. 57.

Threlkeld, J.L., 1970, Thermal environmental engineering, 2nd ed. Englewood Cliffs, NJ: Prentice Hall Book Co.

Zurcher, O., D. Favrat, J.R. Thome, (2002), “*Evaporation of refrigerants in a horizontal tube: an improve flow pattern dependent heat transfer model compared to ammonia data*” International Journal of heat and Mass Transfer, Vol. 45.

Chapter 7 Defrost Experiment

This chapter discusses a field experiment on an industrial evaporator coil during a Hot Gas Defrost Process (HGDP). The main objective of this experiment is to gather sufficient qualitative (visual) and quantitative experimental data to validate the numerical model of the (HGDP) which was previously described in Chapter 6. The intent of the model is to quantify and to illustrate the impact of the hot-gas defrost process on the thermal performance (capacity and efficiency) of the complete refrigeration cycle.

7.1 Experiment Facility

The coil selected for this experimental investigation is the same liquid overfed evaporator that was used in the frosting experiment, described in Chapter 4. The geometric details of the coil and the penthouse enclosure are summarized in (Chapter 4, Table 4-1). The inlet hot gas temperature to the evaporator coil was measured during the HGD and found to be 40.5°C (105°F); the pressure of the hot gas is could not be measured, however it was estimated based on the compressor outlet pressure to be within the range of ~ 1034 kPa (150 psig) with a corresponding saturation temperature of 26°C (79°F). Therefore, the hot gas has approximately 14.2°C (26°F) superheat. The refrigerant condensate (and vapor, if present) is returned to a controlled-pressure receiver (CPR) operating at 620.5 kPa (90 psig). The vapor relief for maintaining the 90 psig CPR set point is connected to a 310 kPa (45 psig) suction level that serves multiple HVAC loads in the plant.

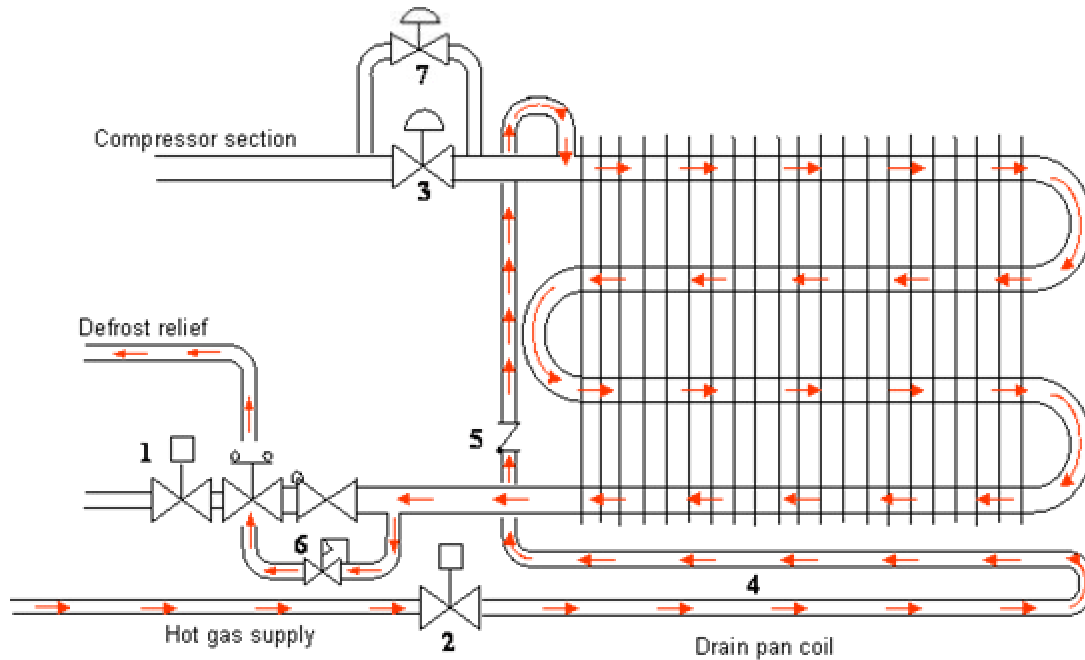
7.2 Design of Experiment

Figure 7.1 shows the hot gas flow direction in the evaporator coil and indicates the main valves that are used during a typical Hot Gas Defrost Cycle (HGDC). An HGDC is divided into four main processes:

- 1 Pump-out: The objective of this initial stage is to remove the cold liquid refrigerant from the evaporator coil before the hot gas supply is initiated. This initial stage of the defrost cycle begins with by closing the Liquid feed Solenoid valve (LSV) while continuing to operate the evaporator fans in order to evaporate as much of the coil's liquid refrigerant as possible.
- 2 Hot gas supply: The purpose of the hot gas supply stage is to increase the coil temperature by an amount that is sufficient to melt all of the frost accumulated on the exterior surfaces of the evaporator coil. Thermal energy must be supplied from the hot gas to the evaporator coil in order to sensibly heat the frost to the melting point of water and then initiate the latent process of converting the frost from its solid state to liquid; the liquid is removed from the coil through a condensate drain line that is connected to the outside of the penthouse.

This hot gas supply stage starts by closing the Suction Stop Valve (SSV) and turning off the evaporator fans. The Hot Gas feed Solenoid Valve (HGSV) is then opened, allowing the high pressure super-heated refrigerant from the discharge of the compressors to pass first through the condensate drain pan. Heating the condensate drain pan avoids any re-freezing of the melted frost. The hot gas (and any condensed liquid) then flows to the evaporator coil through the Pan Check

- Valve (PCV). The PCV prevents liquid refrigerant from flowing into the drain pan coil during normal operation of the refrigeration cycle. The hot gas then flows through the evaporator tubes where it gives up its latent heat of condensation in order to heat the metal coil surface and the attached frost. The condensed liquid refrigerant (as well as any refrigerant vapor that has not condensed) leaves the evaporator, usually, through a Defrost Relief Regulator (DRR).
- 3 Bleed: Once the hot gas dwell period is terminated, the coil must be prepared to be placed back into low temperature service. The “bleed” period is intended to safely manage the reduction of the evaporator pressure from its defrost condition (at high pressure) to its normal operating condition (at low pressure). The bleed period begins by closing the hot gas feed solenoid valve followed by opening a smaller solenoid valve (the Bleed Solenoid Valve – BSV) that connects the evaporator to the suction pressure. The small BSV allows the coil pressure to slowly equalize to the suction pressure and prevents mechanical damage that might occur from a more violent depressurization.
 - 4 Fan delay: Following the bleed period is the “fan delay” period. The fan delay period is the last stage of the defrost cycle, which starts by opening the SSV and closing the BSV. The liquid feed solenoid valve is then opened in order to re-introduce cold refrigerant to the coil. The evaporator fans are turned on for a short period of time and then cycled on and off in order to allow any residual moisture on the coil surface to re-freeze which prevents the water from being blown off of the coil during the subsequent full and continuous fan operation.



- | | |
|---------------------------------------|-----------------------------------|
| 1- Liquid feed Solenoid valve (LSV) | 4- Drain pan heater (DPH) |
| 2- Hot Gas feed Solenoid Valve (HGSV) | 5- Pan check valve (PCK) |
| 3- Suction Stop Valve (SSV) | 6- Defrost Relief Regulator (DRR) |
| | 7- Bleed Solenoid Valve (BSV) |

Figure 7.1 Schematic of flow in the Hot Gas Defrost (HGD) mode.

The current field experiment is divided into four parts; the first part is a visual study of the evaporator coil as it goes through the HGD cycle. The objective of the visual study is to obtain qualitative information related to the frost melting sequence as well as an estimate of the actual time required to fully melt the accumulated frost.

The second part of the experiment involves measuring the water condensate mass flow rate and the total mass of water condensate that exits the coil through the penthouse condensate drain line. The objective of this part of the experiment is to provide some quantitative validation of the frost numerical model by comparing the total mass of frost accumulated at the end of the cooling mode operation. In addition, the frost melt rate

provides quantitative validation of the numerical defrost model in terms of the instantaneous mass flow rate of the melt during the HGD mode operation.

The third part of the experiment involves quantifying the cooling capacity of the evaporator during the pump-out period. This is accomplished by monitoring the air velocity through the coil as well as the enthalpy difference of air across the coil in a manner that is equivalent to the measurement of the cooling capacity during the frosting operation.

The last part of the experiment involves monitoring the penthouse-air temperature at different locations within the penthouse enclosure during the entire HGDC. These data can be compared with the air temperature predicted by the numerical defrost model in order to provide quantitative validation of the model.

7.2.1 Instrumentation

Five thermistors (T_{o1} , T_{o2} ... T_{o5}) are used to measure the average air temperature on the down-stream side of the evaporator coil. The five thermistors are spaced 0.90 m apart diagonally across the down-stream coil face in order to divide the coil face into six equal areas; the thermistors were installed 0.30 m (12 in) away from the downstream face of the coil (Figure 7.2)

Four thermistors (T_{in1} , T_{in2} ... T_{in4}) are used to measure the temperature of the interface between the penthouse-air and the freezer-air. The four thermistors are attached directly to the grate that is located on the up-stream side of the evaporator coil (Figure 7.3).

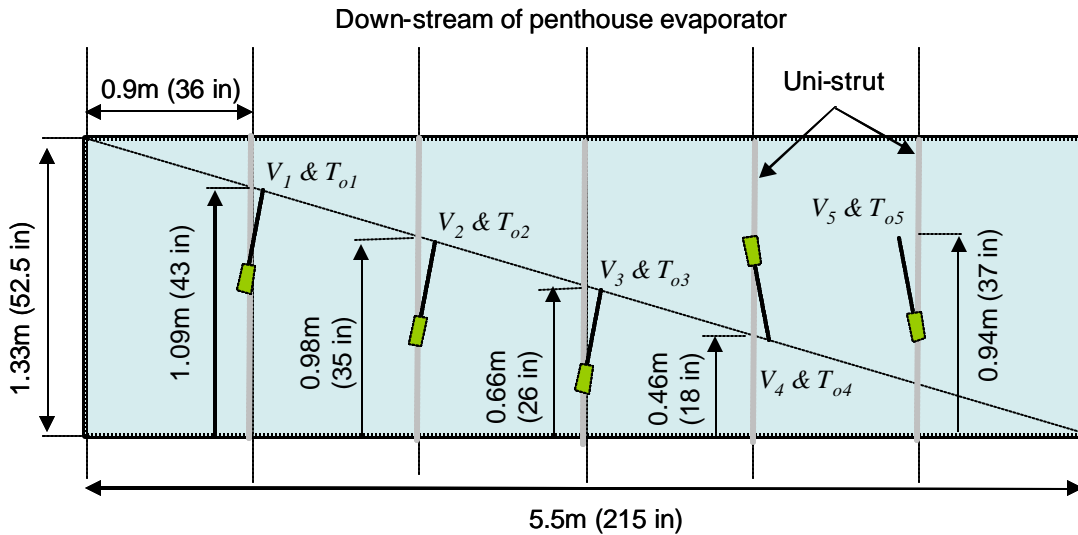


Figure 7.2 Elevation view downstream of the evaporator coil showing the location of each air velocity transducer and thermistor

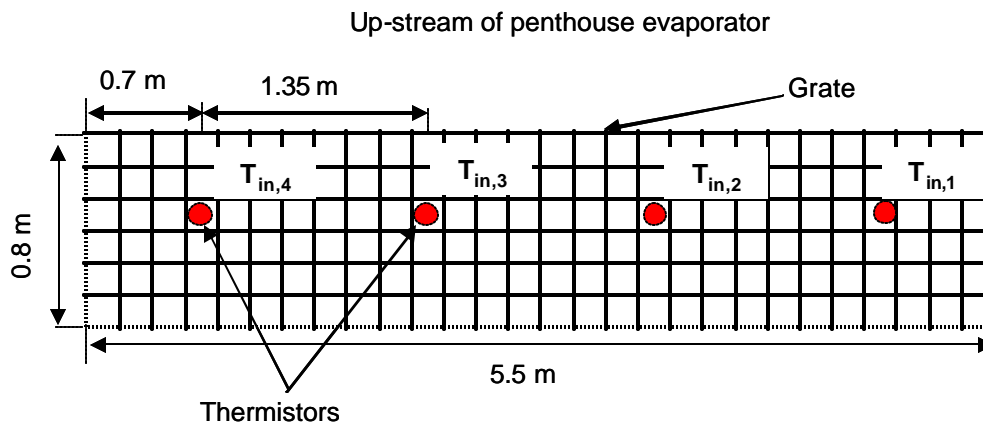


Figure 7.3 Schematic showing the exact location of thermistors used to measure the interface temperature between the penthouse-air and the freezer-air.

Four thermistors ($T_{in,top1}$, $T_{in,top2}$) and ($T_{o,top1}$, $T_{o,top2}$) are used to measure the air temperature just below the penthouse ceiling. The thermistors are organized into two groups (i.e. $T_{in,top1}$, $T_{in,top2}$ and $T_{o,top1}$, $T_{o,top2}$) and are attached at the two top corners on the up-stream (in) and down-stream (o) sides of the evaporator coil, respectively.

Six thermistors (T_{c1} , T_{c2} ... T_{c6}) are used to measure the air temperature between the evaporator fins. The six thermistors are attached to the tip of six thin metal rods that are each 0.45 m in length. The six metal rods were fully inserted at the beginning of the HGD cycle through the frosted evaporator coil 2.25 m away from the evaporator coil sides and 0.15m apart (Figure 7.4)

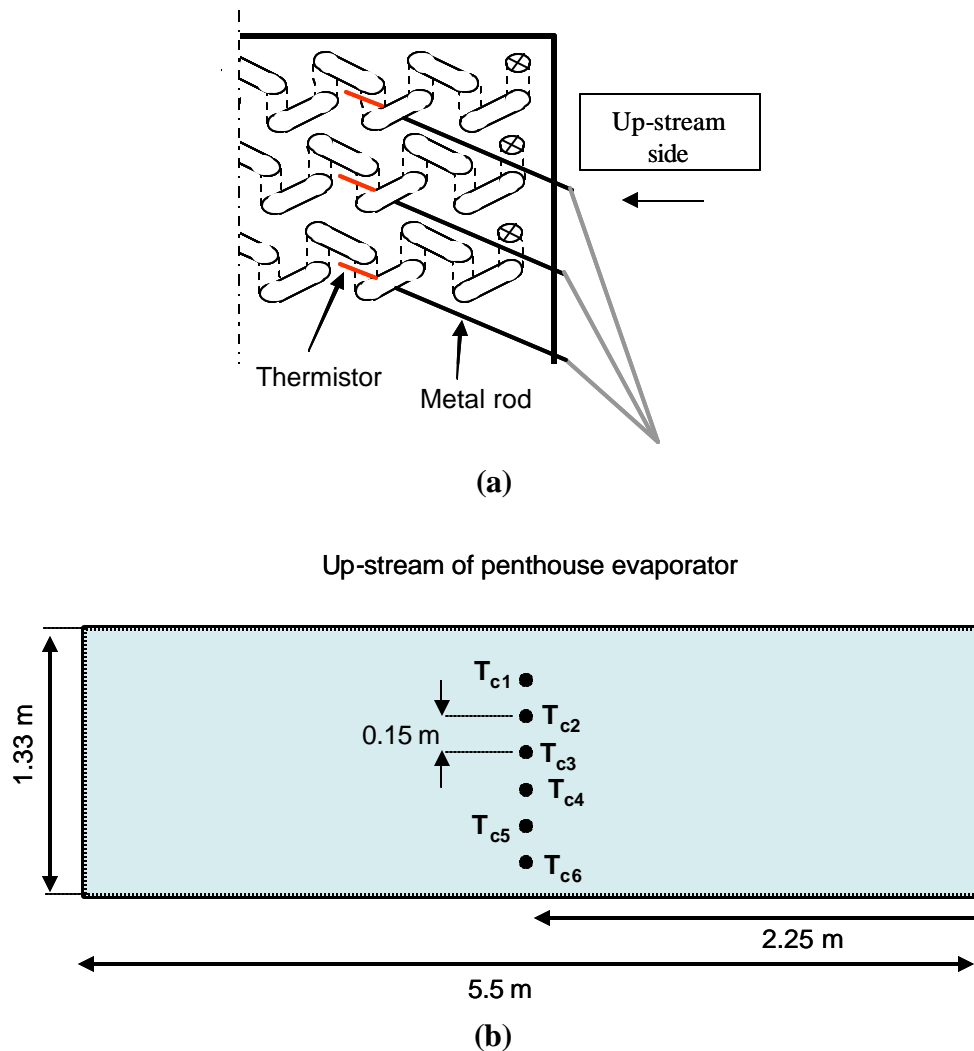


Figure 7.4 Schematic showing the exact location of thermistors used to measure the air temperature between the evaporator coil fins; (a) side-view, (b) front-view.

7.3 Experimental Results

In this section, the experimental results obtained during five different HGD cycles are presented. The time duration for each of the four stages of each HGDC and the time duration of the cooling mode operation prior to each HGDC are summarized in Table 7-1.

Note that the time duration of the HGD stages shown in Table 7-1 for HGDC #1 are the default settings that are programmed into the control system by the warehouse operator.

Table 7-1 Time duration for each of the four main stages for each HGDC and the time duration of the cooling mode operation prior to each HGDC.

HGDC #	Cooling mode	Pump-out	Hot-gas	Bleed	Fan delay
1	24 hours	20 minutes	30 minutes	10 minutes	5 minutes
2	24 hours	20 minutes	40 minutes	10 minutes	5 minutes
3	24 hours	20 minutes	40 minutes	10 minutes	5 minutes
4	48 hours	20 minutes	40 minutes	10 minutes	5 minutes
5	48 hours	20 minutes	40 minutes	10 minutes	5 minutes

7.3.1 Evaporator Capacity during the Pump-out Period

Figure 7.5 shows the capacity of the evaporator as a function time during the five hot gas defrost cycles that are described in Table 7-1. The cooling capacity is calculated as using Eq. (4.1) shown in chapter 4.

It can be seen in Figure 7.5 that the evaporator capacity decreases by more than 35 kW (10 tons) which is in excess of 50% of its normal capacity during the 20 minute pump-out period. The decrease in capacity is due to the termination of the cold liquid refrigerant supply coupled with the continued operation of evaporator fans, which add heat from the space that is being cooled. Note that the capacity shown Figure 7.5 is the gross capacity

of the coil since the measurements were made up-stream of the evaporator fans. The parasitic effects of the fan load will decrease the coil's capacity by approximately 4 tons. Projecting the pump-out period using the rate of capacity decrease during the first 20 minutes would suggest that the net coil capacity would reach zero in approximately another 12 minutes.

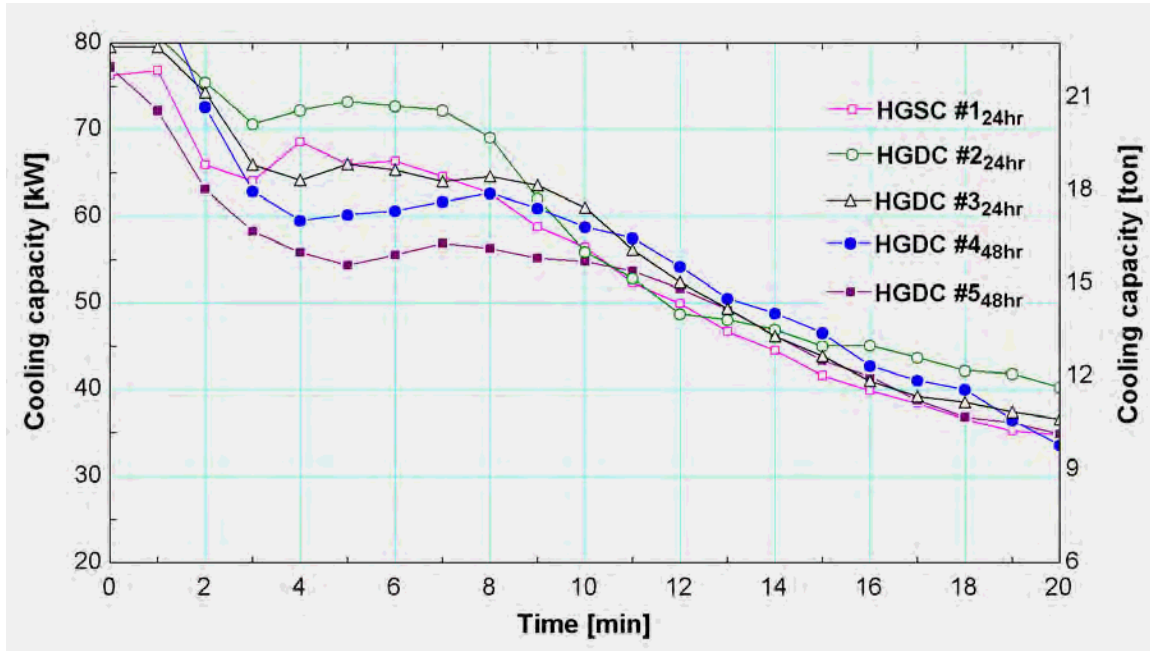


Figure 7.5 Gross evaporator capacity as a function of time for the 5 HGDCs measured during the pump-out period.

7.3.1 Visual Study of the Frost Melting Sequence

Figure 7.6 shows photographs of the accumulated frost on the up-stream side of the evaporator coil during HGDC #1. Figure 7.6(a) shows the frosted evaporator coil during the first stage of the HGDC (i.e., during the pump-out period) whereas Figure 7.6(b) through (j) show the frosted evaporator coil at various times during the second stage of the HGDC (i.e., during the hot gas supply period).

Although the frost covering the evaporator surfaces is continuous, Figure 7.6 shows that the frost can be divided into three parts that behave differently during the HGD cycle; these are: (1) the frost covering the fin tips, (2) the frost covering the two sides of the fin surfaces, and (3) the frost covering the bare tubes.

One of the interesting phenomena that can be seen in Figure 7.6(a) and (b) is that the frost attached to the fin tips begins to melt away as soon as the hot-gas supply process is initiated. This behavior is largely due to the fact that the thickness of the frost covering the fin tips is less than the frost thickness covering the finned surfaces. In addition, the insulating effect of the frost on the fins and the low heat transfer coefficient associated with the natural convection process that governs the defrost process (recall that the fans are turned off) leads to a high fin efficiency during the defrost process (as compared to the fin efficiency of unfrosted fins during normal operation); therefore, the temperature gradient along the fin is small during the defrost process and the fin tip comes to a temperature very near the hot gas temperature. These effects cause the frost covering the fin tips to melt away very quickly. This observation provides some justification for the structure of the numerical model (in Chapter 6) that lumps the entire fin material at the same temperature.

Figure 7.6(a) through (d) also show that all of the frost attached to the bare tube shown will melt outward at almost the same time. Figure 7.6 also shows that the frost covering both sides of the fins starts to melt as soon as the frost covering the coil bare tubes has melted. The frost covering both sides of the fins melts gradually outward (relative to the

tube surface) starting at the refrigerant tube. This observation agrees with the prediction of the numerical model which indicates that the “tube-frost” will melt before the “fin-frost” and justifies dividing the frost into these two components.

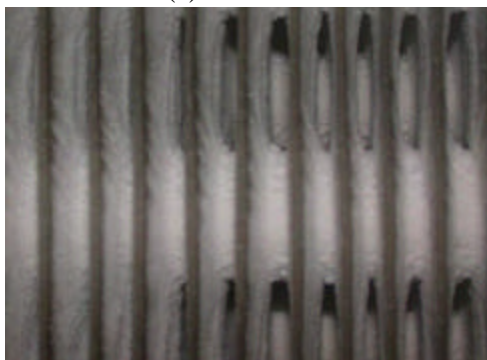
Finally Figure 7.6 shows that the actual time required to melt all of the accumulated frost is approximately 7 minutes even though the default setting of the hot gas supply period is 30 minutes.



(a) 0 minutes



(b) 0.5 minutes



(c) 1.0 minutes



(d) 2.0 minutes



(e) 2.5 minutes



(f) 3.0 minutes

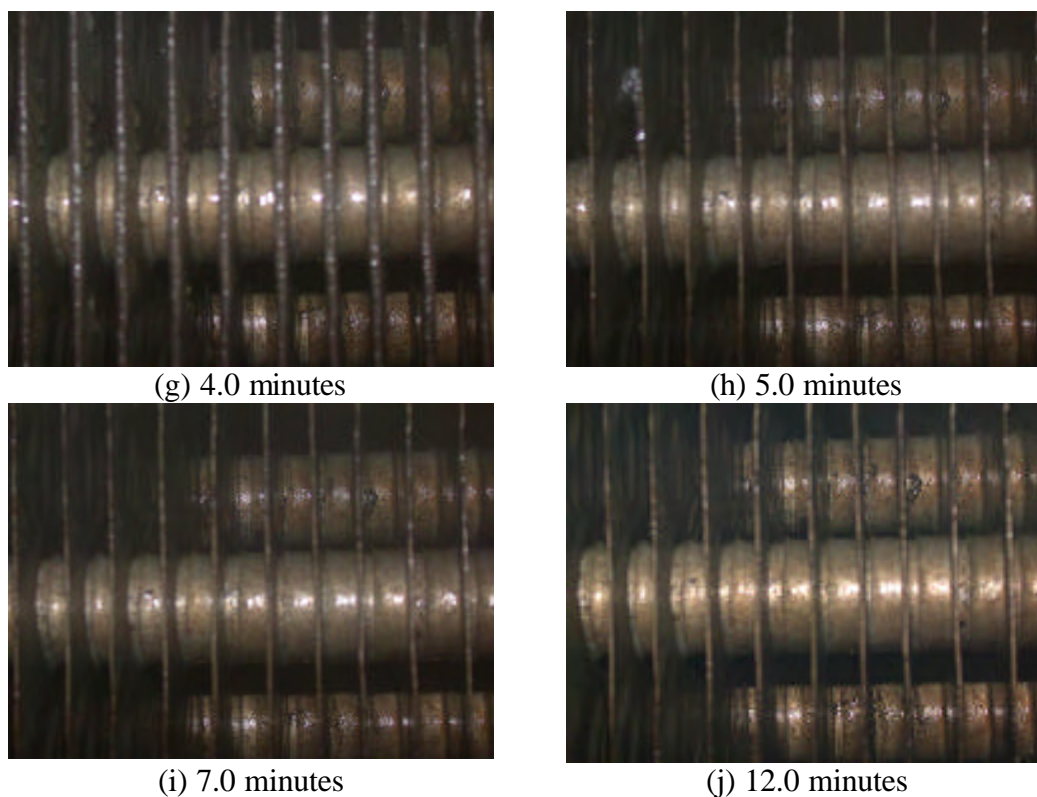


Figure 7.6 Time-lapse photos of the evaporator coil during HGDC #1.

7.3.2 Water Condensate Flow Rate

The water condensate drained from the coil during the melting period is collected using a container of known volume (Figure 7.7) and the time associated with filling each container is measured using a stopwatch. The mass and the volumetric flow rates of the condensate are shown in Figure 7.8 as a function of time. Note that time=0 refers to the beginning of the second defrost stage, the hot gas supply period.

Figure 7.8 shows that approximately 93% of the total drained water has been collected during the first 7 minutes of the hot-gas supply period; this result is in agreement with the visual observation that a complete frost melt is accomplished at about this time, as shown

previously in Figure 7.6. After ten minutes of the hot gas supply, the condensate flow has been reduced to a negligible amount, which is consistent with the coil surface being completely free of frost and only slightly wetted. Also, note from Figure 7.8 that the flow rate of the condensate water flow peaks at approximately 2 minutes.



Figure 7.7 Photograph of the penthouse drain during HGDC #1.

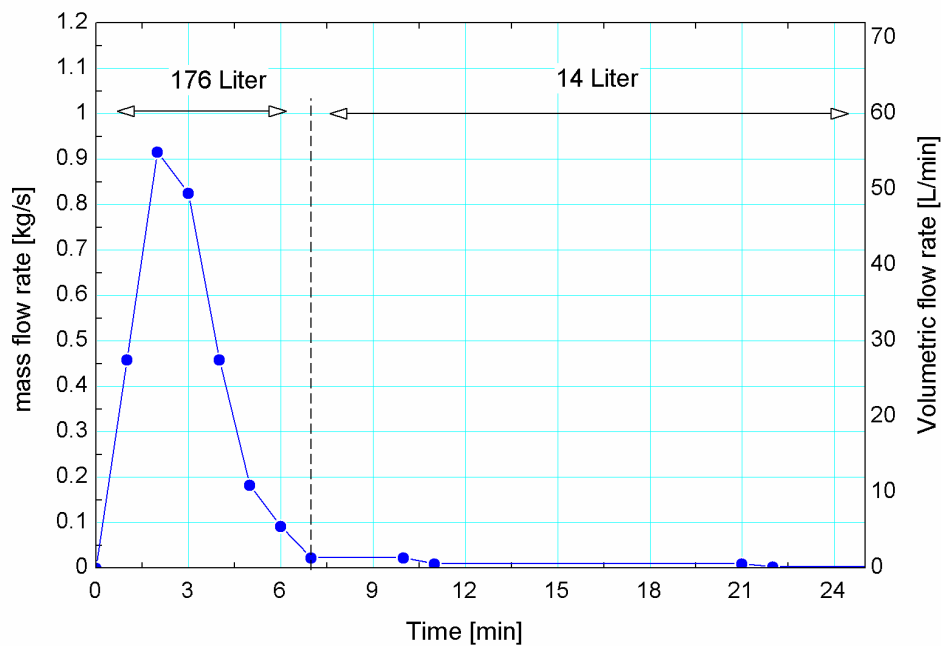


Figure 7.8 Mass and volumetric flow rates of the drained water of HGDC #1.

7.3.3 Penthouse-Air Temperature

Figures 9 through 13 show the penthouse-air temperature at different locations relative to the evaporator coil during the stages of the HGD cycles that were described in Table 7-1. Figure 7.9 illustrates the time variation of the air temperature at the evaporator core at different elevations measured by thermistors (T_{c1} to T_{c6}) during HGDC #1 and shows that during the 20 minute pump-out stage, the air temperature increases gradually from -30°C to almost -26°C due to the termination of the cold liquid refrigerant supply. However, after the evaporator fans are turned off and the hot gas supply period begins, the air temperature increases rapidly over the first seven minutes of the hot gas supply period (from -26°C to 25°C); this behavior is consistent with the time required to remove (melt, evaporate and sublimate) all of the frost, as discussed in Sections 7.3.2 and 7.3.1. After all of the frost has been removed from the coil surfaces the air temperature in the penthouse reaches a steady state and remains at this level throughout the remainder of the hot-gas supply period.

During the ten minute bleed-period, the air temperature begins to decrease gradually from 25°C to 20°C due to the termination of the hot-gas supply and the heat transfer and infiltration air transfer with the freezer space, as shown in Figure 7.9. Once the evaporator fans are turned on, the air temperature drops rapidly (over a period of approximately 4 minutes) from 20°C back to the evaporator's normal operating temperature. Figure 7.9 also shows that the air temperature measured at the evaporator's core is nearly the same at the different elevations at any instant time during the HGDC.

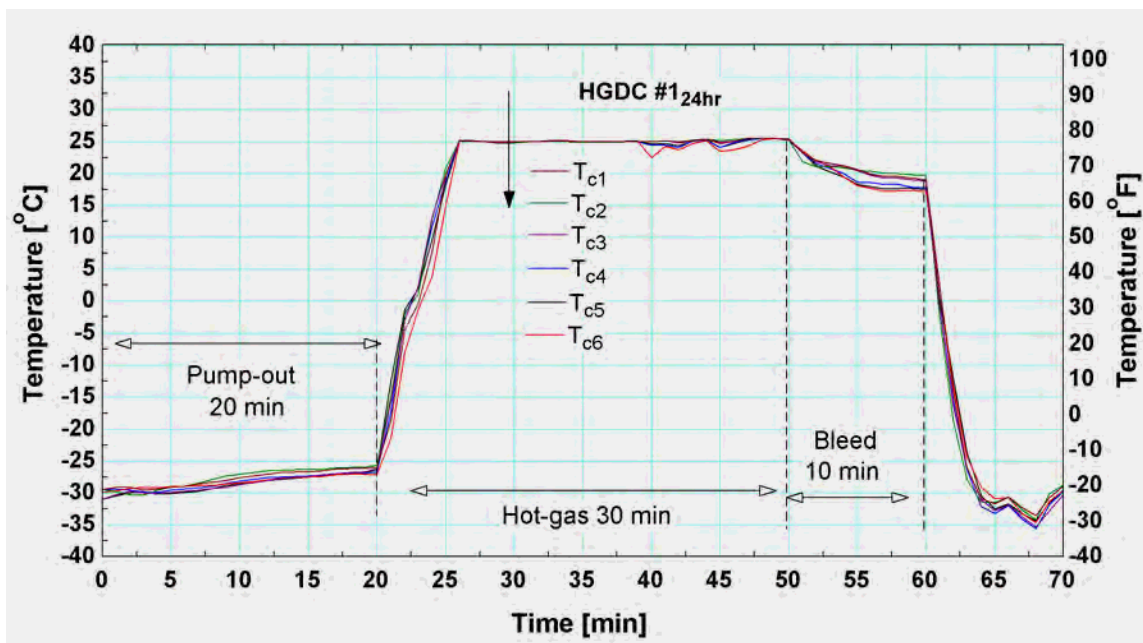


Figure 7.9 Measured air temperature at the evaporator core as a function of time during an HGDC at six different elevations (see Figure 7.4).

Figure 7.10 shows the spatially-averaged air temperature at the evaporator core ($T_{c,ave}$, the average of the 6 measurements shown in Fig. 9) and the down-stream side the evaporator coil ($T_{o,ave}$, the average of $T_{o,1}$ through $T_{o,5}$) as a function of time during HGDC #1. The temperatures, $T_{c,ave}$ and $T_{o,ave}$, are calculated using Eqs (7.1) and (7.2) respectively.

$$T_{c,ave} = \left(\sum_{n=1}^6 T_{c,n} \right) / 6 \quad (7.1)$$

$$T_{o,ave} = \left(\sum_{n=1}^5 T_{o,n} \right) / 5 \quad (7.2)$$

Figure 7.10 shows that $T_{c,ave}$ and $T_{o,ave}$ are nearly identical during the twenty-minute pump-out period; however, as soon as the hot-gas supply period starts, the temperature difference increases to a maximum of 10°C during the first seven minutes followed by a gradual decrease to about 5°C at the end of the hot-gas supply period. During the bleed-

period, the two average temperatures ($T_{c,ave}$ and $T_{o,ave}$) both decrease and their difference decreases slightly from 5 °C to about 4 °C.

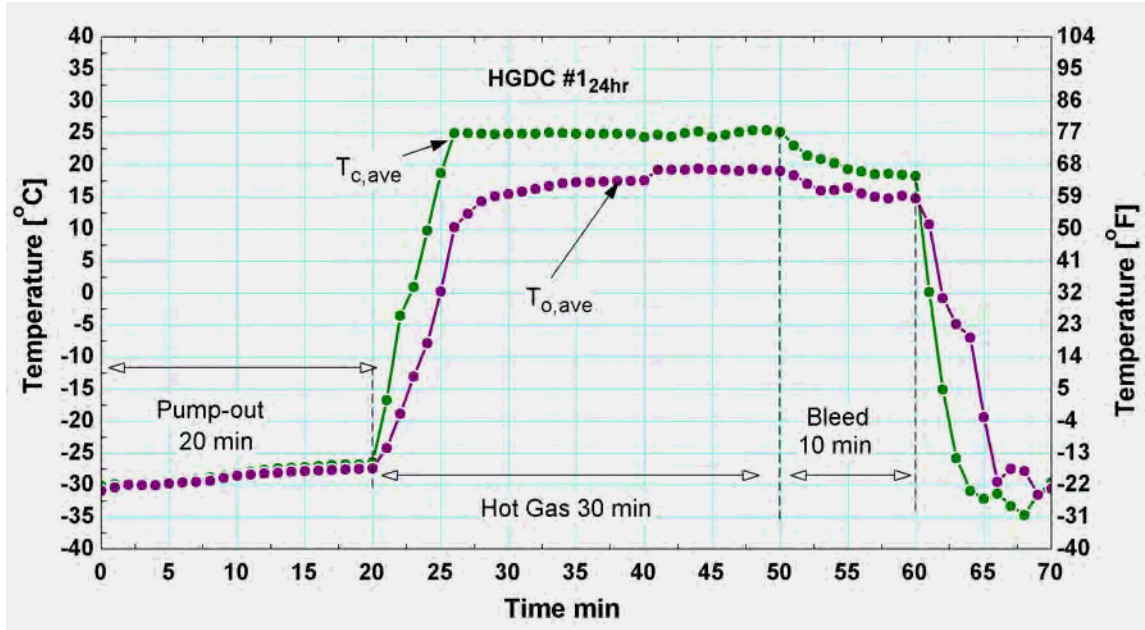


Figure 7.10 Spatially-averaged air temperature at the evaporator core and at downstream side the evaporator coil.

Figure 7.11 illustrates the temporal variation of the air temperature measured on the downstream side evaporator by thermistors $T_{o,1}$ to $T_{o,5}$ during HGDC #2. It can be seen from Figure 7.11 that the temperature distribution measured by the five thermistors is almost the same during the whole HGDC even as the absolute temperature level changes. Also, notice that the air on the downstream side of the evaporator is thermally stratified, with a 5 °C difference between the highest and lowest temperature readings at any instant of time.

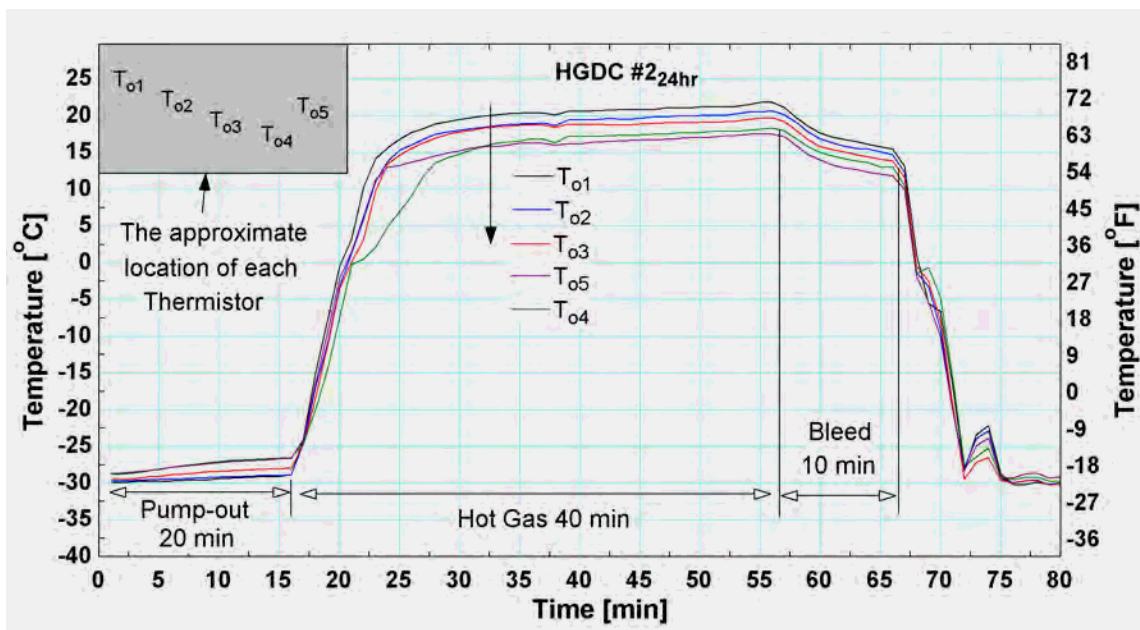


Figure 7.11 Air temperature measured at the down-stream side of the evaporator core at five different elevations as a function of time during an HGDC.

Figure 7.12 shows the spatially-averaged air temperature on the down-stream side of the evaporator coil (T_{oave} , the average of the five measurements shown in Fig. 11) as a function of time during HGDC runs #2-4. Recall from Table 7-1 that the hot-gas defrost settings used for HGDC#2-4 are identical, with the only difference that HGDC#2 and HGDC#3 were carried out after 24 hours of cooling operation while HGDC #4 and HGDC #5 were performed after 48 hours of cooling operation.

It can be seen from Figure 7.12 that the temperature profile on the down-stream side of the evaporator for the four HGD cycles is almost identical with the exception of the first thirteen minutes of the hot gas supply period; during this period of time the air temperature increases faster in HGDCs #2 and #3 than in HGDCs #4 and #5. This difference is due to the larger frost mass and thickness in HGDCs #4 and #5 which is a

result of the longer cooling operation period. The accumulated frost mass and thickness at the beginning of HGDC#4 and HGDC#5 is greater than it is at the beginning for HGDC #2 and #3 and therefore it requires more time to be removed.

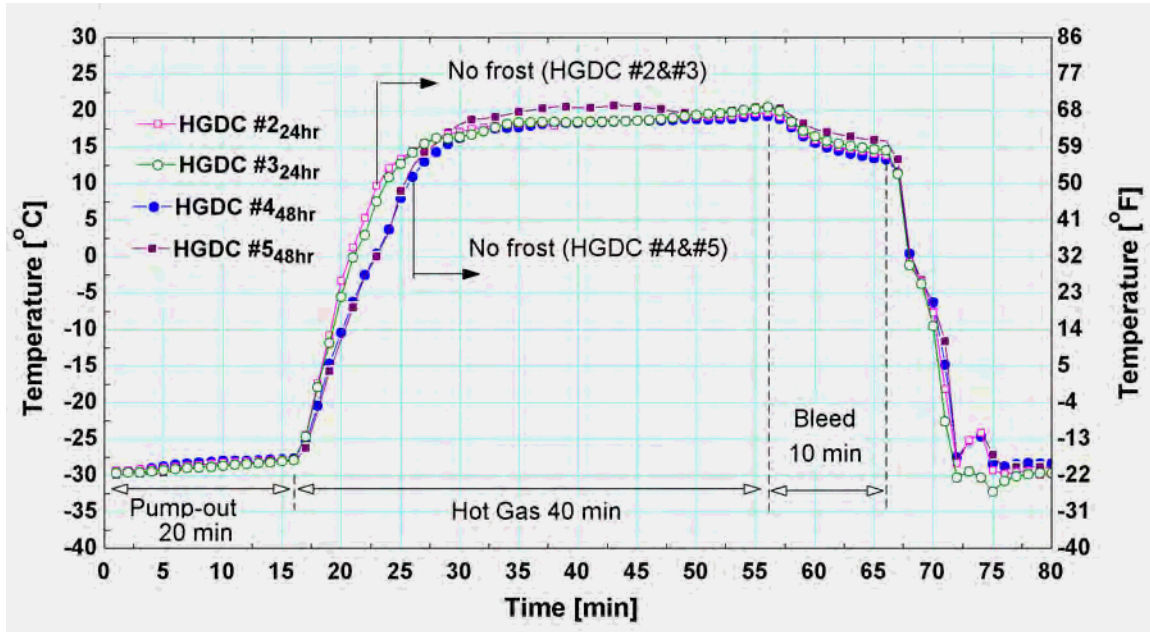


Figure 7.12 Spatially-averaged air temperature at the down-stream side of the evaporator coil during HGDCs #2-5.

Figure 7.12 shows the spatially-averaged air temperature on the up-stream side of the evaporator coil at the penthouse ceiling ($T_{intopave}$) and at the pent house grate (T_{inave}) as a function of time during HGDCs #2-4. The average temperatures, $T_{intopave}$ and T_{inave} , are calculated using Eqs (7.3) and (7.4), respectively.

$$T_{intopave} = (T_{intop,1} + T_{intop,2}) / 2 \quad (7.3)$$

$$T_{intop} = (\sum_{n=1}^4 T_{intop}) / 4 \quad (7.4)$$

It can be seen from Figure 7.13 that the spatially-average air temperature profile at the penthouse ceiling for the four HGD cycles have the same general temperature behavior with the same steady state temperature during the hot gas supply period as the spatially-

averaged air temperature measured on the down-stream side of the evaporator (Figure 7.12). Also, it can be seen from Figure 7.12 and Figure 7.13 that the temperature profile associated with both $T_{o,ave}$ and $T_{in,top,ave}$ for HGDCs #2 and #3 require about seven minutes to achieve steady state after the initiation of the hot gas supply, whereas about 11 minutes are required HGDCs #4 and #5. Figure 7.13 also shows that the spatially-average air temperature profile at the penthouse grate increases gradually throughout the entire HGD cycles; the temperature rises by about 5°C due to the infiltration air transferred between the penthouse and the freezer. As the penthouse air gains sensible and latent heat, the density decreases and therefore the air will have the tendency to rise upward toward the penthouse ceiling rather than leaking out through the grate and entering the freezer. This stable situation is responsible for the relatively low rate of infiltration and the associated small increase in the measured value of $T_{in,ave}$.

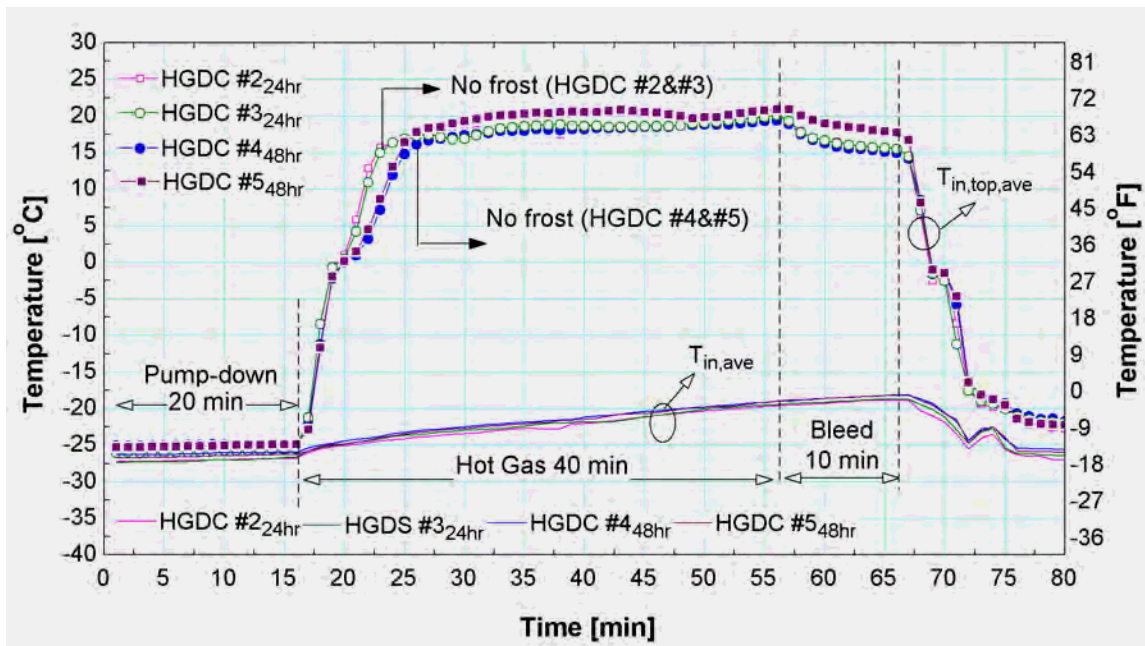


Figure 7.13 Spatially-averaged air temperature at up-stream side of the evaporator coil during HGDC #2-4.

Table 7-2 Summaries the effects of the various hot gas defrost process on the refrigeration system.

Table 7-2 summary of the effects of the various hot gas defrost process on the refrigeration system.

Process	Result	System effect
Pump-out	Removal of refrigeration from coil in preparation for defrost	Decreasing but positive capacity
Hot gas supply	Pre-heating stage: warm coil mass to melt frost	Negative load on system (when the defrost cycle is terminated)
	Melting stage: frost melt	Negligible load on system- energy leaves system by frost condensate draining
	Dry-heating stage: excess hot gas beyond what is required to melt frost	Negative load on system while gas continues to be supplied beyond that required to melt frost
Bleed & Fan delay	Pull down coil in preparation for meeting load	Capacity increases to clean coil capacity over this period

7.4 Summary

There are several important observations from the experiment that are valuable for validation of the defrost theoretical model that was described in the previous chapter:

- 1- During the HGDC, all of the frost covering the tube bare surface melts almost simultaneously and at a faster rate than the frost covering the fin surfaces.
- 2- The time required for the complete removal of frost that is accumulated after 24 hours of cooling operation is between 6 and 7 minutes; it takes longer, approximately 10 to 11 minutes, to remove the frost accumulated after 48 hours of cooling operation.

- 3- During the 10 minute bleed period that follows the hot gas supply, the penthouse-air temperature drops by about 4.5 °C.
- 4- During the HGDC, the mass flow rate of the condensate water that is drained from the coil increases gradually until it reaches a peak (at about 0.92 kg/s for HGDC#1) after which it decreases to zero at a time that is consistent with the complete removal of frost.
- 5- There is almost a 10°C difference between the average air temperature at the evaporator core and at the down-stream side of the evaporator during the first part of the hot-gas period (the melting stage).

Chapter 8 Defrost Model Validation

There are two objectives of this chapter: 1) to compare the predictions of the theoretical model of the Hot Gas Defrost Process (HGDP) described in Chapter 6 with the experimental data shown in Chapter 7; and 2) quantify the direct hot-gas defrost penalties on the freezer space “parasitic heat load” of both the penthouse and the ceiling-hung evaporators. Note that there are indirect penalties due to the HGDP on both the freezer space and on the refrigeration system that are discussed in Chapter 9. In addition, the relative advantage of the penthouse enclosed evaporator versus the ceiling-hung evaporator is considered.

8.1 Validation of the HGD model of the penthouse evaporator

The predictions from the theoretical model of the HGDP described in Chapter 6 are compared with the experiment data described in Chapter 7. The geometry and other characteristics of the evaporator coil used to develop the HGDP theoretical model are shown in Table 8-1 and are identical to those in the penthouse evaporator coil used in the experiment and discussed previously. The refrigerant temperature is assumed to be constant with time at 26.7°C. The theoretical model of frosting operation, described in Chapter 3, is used to predict the initial frost thickness, density, and thermal conductivity in each row of the evaporator at the beginning of the defrost cycle. The two main stages of the HGDC, the hot gas supply stage and the bleeding stage are considered in the comparison. Therefore the initial penthouse air and the initial penthouse wall

temperatures as well as the initial frost temperature in the model were set to be equal to the initial temperature of the penthouse air at the beginning of the hot gas supply stage, experimentally measured to be -26.5°C (-16°F).

Table 8-1 Geometry and operating conditions of the coil used to develop the hot gas defrost model.

Parameter	Value
Fin pitch	0.85 cm
Face area	8.23 m ²
Tube diameter	19.05 mm
Tube length	5.5 m
Number of fans	5
Fan power @ -30°F (-34°C) air temperature	2.33 kW
Rated CFM	1699 m ³ /min
Number of tubes	260
Number of tube row	10
Tube transverse pitch,	57 mm
Tube longitudinal pitch,	44 mm
Evaporation temperature	-34.4°C
Coil temperature difference	5.6°C
Fin material	Aluminum
Number of fins	661
Tube material	Galvanizes steel
Coil mass	3,900 kg
Refrigerant	Ammonia
Evaporator coil type	CPR-fed liquid overfeed

Figure 8.1 shows the spatially-averaged penthouse-air temperature measured at the evaporator core ($T_{c,ave}$) and at the down-stream side the evaporator coil ($T_{o,ave}$). The predicted penthouse-air temperature versus time during HGDC #1 is also shown in Figure 1. Notice that during the frost-melting stage (i.e., the first 6 minutes of the hot gas supply

stage) the predicted penthouse air temperature lies between the two measured temperatures. This behavior is expected since the model assumes that the entire air volume is lumped together and in intimate thermal contact with the evaporator surfaces when, in fact, there are regions of the penthouse air that are somewhat isolated from the defrost process. Also, it can be seen that the model is capable of approximately predicting the time required for complete frost removal (approximately 6 minutes).

Figure 8.1 also shows that the predicted penthouse air temperature during the dry heating stage (i.e., after the frost is completely removed) is slightly lower than both measured temperatures; this discrepancy is due to the infiltration of air from the freezer space which is not considered in the model. The model is predicting the average temperature of the entire penthouse air which is expected to be slightly lower than the temperature measured on the down stream side the evaporator, T_{oave} . Finally, Figure 8.1 shows that during the bleed stage the total drop in the average predicted penthouse air temperature is 4.2 °C which is consistent with the measured drop in the air temperature. This agreement provides some validation of the assumed infiltration rate.

Figure 8.2 shows the mass flow rate of the water condensate predicted by the HGD model and the measured drained water condensate during HGDC#1. The duration of the four main stages of HGDC#1 and the time duration of the cooling mode operation is shown in Table 8-2.

Table 8-2 Time duration for each of the four main stages for each HGDC and the time duration of the cooling mode operation prior to each HGDC

HGDC #	Cooling mode	Pump-out	Hot-gas	Bleed	Fan delay
1	24 hours	20 minutes	30 minutes	10 minutes	5 minutes
2	24 hours	20 minutes	40 minutes	10 minutes	5 minutes
3	24 hours	20 minutes	40 minutes	10 minutes	5 minutes
4	48 hours	20 minutes	40 minutes	10 minutes	5 minutes
5	48 hours	20 minutes	40 minutes	10 minutes	5 minutes

It can be seen from Figure 8.2 that the model predictions agree with the experimental measurements, both in terms of the variation with time as well as the absolute value.

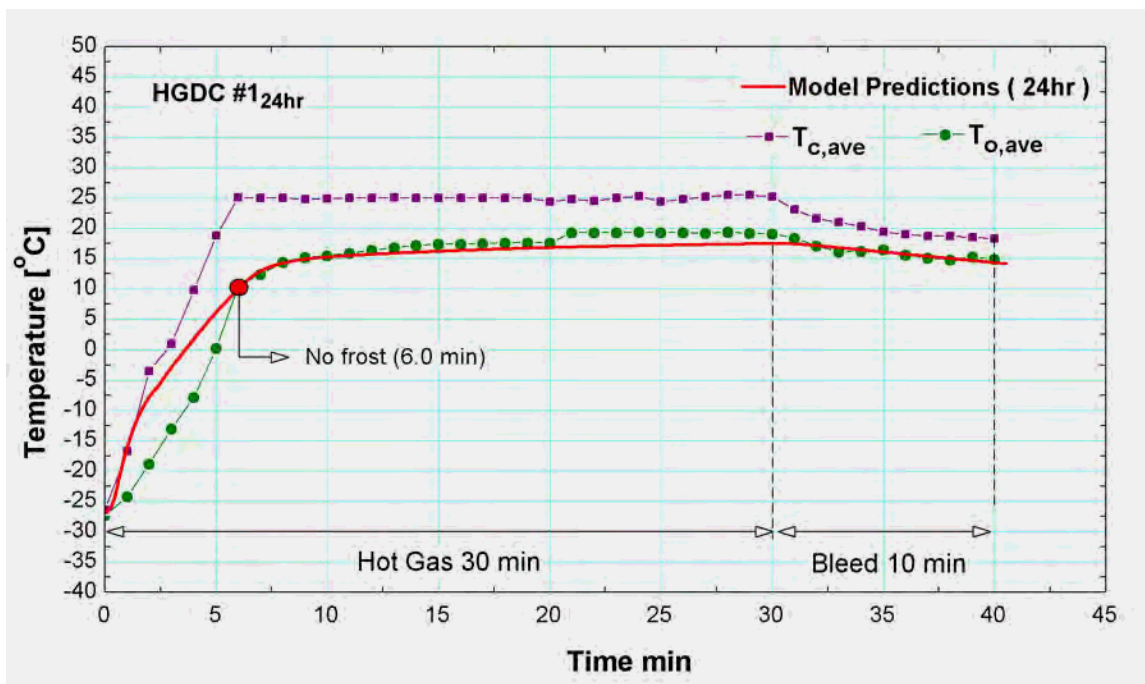


Figure 8.1 Comparison between the average penthouse air temperature predicted by the HGD model and the spatially-averaged air temperature measured at the evaporator core and at down-stream side the evaporator coil during HGDC #1.

Figure 8.3 shows the spatially averaged penthouse air temperature measured at the down stream side the evaporator coil ($T_{o,ave}$) during HGDCs #2-5 and the predicted

penthouse air temperature as a function time. Recall from Table 8-2 that the hot gas defrost settings used for HGDCs #2-5 are identical; the only difference in these hot gas defrost cycles are that HGDC#2 and HGDC#3 were both performed after 24 hours of cooling, whereas HGDC #4 and HGDC #5 were performed after 48 hours of cooling. Therefore, the amount of frost that has formed on the coil at the initiation of HGDCs #4 and #5 is larger.

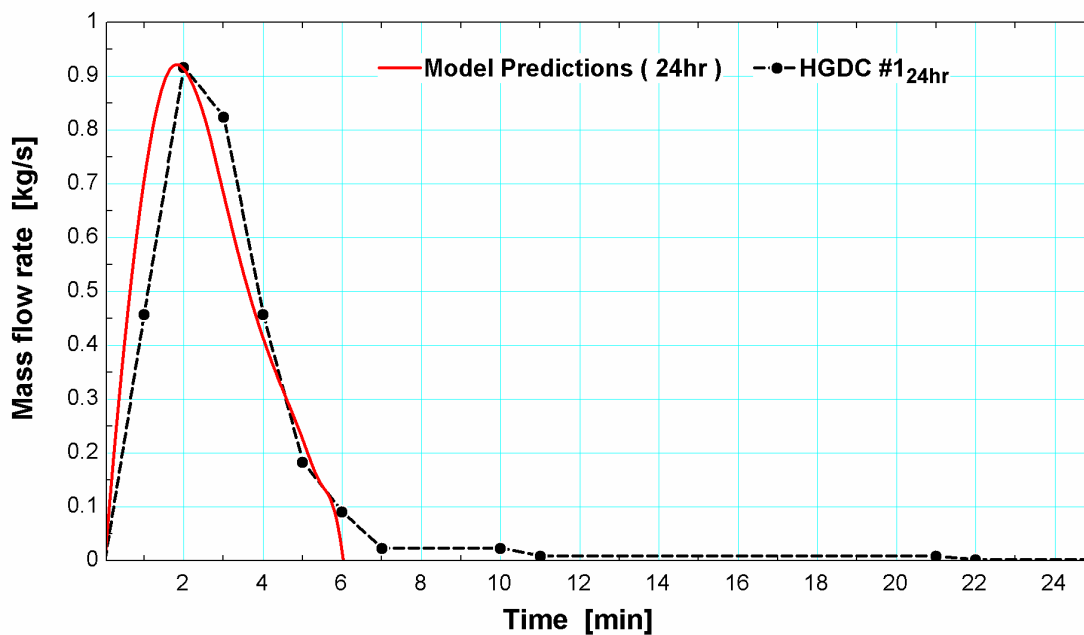


Figure 8.2 Comparison of the average water condensate mass flow rate predicted by the HGD model and the measured during the HGDC#1 as a function of time.

Figure 8.3 shows that the HGD model predictions agree fairly well with the experimental data for both cases in term of the time required for complete frost removal as well as the qualitative features of the variation of the penthouse air temperature with time.

The predicted mass flow rate of the water condensate for the HGDCs that follow 24 hours of cooling mode operation (HGDCs #1-3) and those that follow 48 hours of cooling mode operation (HGDCs #4&5) are shown in Figure 8.4 as a function of time. It can be seen from Figure 8.4 that the model predicts almost 4 minutes difference between the actual time required to remove all of the accumulated frost following the 24 hours and 48 hours of cooling mode operation which agrees with the experimental data.

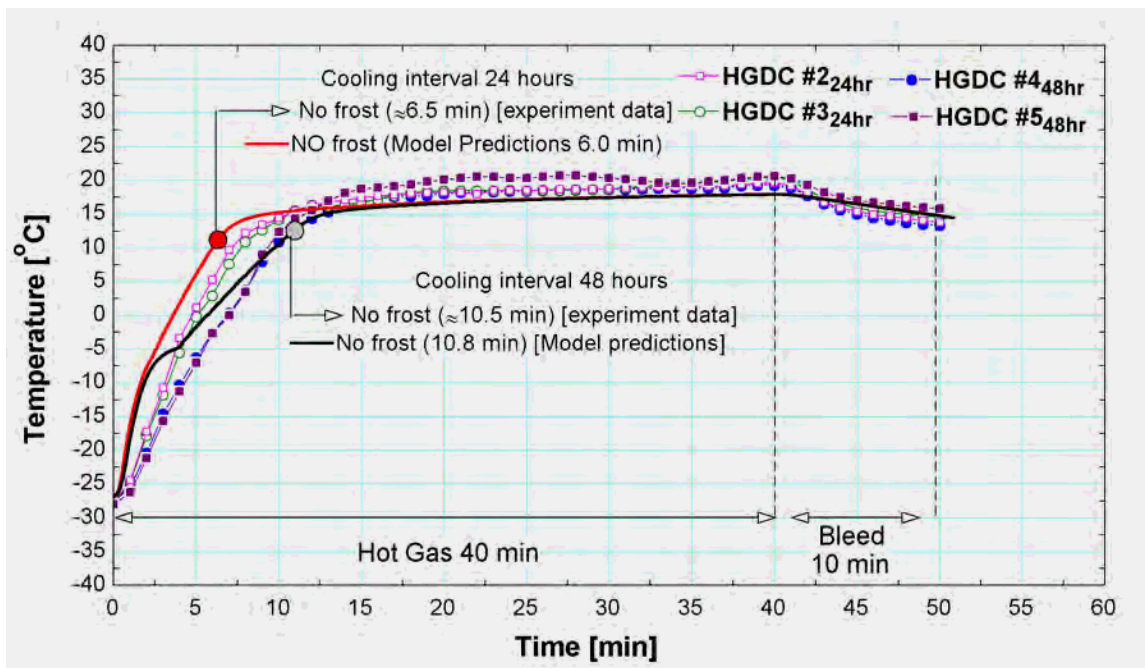


Figure 8.3 Comparison between the average penthouse air temperature predicted by the HGD model and the spatially-averaged air temperature measured at the down-stream side the evaporator coil during HGDC #2-5 versus time.

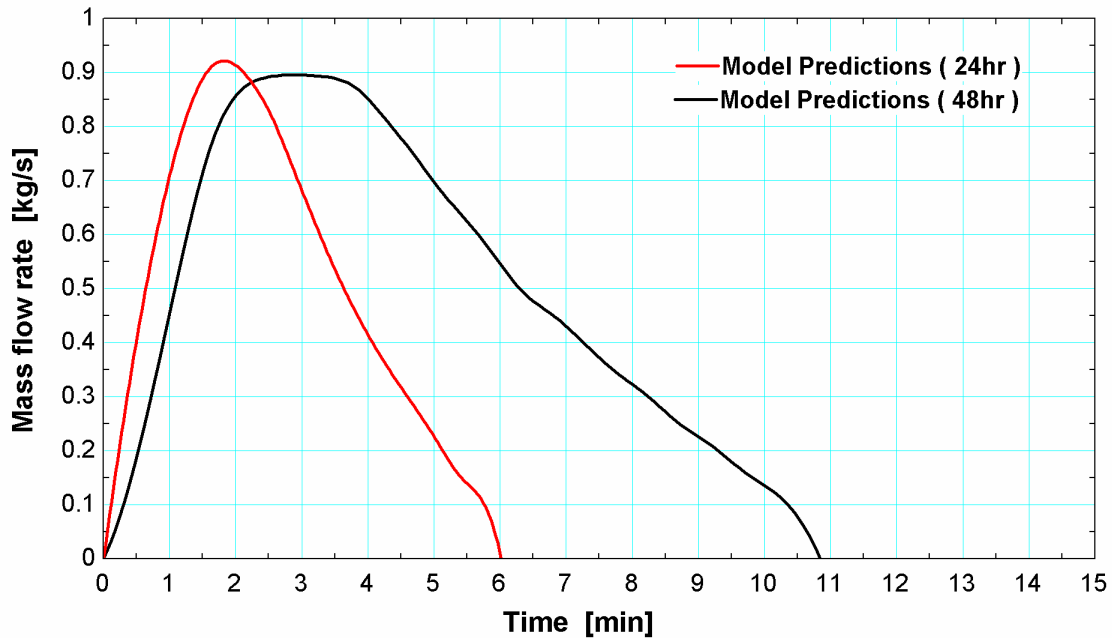


Figure 8.4 Average water condensate mass flow rate predicted by the HGD model prior to 24 and 48 hours of cooling mode versus time.

Figure 8.5 shows the predicted penthouse average air temperature, penthouse-wall average temperature, the hot gas temperature and the total mass of the remaining attached frost for the HGDC process that follows 48 hours of cooling mode operation as a function of time. Figure 8.5 shows that during the melting stage, the average air temperature increases very rapidly until all of the frost is removed after which time the air temperature in the penthouse reaches a steady state value where it remains throughout the remainder of the hot gas supply period. During the ten minute bleed-period, the air temperature decreases gradually due to the termination of the hot-gas supply and due to the heat losses related to infiltration and heat transfer with the freezer space and heat transfer with the penthouse walls. Notice that the penthouse wall temperature continues to increase at a constant rate throughout the HGDC, even during the bleed stage.

Certainly, the model is not predicting the details of the HGD process but rather capturing the gross features of the process which are required in the analysis and the calculation of the HGDP penalties (i.e., the approximate variation in the penthouse air temperature, the mass flow rate of the water condensate and the total actual time required to remove all of the accumulated frost) quite accurately.

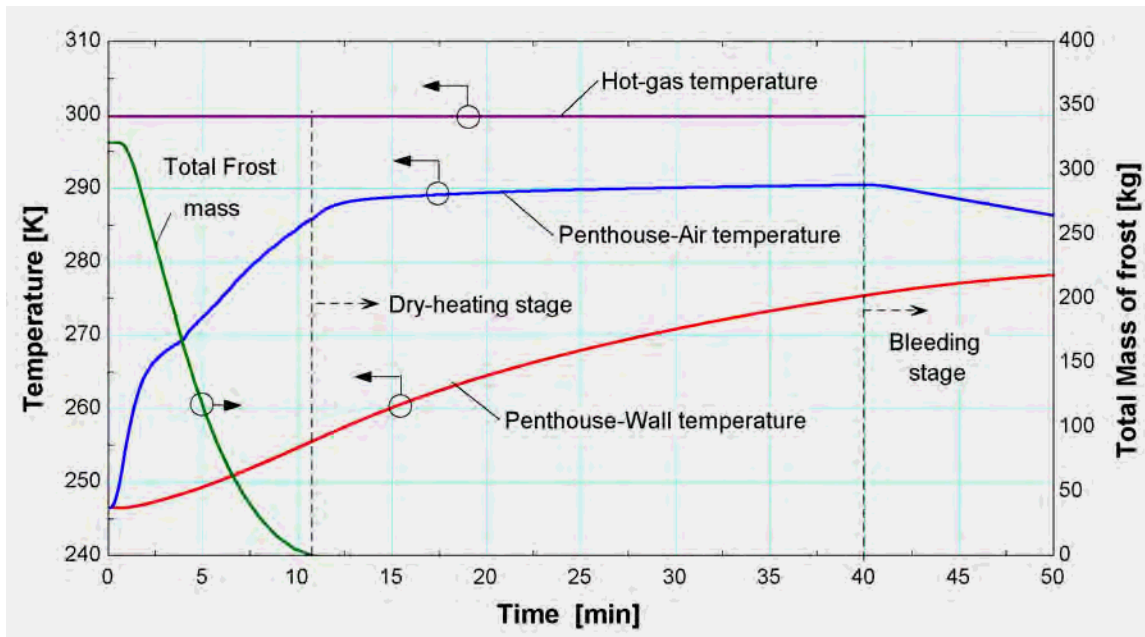


Figure 8.5 The predicted average temperature of the penthouse walls, penthouse air and the hot gas as well as the total mass of the remaining frost for a defrost process that follow 48 hours of cooling operation.

8.2 Heat load calculation

The objective of this section is to quantify the total HGD parasitic heat load and the distribution of the energy that is transferred from the hot gas during the HGDC for both the penthouse evaporator coil as well as a ceiling hung evaporator coil.

The energy flows quantified by the model include:

- Q_{HG} - the total energy transferred to the evaporator coil during a defrost cycle.
- Q_{tFst} and Q_{fFst} - the total energy stored in the frost (both the tube-frost and fin-frost); this is the total energy required to increase the frost temperature to 0 °C and then change its phase from ice to water.
- Q_{coil} - The total thermal energy stored within the fins and tubes during a HGDC.
- Q_{pwall} - The total thermal energy stored within the penthouse walls during a HGDC.
- Q_{air} - The total sensible and latent energy transferred back to the space during HGDC.
- Q_{PHL} - the total parasitic heat load

The HGD setting used in the analysis are summarized in Table 8-3 and are identical to HGDCs#2&3 and HGDCs#4&5 which were shown previously in Table 8-2. The geometry and other characteristics of the fins and tubes of the evaporator coil are shown in Table 8-1 and are identical to the evaporator coil used in the experiment and discussed previously.

Table 8-3 HGDP time setting used for the heat load calculation

Cooling mode operation	Pump-out	Hot-gas	Bleed	Fan delay
48 hours	20 minutes	40 minutes	10 minutes	5 minutes
24 hours	20 minutes	40 minutes	10 minutes	5 minutes

Figure 8.6 shows the total thermal energy stored in the frost (Q_{melt}) along with the total mass of the remaining attached frost (m_{frost}) for both the penthouse and the ceiling hung

evaporator coils throughout the HGDC that occurs following 48 hours of cooling mode operation as a function of time; the value of Q_{melt} is calculated according to:

$$Q_{melt} = \sum_{row=1}^{row=10} N_t \left[\int_{t=0}^{t=time} \dot{Q}_{fFst} dt + \int_{t=0}^{t=time} \dot{Q}_{tFst} dt \right]_{row} \quad (8.1)$$

where N_t is the number of tubes at each row, \dot{Q}_{fFst} and \dot{Q}_{tFst} are the rate of the energy stored in the fin-frost and tube-frost, respectively.

Figure 8.6 shows that the total energy required to melt the entire amount of frost that forms is the same for either the penthouse or the ceiling-hung evaporator coils because the initial mass of the frost that is collected during the cooling mode operation (321 kg) is the same for both evaporators. The energy required to sensibly warm and then melt the 321 kg of frost (Q_{melt}) can also be calculated analytically by multiplying the total mass of frost by the difference in the internal energy of the frost at its initial temperature of (-26.5 °C) and at melting water at 0 °C:

$$Q_{melt} = 321 \text{ kg} \cdot \left[3.857 \times 10^5 \frac{\text{J}}{\text{kg}} \right] = 1.238 \times 10^8 \text{ J} \quad (8.2)$$

Figure 8.6 also shows that the total time required to completely melt the frost is 10.8 min for the penthouse evaporator whereas it takes approximately one additional minute, 11.9 min, for the ceiling hung evaporator. The difference in the time required to melt the frost is related to the indirect heat transfer from the hot gas to the frost through the penthouse-air. During the HGDC, the temperature of the penthouse air increases very rapidly due to the relatively low infiltration rate between the penthouse air and the freezer air, as shown previously in Figure 8.3, which helps to accelerate the melting process.

The rapid increase of the penthouse-air results in a rapid decrease in the temperature difference between the penthouse air and the evaporator surfaces. This process causes the rate of heat transfer between the hot-gas and the penthouse air to be much lower than the heat transfer rate between the hot gas and the freezer air in the case of the ceiling-hung evaporator. Therefore, the parasitic hot gas defrost load transferred back to the freezer space is much lower for the penthouse evaporator than for the ceiling hung evaporator. The total parasitic heat load (i.e., the amount of energy transferred back to the space and stored in the coil) is shown as a function of time for both the penthouse and ceiling-hung coils in Figure 8.7 (for the HGDC that occurs after 48 hours of cooling mode operation).

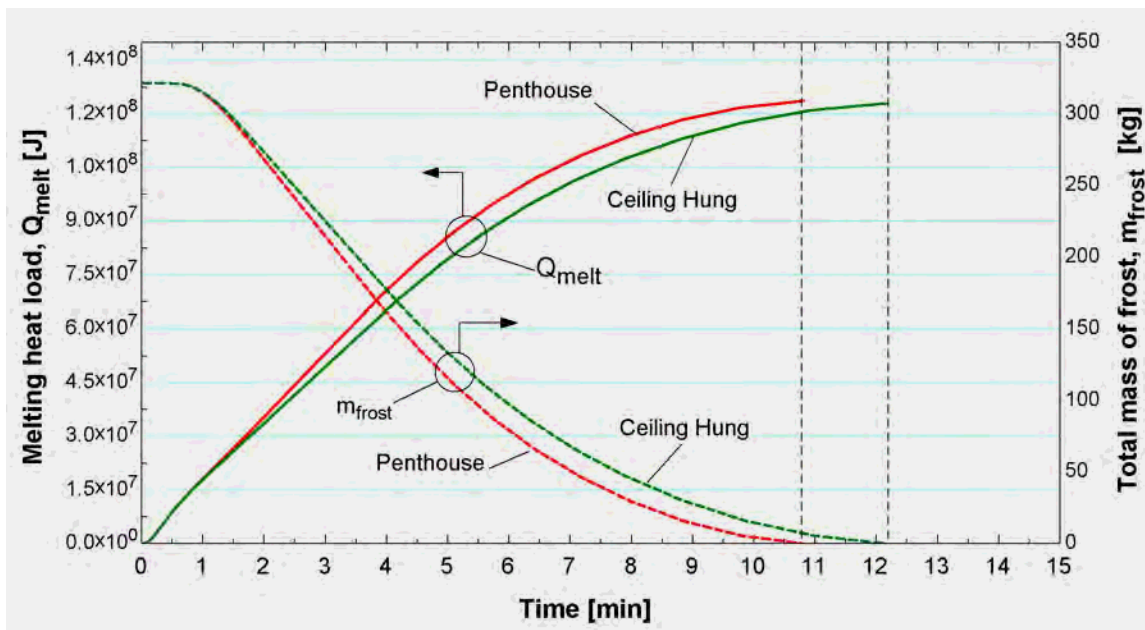


Figure 8.6 Total melting heat load and the total mass of frost for both the penthouse and the ceiling-hung evaporator coils throughout the HGDC prior to 48 hours of cooling versus time

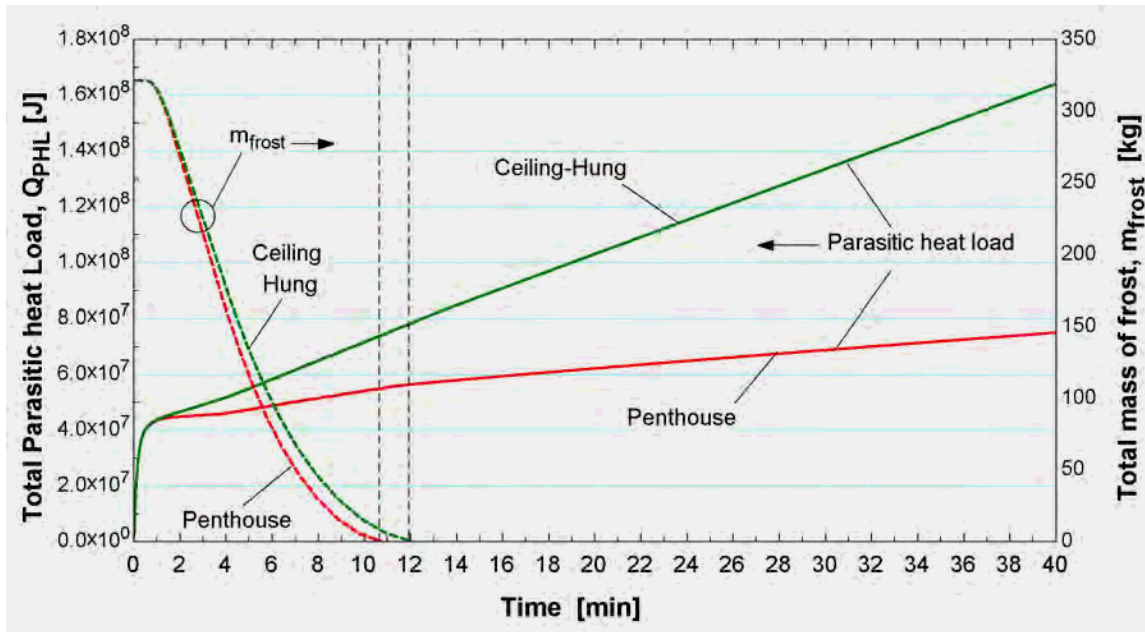


Figure 8.7 Total parasitic heat load and the total mass of frost for both the penthouse and the ceiling-hung evaporator coils throughout the HGDC that occurs after 48 hours of cooling operation.

The total parasitic heat load, Q_{PHL} , is calculated according to:

$$Q_{PHL} = \sum_{row=1}^{row=10} N_t \left[\int_{t=0}^{t=time} \dot{Q}_{HG} dt - \left(\int_{t=0}^{t=time} \dot{Q}_{fFst} dt + \int_{t=0}^{t=time} \dot{Q}_{tFst} dt \right) \right]_{row} \quad (8.3)$$

where \dot{Q}_{HG} is the rate of heat transfer from the hot-gas to the evaporator coil.

Figure 8.8 shows the total mass of the evaporated and sublimated frost (m_L) for both the penthouse and the ceiling-hung evaporator coils throughout the HGDC that occurs after 48 hours of cooling operation. Figure 8.8 shows that the total mass of the evaporated and sublimated frost is only 0.35 kg for the penthouse evaporator, which is only 0.1% of the initial mass of accumulated frost. On the other hand, the total mass of the evaporated and sublimated frost during the HGDC is 2.4 kg for the ceiling-hung evaporator, which is equal to 0.75% of the accumulated frost. Although the total mass of the water vapor that

transfers back the freezer space due to the sublimation and evaporation of the accumulated frost during the HGDC of the ceiling-hung evaporator is almost seven times higher than the from penthouse evaporator, it is still less than 1% of the total mass of the accumulated frost which agrees with the frost experimental data shown previously in Chapter 3 which suggested that the total mass of the frost that sublimate back to the freezer is less than 1.5% of the total accumulated frost. This conclusion is in contradiction with Coley (1983) who stated that during each defrost cycle, at least 15% of the ice sublimates back into the conditioned space to be removed again.

Figure 8.9 shows the total hot-gas load (Q_{HG}) along with the total mass of the remaining attached frost for both the penthouse and the ceiling hung evaporator coils throughout a HGDC that occurs after 48 hours of cooling operation.

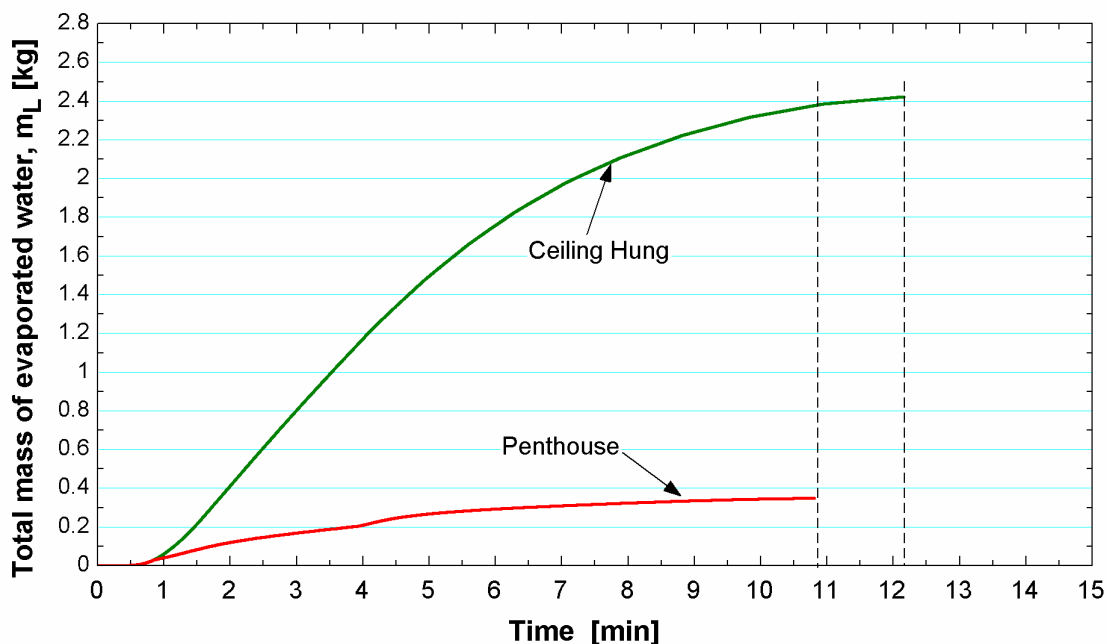


Figure 8.8 Total mass of the evaporated and sublimated frost during the HGDC of the penthouse and the ceiling-hung evaporator coils versus time.

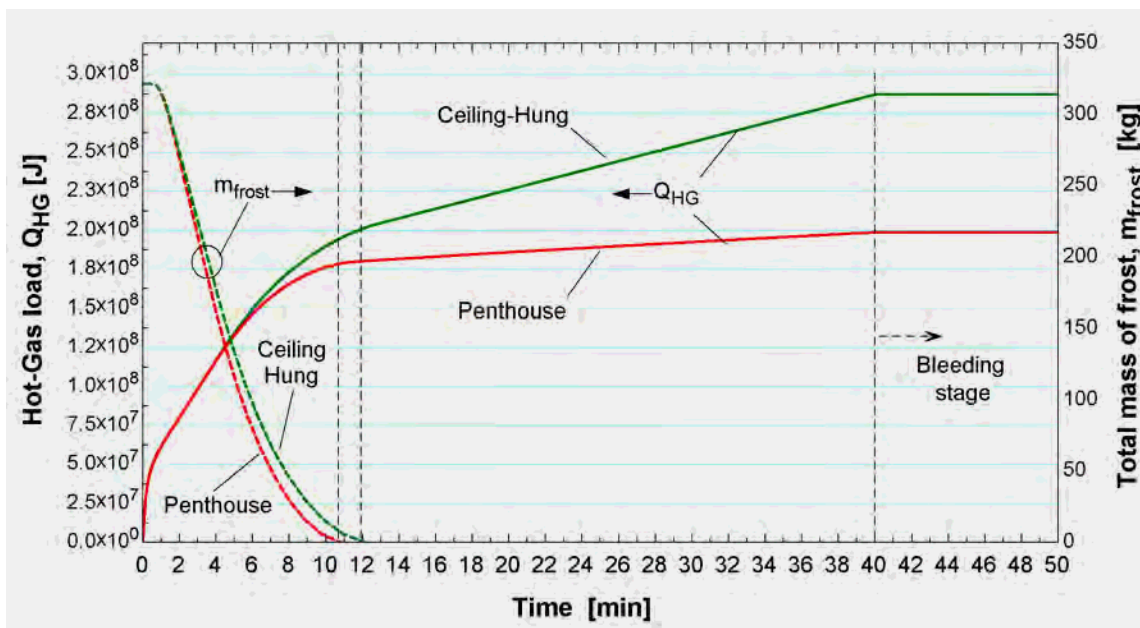


Figure 8.9 Total hot gas defrost load and the total mass of frost during a HGDC that occurs after 48 hours of cooling operation; both the penthouse and the ceiling-hung evaporator are shown.

Figure 8.9 shows that during the first 4 minutes of the hot-gas stage, the total heat transferred from the hot gas to the evaporator metal is almost exactly the same for the penthouse and ceiling-hung evaporator coils. However, as more frost is melted, and therefore more of the evaporator metal surface area is exposed to air, the difference in the Q_{HG} associated with the penthouse and the ceiling-hung evaporators increases significantly. This difference becomes especially evident once all of the frost is melted (i.e., during the dry-heating stage) due to the very large temperature difference that exists between the ceiling-hung evaporator surface area and the surrounding freezer air as compared to the very small temperature difference that exists between the penthouse evaporator surface area and the enclosed penthouse air.

Figure 8.10 shows the HGD efficiency (\mathbf{h}_{HGD}) along with the total mass of the remaining attached frost for both the penthouse and the ceiling hung evaporator coils throughout a HGDC that occurs following 48 hours of cooling operation. The HGD efficiency is calculated according to:

$$\mathbf{h}_{HGD} = \frac{Q_{melt}}{Q_{HGD}} \quad (8.4)$$

and it is equal to the ratio of the energy that is required to melt the frost that was initially adhered to the evaporator surface area to the total energy supplied to the evaporator coil during a defrost cycle. This definition of the defrost efficiency definition is consistent with the one used by Cole, (1989).

Figure 8.10 shows that the defrost efficiency as defined in Eq. (8.4) is depends strongly on the time at which the HGDC process is terminated. The defrost efficiency for both the penthouse and the ceiling-hung evaporators increases to an optimum value that occurs just before all of the frost is melted ($\mathbf{h}_{HGD_{penthouse}} \approx 0.69$ and $\mathbf{h}_{HGD_{ceiling-hung}} \approx 0.62$) and then decreases until the termination of the defrost cycle. However, due to the relatively low infiltration rate associated with the penthouse and consequently lower rate of parasitic heat transfer rate, the defrost efficiency of the penthouse evaporator decreases at a much lower rate than does the defrost efficiency of the ceiling-hung evaporator.

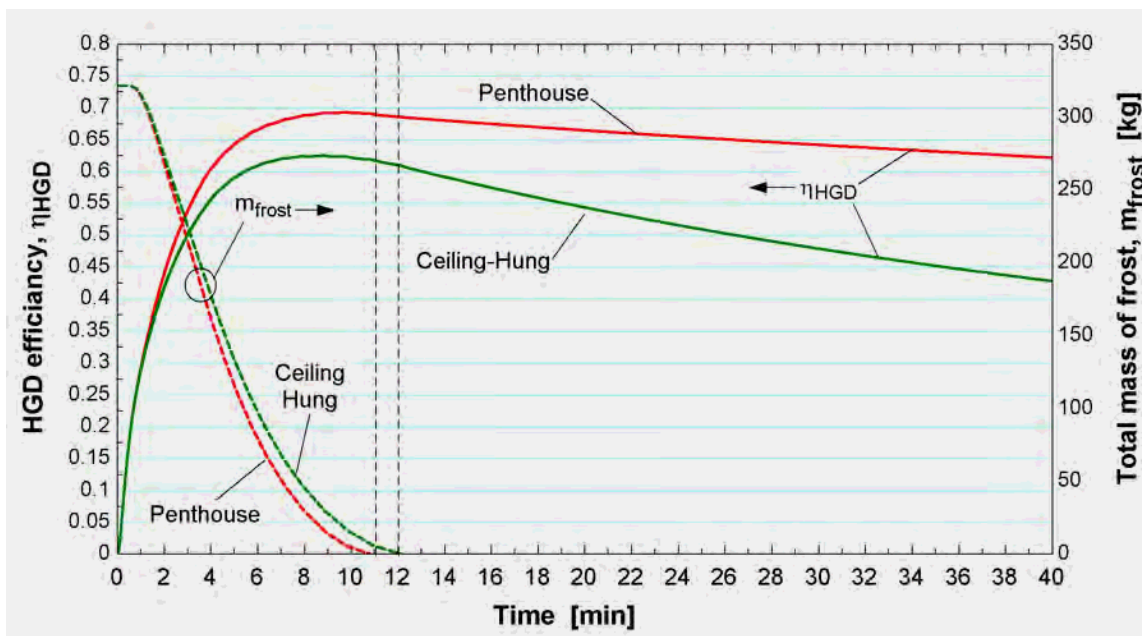


Figure 8.10 hot gas defrost efficiency and the total mass of frost during a HGDC prior to 48 hours of cooling of both the penthouse and the ceiling-hung evaporator coils versus time.

The distribution of the energy transferred from the hot gas during the HGDC that occurs after 48 and 24 hours of cooling for the penthouse evaporator coil are shown in Table 8-4 and 3, respectively. Note that the energy flow distribution is shown at the end of the time that is required to melt all the frost (i.e., for a perfectly timed defrost cycle) and again at the end of a complete 40 minute defrost; this distributions were shown in order to quantify the significance of the excess energy supplied for an improperly terminated defrost cycle.

Table 8-4 shows that increasing the HGD time beyond the actual time required to remove all of the accumulated frost (i.e., from 10.8 minutes to 40 minutes) will increase the parasitic heat load by almost 11% and decrease the hot gas efficiency by 7.0% for the HGDC process that follows 48 hours of cooling (i.e., 69.2% of the total energy provided after 10.8 minutes has been used to melt the frost while only 62.2% of the total

energy provided after 40 minutes is useful).

Table 8-5 shows that increasing the HGD time from the 6.0 minutes required to remove all of the accumulated frost during 24 hours of cooling operation to a standard 40 minute defrost increases the parasitic heat load by almost 19% and decreases the hot gas efficiency by 9.0% (i.e., 56.9% of the total energy provided after 6.0 minutes has been used to melt the frost while only 47.7% of the total energy provided after 40 minutes is useful).

Table 8-4 and Table 8-5 also show that the largest portion of the parasitic heat load in both cases is related to the energy stored in the evaporator coil tubes and fins (Q_{coil}) which has to be transferred back to the refrigerant before cooling mode operation can begin.

The distribution of the energy transferred from the hot gas during the HGDC following 48 and 24 hours of cooling operation of a ceiling-hung evaporator coil are shown in

Table 8-6 and Table 8-7, respectively. It is useful to compare the distribution of energy associated with the penthouse and the ceiling hung evaporator coils.

Table 8-6 shows that the time required to melt all the frost accumulated after 48 hours of cooling operation using the ceiling-hung evaporator is only about 1 minute longer than

it is for the penthouse evaporator; however, the total parasitic heat load of an optimally terminated defrost is almost 13% higher because the parasitic loss throughout the process is substantially larger. The time required to melt all of the frost accumulated after 24 hours of cooling using a ceiling-hung evaporator is only 0.6 minutes longer than for the penthouse evaporator; the increase in the total parasitic heat load is almost 8.5%.

The effect of improperly terminating the defrost process (i.e., increasing the HGDC time beyond the minimum amount of time that is required to melting all of the frost) is much more significant for the ceiling-hung evaporator.

Table 8-6 and Table 8-7 show that the hot gas defrost efficiency is reduced from 60% to 43% (for the defrost process following 48 hours of cooling) and from 52% to 29% (for the defrost process following 24 hours of cooling) for defrost cycles that are terminated after 40 minutes. This difference corresponds to approximately 3 MJ of parasitic heat load for each additional minute of hot gas supply process for a ceiling hung evaporator; this can be compared to 0.7 MJ/minute for the penthouse evaporator.

All the above parasitic heat rate were evaluated using the same approach used in the literature (Cole, (1989) and Al-Mutawa, (1997)) to quantify the direct penalties and the efficiency of the HGDC for both a penthouse and ceiling-hung evaporator to the freezer space as explained in chapter 1. However, there are indirect penalties (i.e. the loss of cooling due to the initiation of the HGDC) that associated with the HGDC that have not

been considered in the literature and would yield to the increase in the overall penalties due to the increase in the time length of the hot-gas stage that are discussed in detail in chapter 9.

Table 8-4 Energy distribution of a HGDS prior to 48 hours of cooling of penthouse evaporator coil.

Mass of frost = 321.5 kg	Time= 10.78 min		Time= 40 min	
Q_{HG}	100%	178.67 [MJ]	100%	198.71 [MJ]
Q_{melt}	69.2%	123.59 [MJ]	62.2%	123.59 [MJ]
Q_{coil}	26.3%	47.000 [MJ]	23.9%	47.481 [MJ]
Q_{air}	3.5%	6.1849 [MJ]	10.9%	21.714 [MJ]
Q_{wall}	1.0%	1.8210 [MJ]	3.0%	5.8556 [MJ]
h_{HGD}	0.69		0.62	

Table 8-5 Energy distribution of a HGDS prior to 24 hours of cooling of penthouse evaporator coil.

Mass of frost = 181 kg	Time= 6.0 min		Time= 40 min	
Q_{HG}	100	121.70 [MJ]	100%	145.26 [MJ]
Q_{melt}	56.94%	69.300 [MJ]	47.7%	69.300 [MJ]
Q_{coil}	38.61%	46.991 [MJ]	32.7%	47.481 [MJ]
Q_{air}	3.61%	4.3907 [MJ]	15.5%	22.491 [MJ]
Q_{wall}	0.84%	1.0193 [MJ]	4.1%	5.9542 [MJ]
h_{HGD}	0.57		0.48	

Table 8-6 Energy distribution of a HGDS prior to 48 hours of cooling of ceiling-hung evaporator coil.

Mass of frost = 321.5 kg	Time= 11.89 min		Time= 40 min	
Q_{HG}	100%	201.67 [MJ]	100%	287.13 [MJ]
Q_{melt}	61.2%	123.45 [MJ]	43%	123.45 [MJ]
Q_{coil}	23%	46.556 [MJ]	16.3%	46.922 [MJ]
Q_{air}	15.9%	32.143 [MJ]	40.8%	117.24 [MJ]
h_{HGD}	0.60		0.43	

Table 8-7 Energy distribution of a HGDS prior to 24 hours of cooling of ceiling-hung evaporator coil

Mass of frost = 181 kg	Time= 6.64 min		Time= 40 min	
Q_{HG}	100%	132.96 [MJ]	100%	235.20 [MJ]
Q_{melt}	51.93%	69.05 [MJ]	29.35%	69.05 [MJ]
Q_{coil}	35.0%	46.570 [MJ]	19.92%	46.871 [MJ]
Q_{air}	13.07%	17.385 [MJ]	50.73%	119.34 [MJ]
h_{HGD}	0.52		0.29	

8.3 Summary

In this chapter, the defrost model was validated through comparison with the experimental data obtained from measurements taken in the field on an instrumented, penthouse mounted evaporator coil. The model in this chapter was subsequently used to evaluate the direct penalties of the HGDP for both a penthouse and ceiling-hung evaporator.

The study showed that:

- 1- The total energy required to heat the evaporator coil metal during the HGDP is large; the energy stored in the evaporator coil metal is between 25% and 37% of the total energy that is consumed during an optimally terminated defrost cycle (i.e., during the defrost time that is required to melt all the frost accumulated during 48 and 24 hours of cooling, respectively) which agrees extremely well with previous work by Coley (1983).
- 2- The hot gas defrost efficiency of the HGDP of a penthouse evaporator is always higher than a ceiling-hung evaporator.

- 3- The effect of increasing the HGDC time beyond the total time required for melting all the frost for the ceiling-hung evaporator is more significant than it is for the penthouse evaporator.
- 4- The difference in the total parasitic heat load due to the increase in the total mass of the accumulated frost at the beginning of the HGDC is very small for the same dwell period of the hot gas stage.

8.4 References

Al-Mutawa, N.K., 1997, Experimental investigations of frosting and defrosting of evaporator coils at freezer temperatures, PhD thesis, Department of Mechanical Engineering, University of Florida

Cole, R.A., 1989, *Refrigeration loads in a freezer due to hot gas defrost and their associated cost.* ASHRAE Transactions, Vol. 95, Part 2

Coley, M.B., 1983, *The cost of frost.* ASHRAE Journal, Vol. 82, No. 9.

Chapter 9 Net Cooling Optimization

The main objective of this chapter is to quantify the total penalty associated with frost accumulation and frost removal during an entire refrigeration cycle (i.e., over an integer number of cooling and defrosting operations) for both the penthouse evaporator and the ceiling-hung evaporator. This is required is needed in order to finally answer the two important questions raised in Chapter 1; 1) what should be the interval between defrost sequences, and 2) for how long should the hot gas be supplied during a Hot Gas Defrost Process (HGDP).

9.1 Penalties considered in the analysis:

It has been shown in Chapters 3 through 8 that the process of frost accumulation on the evaporator coil surfaces during the cooling mode and the process of frost removal during the HGDP diminish the ability of an individual evaporator to extract heat from a space. The frost buildup continuously degrades an evaporator's cooling capacity during normal operation and the frost removal processes most commonly used (hot gas defrost) results in a parasitic heat load to both the space and the refrigeration system during the HGDP. Both of these operational inefficiencies were studied in detail and the magnitude of these losses were quantified in the previous chapters.

The study of the frost and defrost penalties presented in the previous chapters and in the literature has been done individually; that is, it has been assumed that the frost

accumulation and the frost removal process are distinct processes that can be optimized individually. In reality, a more appropriate optimization approach must simultaneously consider both of these processes in an integrated model that will allow the minimization of the total penalty associated with running the refrigeration system, which is the sum of the frost accumulation and defrost parasitic penalties. A comparable optimization will maximize the net heat removal capability of a refrigeration system serving a conditioned space. Ultimately, the optimization of the operation of a refrigeration system cannot be accomplished without considering both aspects of the operation.

In this chapter, the total penalty on the refrigeration cycle is considered, including all major phenomena that may cause a deviation or loss of the actual evaporator cooling capacity, relative to the ideal or rated cooling capacity of the unit. The ideal evaporator cooling capacity is defined as the maximum cooling capacity that can be provided by the evaporator coil as-installed and it is assumed equal to the evaporator's cooling capacity in a frost-free state.

9.1.1 Penalties due to Frost Accumulation

The major penalty associated with the frost accumulation during the cooling mode, as explained in chapter 3, is the continuous decrease in evaporator cooling capacity principally due to the decrease in air flow rate through the evaporator caused by increased pressure drop due to frost as shown in Figure 9.1 and Figure 9.2. Figure 9.1 compares the longitudinal performance of an evaporator accumulating frost (\dot{Q}_{act}) with an ideal evaporator cooling capacity (\dot{Q}_{ideal} , the capacity of the dry coil). The heat removal

capacity that is “lost” due to frost accumulation (Q_{drop}) is represented by the shaded area in Figure 9.1 and calculated according to Eq. (9.1).

$$Q_{drop} = \left[\dot{Q}_{ideal} \times t_{cooling} \right] - \int_0^{t_{cooling}} \dot{Q}_{act} dt \quad (9.1)$$

where $t_{cooling}$ is the total time of cooling mode operation between successive defrosts.

The integrated total cooling energy reduction, Q_{drop} is shown as a function of time in Figure 9.2. Notice that the total refrigeration capacity loss due to the frost accumulation during cooling mode operation increases nearly exponentially with cooling time.

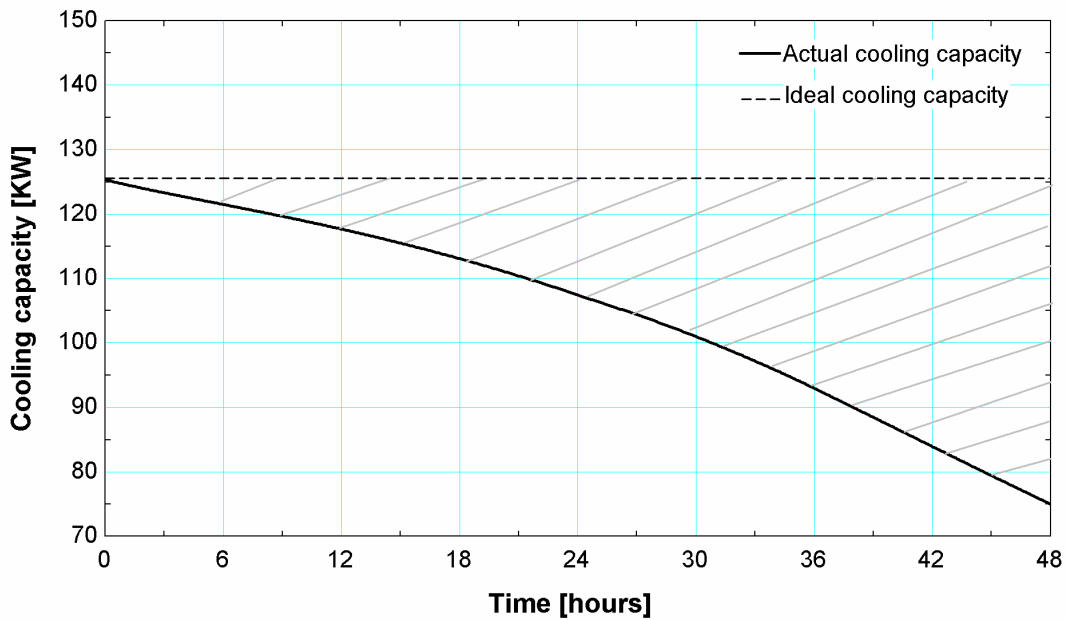


Figure 9.1 Actual and the ideal evaporator cooling capacity versus time during the cooling operation mode.

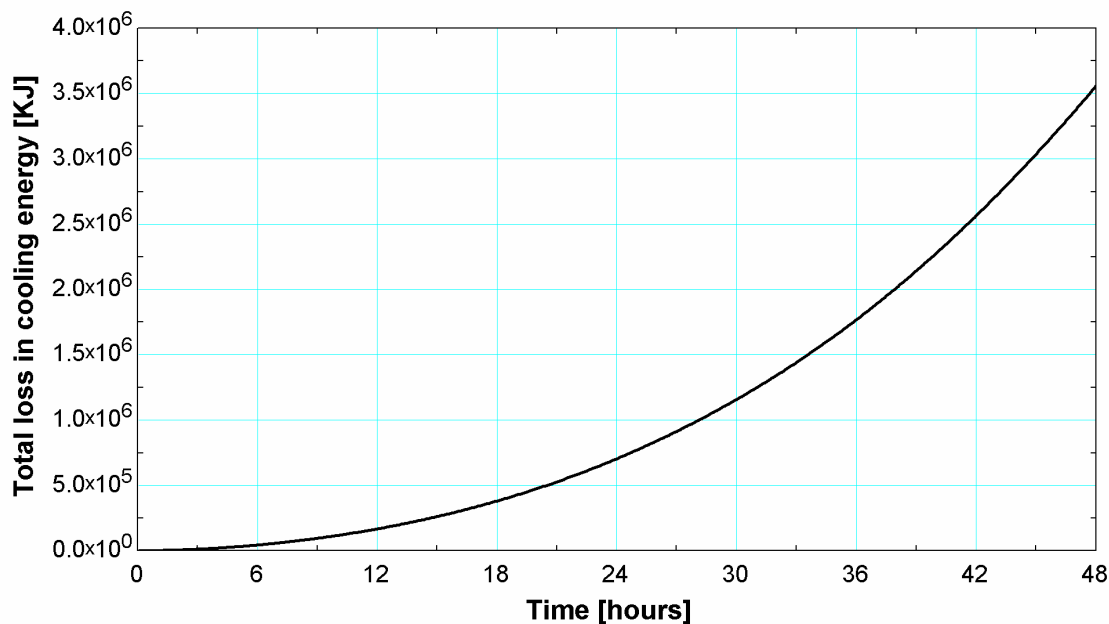


Figure 9.2 Total energy loss during the cooling mode due to frost accumulation versus time during the cooling operation mode.

9.1.2 Penalties due the frost removal

The previous chapter showed that the evaporator coil must pass through several different stages or processes (pump-out stage, hot gas stage, bleed stage) in order to remove the accumulated frost during a complete Hot Gas Defrost Cycle (HGDC). Each of these processes results in a penalty to the refrigeration system and therefore must be included in the current analysis.

There are three major penalties considered here associated with the HGDC:

1. *A decrease in evaporator cooling capacity due to the termination of the cold refrigerant supply during the pump-out stage while the evaporator fans continue operating.*

Although the cold refrigerant supply is terminated as soon as the pump-out stage starts, the evaporator coil will continue to provide some cooling due to the thermal mass of the evaporator, frost, and residual refrigerant charge within the evaporator coils at the time of pump-out initiation. This penalty is modeled as being linear with time based on a curve fit to the experimental data of the evaporator cooling capacity during the pump-out stage, shown previously in chapter 7 and assumed to be constant for all hot gas defrost cycles associated with this evaporator coil. The assumed and measured gross cooling capacity during the pump-out stage for is shown in Figure 9.3.

The total energy loss due to the termination of the cold refrigerant supply during the pump-out stage ($Q_{pump-out}$) is represented by the shaded area shown in Figure 9.3 and calculated according to Eq.(9.2):

$$Q_{pump-out} = \left[\dot{Q}_{ideal} \times t_{pump} - \int_0^{t_{pump}} \dot{Q}_{act} dt \right] \quad (9.2)$$

where t_{pump} is the total time of the pump-out stage.

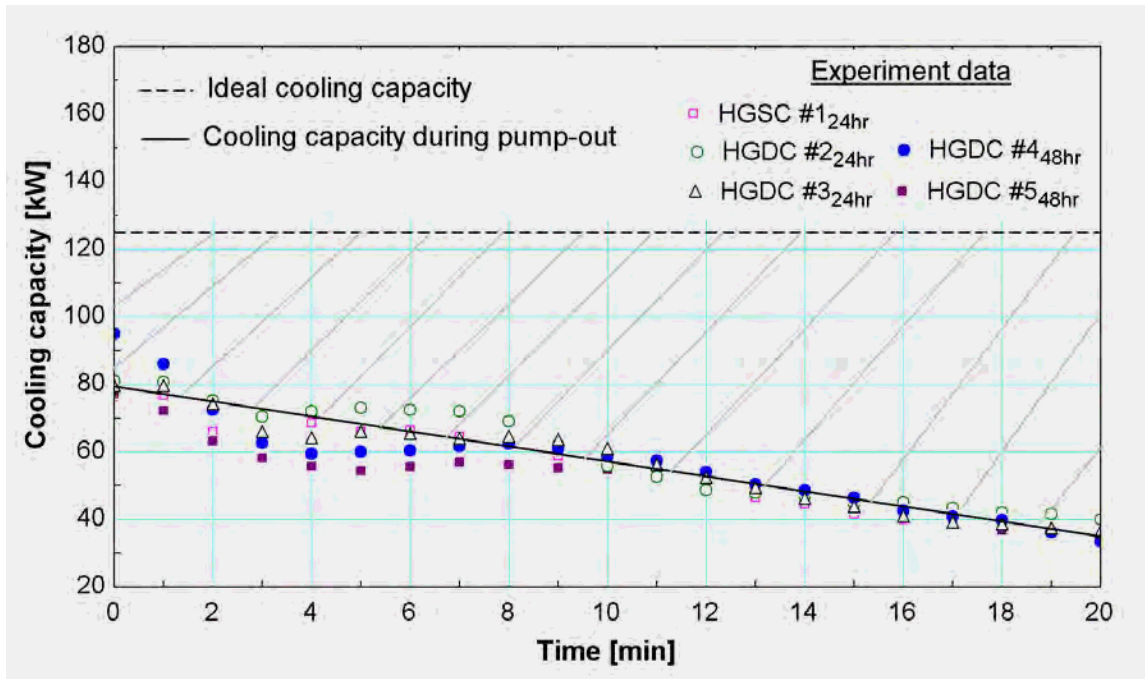


Figure 9.3 Actual and the ideal evaporator cooling capacity as a function of time during the pump-out stage. Also shown are the measured data for gross cooling capacity during pump-out as a function of time for 5 different defrost cycles.

2. *Loss of cooling capacity due to the termination of the cold refrigerant supply and deactivation of the evaporator fans during the Hot-gas and the Bleed stages;*

During the period when hot gas is being supplied and in the subsequent bleed stages of the defrost cycle, the evaporator coil will not provide any cooling; therefore, all of the space cooling requirements have to be met by other evaporators in the space that are continuing to operate. The total energy loss due to this penalty ($Q_{no-cooling}$) is represented by the shaded area shown in Figure 9.4 and is calculated according to Eq. (9.3).

$$Q_{no-cooling} = \dot{Q}_{ideal} \times [t_{HG} + t_{Bleed}] \quad (9.3)$$

where t_{HG} and t_{Bleed} are the time length of the hot-gas stage and the bleed stage , respectively.

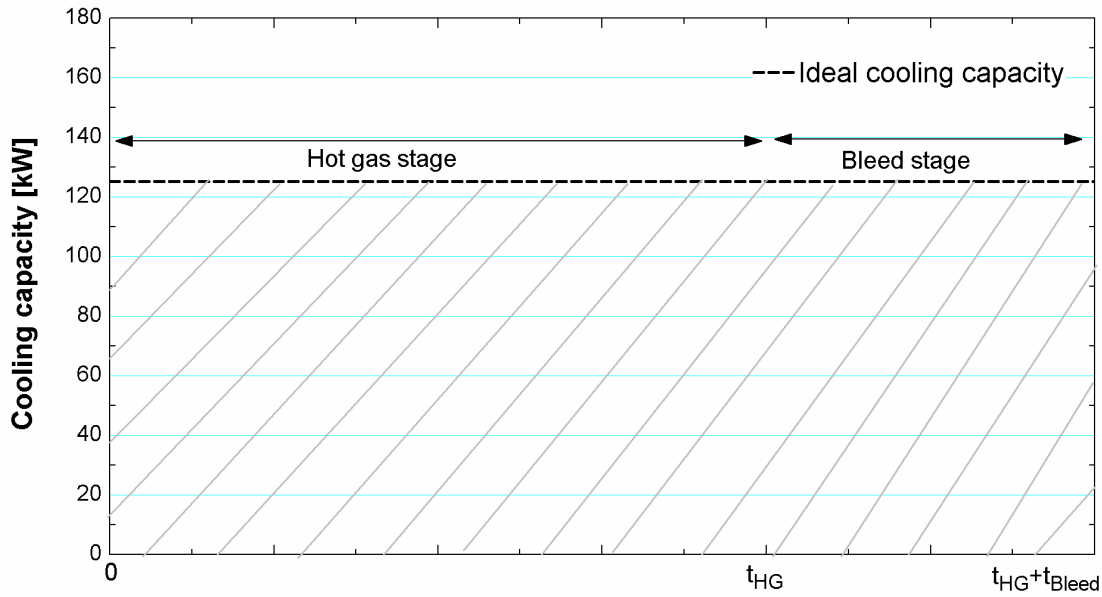


Figure 9.4 Ideal cooling capacity during the hot gas and the bleed stages as a function of time.

3. Negative cooling capacity due to the HGDC parasitic heat load.

Once the hot gas supply is initiated at the start of the hot gas stage, the operation of the evaporator coil, essentially, converts from an evaporator to a condenser. As a result, the evaporator coil will add sensible and, possibly, latent heat to the space rather than extracting heat. The energy stored in the coil mass itself and the energy transferred to the freezer air are both considered to be a form of defrost parasitic heat load. The total parasitic heat load during the hot gas stage is qualitatively shown in Figure 9.5 and is calculated according to Eq. (9.4):

$$Q_{PHL} = \int_0^{t_{HG}} \dot{Q}_{HG} - \dot{Q}_{melting} dt \quad (9.4)$$

where (\dot{Q}_{HG}) is the heat transfer rate from the hot-gas and $(\dot{Q}_{melting})$ is the heat transfer rate actually used to sensibly heat the frost to the melting point and change its phase from solid to liquid.

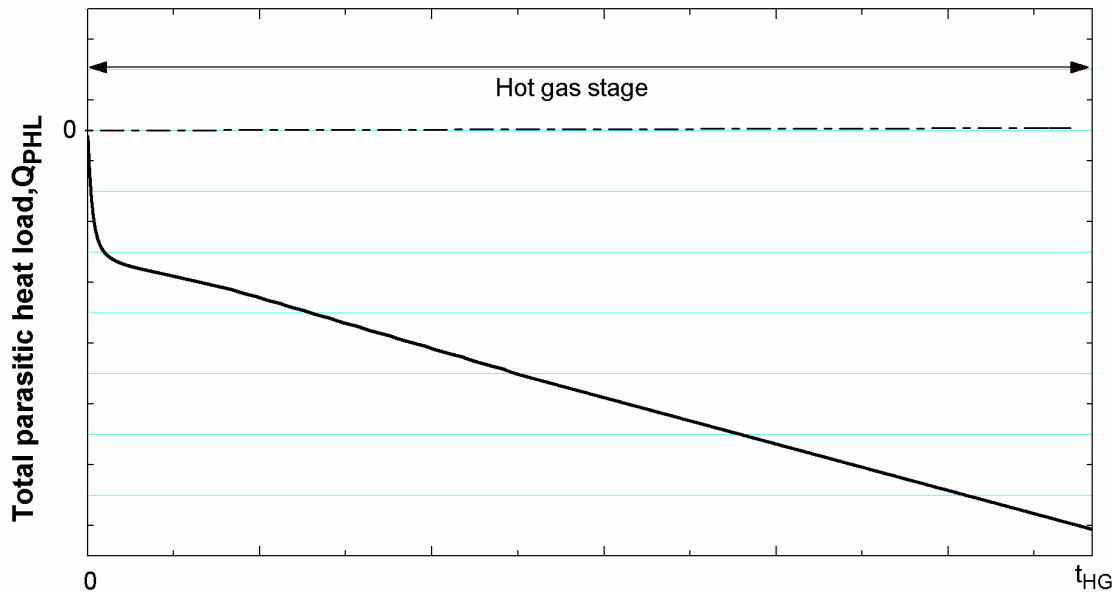


Figure 9.5 Quantitative representation of the total parasitic heat load during the hot gas stage versus time.

Finally the total major penalties associated with frost removal during a hot gas defrost cycle is the sum of those penalties previously discussed:

$$Q_{HGDP} = Q_{pump-out} + Q_{no-cooling} + Q_{PHL} \quad (9.5)$$

and the total major penalty during one complete refrigeration cycle is;

$$Q_{losses} = Q_{HGDP} + Q_{drop} \quad (9.6)$$

9.2 Overall System Efficiency and the Cost of Frost

The overall efficiency of a refrigeration system operating under frosting and defrosting conditions can be defined as the ratio of the actual evaporator coil cooling capacity to the ideal cooling capacity during an entire refrigeration cycle:

$$h_{\text{sys}} = \frac{\dot{Q}_{\text{ideal}} \times (t_{\text{cooling}} + t_{\text{pump}} + t_{\text{HG}} + t_{\text{bleed}}) - Q_{\text{losses}}}{\dot{Q}_{\text{ideal}} \times (t_{\text{cooling}} + t_{\text{pump}} + t_{\text{HG}} + t_{\text{bleed}})} \times 100 \quad (9.7)$$

Note that the time associated with the system efficiency definition is a single frost/defrost sequence of operation. The efficiency associated with any integer multiple of this amount of time will be the same provided that the frost operation begins at the same condition (i.e., frost thickness) that existed at the termination of the defrost operation.

In order to estimate the electrical cost of the losses incurred during a complete refrigeration cycle (Q_{losses}), the cooling operation time of the evaporator coil that would be needed to provide the total loss of the cooling capacity (t_{losses}) is calculated using the ideal evaporator cooling rate:

$$t_{\text{losses}} = \frac{Q_{\text{losses}}}{\dot{Q}_{\text{ideal}}} \times \frac{hr}{3600\text{sec}} \quad (9.8)$$

The energy impact associated with loss of the cooling capacity depends on the refrigeration system efficiency. The current analysis is based approximately on the specific refrigeration system that was used in the experiment. At a suction pressure of

95.6 kPa (14 psia) which is the saturation pressure of ammonia at -34.4°C (-30°F) and a discharge pressure of 1034 kPa (150 psig), a typical modern two stages screw compressor system with an intermediate stage temperature of -11°C will operate at $E_{comp} = 0.654$ HP/kW (2.3 HP/ton)¹ with a motor efficiency of about 0.92. Operation of the heat rejection system (condenser fans and condenser water pumps) will add approximately $E_{cond} = 0.043$ HP/kW (0.15 HP/ton). The five evaporator fans add almost $E_{evap} = 0.114$ HP/kW (0.4 HP/ton)². The corresponding electrical energy demand associated with the total loss of the cooling capacity is therefore:

$$ELC = \frac{\dot{Q}_{ideal} [kW] \times (E_{cond} + E_{evap} + E_{comp}) \left[\frac{HP}{kW} \right] \times \left[0.7457 \frac{kW}{HP} \right] \times t_{losses} [hr]}{h_{motor}} \quad (9.9)$$

9.3 Infiltration load

In low temperature storage freezer applications, the difference in the infiltration load to the conditioned space between different seasons of the year can be a significant factor that may affect the rate of frost accumulation and therefore the required frequency of HGDP. Because the frost and defrost experiments shown previously were conducted during the summer, estimates of a summer infiltration load to the freezer are used. Since the freezer used in the experiment was for long term storage of packaged food products and since the measured specific humidity ratio in the freezer was nearly constant during the experiments (Figure 4.15, chapter 4), all of the collected water condensate is assumed to have been transferred to the freezer due to ambient infiltration. Based on these

¹ FES system incorporation- GEA refrigeration division

² SpaceMax IRF Series Equipment- (King) United Dominion Company

assumptions, the mass flow rate of the water transferred to the freezer due to the infiltration process (per evaporator), $\dot{m}_{water,inf}$ is estimated according to:

$$\dot{m}_{water,inf} = \frac{m_{frost}}{t_{exp}} = \frac{188[kg]}{86400[sec]} = 2.176 \times 10^{-3} \left[\frac{kg}{sec} \right] \quad (9.10)$$

where m_{frost} is the total mass of the collected water condensate and t_{exp} is the duration of the experiment.

A water mass balance on the freezer due to the infiltration process is given by:

$$\dot{m}_{water,inf} = \dot{m}_{air,inf} (\mathbf{w}_{amb} - \mathbf{w}_{frz}) \quad (9.11)$$

where $\dot{m}_{air,inf}$ is the mass flow rate of the infiltrated air, \mathbf{w}_{amb} and \mathbf{w}_{frz} are the humidity ratio of the ambient air and the freezer air, respectively. By rearranging Eq. (9.11) and assuming a typical summer air ambient temperature and relative humidity (state of Iowa, USA) of 25° C and 60%, respectively, it is possible to estimate the infiltration air flow rate (per evaporator), assuming that all of the frost is a result of infiltration.

$$\dot{m}_{air,inf} = \frac{\dot{m}_{water,inf}}{(\mathbf{w}_{amb} - \mathbf{w}_{frz})} = \frac{2.176 \times 10^{-3}}{(0.01194 - 0.0002687)} = 0.17 \left[\frac{kg}{sec} \right] \quad (9.12)$$

The total load due to the infiltration during the 24 hours of the experiment cooling time is:

$$Q_{inf} = \dot{m}_{air,inf} (i_{amb} - i_{frz}) (t_{exp}) = 1190[MJ] \quad (9.13)$$

where i_{amb} and i_{frz} are the enthalpy of the moist ambient and the freezer air, respectively. The total cooling load provided by the evaporator coil during the experiment is:

$$Q_{cooling} = 10123 [MJ] \quad (9.14)$$

The ratio of the total load due to the infiltration to the total cooling load provided by the evaporator coil is:

$$\frac{Q_{inf}}{Q_{cooling}} \times 100 = 11.75\% \quad (9.15)$$

Equation.(9.15) shows that only 11.75% of the total cooling load is due to the infiltration; therefore, the difference in the infiltration load during the different seasons of the year is expected to be small especially when it is compared to the experiment uncertainty. However the impact of the change in the infiltration load may have a severe effect on the frost accumulation rate. In other words, if the infiltration rate of air remains the same but the humidity ratio of outside air drops (as in winter) then the infiltration of water may drop dramatically especially if it is assumed all the infiltration is coming directly from the outside air. Nevertheless, this variation in infiltration is not expected to significantly affect the freezer load but it will impact the degradation rate of the evaporator cooling capacity due to frost formation. In the next section, all the analyses are performed assuming the freezer air is not effected by the change in the outside air moisture content (a constant air and moisture infiltration rate all around the year), whereas (in section 9.5) a sensitivity analysis of the effect of changing the freezer air humidity ratio to the overall system efficiency and to the optimum cooling operation intervals between defrost cycles is shown.

9.4 Optimization results

All of the penalties due to the frost accumulation and removal that were discussed in the previous sections are calculated and used to compute the overall system efficiency as defined in Eq. (9.7), the annual electrical demand based on Eq. (9.9) and the annual electrical cost (cost of frost) for both a penthouse and a ceiling-hung evaporator under various conditions.

A hot gas defrosting following cooling operation intervals (i.e., time between defrost) of 12, 24, 36 and 48 hours of cooling are considered. For each case, penalties are calculated assuming various defrost durations, including:

- 1) perfect termination of the hot gas defrost cycle using the exact time required for all of the frost to be removed,
- 2) a 50% increase relative to the exact time,
- 3) a constant 30 min hot gas stage dwell period, and
- 4) a constant 40 min hot gas stage dwell period.

The dwell period of the pump-out and bleeding stages are fixed and set equal to the facilities' default time settings of 20 and 10 minutes, respectively, for all cases. The penalty associated with the frost accumulation during the cooling mode is assumed to be equal for both the penthouse and the ceiling hung evaporators. A summary of these calculations is provided in Table 9-2 through Table 9-9. The exact time required for complete removal of the frost for each case is calculated using the theoretical model for hot gas defrost and shown in Table 9-1.

Table 9-1 The exact time required for a complete frost removal from a penthouse and a ceiling hung evaporators for a different cooling time length between defrost cycles.

Evaporator	Dwell period between defrost cycles [hours]			
	12	24	36	48
The exact time required for a complete removal of frost [minutes]				
Penthouse	3.2	6.0	8.4	10.8
Ceiling-hung	3.5	6.6	9.4	11.9

The geometry and other characteristics of the evaporator coil used in the analyses are identical to those associated with the penthouse evaporator coil studied in the experiment and discussed previously. The theoretical model of frosting operation, described in Chapter 3, is used to predict the initial frost thickness, density, and thermal conductivity in each row of the evaporator at the beginning of each defrost cycle. Constant values of -27.65 °C (-17.7 °F) inlet air temperature and 90% inlet air relative humidity to the evaporator coil during the cooling mode operation were used for the simulations. The theoretical model of the HGDP, shown previously in Chapter 7, is used to quantify the hot gas parasitic heat load utilizing the approach discussed in Chapter 8.

Figure 9.6 shows the magnitude and origin of the various frost penalties as a function of the cooling operation intervals (i.e., time between defrost cycle) for a total operating time of 48 hours of operation (the lowest common denominator of the operation intervals). By using a common operating interval, the cooling penalties can be compared directly. Figure 9.6 is for a penthouse evaporator coil and includes 3 different cooling operation intervals between defrosts of (12, 24 and 48 hours); therefore, the results shown for the 12 hour interval are consistent with four contiguous refrigeration cycles and the results for the 24 hours interval are consistent with two contiguous refrigeration cycles.

Figure 9.6(a) through (d) are for different hot gas dwell durations (exact time to melt frost, 150% exact time, 30 minutes and 40 minutes, respectively).

It can be seen from Figure 9.6(a) through (d) that the penalty due to frost accumulation during the cooling mode (Q_{drop}) increases as the cooling operation interval increases; this result is expected since the increase in the cooling dwell period increases the mass of the accumulated frost and, as a consequence, decreases the available evaporator cooling capacity. This loss of cooling capacity increases the total loss of cooling exponentially with time, as shown in Figure 9.2.

All of the penalties related to frost removal during the HGDP ($Q_{pump-out}$, $Q_{no-cooling}$, Q_{PHL}) decrease as the cooling operation interval increases. The penalty due to the pump-out process ($Q_{pump-out}$) is constant regardless of the cooling dwell period and therefore its value for a 48 hour operating period depends on the number of defrosts that occurs (i.e., it will be four times higher for a 12 hour operation interval than it was for a 48 hour operation interval).

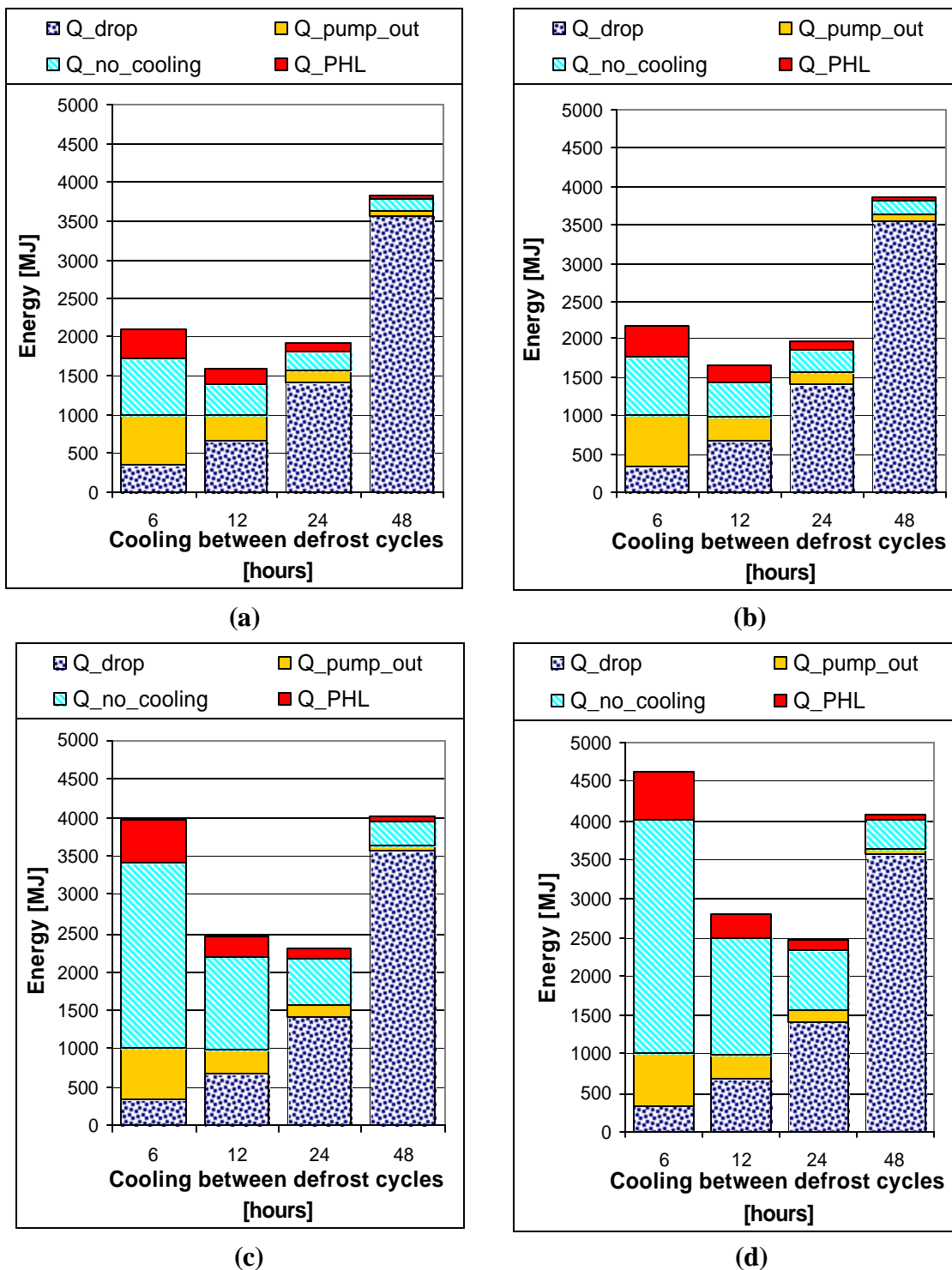


Figure 9.6 Penalties as a function of cooling operation intervals between defrost cycles for two days of continuous penthouse evaporator operation using a hot gas stage dwell period that is equal to ; a) the exact time required to melt the frost, b) 150% of the exact time required to melt the frost, and a constant dwell period of d) 30 minutes, c), and d) 40 minutes.

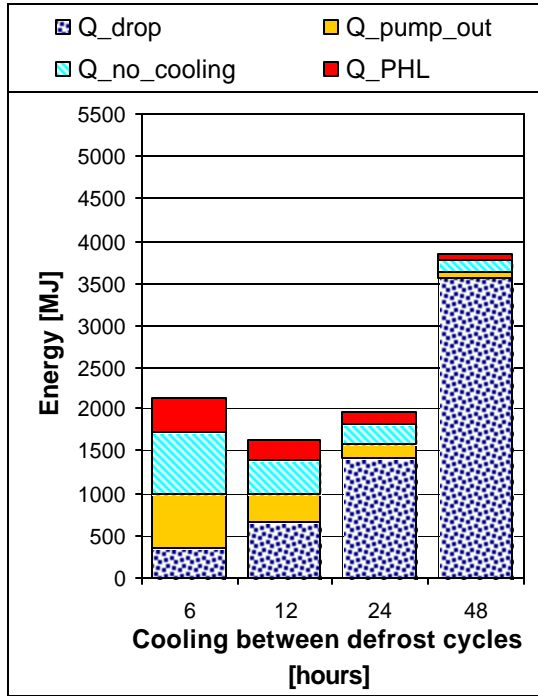
The penalty $Q_{no-cooling}$ is the penalty due to the termination of the cold refrigerant supply and the evaporator fan power during both the hot-gas and the bleed stages. Therefore, this penalty will be directly related to the time required to defrost. The time required to defrost does not depend directly on the time between defrosts due to the bleed stage which is fairly long and it does not depend on the amount of frost accumulated. For example, in the case of a perfect termination of the defrost process, shown in Figure 9.6(a), doubling the cooling interval will approximately double the time required to completely melt all the frost (as shown in Table 9-1); intuitively, this should lead to almost to the same overall hot gas stage dwell period and therefore the same overall value of $Q_{no-cooling}$ for all cases. However, the duration of the bleed stage is assumed to be constant and therefore the value of $Q_{no-cooling}$ actually tends to increase somewhat as the cooling interval decreases even for perfect termination of the defrost process. Notice that the sensitivity of the value of $Q_{no-cooling}$ to the cooling increases for those cases where the hot gas stage duration is held constant (i.e., Figure 9.6c and Figure 9.6d); in these cases the total value of $Q_{no-cooling}$ decreases by one half as the cooling dwell time is doubled.

Finally, it has been shown in Chapter 8 that increasing the initial mass of the accumulated frost at the beginning of the HGDC does not cause a significant change in the total hot gas parasitic heat load; therefore, Q_{PHL} will decrease as the cooling operation interval decreases due to the increased number of hot gas defrost cycles.

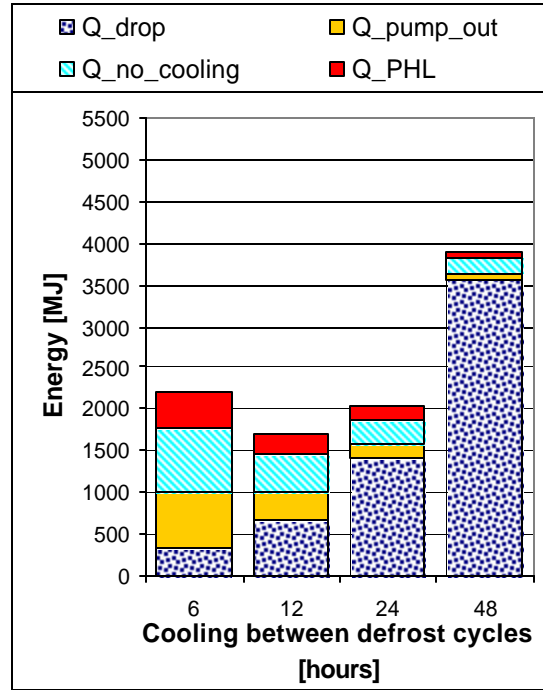
Figure 9.7 shows the calculated penalties as a function of the cooling operation intervals for a period of 48 hours of operation with a ceiling-hung evaporator coil (as opposed to a penthouse coil which was shown in Fig. 6). As with Fig. 6, results are shown for various cooling intervals (12, 24, and 48 hours) and various defrost durations (exact termination, 150% times the exact termination, and 30 and 40 minutes). The same general observations that were discussed previously in the context of Figure 9.6 can be seen in Figure 9.7.

Recall that the main differences between the penthouse and ceiling-hung evaporators included in this analysis are related to the penalty associated with the hot-gas defrost parasitic heat load, Q_{PHL} . This penalty is somewhat higher for the ceiling-hung evaporator due to the larger heat transfer rate that results from the larger temperature difference between the ceiling-hung evaporator coil surfaces and the freezer air temperature. Also, there is a slight increase in time required to completely remove the frost from a ceiling-hung evaporator as compared to a penthouse evaporator. The effects of these differences can be seen clearly in Figure 9.7(c) and (d) where the time length of the hot gas stage is held constant at 30 and 40 minutes, respectively.

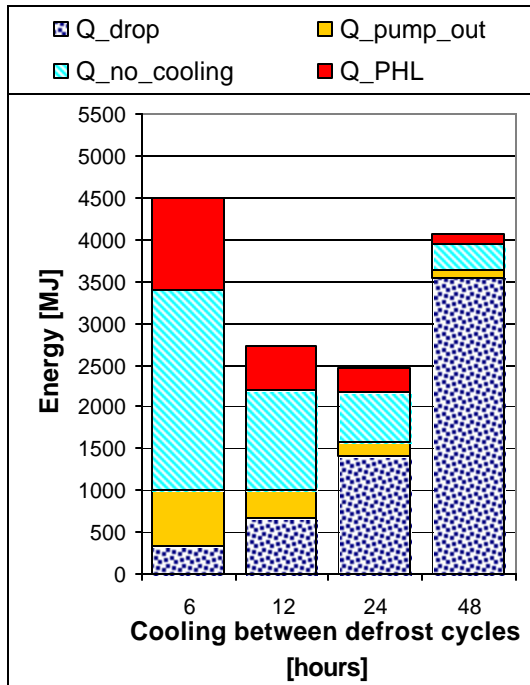
The effect of the different configurations can also be seen in Figure 9.8 and Figure 9.9 which show the percentage of the overall penalty Q_{losses} that can be attributed to the defrost (Q_{PHL}) as a function of the cooling operation interval for different dwell periods of the hot gas stage for the penthouse and the ceiling-hung evaporator, respectively.



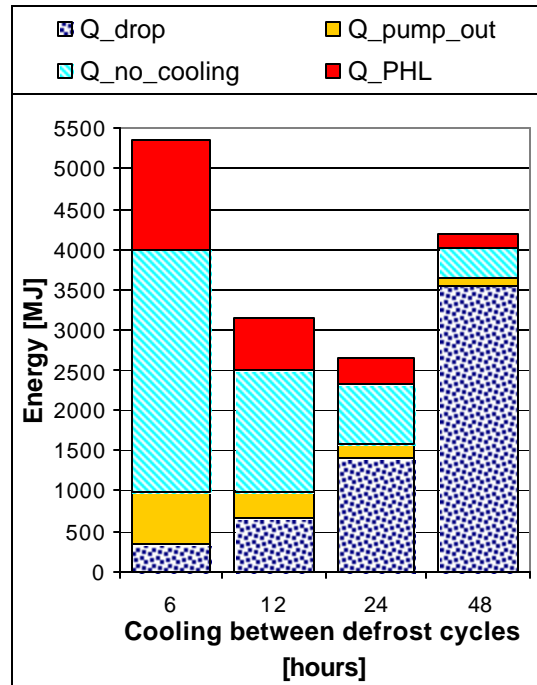
(a)



(b)



(c)



(d)

Figure 9.7 Frost penalties as a function of cooling operation intervals between defrost cycles for two days of continuous operation of a ceiling-hung evaporator using hot gas stage dwell periods that are equal to ; a) the exact time required to melt the frost, b) 150% of the exact time required to met the frost, and a constant dwell period of d) 30 minutes, c), and d) 40 minutes.

It can be seen from Figure 9.8 that the ratio of the hot gas parasitic heat load to the overall penalties associated with frost accumulation and removal varies slightly with increasing the dwell period of the hot gas stage in the case of the penthouse evaporator, whereas increasing the dwell period of the hot gas stage in the case of the ceiling-hung evaporator causes a significant increase of the ratio of the hot gas parasitic heat load to the overall penalties (Figure 9.9).

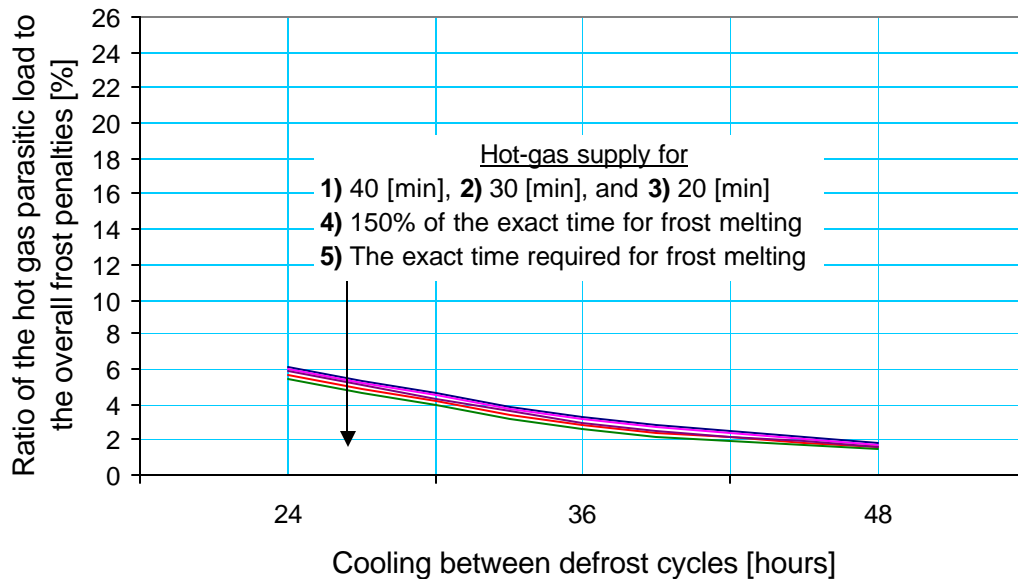


Figure 9.8 Percentage of the overall penalty that is due to the hot gas defrost parasitic heat load as a function of the cooling operation interval for different dwell periods of hot gas stage for the penthouse evaporator coil.

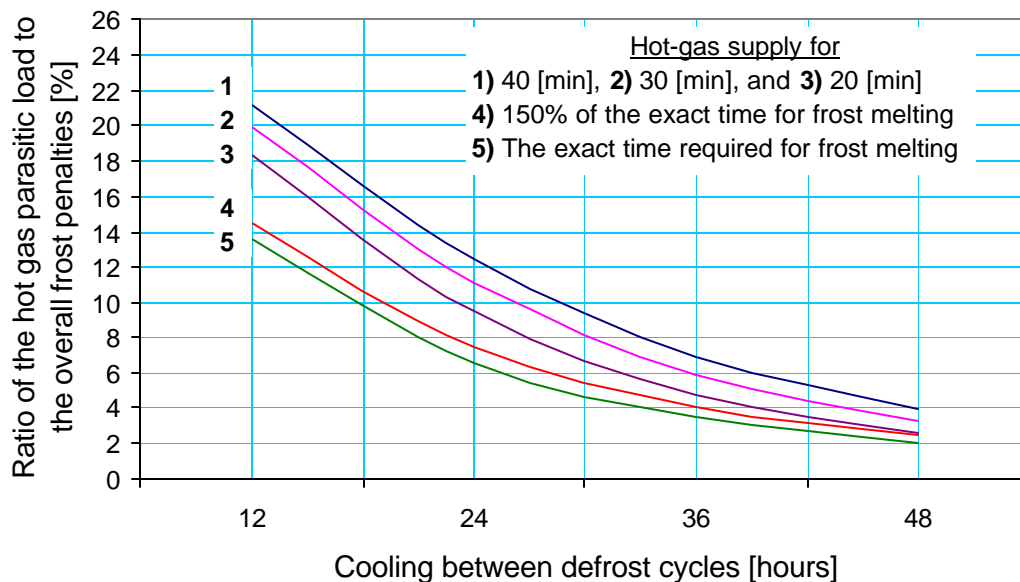


Figure 9.9 Percentage of the overall penalty that is due to the hot gas defrost parasitic heat load as a function of the cooling operation interval for different dwell periods of hot gas stage for the ceiling-hung evaporator coil.

Figure 9.10 shows the percentage increase of the overall penalties associated with frost accumulation and frost removal for the ceiling hung evaporator case compared to the penthouse evaporator as a function of cooling operation interval. It can be seen from Figure 9.10 as well as from Figure 9.6 and Figure 9.7 that the largest difference between the total penalties associated with frost accumulation and frost removal calculated for the ceiling hung and the penthouse evaporators occurs when the cooling dwell period is set to its lowest value (12 hours) and the hot gas stage dwell period is set to a constant value of 20, 30 or 40 minutes; in this case, the percentage increase of the overall penalties increases from less than 2% for the case where a perfect hot gas dwell period is used to 8%, 11% and 13%, respectively, compared to the overall penalties calculated for the penthouse under the same operating conditions (operating interval and hot gas dwell period). This effect is mainly due to the difference in the magnitude of (Q_{PHL}) that exists

for the two different evaporator types, shown previously in Figure 9.8 and Figure 9.9. More interestingly, it can be seen from Figure 9.6 and Figure 9.7 that at these particular cooling operation intervals (12 hours) the most dominant penalty is $Q_{no-cooling}$.

As the cooling operation interval increases, the percentage difference between the overall penalties calculated for the penthouse and the ceiling-hung evaporators decrease. This is due to the significant increase in Q_{drop} which begins to dominate the other penalties.

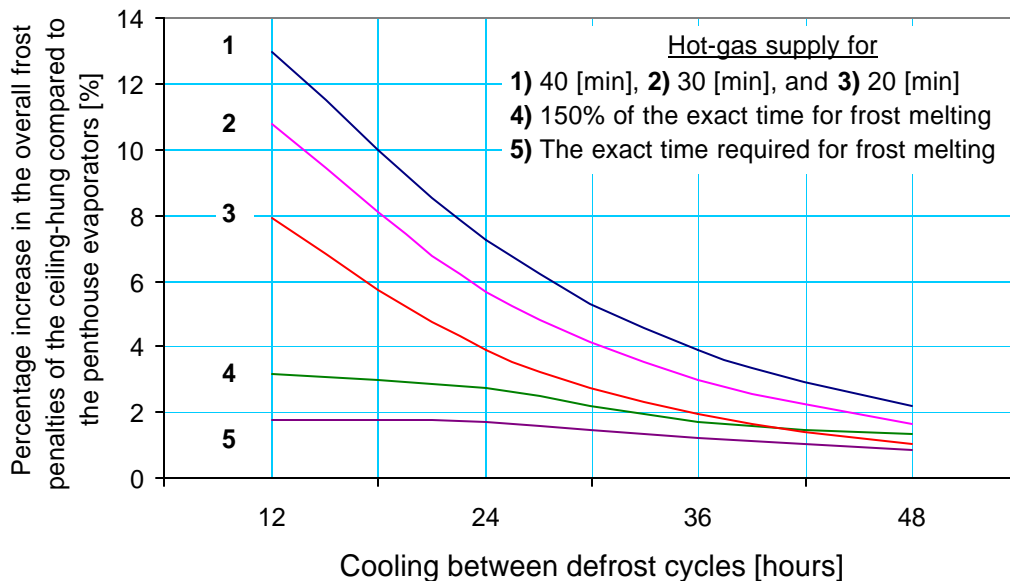


Figure 9.10 Percentage increase in the overall penalty associated with frost accumulation and removal for the ceiling-hung as compared to the penthouse evaporator as a function cooling operation interval for different dwell periods of the hot gas stage.

Figure 9.11 and Figure 9.12 show the overall system efficiency (h_{refg}) as a function of cooling operation interval for different dwell periods of the hot gas stage for the

penthouse and the ceiling-hung evaporators, respectively. One of the interesting results that can be seen from Figure 9.11 and Figure 9.12 is that there is an optimal defrost duration and an optimum interval of cooling operation between defrost cycles at which a maximum refrigeration efficiency can be achieved.

Figure 9.11 and Figure 9.12 show that for all the cases where the hot gas stage dwell period is held constant, a cooling operation interval of 18 hours provides the maximum system efficiency. Also it can be seen that the maximum system efficiency of the penthouse evaporator coil increases from 89.4% to 91.2% as the gas stage dwell period decreases from 40 to 20 minutes. The maximum system efficiency of the ceiling-hung evaporator coil increases from 88.4% to 90.7% as the gas stage dwell period decreases from 40 to 20 minutes. However as the duration of the hot gas stage is set to equal exactly the ideal duration required to melt all the frost, the optimum system efficiency is shifted to a lower cooling operation interval (from approximately 18 to 12 hours). However the difference in the optimum overall system efficiency as the cooling operation intervals shifts from 18 to 12 hours in both the penthouse and the ceiling-hung evaporators is small, only $\sim 0.4\%$.

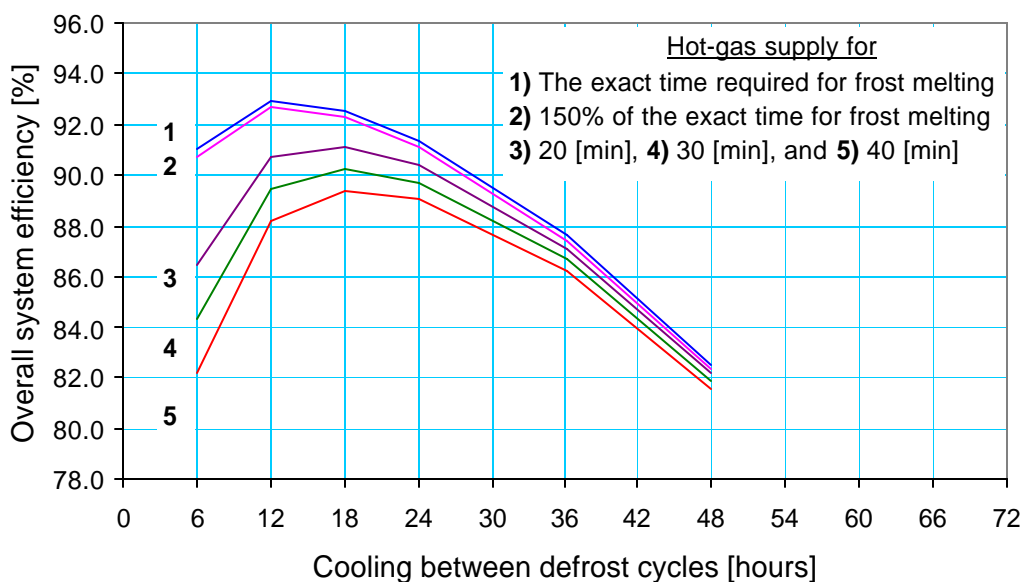


Figure 9.11 Overall system efficiency as a function of cooling operation interval for a penthouse evaporator coil with various hot gas stage dwell periods.

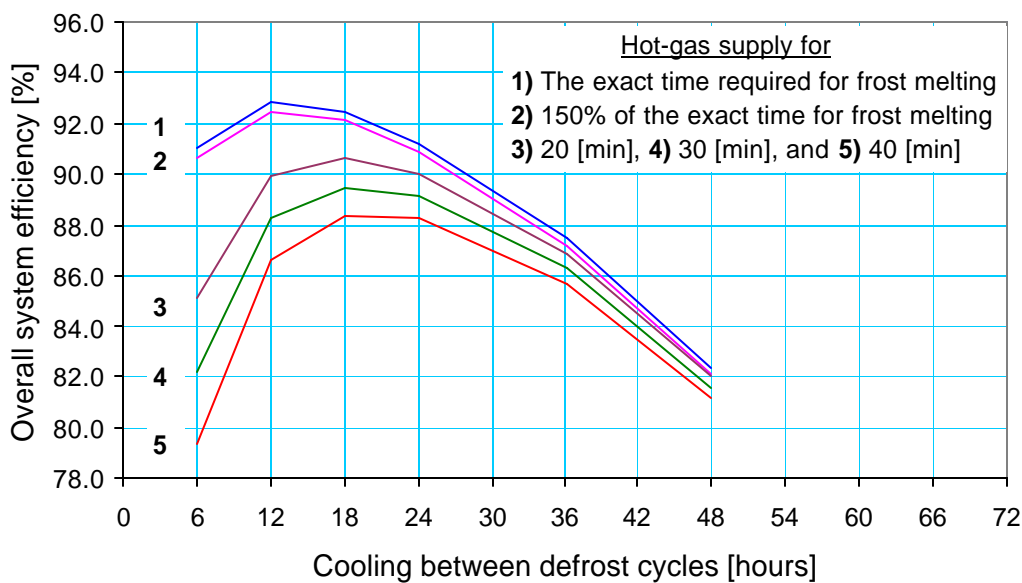


Figure 9.12 Overall system efficiency as a function of cooling operation interval for a ceiling-hung evaporator coil with various hot gas stage dwell periods.

Figure 9.13 and Figure 9.14 show the annual electrical consumption that results from the frost accumulation and frost removal processes per evaporator, calculated using Eq.

(9.9), as a function of cooling operation interval for different dwell periods of hot gas stage for the penthouse and the ceiling-hung evaporators, respectively. The annual electric consumption is calculated for a single evaporator (nominal 125.3 kW) assuming a constant refrigeration load throughout the year and neglecting the change in the infiltration load that may occur during the different seasons; therefore, the demand is likely a maximum value that could be expected since the experimental and simulation conditions were consistent with summer operation when frost accumulation and load are the largest.

Figure 9.13 and Figure 9.14 show that for all cases where the hot gas stage dwell period is held constant, cooling operation intervals of 18 hours provide the minimum electrical usage associated with frost formation and frost removal; this observation is consistent with achieving the highest refrigeration system efficiency. Also notice that the annual electrical penalty associated with the penthouse evaporator coil decreases by 14,500 kWh as the gas stage dwell period decreases from 40 to 20 minutes. On the other hand, the annual electrical penalties the ceiling-hung evaporator coil decreases by almost 18,771 kWh as the gas stage dwell period decreases from 40 to 20 minutes. This difference is related to the higher defrost penalty incurred by the ceiling-hung evaporator; the extra 20 minutes spent defrosting is more costly for a ceiling-hung unit. Also notice that by changing the current warehouse setting from its current setting of cooling interval of 24 hours to the optimal cooling interval of 18 hours and changing the hot gas stage duration from its current setting of 30 minutes to a more optimal setting of 7 minutes (150% of the ideal hot gas stage duration), the annual electrical penalty can be reduced by

19,884 kWh per evaporator coil. This saving in the electrical penalties increases to almost 22,554 kWh for a ceiling-hung evaporator.

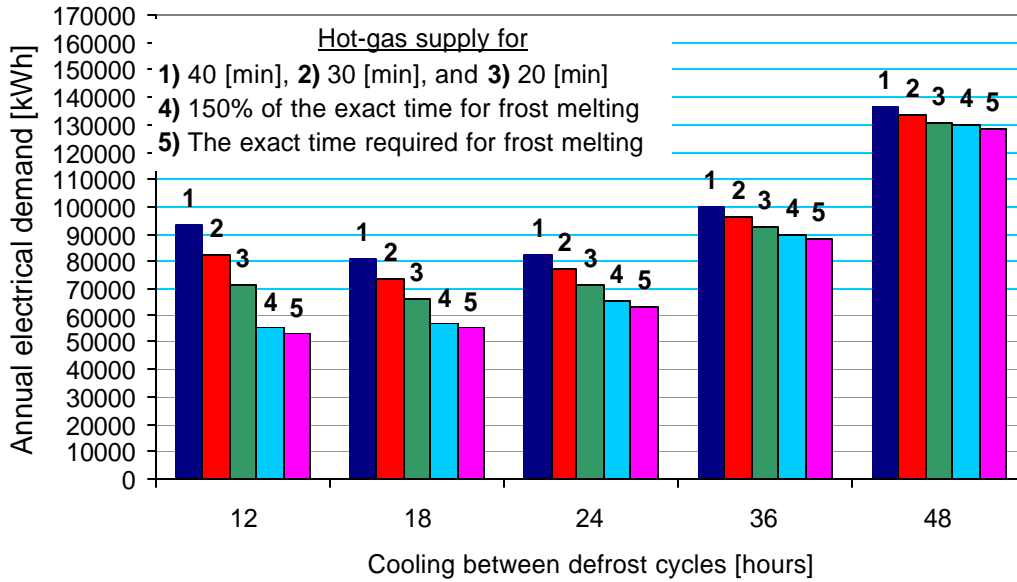


Figure 9.13 Annual electrical penalty as a function of cooling operation interval for a penthouse evaporator coil with various hot gas stage dwell periods.

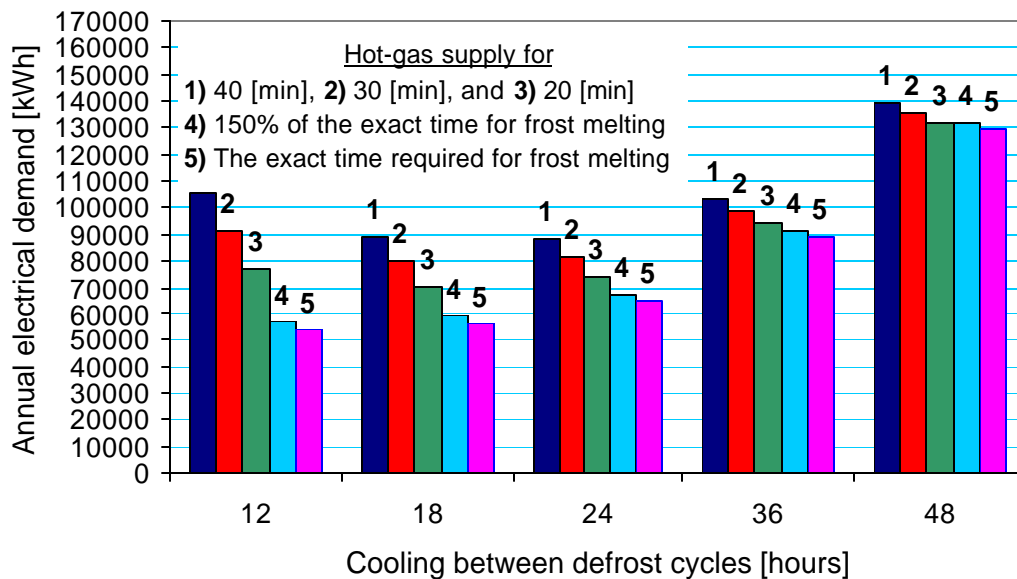


Figure 9.14 Annual electrical penalty as a function of cooling operation interval for a ceiling-hung evaporator coil with various hot gas stage dwell periods.

Figure 9.15 and Figure 9.16 show the annual electrical cost for a single evaporator due to the frost accumulation and frost removal assuming an electrical rate of (\$0.08/kWh) as a function of cooling operation interval for different dwell periods of the hot gas stage, for both the penthouse and the ceiling-hung evaporators, respectively. Notice that by changing the cooling interval from its setting of 24 hours to 18 hours and the hot gas duration from its current 30 minute setting to 7 minutes (150% of the ideal hot gas stage duration), the annual electrical cost can be reduced by \$1,600 per evaporator coil. This saving in the electrical cost would increase to almost \$1,800 in the case of the ceiling-hung evaporator.

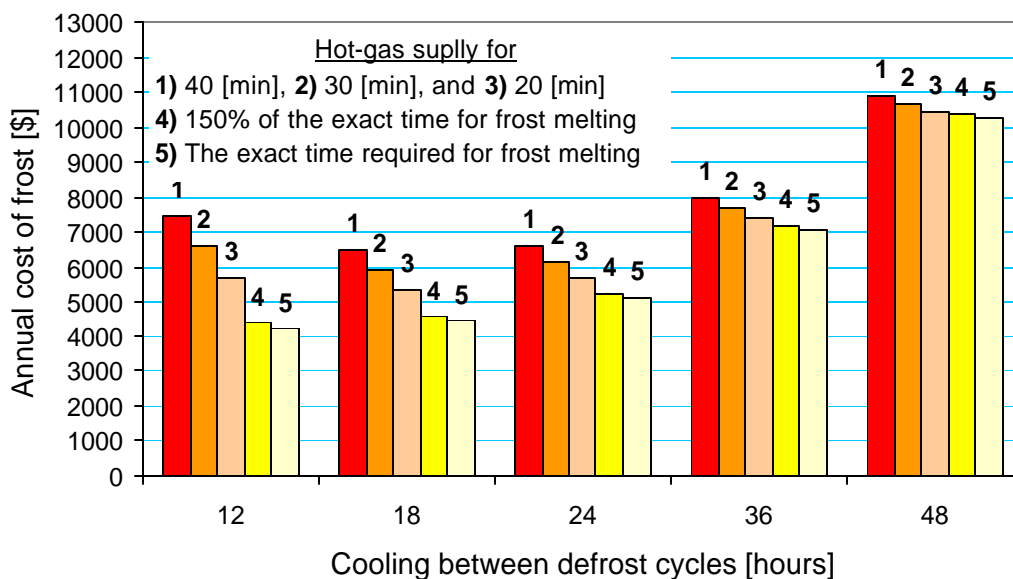


Figure 9.15 Annual cost of frost as a function of cooling operation interval for a penthouse evaporator coil with various hot gas stage dwell periods.

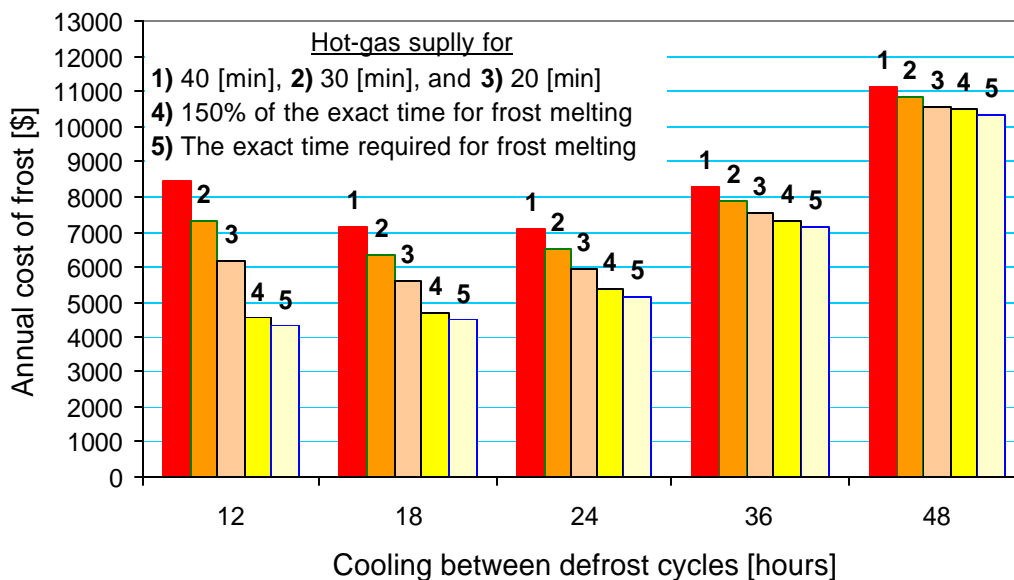


Figure 9.16 Annual cost of frost as a function of cooling operation interval for a ceiling-hung evaporator coil with various hot gas stage dwell periods.

Table 9-2 through Table 9-9 shows the detailed calculations of the frost penalties that were considered above as a function of cooling operation interval for different dwell periods of the hot gas stage and for both the penthouse and the ceiling-hung evaporators. Table 9-2 through Table 9-9 show that the penalty of increasing the hot gas duration beyond the minimum value required (i.e., the exact termination case) can be expressed as an energy per time of defrost. In the previous chapter this excess defrost time penalty was calculated considering only the hot gas defrost parasitic heat (Q_{PHL}) to be the only penalty associated with the frost removal without considering the penalty of not cooling ($Q_{no-cooling}$) which increases with increasing the hot gas stage dwell period.

It can be seen from Table 9-2 through Table 9-9 that by including $Q_{no-cooling}$, the excess defrost time penalty increases from 0.7 MJ/min (which is only based on the hot gas

defrost parasitic heat load) to 8.1 MJ/min for the penthouse evaporator case and from 3 MJ/min to 10.5 MJ/min for the case of the ceiling-hung evaporator coil. This clearly shows that the penalty of not cooling is much higher than the penalty due to the hot gas defrost parasitic load in both the penthouse and the ceiling-hung evaporator.

One difficulty in decreasing the hot gas dwell period is the tendency for many evaporators to accumulate frost in unwanted and hard to defrost areas such as the refrigerant inlet header or the evaporator coil frame (as shown in Figure 9.17) as well as extensive frost accumulation on some parts of the evaporator coil due to poor or non-uniform air circulation or a high moisture infiltration rate (as shown in Figure 9.18). Figure 9.18 shows that excessive ice has accumulated on the bottom row of the evaporator. It is likely that one of the reasons for what would otherwise appear to be an excessively long hot gas dwell period (i.e., far beyond the duration that is required to remove the major portion of the accumulated frost) is the perceived need to apply sufficient energy to melt away the frost in these unwanted areas.

The problem with this strategy is that increasing the hot gas stage dwell period result in an increase in two penalties: the hot gas defrost parasitic heat load as well as the cooling capacity that must be provided by other evaporator coils (as explained in the previous section). As a result, the physical processes that lead to the accumulation of localized regions of excess frost should be understood and eliminated so that the hot gas dwell period can be shortened.

Another penalty that has not been considered in the current analysis is the effect of the hot gas defrost parasitic heat on the food quality. Products stored in close proximity to a defrosting evaporator may experience unwanted and undesirable temperature rise. Increasing the hot gas dwell time or the number of the hot gas defrost cycles may exacerbate this negative food quality impact on the food quality; this is especially true for unpackaged goods.



Figure 9.17 Excessive frost accumulation on the inlet refrigerant header and the frame of the evaporator coil.



Figure 9.18 Excessive frost accumulation on the bottom of the evaporator coil

Table 9-2 Frost penalties and the annual cost of frost for a penthouse evaporator coil with a cooling operation interval of 12 hours and various hot gas stage dwell times.

<i>Cooling for 12 hours, Mass of frost =92 kg</i>								
	Time length of the hot-gas stage [minutes]							
	40		30		5.0		3.2	
Q_{drop}	166.1		166.1		166.1		166.1	
$Q_{pump-out}$	82.2	534.52	82.2	453.2	82.2	247.85	82.2	231.98
$Q_{no-cooling}$	375.9		300.7		112.77		99.24	
Q_{PHL}	76.42		70.26		52.88		50.54	
Q_{losses}	700.62		619.3		413.95		398.08	
Q_{ideal}	5939.2		5864		5676.1		5662.56	
h_{refg}	88.2%		89.4%		92.7%		93.0%	
t_{losses} [hr]	1.55		1.37		0.92		0.88	
Annual ELC [kWh]	83482.65		73790.2		49324.61		47433	
Cost [\$]	6679		5903		3946		3795	
Unit = [MJ], Electrical rate cost of \$0.08/kWh								

Table 9-3 Frost penalties and the annual cost of frost for a penthouse evaporator coil with a cooling operation interval of 24 hours and various hot gas stage dwell times.

<i>Cooling for 24 hours, Mass of frost =181 kg</i>								
	Time length of the hot-gas stage [minutes]							
	40		30		9.0		6.0	
Q_{drop}	703.3		703.3		703.3		703.3	
$Q_{pump-out}$	82.2	534	82.2	452.74	82.2	280.44	82.2	254.89
$Q_{no-cooling}$	375.9		300.7		142.84		120.29	
Q_{PHL}	75.90		69.82		55.4		52.40	
Q_{losses}	1237.3		1156.04		983.74		958.2	
Q_{ideal}	11352.2		11277		11119		11097	
h_{refg}	89.1%		89.7%		91.2%		91.4%	
t_{losses} [hr]	2.74		2.56		2.18		2.12	
Annual ELC [KWh]	73715.5		68874		58609		57086.64	
Cost [\$]	5897		5510		4689		4567	
Unit = [MJ] , Electrical rate cost of \$0.08/kWh								

Table 9-4 Frost penalties and the annual cost of frost for a penthouse evaporator coil with a cooling operation interval of 36 hours and various hot gas stage dwell times.

<i>Cooling for 36 hours, Mass of frost =257 kg</i>								
	Time length of the hot-gas stage [minutes]							
	40		30		13.0		8.4	
Q_{drop}	1768		1768		1768		1768	
$Q_{pump-out}$	82.2	533.62	82.2	452.21	82.2	312.9	82.2	274.12
$Q_{no-cooling}$	375.9		300.7		172.9		138.26	
Q_{PHL}	75.52		69.29		57.8		53.66	
Q_{losses}	2301.62		2220.21		2080.9		2042.1	
Q_{ideal}	16765		16690		16562		16528	
h_{refg}	86.3%		86.7%		87.4%		87.6%	
t_{losses} [hr]	5.10		4.92		4.61		4.53	
Annual ELC [KW]	89131.4		85978.56		80584.4		79082	
Cost [\$]	7131		6878		6447		6327	
Unit = [MJ], Electrical rate cost of \$0.08/kWh								

Table 9-5 Frost penalties and the annual cost of frost for a penthouse evaporator coil with a cooling operation interval of 48 hours and various hot gas stage dwell times.

<i>Cooling for 48 hours, Mass of frost =321 kg</i>								
	Time length of the hot-gas stage [minutes]							
	40		30		16.0		10.78	
Q_{drop}	3558		3558		3558		3558	
$Q_{pump-out}$	82.2	533.15	82.2	451.78	82.2	334.35	82.2	293.4
$Q_{no-cooling}$	375.9		300.7		192.66		156.2	
Q_{PHL}	75.05		68.86		59.49		55.0	
Q_{losses}	4091.15		4009.78		3895		3851.4	
Q_{ideal}	22178.1		22103		21998		21958	
h_{refg}	81.6%		81.9%		82.3%		82.5%	
t_{losses} [hr]	9.07		8.89		8.64		8.54	
Annual ELC [KWh]	121870.65		119446.8		116032.3		114729.5	
Cost [\$]	9750		9556		9283		9178	
Unit = [MJ] , Electrical rate cost of \$0.08/kWh								

Table 9-6 Frost penalties and the annual cost of frost for a ceiling-hung evaporator with a cooling operation interval of 12 hours and various hot gas stage dwell times.

<i>Cooling for 12 hours, Mass of frost =92 kg</i>								
	Time length of the hot-gas stage [minutes]							
	40		30		5.50		3.5	
Q_{drop}	166.1		166.1		166.1		166.1	
$Q_{pump-out}$	82.2	625.5	82.2	519.85	82.2	260.8	82.2	239
$Q_{no-cooling}$	375.9		300.7		116.53		101.5	
Q_{PHL}	167.4		136.93		62.06		55.3	
Q_{losses}	791.6		685.95		426.89		405.09	
Q_{ideal}	5939.22		5864		5679.85		5664.8	
h_{refg}	86.7%		88.3%		92.5%		92.8%	
t_{losses} [hr]	1.75		1.52		0.95		0.9	
Annual ELC [KWh]	94323.4		81734.64		50865.65		48269.02	
Cost [\$]	7546		6539		4069		3862	
Unit = [MJ] , Electrical rate cost of \$0.08/kWh								

Table 9-7 Frost penalties and the annual cost of frost for a ceiling-hung evaporator with a cooling operation intervals of 24 hours and various hot gas stage dwell times.

<i>Cooling for 24 hours, Mass of frost =181 kg</i>								
	Time length of the hot-gas stage [minutes]							
	40		30		10.0		6.64	
Q_{drop}	703.3		703.3		703.3		703.3	
$Q_{pump-out}$	82.2	624.3	82.2	518.68	82.2	307.204	82.2	271.3
$Q_{no-cooling}$	375.9		300.7		150.36		125.10	
Q_{PHL}	166.2		135.76		74.64		64.0	
Q_{losses}	1327.6		1221.98		1010.5		974.6	
Q_{ideal}	11352.18		11277		11126.64		11101.38	
h_{refg}	88.3%		89.2%		90.9%		91.2%	
t_{losses} [hr]	2.94		2.71		2.24		2.16	
Annual ELC [KWh]	79095		72802		60203.50		58064.40	
Cost [\$]	6328		5824		4816		4645	
Unit = [MJ] , Electrical rate cost of \$0.08/kWh								

Table 9-8 Frost penalties and the annual cost of frost for a ceiling-hung evaporator with a cooling operation interval of 36 hours and various hot gas stage dwell times.

<i>Cooling for 36 hours, Mass of frost =257 kg</i>								
	Time length of the hot-gas stage [minutes]							
	40		30		14.0		9.37	
Q_{drop}	1768		1768		1768		1768	
$Q_{pump-out}$	82.2	623.3	82.2	517.56	82.2	348.42	82.2	299
$Q_{no-cooling}$	375.9		300.7		180.43		145.65	
Q_{PHL}	165.2		134.6		85.79		71.28	
Q_{losses}	2391.3		2285.56		2116.4		2067.13	
Q_{ideal}	16765		16689.96		16569.67		16535	
h_{refg}	85.7%		86.3%		87.2%		87.5%	
t_{losses} [hr]	5.3		5.07		4.69		4.58	
Annual ELC [KWh]	92604.3		88509.46		81959.51		80050.60	
Cost [\$]	7408		7081		6557		6404	
Unit = [MJ] , Electrical rate cost of \$0.08/kWh								

Table 9-9 Frost penalties and the annual cost of frost for a ceiling-hung evaporator with a cooling operation interval of 48 hours and various hot gas stage dwell times.

<i>Cooling for 48 hours, Mass of frost =321 kg</i>								
	Time length of the hot-gas stage [minutes]							
	40		30		18.0		11.89	
Q_{drop}	3558		3558		3558		3558	
$Q_{pump-out}$	82.2	622.26	82.2	516.63	82.2	389.69	82.2	325.5
$Q_{no-cooling}$	375.9		300.7		210.5		164.57	
Q_{PHL}	164.2		133.7		97.0		78.70	
Q_{losses}	4180.26		4074.63		3947.7		3883.5	
Q_{ideal}	22178		22102.92		22012.7		21966.5	
h_{refg}	81.2%		81.6%		82.1%		82.3%	
t_{losses} [hr]	9.27		9.03		8.75		8.61	
Annual ELC [KWh]	124525		121378.54		117597.26		115684.07	
Cost [\$]	9962		9710		9408		9255	
Unit = [MJ] , Electrical rate cost of \$0.08/kWh								

9.5 Effects of moisture infiltration to the overall system efficiency

In the previous section, the air and moisture infiltration were assumed to be constant. In this section, the assumption of a constant moisture load is relaxed and the effect of moisture load is investigated by varying the freezer air moisture content (specific humidity). The frost model discussed in Chapter 3 is used to predict the evaporator cooling capacity assuming three different freezer air relative humidity levels (90, 85 and 80%) at a constant temperature of -27.7°C (-17.7°F). The geometry and other characteristics of the evaporator coil are identical to those associated with the penthouse evaporator coil that was used in the experiment and discussed previously.

Figure 9.19 shows the longitudinal cooling coil capacity predicted by the frost model over a range of space relative. As expected, cases with increased inlet air humidity results in a more rapid deterioration in evaporator capacity for two main reasons: 1) higher space humidity results in a greater difference between the air specific humidity and the saturated specific humidity of the frost attached to the evaporator coil surfaces (which is the main mechanism driving the mass transfer), 2) As the frost accumulation rate decreases, the frost density increases therefore the same amount of frost will have more pronounced effects on the air flow rate through the evaporator coil (larger thickness) at a higher inlet air specific humidity than it is for a low inlet air specific humidity as shown in Figure 9.20.

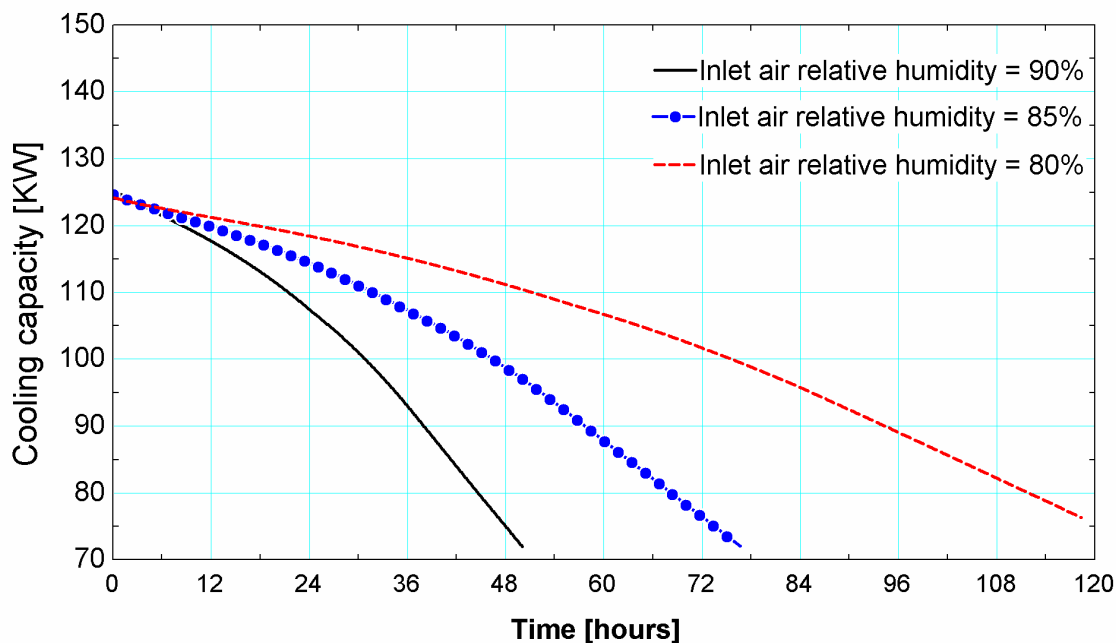


Figure 9.19 Cooling capacity prediction of the frost model for three different inlet air relative humidity versus time of cooling.

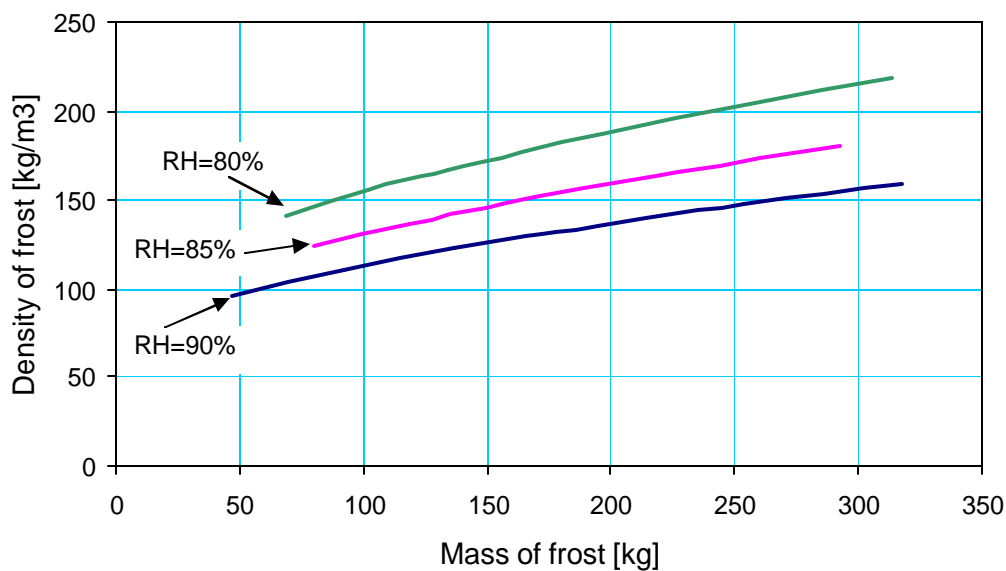


Figure 9.20 Density of frost at a constant inlet air temperature to the evaporator coil with three different inlet air relative humidity versus total mass of accumulated frost.

Figure 9.20 shows the density of the frost at a constant air temperature to the evaporator with three relative humidity values as a function of the mass of the frost. In

order to reflect the effect of varying the inlet air specific humidity to the overall system efficiency defined earlier in Eq. (9.7), all the penalties due to frost accumulation and frost removal are calculated assuming three different inlet air humidity ratios based on the methods discussed in Section 9.2.

The overall system efficiency of the penthouse evaporator coil with three different inlet air relative humidity values (90, 85 and 80%) and a constant temperature of -27.7°C (-17.7°F) is shown in Figure 9.21 as a function of cooling operation intervals between defrosts. Note that dwell period of the hot gas stage used to generate Figure 9.21 is assumed to be equal to 150% of the ideal hot gas stage duration.

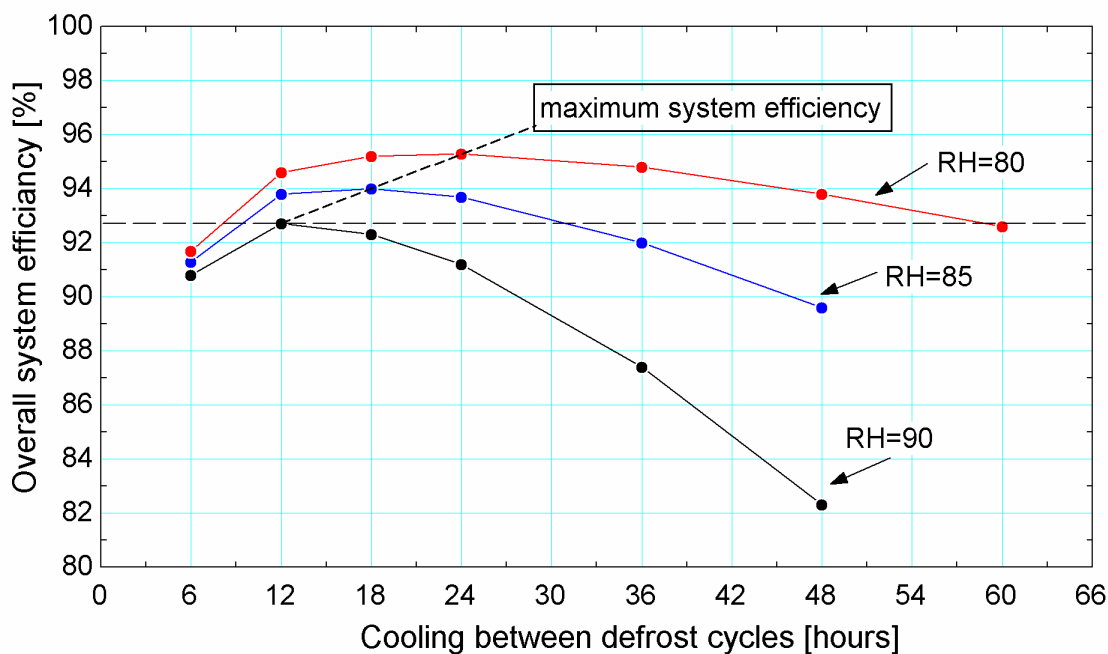


Figure 9.21 Overall system efficiency of penthouse evaporator coil with a constant inlet air temperature and three different inlet air relative humidity as a function of cooling operation interval.

Figure 9.21 shows very interesting results; it shows that as the inlet air relative humidity drops, the maximum system efficiency increases for the same cooling operation

interval between defrosts. It also shows that the required cooling operation interval to achieve the optimum system efficiency increases as inlet air relative humidity drops. The required cooling operation intervals to achieve the optimum system efficiency for an inlet air relative humidity of 90, 85 and 80% are 12, 18 and 24 hours, respectively. Figure 9.21 shows that setting the cooling operation interval of the penthouse evaporator coil equal to a constant value of 18 hours regardless of infiltration (i.e., all year long) is near optimal since the peaks of the curves are relatively broad.

Finally Figure 9.21 shows that if the efficiency is set to equal to a constant value of 92.7% (the maximum system efficiency for the 90% inlet air relative humidity case) all year around then the cooling operation interval can be extended in the winter season from 18 hours up to 30 or even 60 or more hours depending on the freezer specific humidity (which is mainly controlled by the infiltration rate).

Figure 9.22 shows the same overall system efficiencies that were shown previously in Figure 9.21; however in Figure 9.22 they are plotted against the total accumulated frost instead of the cooling operation interval. Figure 9.22 shows that one relatively easy method that can be used to approximately determine the optimum cooling operation interval between defrost cycles is to measure the total mass of the accumulated frost which in turn can be accomplished (at least approximately) by measuring the total mass of the water condensate drained from the coil during the hot gas defrost process. Figure 9.22 shows that a total mass of accumulated frost of around 112.5 kg on the penthouse evaporator coil surfaces used in the experiment yields very nearly the optimum overall

system efficiency regardless of infiltration rate (at least for the three different inlet air relative humidity levels that were considered in this analysis). The 112.5 kg of accumulated frost corresponds to cooling operation intervals of (12.6, 17, 20 hours) for the three different inlet air relative humidity of (90, 85 and 80%), respectively.

Figure 9.22 also shows the overall system efficiency of the evaporator coil for the three different inlet air relative humidities as a function of the Defrost number. The Defrost number is defined in this chapter as:

$$\text{Defrost number} = \frac{V_{\text{water}}}{A_{\text{min}} L_d} \quad (9.16)$$

where V_{water} is the total volume of the water condensate at the end of the HGDC, A_{min} is the minimum air flow area throughout the evaporator coil defined in Eq. (2.13) (see Figure 2.1), and L_d is the depth of the evaporator coil in the air flow direction.

Figure 9.22 shows that the optimum overall system efficiency for the three different inlet air relative humidities of the evaporator used in the experiment is obtained when the defrost number is 0.03. The Defrost number is useful as it scales the acceptable volume of water condensate to the volume of the evaporator coil; when the amount of frost that accumulates represents approximately 3% of the available volume then it is time to defrost.

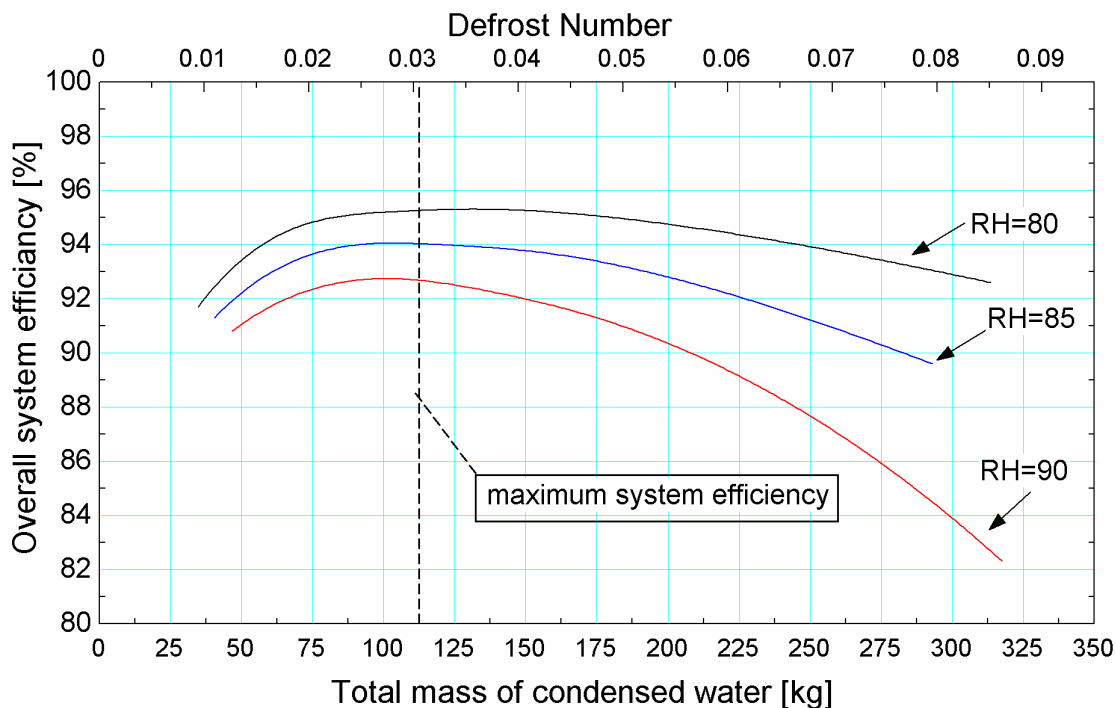


Figure 9.22 Overall system efficiency of penthouse evaporator coil with a constant inlet air temperature and three different inlet air relative humidities as a function of the total mass of the accumulated frost and the Defrost number.

A measurement of the mass of the condensate water can be accomplished relatively easily by mounting a turbine flow meter at the exit water drain. A turbine flow meter can be programmed so that it terminates the HGDP when the mass flow rate of the condensate water reaches a certain, very small value (e.g., 0.5 kg/s as shown in Figure 7.8). Furthermore, the turbine flow meter signal can be integrated in time in order to measure the total mass of the measured water condensate and used to control the initiation of the HGDP in order to approach the optimum cooling operation interval between defrost cycles. This would be accomplished iteratively but automatically so that the total mass of the condensate water at the end of the HGDP is always close to the maximum total mass of condensate water that yields the maximum system efficiency.

9.6 Summary

In this chapter, the previously developed and validated coil frosting and defrosting models were used to simulate evaporator coils performance during both cooling and during the hot gas defrost modes. The cooling and defrost results were coupled in order to optimize the overall process of extracting heat from a refrigerated space – net cooling optimization. The heat extraction capability was maximized by minimizing the overall penalty related to frost accumulation and frost removal (i.e., the cost of frost) for both a penthouse and a ceiling-hung evaporator coil.

The study showed that:

- 1 The penalty due to frost accumulation during the cooling mode increases significantly as the cooling operation interval increases due to the greater buildup of frost and associated performance degradation. The overall penalty due to frost removal during the HGDP decreases as the cooling operation interval increases due to the reduction of the number of hot gas defrost cycles required. Therefore any technique that might reduce the effect of the accumulated frost on the evaporator surface will yield an improvement in the refrigeration system efficiency, particular for those evaporator coils that are defrosted often (2 or 3 times a day).
- 2 The penalty of not cooling during the hot gas defrost process (lost cooling opportunity) is higher than the penalty due to the hot gas defrost parasitic load in both the penthouse evaporator in the ceiling-hung evaporator.

- 3 The penalty due to the frost accumulation increases as the specific humidity of the air inlet to the evaporator coil increases due to the increases in the frost formation rate which leads to the decrease in the average accumulated frost density and a rapid blockage of the air flow path across the evaporator coil.
- 4 The optimum cooling operation intervals that provides the maximum refrigeration system efficiency is inversely proportional to the moisture content of the inlet air to the evaporator coil.
- 5 The cooling operation interval that provides the maximum refrigeration system efficiency (defined as the achieved to maximum possible or rated cooling capacity) is achieved when the penalty due to frost formation is equal to the total penalty due to frost removal during the HGDP throughout one refrigeration cycle. For the evaporator coil used in the analysis, this optimum cooling operation intervals is found to be approximately 18 hours.
- 6 The current setting of the warehouse's hot gas stage dwell period for the penthouse evaporator is almost 4 times longer that is theoretically necessary to remove all the accumulated frost.
- 7 The current study showed that there is always a maximum amount of accumulated frost that results in the highest system efficiency regardless of the frost accumulation rate, for the penthouse evaporator used in the experiment the maximum amount of accumulated frost that results in the highest system efficiency is found to be 112.5 kg. More generally, it is found that the optimal time to initiate a defrost is approximately when the volume of frost (approximately equal to the condensate volume) is equal to nominally 3% of the

evaporator volume where the evaporator volume is defined as the product of the minimum free flow area for air and the evaporator depth in the flow direction. This ratio (frost volume/evaporator volume) is referred to as the Defrost number and provides a generically useful and easily scalable rule that can be used to optimally setup a defrost control strategy.

- 8 One relatively easy method to practically accomplish the optimal defrost control strategy is to measure the total mass of the accumulated frost using a turbine flow meter placed in the condensate line. Such a measurement would allow both optimal termination of the defrost (when the turbine flow was reduced to near zero) and optimal initiation of the defrost (based on iteratively adjusting the cooling interval based on the measured total flow).

Chapter 10 Counter-flow versus Parallel-flow Circuiting Evaporators

The main objective of this chapter is to explore any potential advantages that are associated with the parallel-flow circuiting arrangement as compared to the commonly used, counter-flow circuiting arrangement for liquid ammonia overfeed coils operating under frosting conditions during an entire refrigeration cycle (cooling mode and defrost mode operation).

10.1 Counter-flow versus parallel-flow circuiting during cooling mode operation

Counter-flow circuiting is commonly used in all types of evaporator coils for industrial refrigeration, including direct expansion, natural recirculation and liquid overfed evaporators. One problem associated with using counter-flow circuiting for evaporator coils that operate under frosting conditions is that these evaporators will tend to accumulate more frost in the first few rows that are exposed to the incoming air; this trend has been discussed in the previous chapters. The concentrated frost build up results in a rapid increase in the flow resistance of the evaporator to the air flow and therefore a large reduction in the flow rate of air and therefore the refrigeration capacity.

Several techniques have been proposed in order to reduce the rate of frost accumulation and therefore increase the operating interval between defrost; for example, Ogawa et al. (1993) suggest several modifications to the evaporator geometry such as the use of front

fin staging, side fin staging and partially cut fins. Ogawa et al. showed that each of these techniques can be used to reduce the heat and mass transfer rates at the first few rows of evaporator coils. However, the reduction in heat and mass transfer rate is accompanied by a reduction in the refrigeration capacity that can be provided by the un-modified evaporator coils during dry operation. Also, the modifications to the geometry may be difficult to realize without adding substantial complexity to the fabrication process.

Nelson (1990) developed theoretical models of a counter-flow and a parallel flow circuited ammonia flooded evaporator coil operating under dry condition. Nelson found that by using the same physical geometry and inlet flow conditions in both circuiting arrangements, the parallel-flow circuiting provided a 3-4% greater cooling performance compared to the counter-flow circuiting. This chapter considers this strategy more completely by examining the impact of parallel and counter-flow circuiting on frost buildup and therefore total efficiency of a refrigeration system operating under frosting/defrost conditions

10.1.1 Formulation of the frost model

In order to simulate and compare the performance of both evaporator coil designs (counter-flow and parallel-flow circuiting) operating under frosting conditions, the frost model presented in Chapter 3 is modified so that the refrigerant inlet can be reversed; the refrigerant enters from the front side of the evaporator coil (i.e., the air inlet side) in order to simulate a parallel flow circuiting arrangement, as shown in Figure 10.1 and Figure 10.2. The physical geometry of the evaporator coil and the air and refrigerant flow conditions are identical for both evaporators and also identical to the counter-flow

circuiting evaporator used in the frost and the defrost experiments described in chapter 3. The only difference between the theoretical models of the two circuiting designs is the refrigerant flow direction.

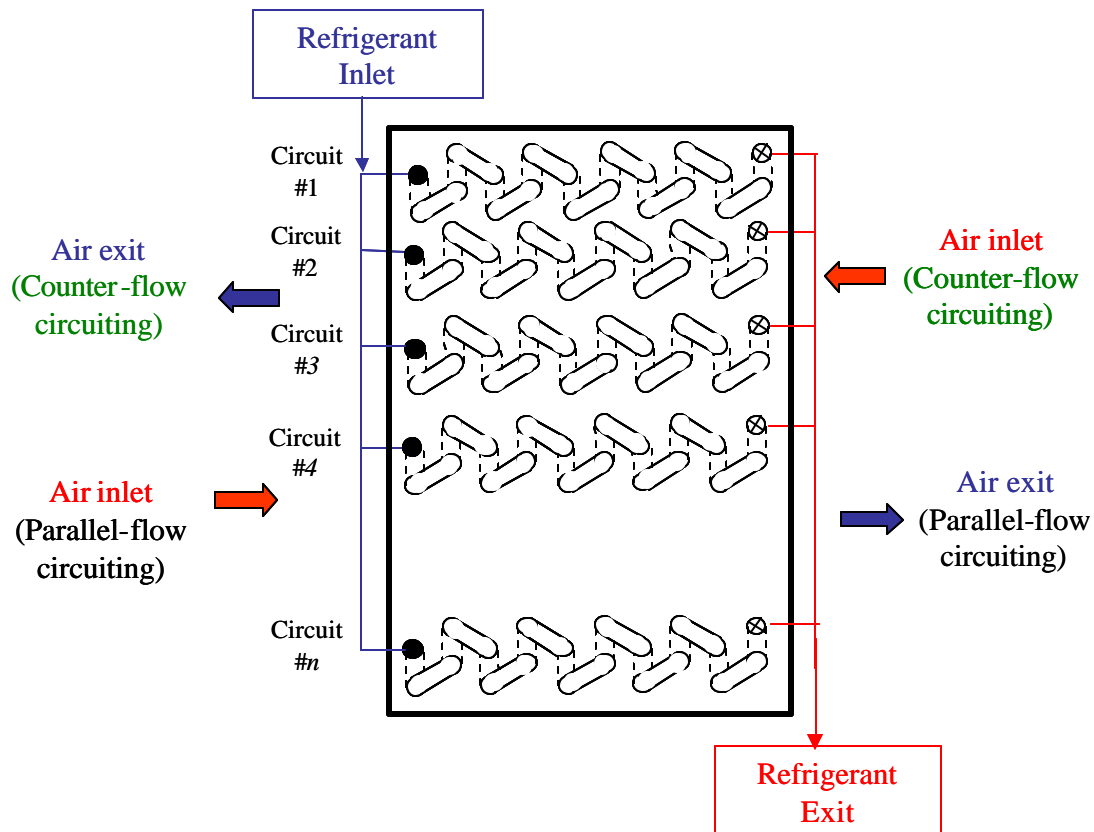


Figure 10.1 Schematic diagram showing evaporator coil with multiple rows of finned tubes with multiple refrigerant circuits and the direction of the air and the refrigerant flow for both the counter-flow and parallel-flow arrangements

Figure 10.3 compares the evaporator cooling capacity predicted by the frost model with the counter-flow and parallel-flow circuiting; again, the physical geometry of the evaporator coil and the operating conditions are the same.

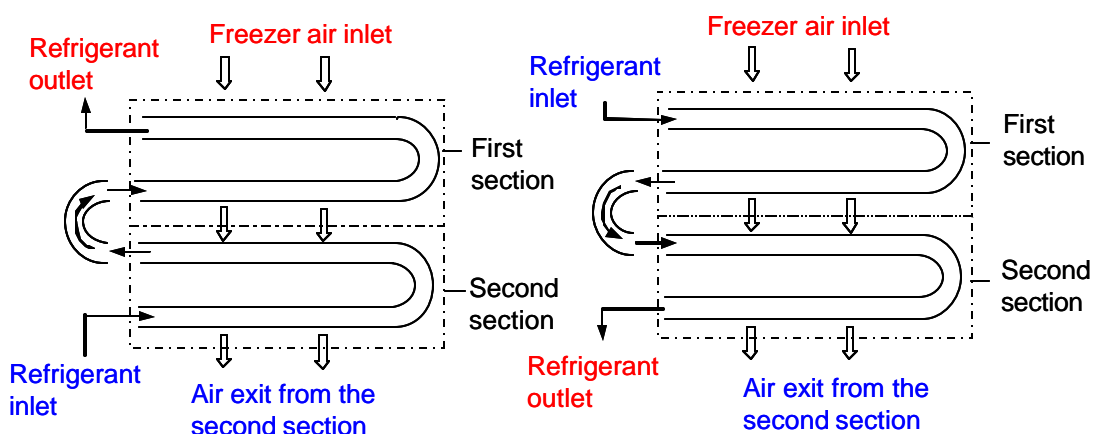


Figure 10.2 Schematic of the first and the second evaporator coil sections as well as the direction of the air and refrigerant flow for counter-flow (left) and, parallel-flow (right) flow arrangement.

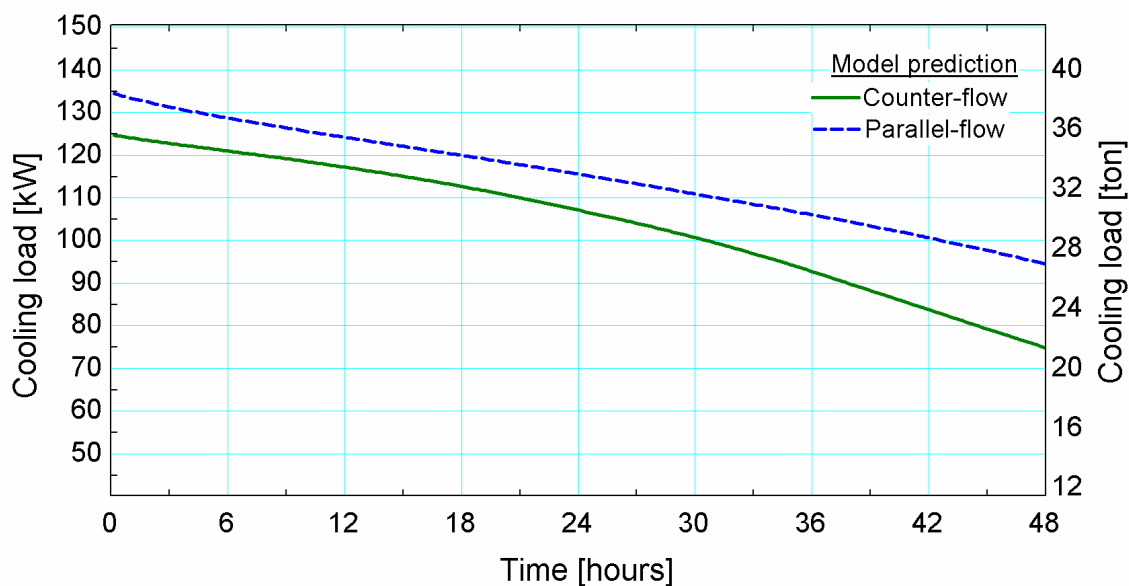


Figure 10.3 Comparison between the evaporator cooling capacity predicted by the counter-flow frost model and the parallel-flow frost model versus time.

Figure 10.3 shows that there are several advantages associated with using the parallel-flow configuration when compared to the more conventional, counter-flow circuiting arrangement during the cooling mode operation. The cooling capacity predicted by the

parallel-flow frost model at the beginning of the simulation (i.e., at time = 0 in Figure 10.3, which corresponds to a dry coil with no accumulated frost) is 8% higher than the cooling capacity predicted by the counter-flow frost model; this observation agrees well with the predictions of Nelson (1990). The reason for this dry-coil performance advantage is evident by observing the trends shown in Figure 10.4 and Figure 10.5.

Figure 10.4 shows a row-by-row comparison of the refrigerant temperature, air temperature, and the overall heat transfer coefficient at the beginning of the simulation (i.e., at time = 0) for the (a) parallel- and (b) counter-flow arrangements. Figure 10.4(a) shows that the temperature difference between the ammonia refrigerant and the air in a parallel-flow configuration decreases slightly for the coils that are deeper into the evaporator (i.e., coils with higher row numbers) whereas the overall heat transfer coefficient increases with row number. These effects balance and the result is a nearly uniform distribution of the cooling load; as shown in Figure 10.5. The decrease in the refrigerant temperature is due to the decrease in refrigerant pressure that occurs with frictional and inertial pressure loss. The change in the overall heat transfer coefficient is due to the change in the refrigerant quality that occurs as it evaporates. Figure 10.4(b) shows that the temperature difference between the ammonia refrigerant and the air in a counter-flow configuration will decrease significantly with increasing coil row as will the overall heat transfer coefficient. As a result, most of the cooling capacity will be provided by the first few coil rows, as shown in Figure 10.5. Overall, the effectiveness of the counter-flow configuration is somewhat lower than the effectiveness of the parallel-flow configuration which results in a slight reduction in the initial cooling capacity of the

coil. It is interesting that this trend towards higher effectiveness for a parallel-flow configuration is exactly the opposite of what is expected for a conventional heat exchanger; this counter-intuitive result occurs because the temperature of the refrigerant (which is increasing in enthalpy) will actually decrease in the direction of flow due to the refrigerant-side pressure drop.

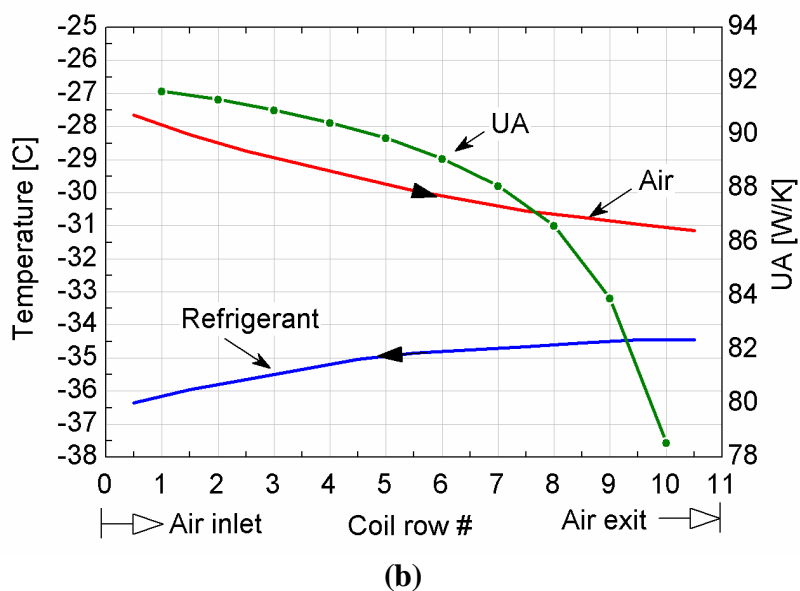
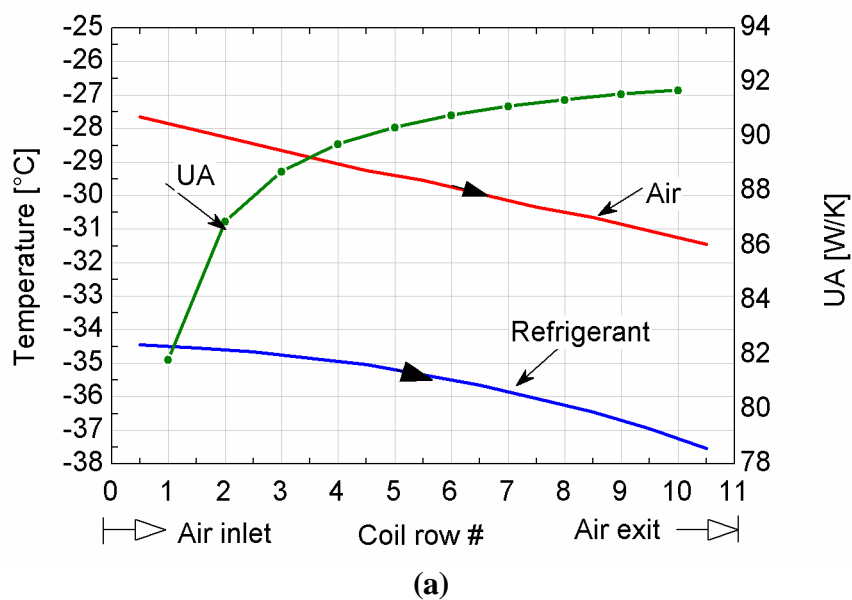


Figure 10.4 Predicted air and refrigerant temperature and UA across the evaporator coil for (a) parallel-flow and (b) counter-flow configuration.

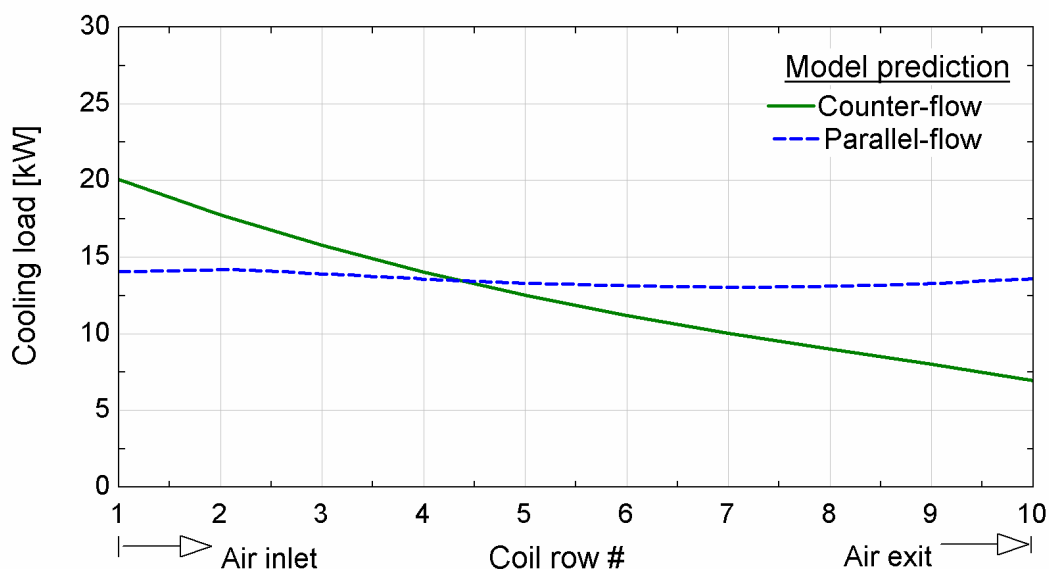


Figure 10.5 Cooling capacity across the evaporator for the counter-flow and parallel-flow configuration.

Another advantage of the parallel-flow over the counter-flow circuiting arrangement is related to the manner in which frost accumulates on the coil surface; this advantage is potentially more significant than the improvement in the dry-coil performance. The performance advantage of the parallel-flow configuration tends to increase with time as frost accumulates. This effect is shown in Figure 10.3; notice that the predicted cooling capacity for the parallel-flow circuiting arrangement is 15% higher than the cooling capacity for the counter-flow frost model at the end of the simulation. The improvement in the cooling performance under frosting conditions is primarily due to the distribution of the accumulated frost and the associated impact on the air-side pressure drop. Just as the first few rows of the counter-flow configuration tend to supply most of the refrigeration, these rows also tend to accumulate most of the frost. Therefore, after the same amount of operating time, the minimum air-side flow area for the counter-flow

configuration will be much less than for the parallel-flow configuration and the air-side flow resistance will be much higher. Figure 10.6 shows the calculated air velocity as a function of time and illustrates that the air flow reduction due to frost buildup is substantially higher for the counter-flow configuration even though the total mass of the accumulated frost is actually slightly smaller (see Figure 10.7).

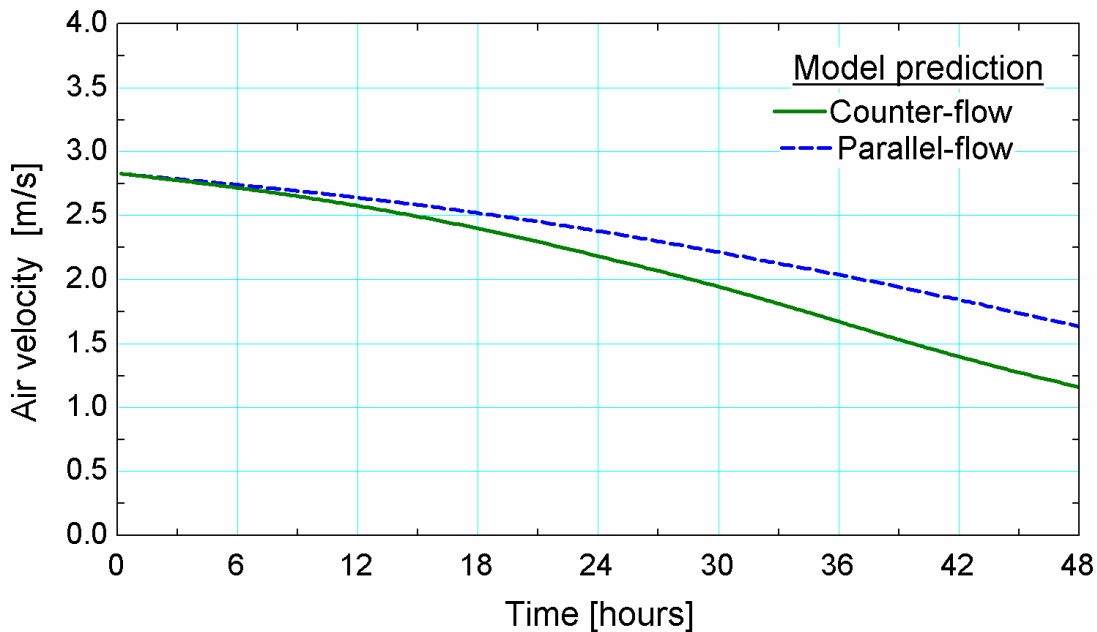


Figure 10.6 Comparison between the air velocity predicted by the counter-flow frost model and the parallel-flow frost model over time.

Figure 10.8 illustrates the distribution of the rate of frost accumulation after 1 hour of simulation for the parallel-flow and counter-flow configurations and shows that the frost accumulates more uniformly for the parallel-flow circuit. Figure 10.9 shows the percent blockage as a function of time for selected rows in the coil for the (a) counter-flow and (b) parallel-flow configurations; note that the counter-flow arrangement results in almost a 50% difference in the percent blockage between the first and the last rows at the end of the simulation while there is only a 9% difference for the parallel-flow arrangement.

Moreover, Figure 10.9 shows that the first row of the counter-flow coil will reach 80% blockage at the end of the simulation as compared to only 63% blockage for the last row of the parallel-flow arrangement.

Figure 10.8 illustrates the rate of frost accumulation associated with each coil for the two configurations after 1 hour of simulation; notice that the rate of frost accumulation is much more uniform for the parallel-flow circuit. Figure 10.9 shows the percent blockage as a function of time for selected rows in the coil for the (a) counter-flow and (b) parallel-flow circuiting configurations; note that the counter-flow arrangement results in almost a 50% difference in the percent blockage between the first and the last rows at the end of the simulation while there is only a 9% difference for the parallel-flow arrangement. Also note in Figure 10.9 that the first row of the counter-flow coil will reach 80% blockage at the end of the simulation as compared to only 63% blockage for the last row of the parallel-flow arrangement.

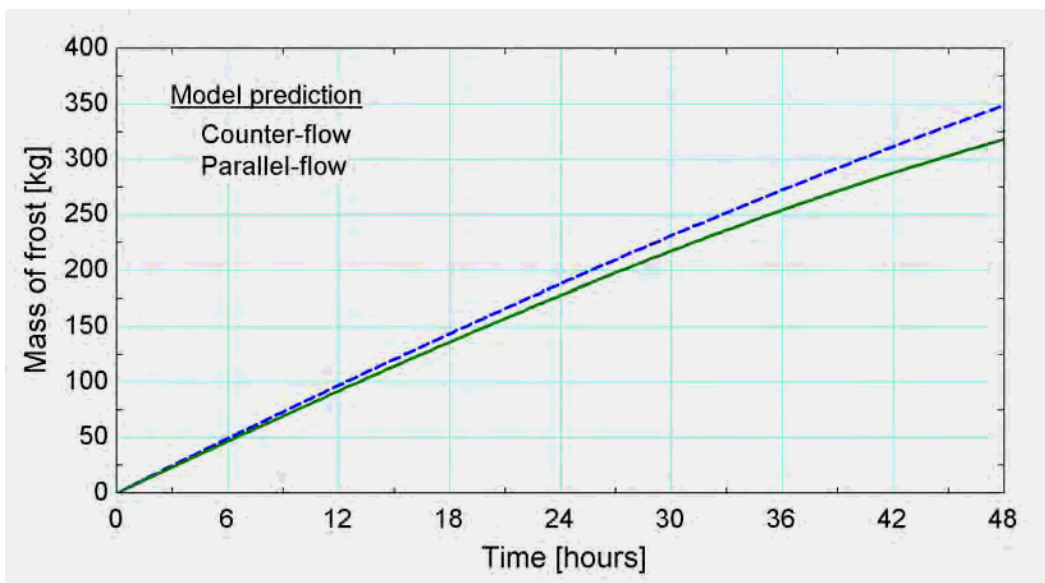


Figure 10.7 Comparison between the total mass of the accumulated frost predicted by the counter-flow and the parallel-flow frost model over time.

Finally by comparing Figure 10.8 and Figure 10.9(a) it is evident that even though the frost accumulation rate for the parallel-flow circuiting arrangement decreases slightly for the coils that are deeper into the evaporator, the density of the accumulated frost is also slightly reduced for the coils that are deeper into the evaporator; therefore, the frost thickness is actually slightly larger on the last row than it is for the first row in the parallel-flow arrangement.

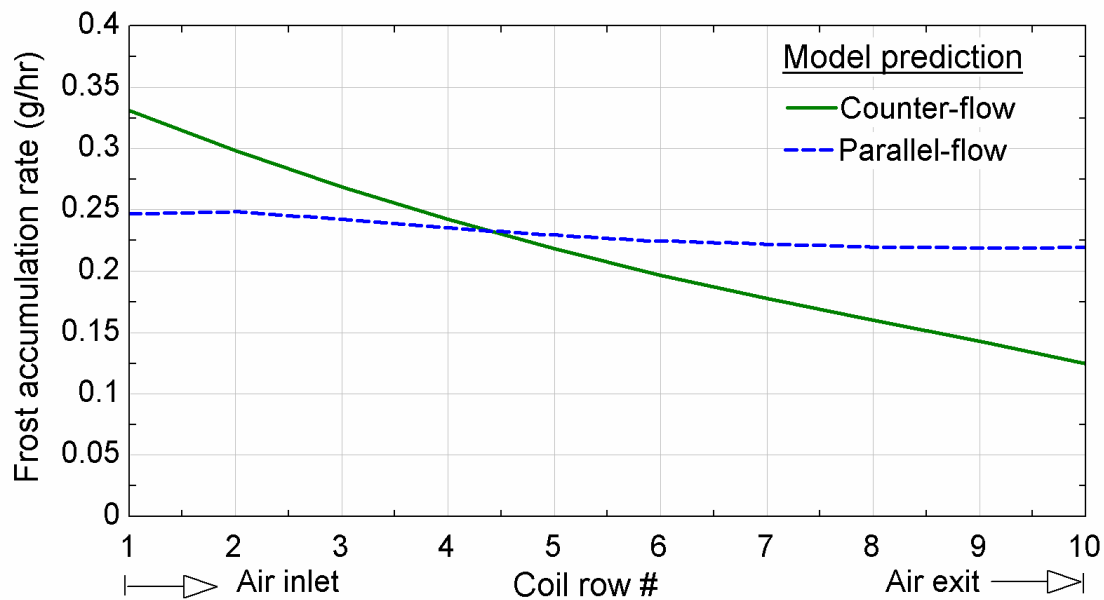
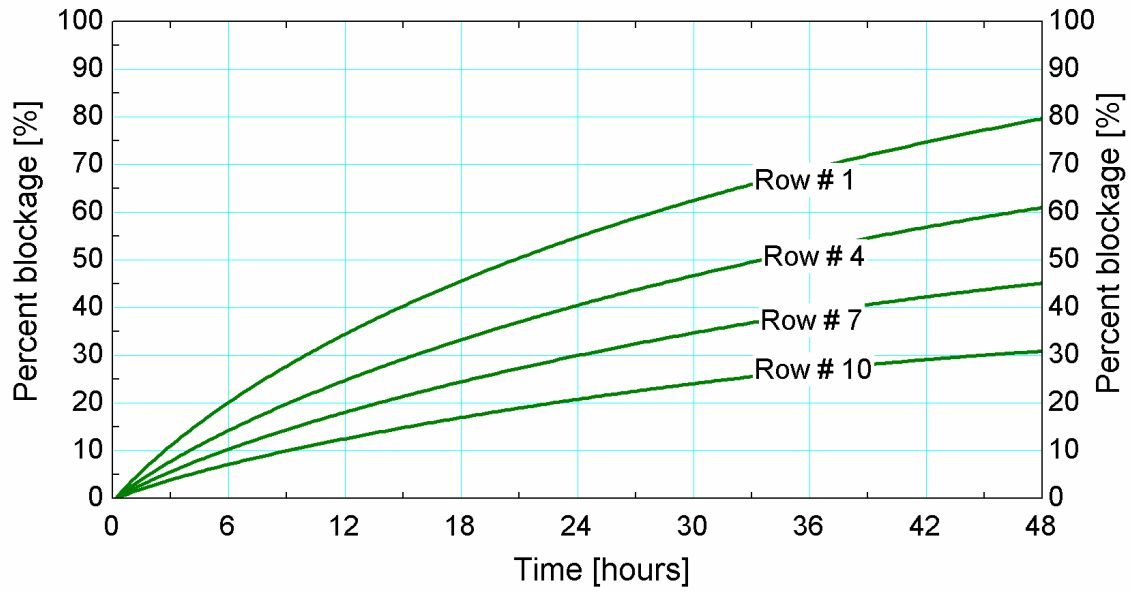
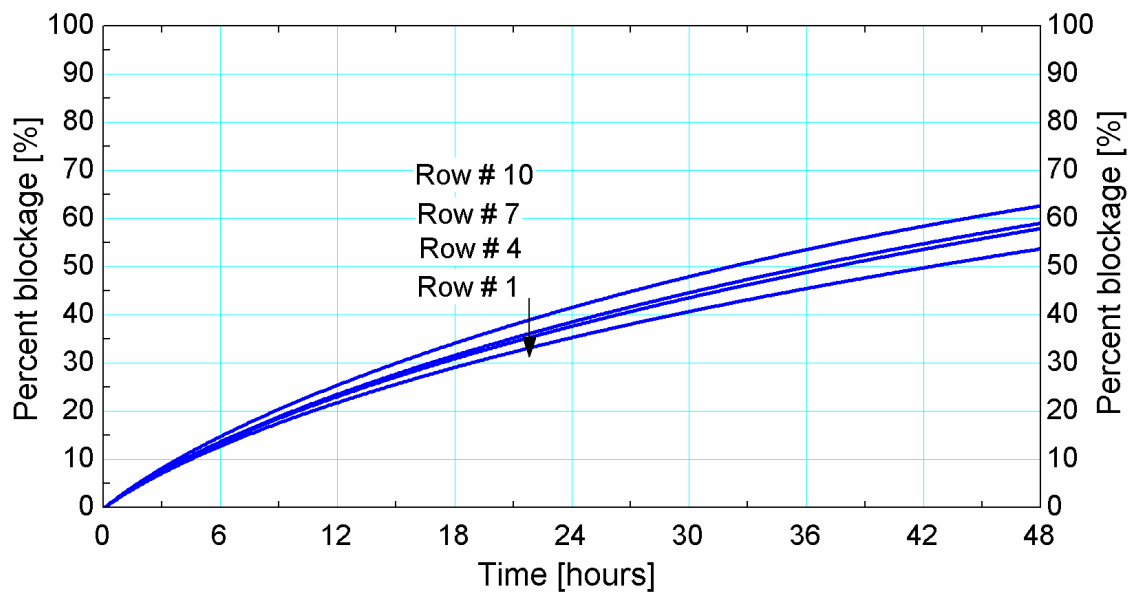


Figure 10.8 Comparison of the frost accumulation rate at each row predicted by the counter-flow frost model and the parallel-flow frost model.



(a)



(b)

Figure 10.9 Percentage of the blockage of the air path caused by frost accumulation at different rows of the evaporator coil over time for (a) counter-flow and (b) parallel-flow circuiting.

10.2 Counter-flow versus parallel-flow circuiting performance over an entire refrigeration cycle

Section 10.1 showed that the parallel-flow circuiting design provides a higher total cooling capacity compared to the counter-flow circuiting evaporator for the same duration of cooling mode operation. In this section, the two designs are compared in term of the overall system efficiency associated with an entire refrigeration cycle (i.e., an integer multiple of cooling and defrosting modes).

All of the various penalties related to frost formation and frost removal discussed in the previous chapter are calculated and applied to both the counter-flow and the parallel-flow circuiting designs; the results are summarized in Table 10-1 for a cooling operation interval of 12 hours between defrost events and a hot gas stage dwell period that is equal to 150% of the ideally terminated hot gas stage duration.

Note that all the penalties due to frost accumulation and frost removal for both the counter-flow and the parallel-flow circuiting design, were calculated with respect to the ideal cooling capacity of the parallel-flow circuiting evaporator since it is the maximum cooling capacity that can be provided by the evaporator coil (Figure 10.10), therefore the magnitude of the penalties provided in Table 10-1 for the counter-flow circuiting case are different than the one shown in the previous chapter which were calculated with respect to ideal cooling capacity of the counter-flow circuiting design.

Table 10-1: Summary of total system efficiency for the counter-flow and parallel-flow circuiting designs for a 12 hour defrost interval and a hot gas stage duration that is 150% of the ideally terminated value.

<i>Cooling for 12 hours</i>			
	Counter-flow		Parallel-flow
m_{frost} [kg]	91.7		97
t_{HG} [minutes]	4.75		3.6
$Q_{cooling}$ [MJ]	5247		5590
Q_{drop} [MJ]	589.46	855.86	246.12
$Q_{pump-out}$ [MJ]	93.96		93.96
$Q_{no-cooling}$ [MJ]	119.56		110.3
Q_{PHL} [MJ]	52.88		51.5
Q_{losses} [MJ]	855.86		490
Q_{ideal} [MJ]	6118		6108.73
h_{sys}	86.0%		92%

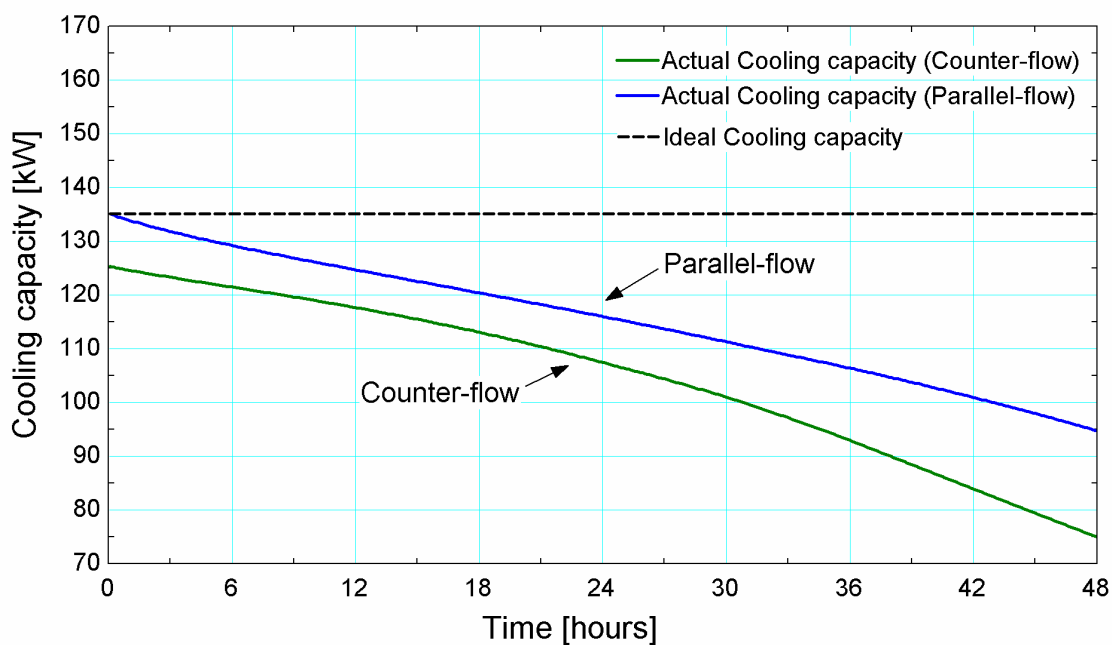


Figure 10.10 Actual and the ideal evaporator cooling capacity of the counter-flow and the parallel-flow circuiting evaporators versus time during the cooling operation mode.

Table 10-1 shows that even though the initial total mass of frost (m_{frost}) that is present at the beginning of the HGDP for parallel-flow circuiting evaporator is higher than it is for the counter-flow circuiting evaporator, the ideal time required to completely remove the frost (t_{HG}) from the parallel-flow circuiting evaporator is less than it is for the counter-flow circuiting evaporator (2.4 minutes vs 3.17 minutes). This is mainly due to the more uniform frost distribution across the evaporator coil.

Table 10-1 also shows that the integrated total cooling energy supplied by the parallel-flow circuited evaporator ($Q_{cooling}$) is higher than for the counter-flow circuiting during the 12 hours of cooling operation (5590 MJ vs 5247 MJ). This is due to the higher effectiveness of the parallel-flow circuiting evaporator and due to the more uniform distribution of the accumulated frost which reduces the penalty associated with the frost build up, as discussed in Section 10.1.

It can be seen from Table 10-1 that the integrated total cooling energy reduction of the counter-flow circuiting evaporator (Q_{drop}) is almost double of the parallel-flow circuiting at the end of the 12 hours of cooling operation (589.46 MJ vs 246.12 MJ).

Finally it can be seen from Table 10-1 and Figure 10.11 that the maximum efficiency of the parallel-flow circuiting evaporator is almost 6% higher than the maximum efficiency of the counter-flow circuiting evaporator.

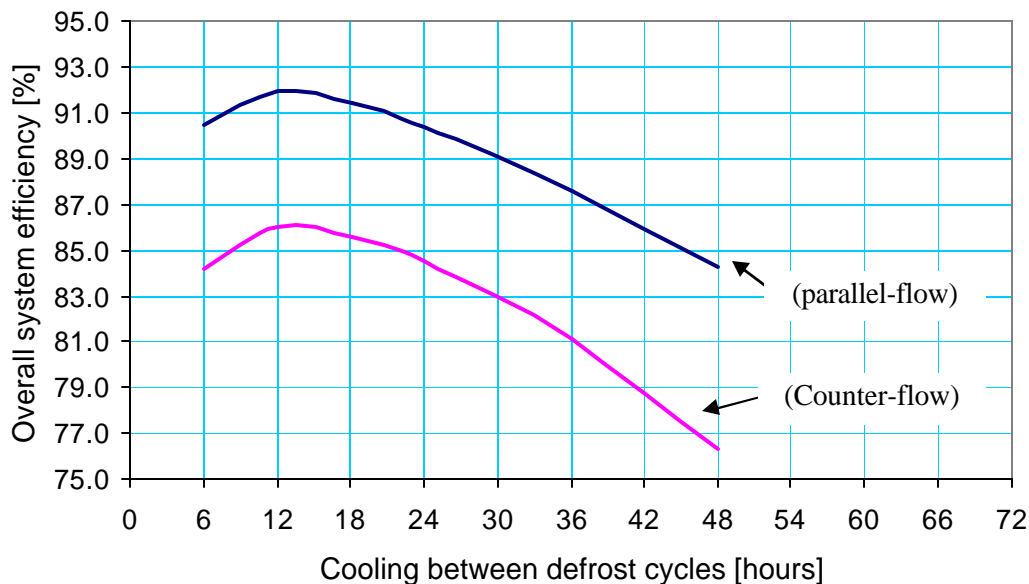


Figure 10.11 Overall system efficiency of counter-flow and parallel-flow circuiting evaporator coils versus cooling operation intervals between defrost

The above analysis clearly shows that changing the circuiting of the industrial evaporator tubes from counter-flow to parallel-flow (which can be done either by changing the refrigerant or the air flow direction) will result in an increase in the evaporator coil effectiveness as well as a more uniform distribution of the frost buildup and therefore a higher overall system efficiency and a longer allowable cooling operation time between defrost.

10.3 Summary

The frost theoretical model is used to compare the performance of counter-flow and parallel-flow circuiting under frosting conditions. The impact of using parallel-flow as opposed to counter-flow circuiting is evaluated in terms of the frost distribution across the evaporator coil, the associated temporal reduction in cooling capacity during operation and the overall system efficiency.

The current study shows there are two key advantages of the parallel-flow versus the counter-flow evaporator coils. First, the effectiveness of the counter-flow overfired industrial evaporator coils is slightly less than the effectiveness of the parallel-flow overfired industrial air-cooling evaporator coils and; therefore, the parallel-flow configuration provided slightly higher initial coil cooling capacity. Second, the cooling coil capacity advantage of the parallel-flow versus the counter-flow configuration tends to increase with time as frost accumulates, due primarily to the distribution of the accumulated frost and its effect on the air-side pressure drop.

The optimum system efficiency of the parallel-flow circuiting evaporator is almost 6% higher than the optimum system efficiency of the counter flow circuiting evaporator.

The parallel-flow evaporator provides greater advantages for some refrigeration applications where operating exactly at the maximum system efficiency is not as important as the maximum time that the evaporator coil can be used before it gets completely blocked such as those evaporator coils used to pre-refrigerate food product during the packaging process or those used in the blast freezer where setting the evaporator coil to the defrost mode requires a temporarily termination of the food production.

10.4 Nomenclature

Symbol	Description	Dimensions
m_{frost}	= Total mass of frost	[kg]
t_{HG}	= Dwell period of the hot gas stage	[min]
Q	= Integrated total energy	[MJ]
<i>Greek symbols</i>		
h_{sys}	= Overall system efficiency	[-]
<i>Subscripts</i>		
PHL	= Parasitic heat load	

10.5 References

Ogawa K., Tanaka N.O, Takeshita M., 1993, "Performance improvement of plate fin-and-tube heat exchangers under frosting conditions", ASHRAE Transaction, Vol. 99, No. 1.

Nelson, B., "Design of Evaporators for Liquid Overfeed Systems", *ASHRAE Transactions*, Vol. 96, No. 1, (1990).

Chapter 11 Conclusion

The primary goal of this research is to investigate the effects of frost formation and frost removal (Hot Gas Defrosting) processes with the aim of optimizing the overall operation of a refrigeration system cycle (cooling mode and defrosting mode). This chapter summarizes the significant findings of the present work and presents recommendations for directions and areas that might be the focus of future investigations related to this topic.

11.1 Conclusions

In order to achieve the primary objective of this research, that is the optimization of the overall operation of the industrial refrigeration system by focusing on the evaporator coil during the cooling mode operation (frosting) and the frost removal mode operation (defrosting); two numerical models (frost model and defrost model) were developed and validated.

The frost theoretical model predicts the frost formation rate and the heat extraction rate of the evaporator coil during the cooling mode operation. The frost model also predicts the frost thermal properties and the frost thickness at the end of the cooling mode which are required inputs for the defrost theoretical model.

The defrost numerical model is predicts the industrial evaporator coil behavior during the Hot Gas Defrost Process (HGDP) in order to quantify the parasitic (sensible and latent) load during the defrost process based on the frost properties and the amount of

frost on the coil (inputs obtained from the frost model) and also predicts the time required to complete defrost cycle.

The two numerical models mentioned above were validated with data obtained from two field experiments that were conducted on a full-scale and installed industrial evaporator coil during cooling and defrost mode operation. Finally the two numerical models were integrated in order to optimize the entire refrigeration cycle based on the penalties associated with the frost accumulation during the cooling mode operation and the penalties associated with the frost removal during the defrost mode operation. The following sections summarize the findings of the aforementioned efforts.

11.1.1 Frost numerical model and frost experiment

The degradation in the frosted evaporator coil performance during cooling mode operation is related to the low conductivity of the frost layer which adds an additional thermal resistance between the air and the refrigerant and, more importantly, the reduction in air flow rate that is caused by the increased resistance to air flow through the narrowing channels due to the growing frost layer. The higher flow resistance reduces the amount of air that the evaporator fan can move through the coil.

As the mass flow rate of the air passing through the evaporator coil decreases, its temperature drop increases causing a slight increase in the effectiveness of the evaporator coil; however, the slight improvement in the effectiveness is not sufficient to make up for the overall reduction in the coil refrigeration capacity associated with the reduction of the flow rate.

One relatively easy method to improve the performance of industrial overfled evaporators operating under frosting conditions is by changing the tubes circuiting arrangement from counter-flow (the most commonly used tube configuration) to parallel-flow. This can be done either by changing the refrigerant or the air flow direction. The current research showed that this change in the tube circuiting arrangements causes an increase in the effectiveness of the evaporator coil and therefore the parallel-flow configuration provides slightly higher initial (i.e., dry coil) cooling capacity. Also the distribution of the accumulated frost on the evaporator coil that occurs with parallel-flow circuiting is more uniform than it is for the counter-flow circuiting. Counter-flow circuiting leads to the accumulation of more frost on the first few coil rows (i.e., the rows that first exposed to the incoming freezer air) as compared to the last rows. Therefore the cooling coil capacity advantage of the parallel-flow versus the counter-flow configuration tends to increase with time as frost accumulates; this is due primarily to the distribution of the accumulated frost and its effect on the air-side pressure drop.

11.1.2 Defrost numerical model and defrost experiment

The Hot Gas Defrost Cycle (HGDC) is divided into four main processes; Pump-out, Hot gas supply, Bleed and Fan delay. During the pump-out stage, the evaporator cooling capacity decreases rapidly due to the termination of the cold liquid refrigerant supply, while continuing to operate the evaporator fans in order to evaporate as much of the coil's liquid refrigerant as possible. The evaporator cooling capacity decreases by more than 50% during the 20 minutes pump-out-period.

During the hot gas supply, heat is transferred from the evaporator coil to the surrounding environment. In the case of a penthouse evaporator, the temperature of the inclosed air in the penthouse will increase rapidly due to the heat transfer from the hot gas. However, as soon all of the frost is removed from the coil surfaces the air temperature in the penthouse reaches a steady state and remains at this level throughout the remainder of the hot gas supply period.

The time required for a complete removal of the frost that is accumulated after 48 hours of cooling operation is almost 60% longer than the time required to remove the frost accumulated after 24 hours of cooling operation. The total energy required to heat the evaporator coil metal during the HGDP is large; the energy stored in the evaporator coil metal is between 25% and 37% of the total energy that is consumed during an optimally terminated defrost cycle (i.e., during the defrost time that is required to melt all the frost accumulated during 48 and 24 hours of cooling, respectively) which agrees with observations by Coley (1983).

The hot gas defrost efficiency of the HGDP of a penthouse evaporator is always higher than a ceiling-hung evaporator. Therefore the effect of increasing the HGDC time beyond the total time required for melting all the frost for the ceiling-hung evaporator is more significant than it is for the penthouse evaporator. The difference in the total parasitic heat load due to the increase in the total mass of the accumulated frost at the beginning of the HGDC is very small for the same dwell period of the hot gas stage.

11.1.3 Net cooling optimization

When the cooling and defrost results were coupled in order to optimize the overall process of extracting heat from a refrigerated space by maximizing the net cooling provided by the evaporator, the following conclusion were made.

The penalty due to frost accumulation during cooling mode operation increases significantly as the interval between defrost increases due to the greater buildup of frost and the associated performance degradation. The overall penalty due to frost removal during the HGDP decreases as the cooling operation interval increases due to the reduction of the number of hot gas defrost cycles required. Therefore any technique that might reduce the effect of the accumulated frost on the evaporator surface will yield an improvement in the refrigeration system efficiency, particularly for those evaporator coils that are defrosted often (2 or 3 times a day).

The penalty of not cooling during the hot gas defrost process (i.e., the lost cooling opportunity) is higher than the penalty due to the hot gas defrost parasitic load in both the penthouse evaporator in the ceiling-hung evaporator.

The penalty due to the frost accumulation increases as the specific humidity of the air inlet to the evaporator coil increases due to the increase in the rate of frost formation; the larger rate of frost formation not only results in a larger mass of frost on the coil surface but also leads to a reduction in the average accumulated frost density and therefore has a nonlinear effect on the blockage of the air flow path across the evaporator coil.

The optimum interval between defrost (i.e., the interval that provides the maximum refrigeration total system efficiency) is inversely proportional to the moisture content of the inlet air to the evaporator coil.

The cooling operation interval that provides the maximum refrigeration system efficiency (defined as the achieved to maximum possible or rated cooling capacity) is achieved when the penalty due to frost formation is equal to the total penalty due to frost removal during the HGDP throughout one refrigeration cycle. For the evaporator coil used in the analysis, this optimum cooling operation intervals is found to be approximately 18 hours.

The current study showed that there is always a specific amount of accumulated frost that is associated with achieving the highest system efficiency; for a particular evaporator, this mass of accumulated frost is approximately constant regardless of the frost accumulation rate. For the penthouse evaporator used in the experiment, the amount of accumulated frost at the onset of a defrost process that will result in the highest system efficiency is found to be 112.5 kg.

One relatively easy and practical method that can be used to setup a defrost system is to set the interval between defrost such that the total accumulated frost at the beginning of the HGDP is equal to the optimum mass (i.e., the previously discussed mass that results in the highest overall system efficiency which is 112.5 kg for the evaporator considered here). This can be accomplished practically by measuring the total mass of the accumulated frost which in turn can be obtained from a measurement of the total mass of the water condensate drained from the coil during the hot gas defrost process using a turbine flow meter. The same turbine flow can be also used to terminate the defrost cycle based on the mass flow rate of the drained water condensate. Furthermore, the optimal mass of accumulated is nominally 3% of the evaporator volume based on the product of the minimum air flow area and the depth of the evaporator in the air flow

direction. This value of 3% provides a useful method for applying the results of this analysis to other evaporators.

Appendix A

A summary of frost growth investigations performed for surfaces with simple geometries

Cylinders in cross-flow studies:

Andrichak, S.M., 1962, "*Formation of a layer of frost on a cylinder in cross-flow of air.*" M.S. thesis, Ohio State University, Columbus.

Aoki, K., M. Hattori, and Y. Hayashi., 1979a, "*Frost formation on a cylinder surface under forced convection.*" Fifteenth International Congress of Refrigeration, Venice, Paper No. B 1/55.

Bronson, J.C., 1970, "*Frost formation on a cylinder at cryogenic temperatures.*" In *Advances in Cryogenic Engineering*, K.D. Timmerhaus (ed.), Vol. 15. New York: Plenum Press.

Chung, P.M., and A.B. Aigren., 1958, "*Frost formation and heat transfer on a cylinder surface in humid air cross flow, Part I and II.*", *Heating, Piping and Air Conditioning*, September.

Ismail, K.A., C. Salinas, and Goncalves., 1997, "*Frost growth around a cylinder in wet air stream.*" *International journal of Refrigeration*. Vol. 20, No. 2.

Lee, D., D. Yang, and K. Lee, 2004, "*Frost formation on a cold cylinder surface in cross flow*" *International Refrigeration and air conditioning Conference at Purdue*, July.

Mango, P. and S. Sherif, 2003, "*Heat and mass transfer on a cylinder surface in cross flow under supersaturated frosting conditions*" *International Journal of Refrigeration*. Vol. 26.

Parish, H.C. 1970., "*A numerical analysis of frost formation under forced convection.*" M.S. thesis, Ohio State University, Columbus.

Parish, H.C., and C.F. Sepsy., 1972, "*A numerical analysis of frost formation under forced convection.*" *ASHRAE Transactions*, Vol. 78, Part 1.

Richards, R.J., D.K. Edmonds, and R.B. Jacobs., 1962. "*Heat transfer between a cryosurface and a controlled atmosphere.*" *International Institute of Refrigeration Annex- Supplementary Bulletin*.

Schneider, H.W., 1969, "*Temperature distribution in a frost layer formed on a cylindrical tube in cross flow.*" Annexe au Bulletin de l'Inst. Int. du Froid, Vol. 7.

Schneider, H.W., 1972, "*Transferred mass and density of frost formed on a cylinder in cross flow.*" IIR-Commissions B1, B2, and E1 (Freudenstadt), September, Int. Institute of Refrigeration, Paris, France.

Schneider, H.W., 1978, "*Equation of the growth rate of frost forming on cooled surfaces.*" International Journal of Heat Mass Transfer, Vol. 21.

Smith, R.V., D.K. Edmunds, E.G.F. Brentari, and R.J. Richards, 1964a, "*Analysis of the frost phenomena on a cryosurface.*" Advances in Cryogenic Engineering, Vol. 9, pp. 88-97. New York: Plenum Press.

Smith, R.V., D.K. Edmunds, E.G.F. Brentari, and R.J. Richards, 1964b. "*Analysis of the frost phenomena on a cryo-surface.*" Journal of Franklin Institute, Vol. 277, No.3, pp. 293-294, March.

Free convection to flat plate studies:

Whitehurst, C.A., 1962b, "*An investigation of heat and mass transfer by free convection from humid air to a metal plate under frosting conditions.*" Ph.D. dissertation, Mechanical Engineering Dept., Agricultural and Mechanical College of Texas, College Station, TX

Barron, R.F., and L.S. Han, 1965, "*Heat and mass transfer to a cryo-surface in free convection.*" Journal of Heat Transfer, Vol. 87, No.4.

Mulligan, J.G., 1967, "*Properties of frost forming on a cold plate in still air.*" Ph.D. dissertation, Tulane University, New Orleans, LA.

Mulligan, J.G., 1968, "*Model for heat transfer in frost and snow.*" Journal of Geophysical Research, Vol. 73, No.8.

Tajima, O., H. Yamada, Y. Kobayashi, and C. Mizutani, 1972, "*Frost formation on air coolers-part I: natural convection for a cooled plate facing upward.*" Heat Transfer Japanese Research, Vol. 1, No.2, pp. 39-48.

Tajima, O., E. Naito, Y. Tsutsumi, and H. Yoshida, 1973, "*Frost formation on air coolers-part 2: natural convection for a flat plate facing downwards.*" Heat Transfer Japanese Research, Vol. 2, No.4.

Tajima, O. E. Naito, K. Nakashima, and H. Yamamoto, 1974, "*Frost formation on air coolers-part 3: natural convection for the cooled vertical plate.*" Heat Transfer Japanese Research, Vol, 3, No.4.

Tajima, O., E. Naito, T. Goto, S. Segawa, and K. Nishimura., 1975, "*Frost formation on air coolers--part 4: natural convection for two vertically opposed cooled plates.*" Heat Transfer-Japanese Research, Vol. 4, No.3.

Goodman, J., and L.A. Kennedy., 1972, "*Free convection frost formation on cool surfaces.*" Proceedings 1972 Heat Transfer and Fluid Mechanics Institute, CA: Stanford University Press.

Forced convection to flat plate studies:

Abdel-Wahed, R.M., M.A. Hifni, and S.A. Sherif., 1984, "*Heat and mass transfer from a laminar humid air stream to a plate at subfreezing temperature.*" International Journal of Refrigeration, Vol. 7, No.1.

Coles, W., and R. Ruggei., 1954, "*Experimental investigation of sublimation of ice at subsonic and supersonic speeds and its relation to heat transfer.*" National Advisory Committee for Aeronautics, TN 3104.

Glomb, J.W., and L.A. Wenzel., 1964, "*Forced convection frost deposition on a cold horizontal surface.*" AIChE Paper No. 25b, American Institute of Chemical Engineers 53rd National Meeting.

Hosoda, T. and H. Uzuhashi., 1967, "*Effects of frost on the heat transfer coefficient.*" Hitachi Review, Vol. 16, No. 6.

Jones, B.W., and J.D. Parker., 1975, "*Frost formation with varying environmental parameters.*" Journal of Heat Transfer, Vol. 97, No.2.

Lee, K., W. Kim, and T. LEE., 1997, "*A one dimensional model for frost formation on a cold flat surface*" International Journal of Heat Mass Transfer. Vol. 40, No. 18.

Lee, K., S. Jhee, and D. Yang., 2003, "*Prediction of the frost formation on a cold flat surface*" International Journal of Heat Mass Transfer. Vol. 46, pp. 3789-3796

Seker, D., H. Karatas, and N. Egrican., 2004a "*Frost formation on fin-and-tube heat exchangers. Part I- Modeling of frost formation on fin-and-tube heat exchanger.*" International Journal of Refrigeration, Vol. 24

Seker, D., H. Karatas, and N. Egrican., 2004b "*Frost formation on fin-and-tube heat exchangers. Part II- Experimental investigation of frost formation on fin-and-tube heat exchanger.*" International Journal of Refrigeration, Vol. 27

Sherif, S.A., R.M. Abdel-Wahed and M.A. Hifni., 1988, "*A mathematical model for the heat and mass transfer on a flat plate under frosting conditions.*" ASME Proceedings of the 1988 National Heat Transfer Conference, HID-Vol. 96, Vol. 3.

Tao, Y., R. Besant, and Y. Mao., 1993, "*Characteristics of frost growth on a flat plate during the early growth period*" ASHRAE Transaction, Vol. 99, part 1.

Trammel, G.J., D.C. Little, and E.M. Killgore., 1968, "*A study of the frost formed on a flat plate held at sub-freezing temperatures.*" ASHRAE Journal, Vol. 10, No.7, July.

Wagner, W.B., 1963, "*Frost formation on an extended surface heat exchanger in cross-flow of humid air.*" M.S. thesis, Ohio State University, Columbus.

Yonko, J.D., 1965, "*An investigation of the thermal conductivity of frost while forming on a flat horizontal plate.*", M.S. thesis, Ohio State University, Columbus.

Yonko, J.D., and C.F. Sepsy., 1967, "*An investigation of the thermal conductivity of frost while forming on a flat horizontal plate.*" ASHRAE Transactions, Vol. 73, Part 2.

Appendix B

Table B.1: The key assumption made by Kondepudi et al. (1991) to develop a numerical model of frost formation for a finned-tube heat exchanger

1.	all local heat transfer surface temperatures are below frost point,
2.	there is a homogeneous distribution of frost on the entire heat exchanger coil,
3.	the problem is assumed to be quasi-steady state in nature,
4.	the frost layer is to be characterized by average properties,
5.	the thermal conductivity of frost varies with its density,
6.	radiation exchange between the moist air and frost is negligible.

Table B.2: The heat exchanger geometry and operating conditions used by Kondepudi et al. (1991)

Parameter	Value
Tube material	Copper
Fin material	Aluminum
Number of tube row	1
Tube diameter	9.525mm
Tube wall thickness	0.5 mm
Tube spacing	25.4 mm
Row spacing	22 mm
Number of fins	591
Number of tubes	18
Face area	0.209 m ²
Ambient temperature	0°C
Inlet relative humidity	85 %
Face velocity	0.762 ms ⁻¹
Evaporation temperature	-5°C

Table B.3: Heat exchanger geometry and operating conditions used by Yao et al. (2004)

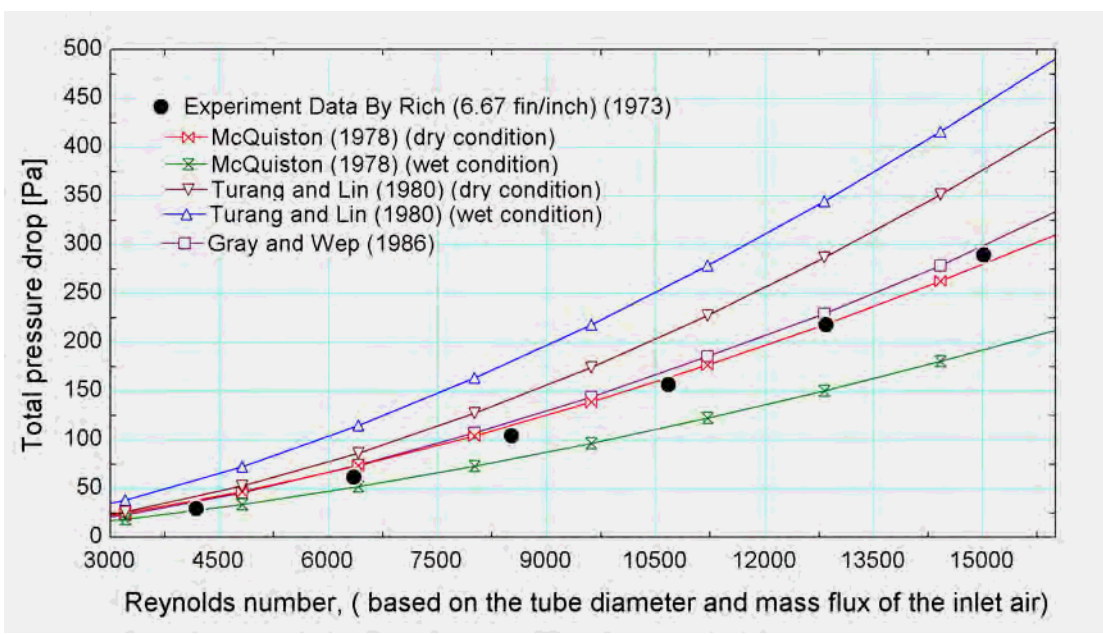
Parameter	Value
Tube material	Copper
Fin material	Aluminum
Number of tube row	4
Tube diameter	10
Tube spacing	25.4 mm
Row spacing	22 mm
Fin pitch	2 mm
Single pipe length	16 m
Number refrigerant circuits	10
Ambient temperature	-4 and 1.5 C
Relative humidity	65,75 and 85 %
Air flow	1061.3 m ³ /h
Evaporation temperature	-13C
Flow of refrigerant	0.0096 and 0.00816 kg/s

Table B.4: Heat exchanger geometry and operating conditions used by Oskarsson et al. (1990)

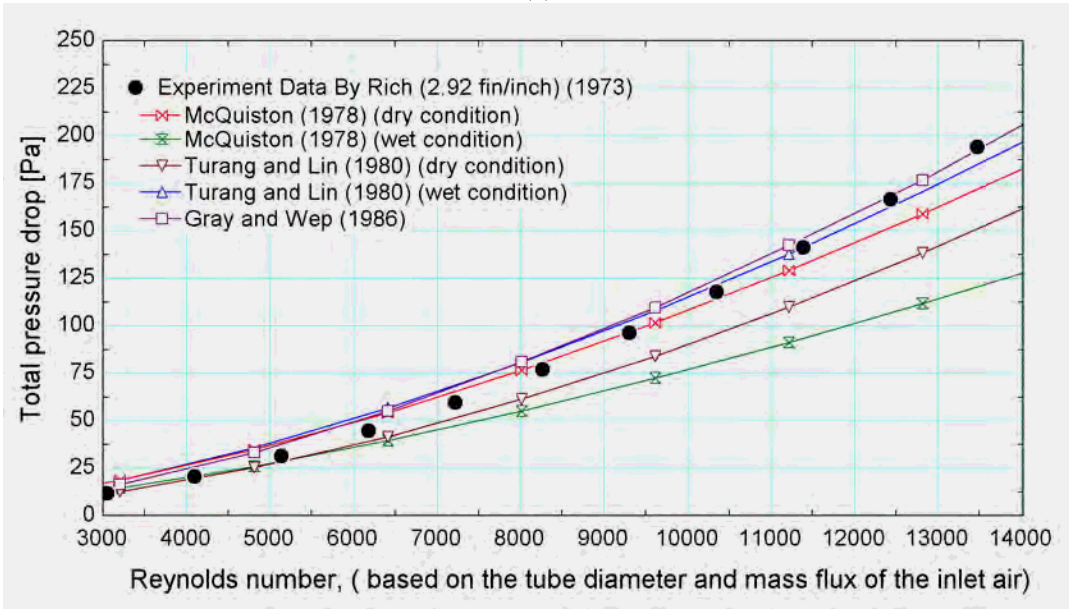
Parameter	Value
Face area	0.37 m ²
Number of tubes	24
Number of tube row	6
Tube diameter	12.7
tube length	9.37 m
Fin pitch	8/inc
Ambient temperature	1 C
Relative humidity	65,75 and 85 %
Air flow rate	2557 kg/h
Evaporation temperature	-13C
Flow of refrigerant	24.27kg/h

Appendix C

Air side pressure drop and heat transfer coefficient:

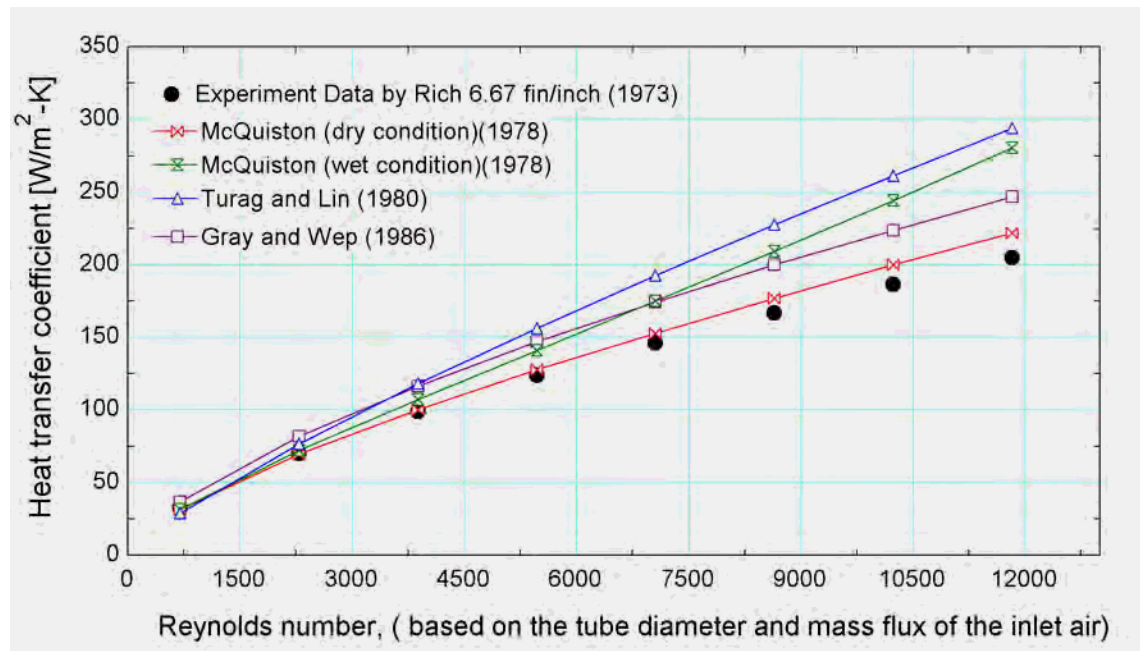


(a)

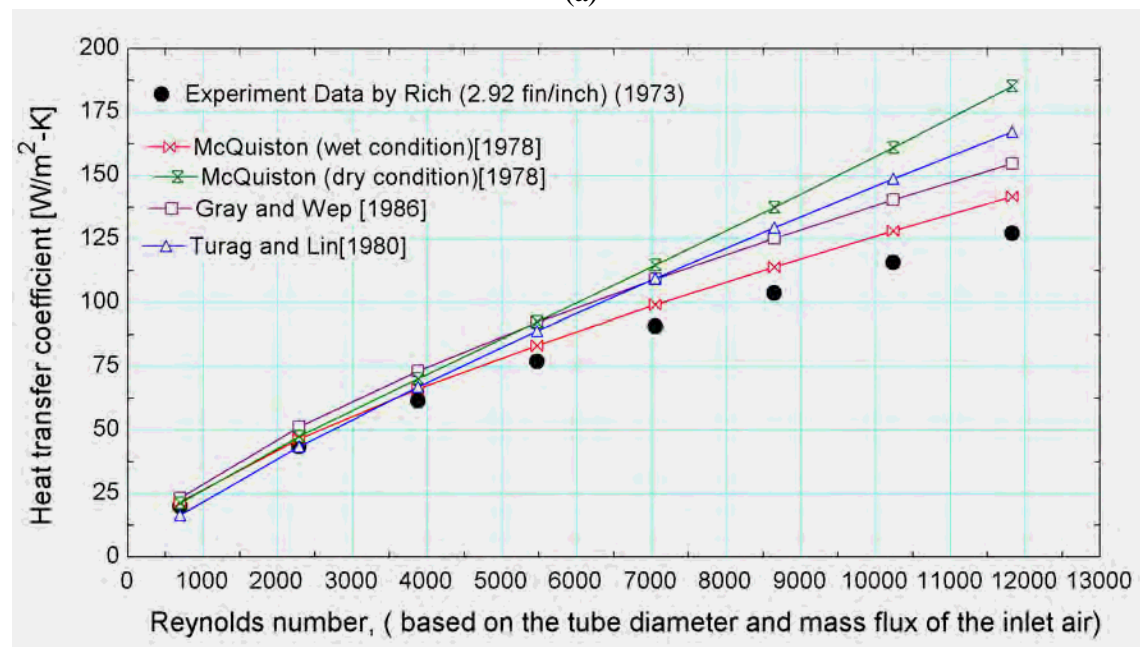


(b)

Figure C.1 Air side pressure drop (calculated using the friction factor predicted by the various correlations shown in the figure) versus the Reynolds number (calculated based on the coil tube diameter and the inlet air mass flux) and compared to experimental data provided by Rich (1973) for (a) 6.67 fpi and (b) 2.92 fpi.



(a)



(b)

Figure C.2 Air side convective heat transfer coefficient predicted by the various correlations shown in the figure versus the Reynolds number (calculated based on the coil tube diameter and the inlet air mass flux) and compared to experimental data provided by Rich (1973) for (a) 6.67 fpi and (b) 2.92 fpi.

Gray, D.L., and Webb, R.L., 1986, "Heat transfer and friction correlations for plate finned-tube heat exchangers having plain fins," International Heat Transfer Conference, 8th.

McQuiston, F.C., 1978, "Heat, mass and momentum transfer data for five plate-fin-tube heat transfer surfaces," ASHRAE Transactions, Vol, 84, Part 1.

Rich, D.G., 1973, "The Effects of Fin Spacing on the Heat Transfer and Friction Performance of Multi-Row, Smooth Plate-Fin-Tube Heat Exchangers," ASHRAE Transactions, Vol, 79, Part 2.

Turag, M., Lin, S., 1980, "Correlations for heat transfer and pressure drop factors for direct expansion air cooling and dehumidifying coils"

Refrigerant pressure drop:

Table C-1 Comparison of percentage of average relative error RE and the percentage of predicted values within $\pm 10\%$ and $\pm 30\%$ between the various correlation and data for pure fluids obtained by Muller and Heck (1986). The table was prepared by Muller and Heck (1986).

Reference	RE (%)	RE < 10% (%)	RE < 30% (%)
Bandel (1973)	32.6	25.8	59.9
Bankoff (1960)	11525.8	7.5	16.4
Chawla (1967)	8697.6	5.5	15.3
Chawla-Bankoff (1974)	142.3	18.1	40.9
Chisholm-Baroczy (1973)	340.0	16.5	38.2
Cicchitti(1960)	65.7	15.8	42.0
Dukler(1964)	37.0	14.7	43.9
Friedel(1979)	111.6	18.1	44.6
Gronnerud(1972)	44.6	16.0	46.5
Kesper-Moussalli(1983)	69.9	12.5	29.9
Lockhart-Martinelli(1949)	62.8	21.0	52.4
Lombardi-Pedrocchi(1972)	152.3	14.2	29.5
Reza-Chavez(1985)	35.5	18.1	54.6
Storek-Brauer(1980)	36.5	22.2	58.7
Muller and Heck (1986)	41.9	17.3	49.5

Muller, H., Heck, K., 1986, "A simple friction pressure drop correlation for tow phase flow heat transfer of ammonia," Chemical Engineering Processing, Vol.20, No.6

Refrigerant convective heat transfer:

Table C-2: Comparison of percentage deviation between the various correlation and data for pure fluids obtained by Jung (1989). The table was prepared by Jung (1989).

Fluid	# of data points	Chen(1963)		Shah(1982)		Gunggor & Winterton (1986)		Jung(1989)	
		Mean	Ave.	Mean	Ave.	Mean	Ave.	Mean	Ave.
R22	378	16.7	14.3	13.0	-11.0	15.0	3.62	5.77	-0.7
R114	198	12.8	6.16	11.3	-10.3	13.6	4.6	9.3	3.0
R12	286	15.3	9.0	12.9	-10.5	17.3	4.35	7.6	0.5
R152a	376	17.4	14.4	12.3	-10.3	21.4	10.8	7.4	-3.3
R500	350	14.8	8.0	13.9	-12.7	18.3	3.9	7.82	-1.7
All	1588	15.7	7.8	12.8	-11.0	17.5	5.64	7.2	-0.89

Jung, D.S., Didion, D.A., 1989, "Horizontal Flow Boiling Heat Transfer using Refrigerant Mixtures," ER-6364, EPRI Project 8006-2.

Frost thermal conductivity

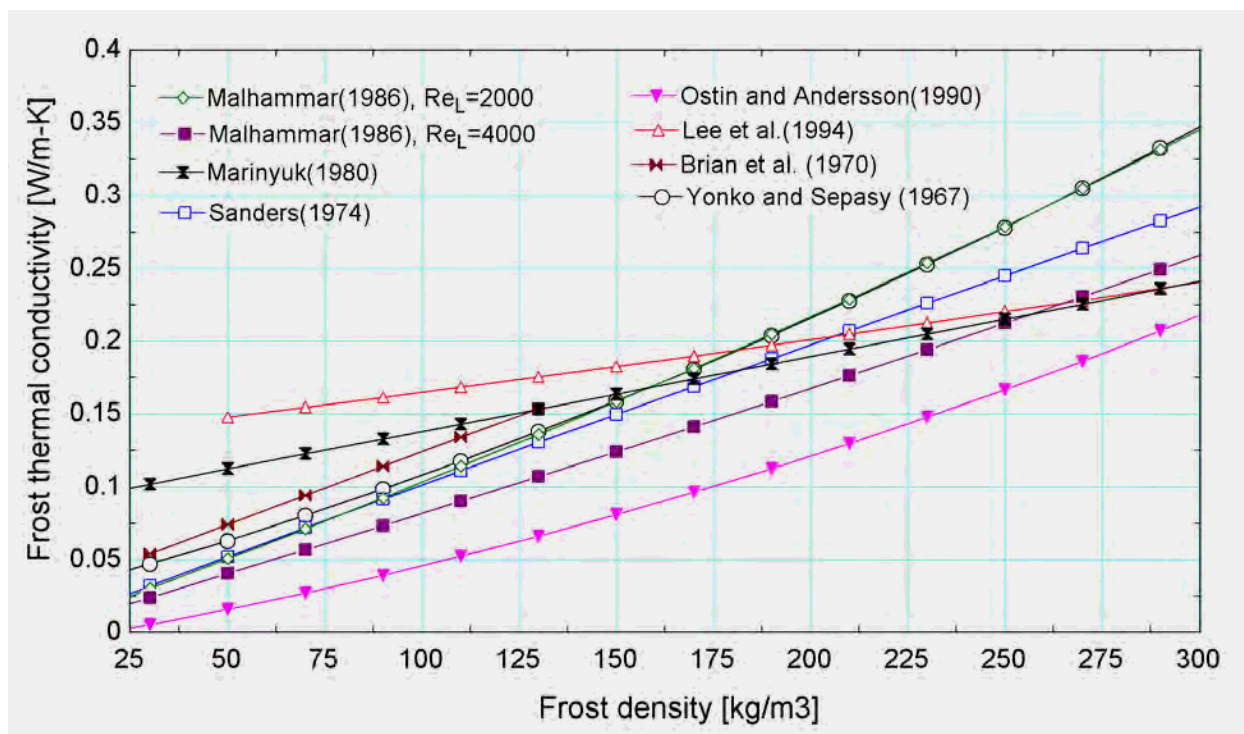


Figure C.3: Frost conductivity as a function of frost density predicted by the various correlation shown in the figure.

Malhammar, A., 1986, "Frostpaslag via flansade ytor," Doktorsav handling, Kungliga Tekniska Hogskolan, Stockholm, Sweden

Marinyuk, B.T., 1980, "*Heat and mass transfer under frosting conditions,*" International Journal of Refrigeration, Vol. 3, No. 6.

Sanders, C.T., 1974, "Frost formation: the influence of frost formation and defrosting on the performance of air coolers," PhD. Thesis, Technische Hogeschool, Delft, The Netherlands.

Ostin, R., Andersson, S., 1990, "*Frost growth parameters in a frosted air stream,*" International Journal of Heat and Mass Transfer, Vol. 34, No.45.

Lee, K.S., Lee, T.H., Kim, W.S., 1994, "*Heat and mass transfer of parallel heat exchanger under frosting condition,*" SAREK journal, Vol. 6 No. 2.

Brian, P.L.T, Reid, R.C., Shah, T.T., 1970, "*Frost deposition on cold surfaces,*" Industrial and Engineering Chemistry Fundamentals, Vol.9, No.3.

Yonko, J.D., and Sepsy, C.F., 1967 "*An investigation of the thermal conductivity of frost while forming on a flat horizontal plate*", ASHRAE transaction. Vol.99, No. 5

Appendix D

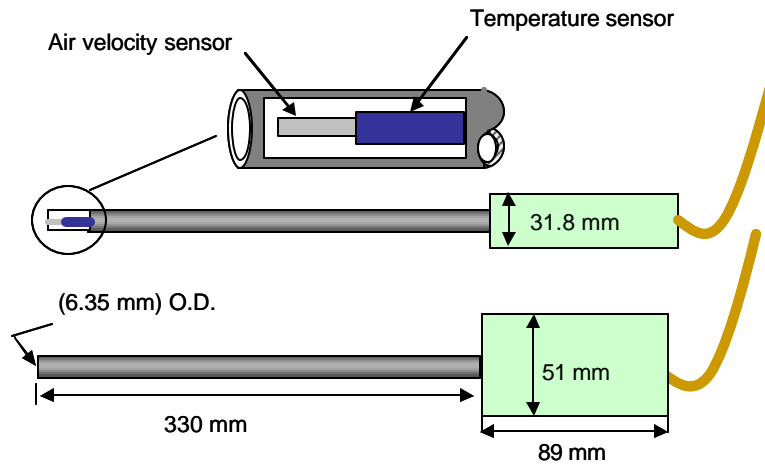


Figure D.1: Schematic showing the air velocity mass flow transducer

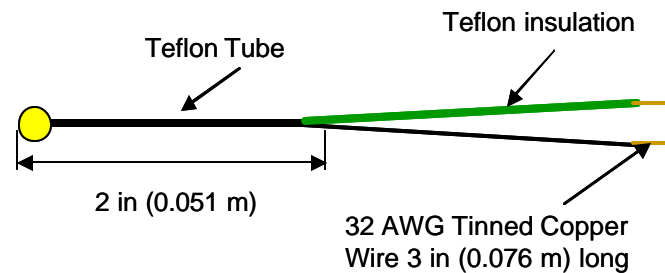


Figure D2: Schematic showing the thermistor

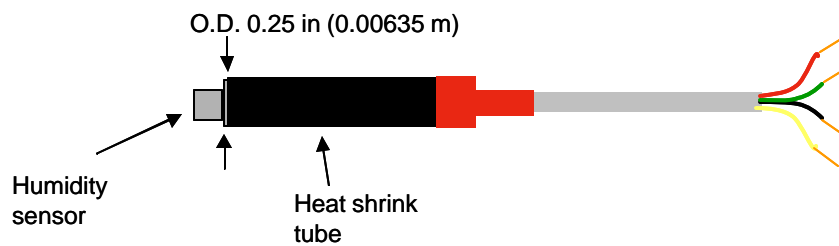


Figure D3: Schematic showing the relative humidity sensor

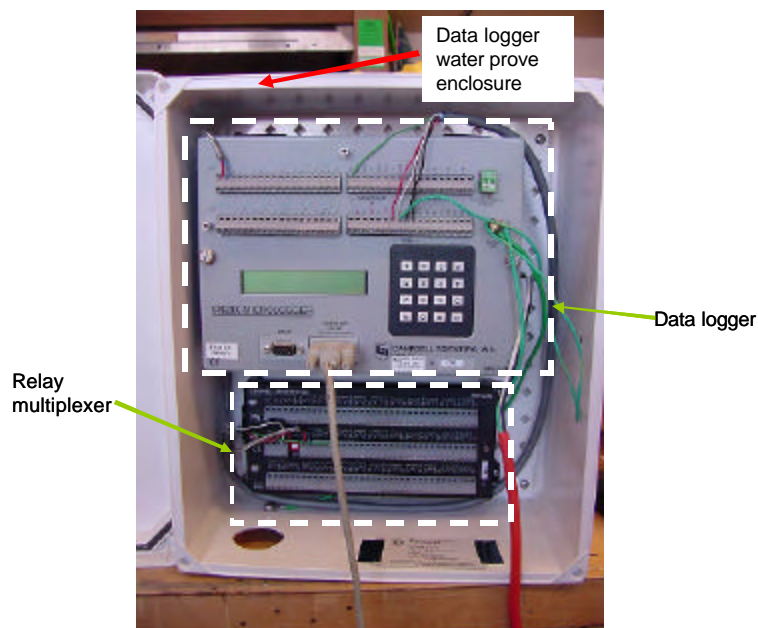


Figure D.4: Photograph for the data-logger and the multiplexer enclosure.

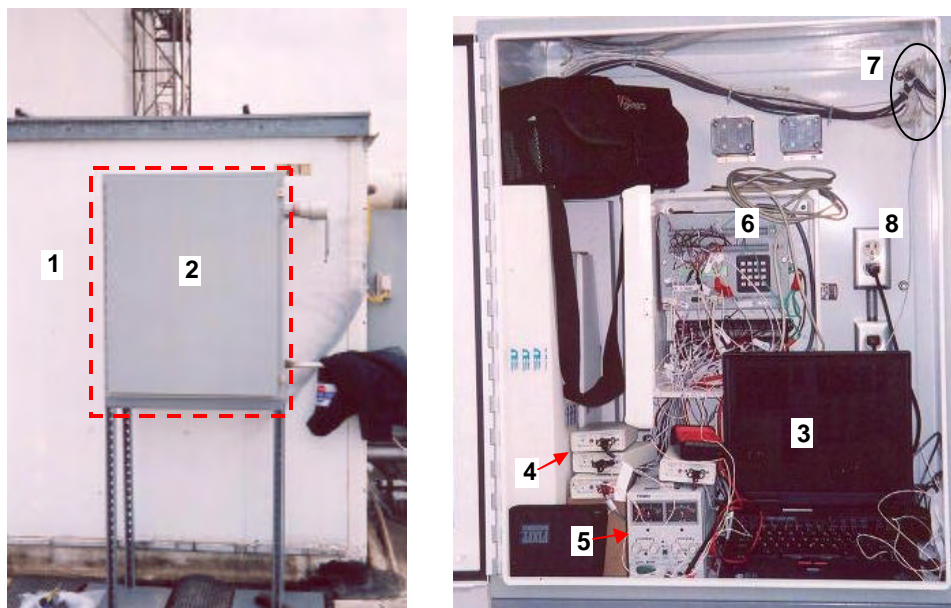


Figure D.5: Photograph for the instrument enclosure; 1) penthouse, 2) instrument enclosure, 3) computer, 4) current supplies for the thermistors, 5) power supply for the air velocity meters, 6) data logger, 7) wiring from inside the penthouse to the data logger, and 8) power supply for the data logger.

Run # 3					
Time min	T_{inave} °C	T_{oave} °C	V_{ave} m/s	RH_{inave} %	RH_{oave} %
0	-27.73	-30.87	2.87	90.34	91.85
60	-27.66	-30.73	2.84	90.20	91.74
120	-27.49	-30.54	2.78	90.14	91.75
180	-27.44	-30.60	2.71	90.00	91.73
240	-27.67	-30.90	2.66	89.75	91.5
300	-27.81	-30.99	2.60	89.63	91.28
360	-27.83	-31.02	2.55	89.55	91.05
420	-27.81	-31.08	2.51	89.46	90.93
480	-27.72	-31.04	2.47	89.42	90.74
540	-27.80	-31.17	2.44	89.28	89.75
600	-27.97	-31.37	2.42	89.10	88.13
660	-28.05	-31.46	2.40	88.98	86.75
720	-28.02	-31.43	2.34	88.93	85.16
780	-27.94	-31.44	2.30	88.85	85.03
840	-27.92	-31.50	2.30	88.75	85.19
900	-28.08	-31.62	2.29	88.61	83.48
960	-28.26	-31.79	2.27	88.47	81.85
1020	-28.25	-31.83	2.27	88.41	81.32
1080	-28.12	-31.70	2.27	88.46	82.61
1140	-27.97	-31.61	2.24	88.49	84.88
1200	-27.75	-31.55	2.17	88.51	86.74
1260	-27.61	-31.54	2.10	88.49	87.32
1320	-27.61	-31.53	2.03	88.47	86.69
1380	-27.79	-31.71	1.96	88.34	85.26
1440	-27.86	-31.86	1.95	88.23	85.44
1500	-27.63	-31.68	1.92	88.30	87.77
1560	-27.46	-31.56	1.88	88.35	89.27
1620	-27.55	-31.57	1.87	88.34	87.28
1680	-27.70	-31.66	1.87	88.27	84.24
1740	-27.61	-31.62	1.85	88.27	84.52
1800	-27.52	-31.65	1.83	88.23	85.06
1860	-27.50	-31.70	1.82	88.19	85.69
1920	-27.43	-31.59	1.80	88.23	86.28
1980	-27.43	-31.69	1.78	88.14	85.45
2040	-27.57	-31.80	1.77	88.03	84.13
2100	-27.64	-31.82	1.77	87.99	83.91
2160	-27.59	-31.85	1.75	87.93	84.57
2220	-27.43	-31.74	1.73	87.97	86.57
2280	-27.32	-31.80	1.70	87.91	87.83
2340	-27.53	-32.12	1.66	87.68	85.07
2400	-27.78	-32.35	1.63	87.51	82.31
2460	-27.84	-32.41	1.61	87.44	82.24
2520	-27.73	-32.40	1.60	87.41	84.07

Run # 4				
T_{inave} °C	T_{oave} °C	V_{ave} m/s	RH_{inave} %	RH_{oave} %
-27.73	-30.71	2.83	90.63	92.19
-27.75	-30.74	2.82	90.35	92.06
-27.78	-30.81	2.79	90.12	91.97
-27.86	-30.92	2.77	89.93	91.83
-27.99	-31.10	2.75	89.74	91.62
-27.96	-31.14	2.74	89.63	91.53
-27.80	-30.97	2.70	89.67	91.47
-27.65	-30.81	2.62	89.71	91.47
-27.56	-30.88	2.51	89.63	91.48
-27.50	-30.95	2.43	89.51	91.28
-27.61	-31.06	2.38	89.38	90.52
-27.67	-31.17	2.33	89.25	90.04
-27.67	-31.20	2.28	89.17	89.57
-27.77	-31.27	2.24	89.08	88.82
-27.72	-31.22	2.22	89.05	88.24
-27.68	-31.22	2.23	89.02	87.13
-27.83	-31.39	2.26	88.89	85.06
-28.03	-31.64	2.30	88.69	82.8
-27.94	-31.62	2.29	88.64	83.52
-27.73	-31.39	2.25	88.74	85.79
-27.53	-31.23	2.19	88.81	87.02
-27.41	-31.17	2.11	88.81	87.26
-27.5	-31.26	2.04	88.74	85.98
-27.68	-31.39	1.96	88.65	84.40
-27.79	-31.42	1.92	88.59	83.93
-27.70	-31.34	1.91	88.61	84.87
-27.58	-31.22	1.91	88.67	85.32
-27.64	-31.29	1.89	88.73	84.93
-27.83	-31.56	1.86	88.59	83.09
-27.9	-31.71	1.86	88.39	81.99
-27.76	-31.66	1.87	88.38	83.17
-27.57	-31.38	1.85	88.52	83.99
-27.35	-31.19	1.83	88.61	85.14
-27.34	-31.37	1.83	88.47	85.11
-27.59	-31.68	1.80	88.24	83.39
-27.72	-31.78	1.78	88.14	83.28
-27.55	-31.64	1.74	88.18	85.57
-27.43	-31.62	1.73	88.16	86.84
-27.43	-31.69	1.74	88.09	86.46
-27.52	-31.80	1.71	87.99	85.07
-27.76	-32.04	1.67	87.82	82.25
-27.87	-32.15	1.65	87.72	80.78
-27.73	-32.08	1.62	87.72	83.19

Run # 5					
Time min	T_{inave} °C	T_{oave} °C	V_{ave} m/s	RH_{inave} %	RH_{oave} %
0	-27.05	-30.35	2.88	90.89	92.39
60	-27.31	-30.52	2.88	90.55	92.04
120	-27.32	-30.52	2.86	90.37	91.90
180	-27.37	-30.57	2.82	90.19	91.71
240	-27.53	-30.74	2.79	89.97	91.38
300	-27.73	-31.03	2.78	89.71	90.94
360	-27.81	-31.15	2.76	89.55	90.39
420	-27.78	-31.10	2.71	89.51	89.17
480	-27.69	-31.05	2.63	89.50	88.29
540	-27.66	-31.08	2.55	89.43	87.59
600	-27.79	-31.29	2.50	89.24	85.75
660	-27.92	-31.45	2.48	89.07	83.30
720	-27.88	-31.43	2.47	89.00	82.30
780	-27.82	-31.45	2.46	88.92	81.72
840	-27.75	-31.52	2.35	88.84	82.33
900	-27.66	-31.40	2.28	88.84	83.16
960	-27.73	-31.34	2.34	88.79	82.46
1020	-27.85	-31.48	2.34	88.65	81.76
1080	-27.88	-31.53	2.33	88.58	81.44
1140	-27.81	-31.54	2.30	88.54	82.37
1200	-27.76	-31.57	2.27	88.51	83.00

Appendix E